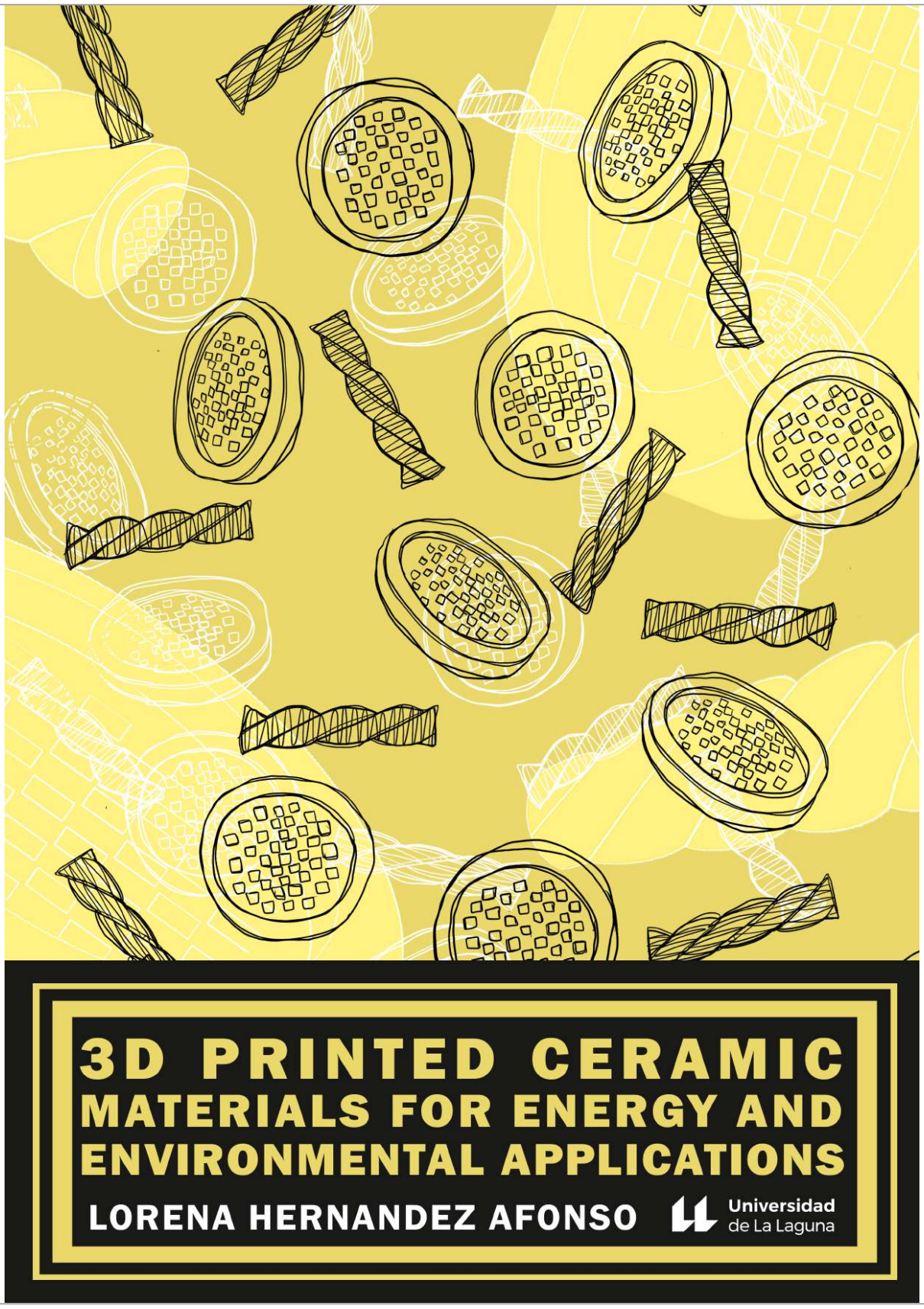

3D Printing ceramic materials for energy and environmental applications

Lorena Hernández Afonso

A thesis submitted for the Degree of Philosophical Doctor (PhD) in Chemistry of the University of La Laguna

Supervisors

Dr. Albert Tarancón Rubio – Director

Dr. Jesús Canales Vázquez – Codirector

Dr. Pedro Carlos Esparza Ferrera – Codirector and Tutor

November 2020

Somos inmortales cuando transmitimos y dejamos huella en otros, para

que nuestro eco siempre sea eterno.

- No es por ti

Jairo Adrián Hernández

A Juan Carlos Ruiz Morales,

mentor, compañero y todo un ejemplo a seguir.

Gracias por todo.

ACKNOWLEDGEMENTS / AGRADECIMIENTOS

Probablemente, escribir esta parte de la tesis sea la más dura a la que me haya enfrentado hasta ahora, debido a que ha llegado el momento en el que tengo que buscar palabras para agradecer a todas esas personas que me han ayudado y apoyado durante esta parte tan importante de mi vida profesional, aun sabiendo que la gratitud es tanta, que unas simples líneas se quedarán cortas para lo que realmente siento.

No sabía agradecerte al primero o al último, pero si hago una retrospectiva de este momento y me remonto al origen de todo, tu nombre es el primero que aparece. Juan Carlos, por desgracia la frase de "no tendré vidas suficientes para agradecerte todo" es más real que nunca, pero quiero que quede constancia en que si a alguien le debo agradecer es a ti. Por esa reunión hace cinco años en los que la idea de empezar una tesis brotó en ese despacho. Por tu *pofesionalidad*, por enseñarme a investigar sin perder el lado personal del que la investigación muchas veces nos priva. Por no perder tu alegría, tu determinación y tus mil y unas soluciones para los problemas, haciendo fácil lo difícil. Gracias por confiar en mí, por ser ese director *unicornio* del que hablan en los libros y por haberme permitido creer en la magia de las personas que se dedican a esto. Porque, aunque hagamos ciencia, lo que llevamos dentro para seguir con la misma emoción del principio es pura pasión y la tuya era mágica. Ojalá haberme despedido, aunque no supiese cómo. Pero si de algo estoy segura es que has sido el mejor ejemplo a seguir, al que guardaré siempre en mi corazón y en mi memoria. Mil e infinitas veces, gracias de corazón.

Jesús contigo no me quiero quedar corta tampoco. He visto muchas veces la personalidad de Juan Carlos reflejada en la tuya y eso se ha sentido como arropo para el frío. Gracias por estar ahí desde el principio, por ese apoyo incondicional. Pero tener esa personalidad que vale oro y mostrarte humano en el mundo de la investigación. Admiro tu carrera, tu trabajo y tu humildad, porque a pesar de haber llegado a lo alto, tratas a las personas como un igual. Gracias por mirar los detalles, por enseñarme que "todo cuenta" que nuestro trabajo es generar conocimiento y también por enseñarme a no perderme tras una máscara de resultados sólo positivos. Además, no puedo olvidar agradecerte tus *english tips*, por tu paciencia, y por no haber cerrado el documento de la tesis después de haberte encontrado por septuagésima quinta vez *corroborated* en lugar de *confirmed*. Y, sobre todo, gracias por haberme hecho sentir en casa cuando estaba a kilómetros de la mía. Soy consciente de la suerte que he tenido de tenerte en como codirector.

Pedro, gracias por adoptarme tras el desastre, por tener palabras de calma para los problemas e incluso ese toque de humor que no hay que perder ante las personas que se dedican a generar angustias en lugar de solventarlas. Y gracias por darme la libertad y el apoyo científico del que me habría brindado Juan Carlos.

Albert, agradecerte a ti también el haber acudido a mi rescate. Jamás sabréis lo muy apoyada que me sentí en esos momentos. Gracias por enseñarme la determinación necesaria para esta carrera, por acogerme en el IREC en varias ocasiones, y por esos emails de apoyo.

A la Universidad de La Laguna por ser mi casa, en especial a todo el personal del área de química inorgánica, por ampararme durante este tiempo y los docentes por darme la base de lo que es mi carrera profesional. Dentro del área de química inorgánica, quiero agradecer especialmente a Selene por aguantarme durante todos tantos años y haber dado alegría al laboratorio; a Luis, Conchi y Fran por acudir siempre a las llamadas de socorro; a Pili e Isa por ser ese abrazo cálido dentro de la fría facultad; a Asun, Manolo y Beatriz, por tener siempre una respuesta administrativa además de una gran sonrisa; al personal de seguridad del campus Anchieta, porque tras los años terminaron por aprenderse mis rutas cuando iba fuera de hora y hacían que ir a trabajar los fines de semana o en vacaciones valiese la pena, porque al menos habría alguien esperando con una sonrisa y un "que sea leve". Además agradecer a Diego y David, por recibir las propuestas con los brazos abiertos, tener una filosofía de trabajo similar a la mía y por marcar la diferencia.

Agradecer a todo el personal del IREC, del Instituto de Energía Renovables de la UCLM, al personal de la DTU del campus Risø y al equipo de trabajo de la Universidad de St. Andrews, porque todos tuvisteis que dejar a un lado vuestro trabajo para echarme una mano durante mis estancias.

A Arianna, por ser compañera y amiga de tesis, por ser la única que me entiende cuando me he desahogado de la guerra que han dado las impresoras, por ser pañuelo de lágrimas y también por estar siempre disponible para todo. Gracias por ser la única que puede entender lo que significa salir del laboratorio con pasta blanca en el pelo o en las gafas, y abolir palabras a cambios de abrazos. Has sido muy importante para mí estos dos últimos años, y admiro tu destreza y tu forma de trabajar tan organizada, constante y con una meta fija, para terminar esto de la mejor manera.

A mi otra amiga de estancia, Anna, llegaste como agua de mayo a St. Andrews y si la despedida fue dura es porque tú estabas ahí. Creo que ignoras cuán de apoyo fuiste durante esos meses, gracias de verdad. Y a mis compañeros Andrea, Carlos y Mahmood por haber compartido risas cuando todos éramos huéspedes en un nuevo país.

Al personal técnico del SEGAI, en especial a Juan Luis y Marcos, por recibirme con los brazos abiertos siempre y por estar ahí desde antes de empezar esta batalla.

A Emma Borges del Dpto. de Ingeniería química por contribuir a visibilizar las aplicaciones ingenieriles de la impresión 3D.

A estas alturas, me gustaría agradecer también a mis compañeros y amigos de carrera. En su momento no agradecí porque mi camino en la universidad seguía, pero ahora termina. A Manu,

Adrián, Idaira, Priscila, Helena, Ale Gomero, por compartir más que risas entre esas cuatro paredes y fuera. Y en especial a Carmen, si algo bueno me ha dado la carrera fuiste tú, estas líneas se quedan cortas, pero me quedo tranquila sabiendo que la Lorena del pasado se intensificaba a base de cartas, gracias por esa esa familia dentro de la uni durante esos años.

Y hablando de familia, a mi familia reciente de la universidad, a ese grupito que llegó a mi vida justo en el momento más difícil del doctorado y fuisteis la razón para levantarme cada día y e ir a trabajar con ganas, a Eva, Fer y Jacque, por haber hecho del depar un hogar, y sobre todo por acompañarme tantas horas en la que la soledad se apoderaba de esta doctoranda. De verdad, no sabéis lo que para mí ha significado poder sentarme a comer en familia estando en el depar, dentro de nuestro tan querido y polémico *"guachinche"*, hablar de cómo nos ha ido el día y buscar de dónde sacar un momento de risas. Al igual que todas aquellas personas que han hecho que esta familia aumentase, Brenda y Yara.

Agradecer también a David Ujja, por tu disposición y profesionalidad al realizar la ilustración de esta tesis. Amigo, tu trabajo vale mucho.

Para ir finalizando me centraré en algo más personal, en esas personas que han estado ahí sin estar vinculados a mi carrera. A mis amigos de siempre, a Luis, Ana, Desi, Dani, Vane y Marbe, Alba, Cristi e Inés. Llevamos más de una década juntos, y si algo me ha quitado el doctorado es tiempo para compartir con ustedes. Hemos madurado juntos y las anécdotas son infinitas. Gracias por ser esa familia que uno escoge.

A Jairo, porque tú perteneces a esa familia que uno escoge, pero esta batalla la hemos luchado juntos. A pesar de que nuestros bandos sean antiguos enemigos (Letras vs Ciencias) la investigación nos ha unido más que nunca. Hemos tenido que ir sorteando los baches de la investigación, lo cual nos ha llevado a estar a kilómetros de casa. Sin embargo, fuiste esas palabras de aliento que llegaron en un momento duro, esas palabras a las que he recurrido numerosas veces cuando han dado ganas de tirar la toalla… para eso amigo, no tendré suficientes palabras para agradecértelo. Solo yo sé que si algo me hacía ilusión es poder entrar juntos a ese nombramiento de nuevos doctores de la ULL y poder lucir esos colores, que, a pesar de ser distintos, tienen de base el azul, representando la unión entre nosotros a pesar de las diferencias.

A Belén y Julia por haber significado tanto en esos momentos donde he necesitado dejar de lado el doctorado a base de palas.

A mi familia, tanto de Tenerife como Barcelona, os quiero. También agradecer Monste, por ser mi nueva familia, por hacer de su hogar el mío tantas veces y tratarme como una hija más.

A mis pequeños hermanos no de sangre, Paula y Eduardo. Porque el tiempo y la educación ha hecho que formemos lazos irrompibles.

Y por último a mis pilares. Sin ellos tengo claro de que no hubiese llegado aquí ni de lejos. A Alejandro por estar ahí más de la mitad de mi vida y verme crecer. A mi hermano Alelu, no sabes lo orgullosa que estoy de ti, aunque el saber que me tengas de referencia me pone mucha presión. Ten claro que si algo se quiere se puede, aunque eso no significa que sea fácil. Eso es lo mejor que te puedo enseñar de la vida, la constancia y luchar por las metas y este trabajo es fruto de esa filosofía. Te apoyaré siempre, te quiero.

A Eva, mi cosmos. Gracias por estar ahí de verdad, por apoyarme en mis decisiones, por llorar conmigo, por robarme risas y momentos que no se desprenderán nunca de mi retina, por hacerme fuerte y hacerte la fuerte cuando la cosa se ponía dura. Si algo me ha regalado el doctorado, has sido tú. Nos queda todo un universo para descubrir el resto de nuestras vidas, y contigo sé que podremos enfrentar todo lo que se venga por delante, incluso llegar a recordar esta época de estrés tras los años sentadas en nuestro sillón. Te quiero.

Y, por último, pero no menos importante, a mi madre. Mamá sin ti no sería quién soy ahora. La constancia, la determinación, el plantarle cara a la vida, el luchar ante las injusticias…eso me lo has enseñado tú. No lo has tenido fácil, sin embargo, tu trabajo ha sido impecable. Eres el mayor ejemplo de mi vida y serás siempre incondicional en ella. El gracias contigo se queda muy corto. Te quiero.

ABSTRACT

New activities that arose during the Industrial Revolution caused the development of novel production sector, changes in the organisation of production, new forms of capital business, development of a global market and the use of new energy sources. However, it also led to the use of fossil fuels that in the long-term brought severe environmental issues due to diverse activities carried out during the revolution. Nowadays, it is known that these activities are the cause of the current environmental crisis involving a fast climate change and global warming. Most of the environmental problems, i.e. degradation of the ozone layer, acid rain, air and water pollution or waste reduction, cannot be managed by a single nation. Consequently, a lot of countries have implemented many agreements last decades with the purpose of the Zero Emission concept, trying to promote synergistic processes with very low impact on the environment and reducing the volume of waste and harmful emission without affecting the industrial benefits.

Over the last years, a lot of research groups have been focused on the development of new materials and new manufacturing techniques in order to achieve this environmental goal. This thesis is focused on the introduction of new manufacturing methods using well-known materials saving energy, time and money while reducing waste. More precisely, this work complements the current state-of-the-art of rapid prototyping of ceramics, covering the key aspect of microstructural control to improve the performance of different devices, such as Solid Oxide Fuel Cells and catalytic reactors for wastewater cleaning and for solar fuels generation.

On one hand, this thesis employed the binder jetting technique to produce ceramic support of $CaSO_4$ which acts as support of the catalyst for the removal of contaminants from wastewater. Different routes were explored regarding the functionalisation of the support. Thanks to the porosity of the support, the TiO_2 catalyst was synthesised *in situ* via $TiCl_4$ hydrolysis, which was the most adequate strategy for the activation of the 3D printed ceramic support. Then, an exhaustive study on the microstructure (SEM), composition (TGA and XDR) and performance (photodegradation test employing methylene blue as contaminant) of the monolith were carried out. Finally, target values of photodegradation test were obtained achieving a nearly complete, i.e. 92%, conversion of methylene blue after 24 hours.

However, another route was explored as well, printing directly the catalyst avoiding the use of supports. For this purpose, during this thesis a ceramic TiO_2 filament compatible with fused deposition modelling printers was developed in collaboration with Print3D Solutions. An exhaustive study on the composition of the filament and the optimisation of the printing parameters was carried out. In order to compare the results, the design of the monoliths was the same than that employed for the printed supports. TiO_2 porous and dense structures were

achieved and their photocatalytic performance tested. In this case, similar conversion of methylene blue conversion was achieved, 89% for the porous structure and 87% using the dense monolith. The recyclability of the catalyst was evaluated, with a clear difference between both monoliths as the re-activated porous catalyst lost 8% of the original efficiency, while the re-activated dense catalyst lost 72%.

On the other hand, related to the energy application, this thesis is focused ceramic electrolyte fabrication for solid oxide fuel cell via additive manufacturing as a contrast to traditional technologies. These devices are considered as Zero Emission technology because they only produce heat and water as final products when hydrogen is used as fuel. In, this work a prototype of digital light processing (DLP) printer was used for electrolyte manufacturing that were compared with electrolytes obtained by a commercial stereolithography printer. A thorough research of this work was dedicated to the production of 8% YSZ printable slurries. Once the slurry and the printing parameters were optimised, plane and structured electrolytes were obtained with a thickness average of 500 μm and an active area of 2.42 cm^2 which were sintered at 1350°C. The cathode electrochemical performance was tested on symmetrical cells, LSM-YSZ/YSZ/YSZ-LSM, to study the ionic conductivity. The highest ionic conductivity 0.054 S/cm was achieved at 900°C for the cathode fixed at 1100°C, being its specific area resistance 1.762 $\Omega \cdot cm^2$. Thus, these results confirmed that 3D printing technology can be employed for reduce the number steps, the time and the cost of solid oxide fuel cell.

RESUMEN

Las nuevas actividades que surgieron durante la Revolución Industrial provocaron el desarrollo de un sector novedoso de producción, cambios en la organización de la producción, nuevas formas de negocio, desarrollo de un mercado global y el uso de nuevas fuentes de energía. Sin embargo, también propició el uso de combustibles fósiles que, a largo plazo, trajeron graves problemas ambientales debido a las diversas actividades realizadas durante la revolución. Hoy en día se sabe que estas actividades son la causa de la actual crisis ambiental que involucra un rápido cambio climático y calentamiento global. La mayoría de los problemas ambientales, como, por ejemplo, la degradación de la capa de ozono, la lluvia ácida, la contaminación del aire y el agua o la reducción de desechos, no pueden ser gestionados por una sola nación. En consecuencia, muchos países han implementado muchos acuerdos en las últimas décadas con el propósito del concepto Emisión Cero, tratando de promover procesos sinérgicos con muy bajo impacto en el medio ambiente y reduciendo el volumen de residuos y emisiones nocivas sin afectar los beneficios industriales.

Durante los últimos años, muchos grupos de investigación se han centrado en el desarrollo de nuevos materiales y nuevas técnicas de fabricación para lograr este objetivo medioambiental. Esta tesis se centra en la introducción de nuevos métodos de fabricación, utilizando materiales conocidos, que ahorran energía, tiempo y dinero y reducen los residuos. Concretamente, este trabajo complementa el estado actual de la técnica de prototipado rápido de cerámicas, abarcando el control microestructural como punto clave para mejorar el rendimiento de diferentes dispositivos, como las pilas de combustible de óxido sólido y los reactores catalíticos para la limpieza de aguas residuales y para generación de combustibles solares.

Por un lado, en esta tesis se utilizó la técnica de Binder Jetting para producir un soporte cerámico de $CaSO_4$ que actúa como soporte del catalizador, con el fin de remover contaminantes de las aguas residuales. Se exploraron diferentes rutas en cuanto a la funcionalización del soporte. Gracias a la porosidad del soporte, el catalizador de TiO_2 se sintetizó in situ mediante hidrólisis de $TiCl_4$, la cual fue la estrategia más adecuada para la activación del soporte cerámico impreso en 3D. A continuación, se realizó un estudio exhaustivo sobre la microestructura (SEM), composición (TGA y XDR) y rendimiento (ensayo de fotodegradación empleando azul de metileno como contaminante) del monolito. Finalmente, se obtuvieron los valores objetivo de la prueba de fotodegradación logrando una conversión casi completa, es decir, 92%, de azul de metileno después de 24 horas.

Sin embargo, también se exploró otra ruta, imprimir directamente el catalizador evitando el uso de soportes. Para ello, durante esta tesis se desarrolló en colaboración con Print3D Solutions un filamento cerámico de TiO_2 compatible con impresoras de modelado de deposición fundida

(FDM). Se realizó un estudio exhaustivo sobre la composición del filamento y la optimización de los parámetros de impresión. Para comparar los resultados, el diseño de los monolitos fue el mismo que el empleado para los soportes impresos. Se lograron estructuras densas y porosas de TiO_2 y se estudió su rendimiento fotocatalítico. En este caso, se logró una conversión similar de conversión de azul de metileno, 89% para la estructura porosa y 87% usando el monolito denso. Se evaluó la reciclabilidad del catalizador, con una clara diferencia entre ambos monolitos ya que el catalizador poroso reactivado perdió un 8% de la eficiencia original, mientras que el catalizador denso reactivado perdió un 72%.

Por otro lado, en relación con la aplicación energética, esta tesis se centra en la fabricación de electrolitos cerámicos para pilas de combustible de óxido sólido mediante impresión 3D como contraste con las tecnologías tradicionales. Estos dispositivos se consideran tecnología de emisión cero porque solo producen calor y agua como productos finales cuando se utiliza hidrógeno como combustible. En este trabajo, se utilizó un prototipo de impresora de procesamiento de luz digital (DLP) para la fabricación de electrolitos, que se compararon con electrolitos obtenidos por una impresora de estereolitografía comercial (SLA). Se realizó un estudio exhaustivo en este trabajo a la producción de pastas imprimibles de 8% YSZ. Una vez optimizados la pasta y los parámetros de impresión, se obtuvieron electrolitos planos y estructurados con un espesor promedio de 500 µm y un área activa de 2,42 cm^2 que se sinterizaron a 1350°C. El rendimiento electroquímico del cátodo se probó en celdas simétricas, LSM-YSZ/YSZ/YSZ-LSM, para estudiar la conductividad iónica. La conductividad iónica más alta fue de 0.054 S/cm la cual se obtuvo a 900°C, para el cátodo fijado a 1100°C, siendo su resistencia de área específica 1.762 $\Omega \cdot cm^2$. Por lo tanto, estos resultados confirmaron que la tecnología de impresión 3D se puede emplear para reducir el número de pasos, el tiempo y el costo de la celda de combustible de óxido sólido.

INDEX

TABLE OF ABBREVIATIONS

ABS	Acrylonitrile Butadiene Styrene
AEMET	State Meteorological Agency of The Government of Spain
AFC	Alkaline Fuel Cell
ALD	Atomic Layer Deposition
AM	Additive Manufacturing
Am	Acrylamide
ASR	Area Specific Resistance
ASTM	American Society for Testing and Materials
BisA	N-N'-Methylenebisacrylamide
BJ	Binder Jetting
BSE	Backscattered Electrons
CAD	Computer-Aided Design
CECs	Contaminants Emerging Concern
CHP	Combined Heat and Power
CIP	Ciprofloxacin
CVD	Chemical Vapour Deposition
DIP	Direct Inkjet Printing
DLP	Digital Light Processing
DMD	Digital Micromirrors Device
ECs	Emerging Contaminants
EIS	Electrochemical Impedance Spectroscopy
EPs	Emerging Pollutants
EU	European Union
FDM	Fused Deposition Modelling
GDC	Gadolinium Doped Ceria
HA	Hydroxyapatite

HFC	Hydrofluorocarbons
IEA	International Energy Agency
IR	Infrared
IREC	Catalonia Institute for Energy Research
ISO	International Organization for Standardization
LCD	Liquid-Crystal Display
LED	Light-Emitting Diode
LOM	Laminated Object Manufacture
LSCF	Lanthanum Strontium Cobalt Ferrite
LSM	Lanthanide Manganites Doped with Strontium
MB	Methylene Blue
MCFC	Molten Carbonate Fuel Cell
MIEC	Mixed Ionic-Electronic Conductors
NOAA	National Oceanic and Atmospheric Administration
OCV	Open Circuit Voltage
ORR	Oxygen Reduction Reaction
PAFC	Phosphoric Acid Fuel Cell
PC	Polycarbonate
PE	Polyethylene Oxide
PE	Primary Electrons
PEC	Photoelectrochemical Cell
PEG	Portable Electric Generator
PEG	Polyethylene Glycol
PEGDA	Polyethylene Glycol Diacrylate
PEMFC	Proton-Exchange Membrane
PFC	Perfluorocarbons
PG	Propylene Glycol
PLA	Polylactic Acid

PMMA	Poly (Methyl Methacrylate)
PVP	Polyvinylpyrrolidone
RL	Roughness Layer
RP	Rapid Prototyping
SE	Secondary Electrons
SEG	Stationary Electric Generator
SEGAI	General Research Support Service of the University of La Laguna
SEM	Scanning Electron Microscopy
SLA	Stereolithography
SLM	Selective Laser Melting
SLS	Selective Laser Sintering
SOFC	Solid Oxide Fuel Cell
TCP	Tricalcium Phosphate
TEMED	Tetramethylethylenediamine
TG-TGA	Thermogravimetry Analysis
TPB	Triple-Phase Boundary
UCLM	University of Castilla La Mancha
ULL	University of La Laguna
UV	Ultraviolet
Vis	Visible
YSZ	Yttria-Stabilized Zirconia
ZSM	Zeolite Socony Mobil

Chapter-1:

INTRODUCTION

1.1 Motivation: towards a zero-emissions and sustainable society

The greatest social transformation taking place in the last centuries was caused by the Industrial Revolution. It was a period during which society and economy based on manual work was replaced by industry and manufacturing, which took place between 18th and 19th centuries. Industrialization marked a shift towards powered, special purpose, machinery, factories and mass production. It was based on new inventions for manufacturing, among them, the steam engine (James Watt), the electrical battery (Volta), the slotting machine (Richard Roberts), the steam locomotive (Stephenson), the telegraph (Morse), etc. Overall, an unprecedented technology advantage was promoted and deployed.[1]

The Industrial Revolution was characterized by the development of new production sectors, changes in the organisation of production, new forms of capital business, the formation of a global extension market and the use of new sources of energy. If steam was the main source of energy during the First Industrial Revolution, oil and electricity sustained the Second Industrial Revolution.[2] This deep transformation in the goods production and the use of fossil fuels brought severe environmental problems, such as accelerated degradation of environment, serious exploitation of fossil fuels and mineral resources, energy and biological resources exhaustion and surface waters or soils and atmosphere pollution as a consequence of industrials waste. These activities have now proved a direct correlation with the current environmental crisis involving a fast climate change and global warming.[3]

Especially, global warming has been increasing due to the exponential growth of CO_2 emissions since the start of the Industrial Revolution.[4] According to the National Oceanic and Atmospheric Administration (NOAA),[5] the emissions level of carbon dioxide measured by The Global Monitoring Division, reached a historical record in March 2019 with 411.04 ppm (exceeding one hundred units the maximum value of 300 ppm during the ice age). The State Meteorological Agency (AEMET) exceeded the threshold of 415 ppm too, in the Izaña Atmospheric Observatory, Tenerife.[6,7]

Considering this change of CO_2 concentration along our history, it is deduced that this drastic increase, *Figure 1. 1 & 1. 2,* is due to the massive burning of fossil fuels and the growing energy demand since 1765.[8] Moreover, it likely has contributed to a continuous temperature increase of +0.17°C per decade, as shown in *Figure 1. 3*.[9]

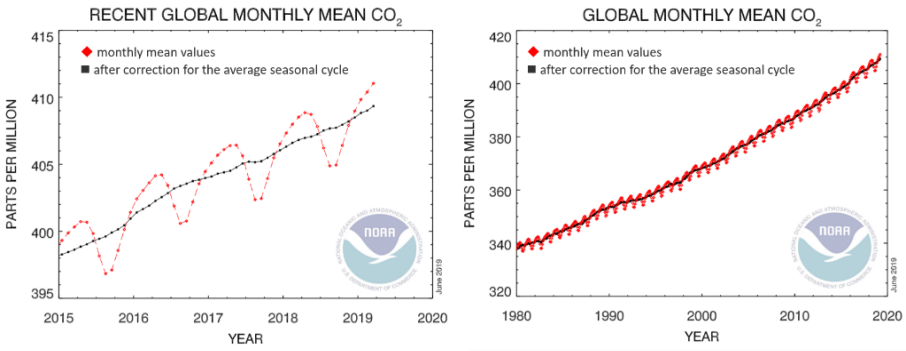

Figure 1. 1 a) [CO_2] ppm measured over the last five years by NOAA b) [CO_2] ppm measured over the last 39 years by NOAA (Data are reported as a dry air mole fraction defined as the number of molecules of carbon dioxide divided by the number of all molecules in air, including CO_2 itself, after water vapor has been removed)[8]

Some of these global environmental problems like degradation of the ozone layer, acid rain and air and water pollution are difficult, if not impossible, to be managed by a single nation, implying international cooperation.[10] Consequently, many agreements have been implemented by most countries, like the Conference of the Parties (COP22)[11] in 2016 where 196 countries met in Marrakech in order to look for a solution and reduce the emissions of gases that contribute to the greenhouse effect in relatively short periods of time.

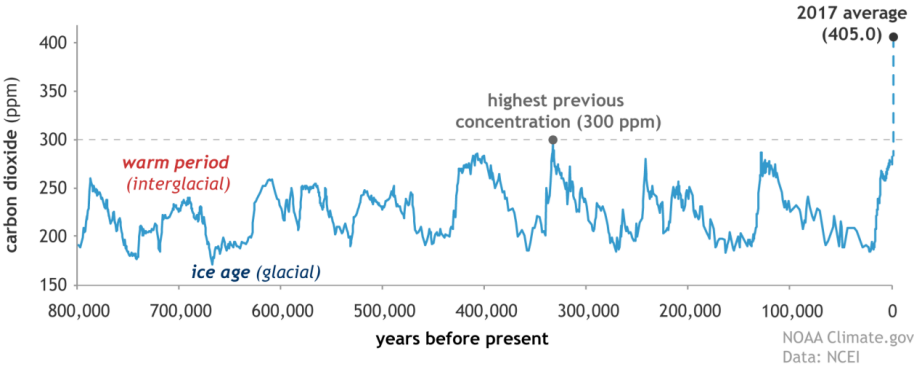

Figure 1. 2 CO_2 concentration 800. 000 years ago (Data are reported as a dry air mole fraction defined as the number of molecules of carbon dioxide divided by the number of all molecules in air, including CO_2 itself, after water vapor has been removed)[12]

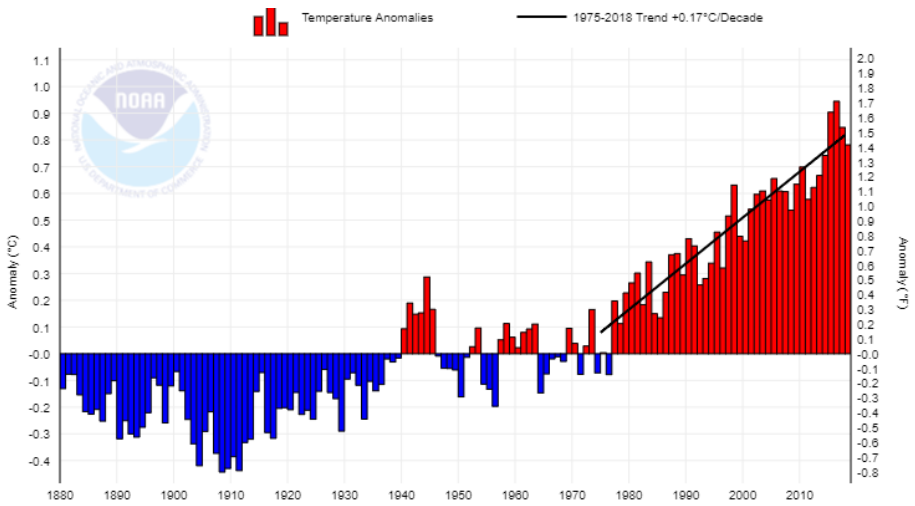

Figure 1. 3 Temperature evolution since 1880 (global land and ocean temperature anomalies, January-December)[9]

The protocol aims to reduce six greenhouse gas emissions that take part in global warming, as carbon dioxide (CO_2), methane (CH_4), nitrous oxide (N_2O), hydrofluorocarbons (HFC), perfluorocarbons (PFC) and sulphur hexafluoride (SF_6), following the zero emission approach, reducing waste and harmful emissions to zero and make money in the process. The Zero Emissions concept considers that inevitable emissions can be used by other industrial or natural processes, making a synergy process that does not impact on the environment, and that a reduction of the volume of waste and harmful emissions can be obtained by improving the industrial performance and efficiency.[13,14]

According to the International Energy Agency (IEA),[15] fossil fuels are leading the final energy consumption, *Figure 1. 4 (a)*, being the transport sector the one with the highest energy consumption at the end of 2016, *Figure 1. 4 (b)*. However, the transport sector is the second in the top six ranking of CO_2 emitting contributions with a 20% and is exceeded with 48% of emissions by other industries including agriculture, mining and construction, *Figure 1. 4 (c)*.

Regarding electricity, 75% of the production in 2017 was based on non-renewable processes.[16] In conclusion, on account of the environmental impact and the limited fossil fuels resources, the

search for alternative energy sources is mandatory to promote a gradual change towards a more sustainable and efficient model.

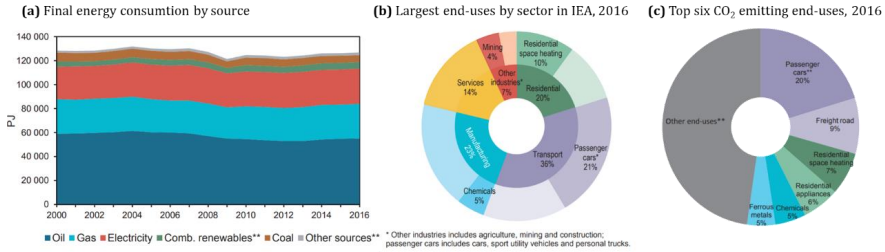

Figure 1. 4 (a) Final energy consumption by source (b) final energy consumption in 2016 (c) Top six CO_2 emitting end-uses; 2016 (All Figures belong to International Energy Agency (IEA) [15]

1.2 Energy and environmental technologies based on advanced ceramics

A wide variety of advanced ceramics have been typically developed in three application fields: (i) electronics, information and communication; (ii) mechanical and (iii) energy and environment. Therefore, advanced ceramics represent a key technology that has a considerable impact for a wide spectrum of industries.

From a broad perspective, the advanced ceramics sector involves different segments by type:[17]

a) **Functional ceramics:** ceramic designed for special applications requiring electric, magnetic and/or optical properties. For example, electrical and magnetic ceramics, catalysts, superconductive ceramics, etc.

b) **Structural ceramics:** ceramic have enhanced mechanical properties under demanding conditions. For example: ceramic-based composites, reinforced ceramics, self-healing ceramics, etc.

c) **Bioceramics:** ceramic that are biocompatible. For example: prothesis, regenerative medicine (scaffold), tissue engineering and systems for controlled drug release, etc.

d) **Ceramic coatings:** ceramic that protect interior and exterior surfaces from common blemish causing materials. For example: oxides, nitrides, carbides, borides, cermets and diamond-like, etc.

e) **Special glasses:** glass materials with specific properties that make them ideal for specific applications. For example: optoelectronics, sealing, thermally, insulating, etc.

In the field of energy, some structural ceramics may be a solution for the expected scenarios when fossil fuels are used to generate electricity. In addition, they can be used in solar thermal energy because they may demand heat exchangers for the high-temperature regime. On the other hand,

functional ceramics can be used for high temperature fuel cells, since these systems require ionic conductive and catalyst materials for the cells. Of course, the role of other functional ceramics in high temperature superconductors and batteries will bring improved opportunities for energy storage.

Moreover, several ceramics have an important role in the environmental field too. Ceramics filter membranes and catalytically active materials are used in technologies to decontaminate and transform polluted water in drinking water, or in the production of biofuel and solar fuel. All these uses are discussed and proposed in the roadmap of Advanced Ceramics for energy and environment, *Figure 1. 5*, which was published in 2013 by J. Rödel *et. al.*[18]

Components used in the aforementioned applications are based on ceramics, composites or cermets, which have extraordinary properties that strongly depend on the composition and the microstructure. The design of these microstructures can affect key parameters such as performance, mechanical stability, optimisation of gas flow-paths to/from the reaction sites, thermal instability and, depending on the materials, resiliency to redox cycling.

Overall, ceramics exhibit a combined wide range of highly relevant technological properties.[19] However, the application of ceramics has been somewhat limited as shaping is complicated and machining costs are usually very high. For this reason, the key for an expansion of the ceramic manufacturing industry may rely on a reliable freeform production of devices and/or components that perform correctly at cost-effective prices.

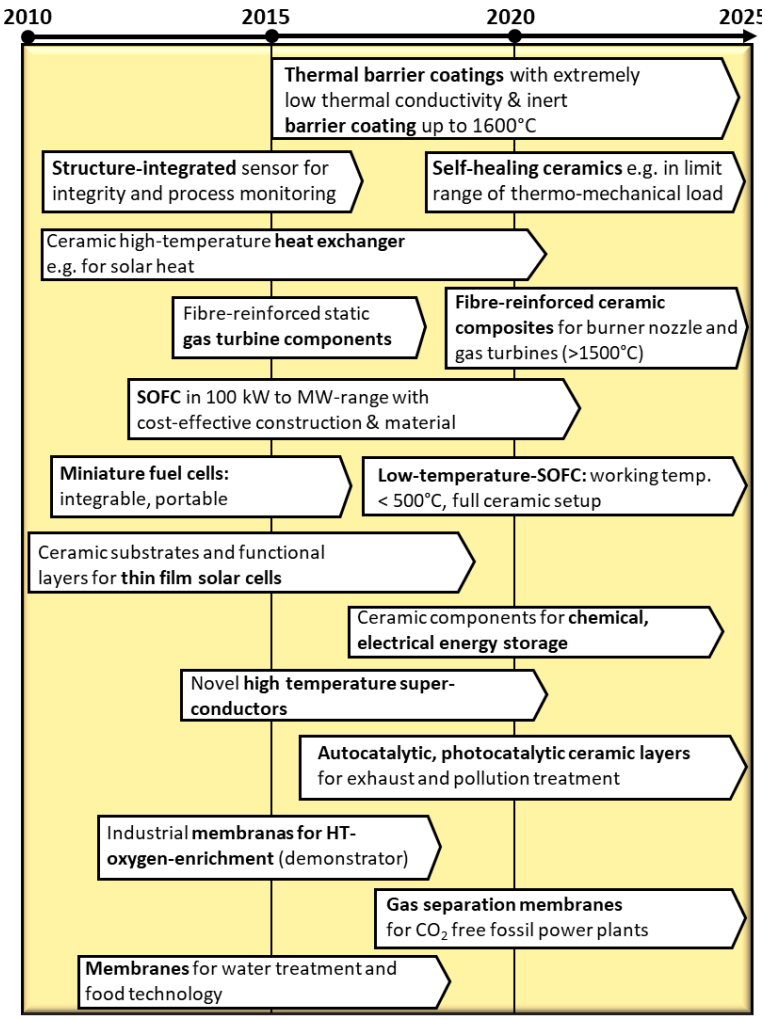

Figure 1. 5 Roadmap of Advanced Ceramics for energy and environment [18]

1.2.1 Solid oxide fuel cells

1.2.1.1 Principles and types of Fuel Cells.

Fuel cells are one of the main candidates to change the traditional technologies for power production as a complement to renewable energies. These electrochemical devices convert chemical energy directly into electrical energy with a low environmental impact because they only produce heat and water as final products when hydrogen is used as fuel (Zero Emission

Technology). They have excellent adaptability in applications as stationary plants, in automotive, as well as coupled to different energy sources and technologies and heat pumps.[20–22]

Fuel cell power systems consist of different parts: unit cells, stacks and balance of plant. Fuel cells consists of two electrodes, anode and cathode, which are separated by the electrolyte. Fuel feeds the anode (negative electrode), where the oxidation reaction takes place and electrons flow through an external circuit. And, on the other side, an oxidant (typically air) feeds the cathode (positive electrode), where electrons arrive from the external circuit and the reduction reaction occurs. The produced oxide ions flow through the electrolyte from the cathode to the anode completing the circuit, *Figure 1. 6*.

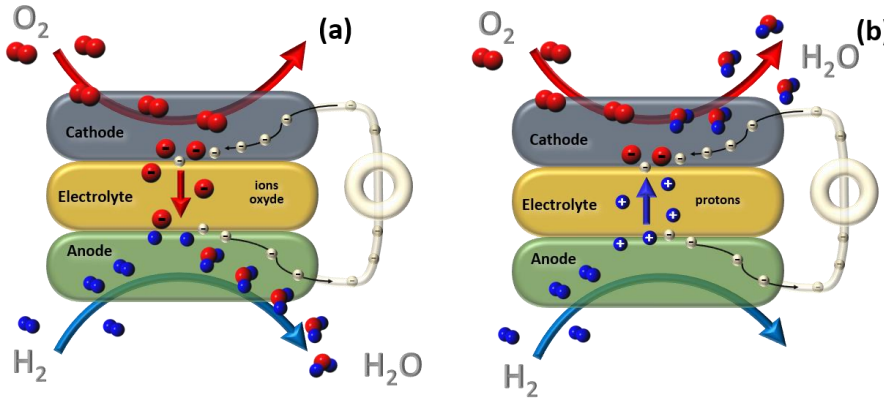

Figure 1. 6 Basic outline of the reactions that occur in a fuel cell, (a) when the electrolyte is an oxide ionic conductor and (b) when it is a protonic conductor

The **main advantage** of fuel cells is the production of electrical energy in one step instead of conventional thermal processes where chemical energy must be converted into thermal energy prior to mechanical energy that finally becomes electrical energy, (with notable energy losses).

Other important aspects to consider are:

- **High conversion efficiency:** around 40% – 60% because the previously mentioned direct conversion energy is not limited by Carnot Cycle. The high-quality residual heat of high temperature fuel cells can be used to produce water steam to generate more electricity coupling a turbine, reaching 80% - 85% overall efficiency.
- **Environmental compatibility:** usually hydrogen is the fuel in these devices. In addition to hydrogen, some other conventional fuels can be used to feed fuel cells. Due to their high efficiency, they will produce emissions although to a lesser extent such is the case of electrical generators.

- **Modularity:** fuel cells are made by units, so the system size can be modified depending on the application from the μW to the MW.
- **Fuels versatility:** whatever hydrogenated compound, which can be oxidized, can be used as a fuel.

Fuel cells can be classified according to the type of fuel, the composition of the electrolyte and the working temperatures, which determines the electrode reactions and the type of ions that flow across the electrolyte. There are five types of fuel cells, which are divided depending on temperature operation. Solid oxide fuel cell (SOFC) and molten carbonate fuel cell (MCFC) are characterized by their high operation temperature. While, alkaline fuel cell (AFC), proton-exchange membrane fuel cell (PEMFC) and phosphoric acid fuel cell (PAFC) have a lower operation temperature. All of them have different features, as summarised in *Table 1. 1*.[4,21,23]

This work is focused on SOFCs, that operate based on oxide ion transport of some oxides at high temperatures (600°C - 1000°C), getting an efficiency between 60% and 85%. They do not need pure hydrogen as a fuel, hence conventional fuels can be used due to the high operating temperatures. However, the cell durability is affected by this high working temperature.

Table 1. 1 Types and specific features of the whole family of fuel cells. [4,21,23]

	SOFC	MCFC	AFC	PEMFC	PAFC
Electrolyte	Ceramic oxide	Molten Carbonate in $LiAlO_2$	KOH	Polymer/Nafion	H_3PO_4 in SiC
Charge carrier	O^{2-}	CO_3^{2-}	OH^-	H^+	H^+
T (K)	1073 - 1273	903 - 923	323 - 483	323 - 353	433 - 473
Fuel	-H_2 -Hydrocarbons	-H_2 -Hydrocarbons	H_2	-H_2 -Methanol	-H_2 -CO
Applications	- SEG[a], CHP[b]	- SEG, CHP	- Space - Military	- Transport - PEG[c], CHP	- Transport - SEG, CHP
Efficiency	65-85%	60-80%	50%	40-50%	40-80%
Advantages	- High efficiency - Fuel flexibility	- High efficiency - Fuel flexibility	- Fast cathode reaction - High yield	- Low Temp. - Fast start-up -Low corrosion	- Can use not pure H_2 - High efficiency (CHP)
Disadvantages	- Slow start up - High Temp	- Two gas fluxes - High Temp.	- Expensive reagents - Gases without CO_2	-High purity fuel -Hydration -Too much Pt - CO free fuel	- Corrosive electrolyte -Bulky system

[a] SEG: Stationary Electric Generator

[b] CHP: Cogeneration or Combined Heat and Power

[c] PEG: Portable Electric Generator

SOFCs are composed of a dense electrolyte that is between two porous electrodes layers. The molecular oxygen gets adsorbed on cathode surface. When it accepts incoming electron from external circuit, it reduces to oxide ions, *Equation (1.1)*. Then, oxide ions are transported through the dense electrolyte to the anode. After that, oxide ions participate the oxidation of the fuel, *Equation (1.2)*, generating water as a by-product, *Equation (1.3)*. The electricity is produced by the flow of electrons, from the anode to the cathode, in the external circuit, *Figure 1. 7* (a).[4,24]

$$(cathode) \quad O_2 + 4e^- \rightarrow 2O^{2-} \qquad \textit{Equation (1.1)}$$

$$(anode) \quad H_2 \rightarrow 2H^+ + 2e^- \qquad \textit{Equation (1.2)}$$

$$(global) \quad 2\,H_2 + O_2 \rightarrow 2H_2O \qquad \textit{Equation (1.3)}$$

The performance of SOFCs is determined by the Triple-Phase Boundary (TPB), *Figure 1.7*, which is the interphase where the fuels get in contact with the electrode, and in turn the electrode is touching the electrolyte, so is the place where electrochemical reactions take place. Specifically, the electrochemical performance depends on the density and the nature of the three phase regions.

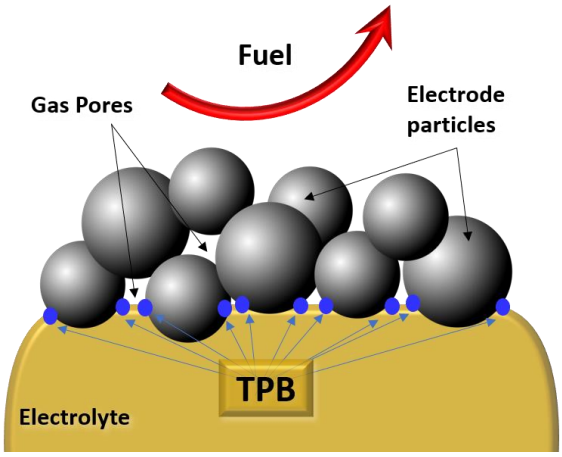

Figure 1. 7 Triple Phase Boundary between electrolyte and electrode

The power density obtained from the cell (P) is given by the product of the current density (j) by the voltage (E):

$$P = j * E \qquad \textit{Equation (1.4)}$$

Thus, as a consequence of Ohm's law, power reciprocally depends on the resistance of the cell components. In other words, it is highly relevant to fabricate the cell components searching for the minimization of their resistive contributions

1.2.1.2 Solid Oxide Fuel Cell components and materials

1.2.1.2.1 Electrolyte

The main requirements that the electrolyte must achieve are: [4,21]

- **Conductivity:** it should have high ionic conductivity to minimize the ohmic losses, and a negligible electronic conductivity to avoid short-circuit. As a reference, the value must be higher than 0.01 S/cm at 800°C for an efficient operation.
- **Compatibility:** it should be chemically and thermally compatible with the electrode materials at working and fabrication temperatures of the cells. This will prevent the formation of undesirable phases in the interphase.
- **Stability:** it separates the anode and cathode, for this reason the material should be stable in both oxidizing and reducing atmospheres.
- **Gas tightness:** analogously, it is a gas separator of both atmospheres, therefore it should be gas tight to prevent the mixture of fuel and oxidising agent, which implies densities close to 100%.

The SOFC electrolyte could be oxide ionic or protonic conductor. This work is focused on oxide ion conductors, specially YSZ yttria-stabilized zirconia. The 8% mol Y_2O_3 -ZrO_2 YSZ has a stabilized cubic phase with a reasonable ionic conductivity at high temperature while 3 YSZ has a tetragonal phase and the conductivity at high temperatures is a bit lower. In this doped oxide, the Zr^{4+} in replaced by Y^{3+} cation, E*quation 1. 5*, which has a similar size, creating oxygen vacancies that allow oxygen ions to migrate, i.e. a high ionic conductivity, *Figure 1. 8*.[25]

$$Y_2O_3 \rightleftharpoons 2Y_{Zr}{}' + V_O{}^{\cdot\cdot} + 3O_O{}^{x} \qquad \textit{Equation (1.5)}$$

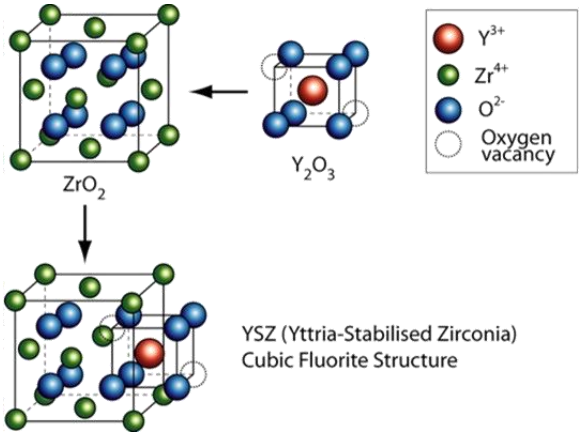

Figure 1. 8 YSZ Structures (ZrO_2 Doping process with Y_2O_3) [25]

This property is intrinsic to some crystallographic families, but it is possible to improve it by using doping. For example, zirconium oxide has an intrinsic low ionic conductivity and is thermally unstable. However, if it is doped with divalent or trivalent cations (Ca^{2+}, Y^{3+}, Sc^{3+}) the ionic conduction and mechanical properties improve. At room temperature, ZrO_2 has a monoclinic structure, which changes to tetragonal around 1170°C and to cubic around 2370°C, *Figure 1. 9*.[26]

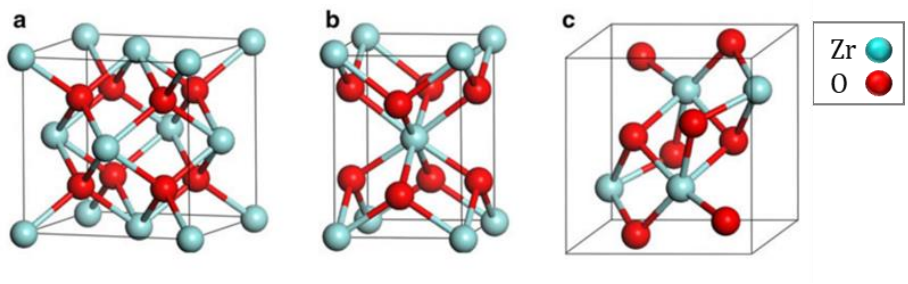

Figure 1. 9 ZrO_2 structures (a) cubic (b) tetragonal (c) monoclinic [26]

On account of the excellent stability in reducing and oxidizing conditions, the good mechanical stability, the high quality of starting material and the durability in the long-term (40.000h), 8 YSZ is the selected material for developing the SOFC electrolytes in this work.

1.2.1.2.2 Electrodes: the anode and the cathode

Contrary to the electrolyte, the electrodes must be porous to provide larger TPBs, that will increase the surface for electrochemical reactions. In a typical fuel cell, there are two electrodes, namely, the anode and the cathode.

Anode

The electrochemical oxidation of the fuel takes place at the anode, *Equation (1.2) & (1.3)*. Despite there is a wide range of materials that have been used as anode, the most well-known are cermets of nickel and YSZ. The general requirements of an efficient anode material are the following: [21]

- **Conductivity:** it must have electronic conductivity in reducing conditions at operation temperature and cannot be affected by the changes in the oxygen partial pressure during the process of water formation.
- **Porosity:** this aspect can define the performance and efficiency of the SOFC. As mentioned above, the porosity provides the important TPB region to increase the surface reaction area while allows evacuating the by-products of the reaction (water).

- **Chemical stability:** the anode material should be chemically and morphologically stable in reducing conditions. If the fuel is a hydrocarbon, coke formation can be an intermediate product. In this case, it is beneficial if coke deposition is controlled, because it could improve the electric contact, but deleterious if blocking actives sites. Anode materials should also be stable under sulphur eventually remaining at some fuels, because it could cause poisoning and corrosion in the long-term at the anode.
- **Thermal and mechanical stability:** it should be thermal and mechanically stable with the electrolyte at operation temperatures.
- **Catalytic activity:** it should have catalytic activity for promoting the fuel electrochemical oxidation.

Cathode

The electrochemical reduction of the oxygen to generate oxide ions takes place at the cathode, *Equation (1.2)*. The Oxygen Reduction Reaction (ORR) has a limiting step that depends on the oxygen partial pressure, working temperature and cathode and electrolyte material. For example, if they are mixed ionic-electronic conductors (MIEC), there are more active sites, that means the TPB region increases.[21,24]

Currently, the most used cathode materials for SOFCs are lanthanide manganites doped with strontium (LSM). This material is a p-type electronic conductor, which presents few oxygen vacancies working well between 800°C and 1000°C. Nevertheless, LSM reacts with YSZ at high temperature (forming insulating $SrZrO_3$ phases) yielding a lower performance. This issue could be solved using cathode materials with lanthanum deficiency or decreasing the temperature of LSM fabrication.

For an efficient operation of SOFCs, the cathode should possess the following functionalities: [4,21]

- **Chemical stability:** the cathode material must have a good chemical compatibility and relatively low interaction with the electrolyte producing undesirable reactions during both working and manufacturing processes. Moreover, it must be stable under oxidizing atmospheres too.
- **Conductivity:** the chosen material should show high electronic conductivity, in oxidizing atmosphere to facilitate the electrons arrival to active sites.
- **Porosity:** the cathode must allow fast diffusion of the oxidant gas through the active sites while contributing to an adequate gas evacuation of the exhaust (water).
- **Thermal and mechanical stability:** it must be thermally and mechanically stable at operating and manufacturing temperature.
- **Catalytic activity:** it should have high catalytic activity to promote the reduction of oxygen.

1.2.2 Water splitting

As mentioned before, in order to solve the devastating environmental issues due to the far too vast use of fossil fuels, it is necessary researching, improving, exploiting and the utilization of renewable energies. Hydrogen is known as an energy vector that may play a very important role in a renewable energy-based model. However, obtaining elemental hydrogen is complicated due to the very low concentration in the atmosphere. For this reason there are different options to produce it, such as: (i) pyrolysis, steam and plasma reforming of natural gas; (ii) gasification and partial oxidation of coal or oil; (iii) electrolysis, photolytic and thermal splitting, via solar energy; (iv) water electrolysis via wind, hydro or wave energy; (v) water electrolysis or thermal splitting via fission or fusion, and (vi) fermentation, gasification and pyrolysis of biomass.[27] In this section, water splitting via photolysis/photocatalyst will be described.

Photolysis of water happens in a system where redox reactions take place on the surface of a catalytic material in contact with an aqueous solution. When photons from irradiation are in contact with the catalyst, valence electrons are excited promoting to conduction band, producing in turn holes. So, excited electrons may be used in reduction processes, whereas holes may participate in oxidation reactions, *Figure 1. 10*. One requirement for a promising photocatalytic material is having a band gap higher than 1.8 eV, and the interval between its conduction and valence band must include redox potentials of hydrogen and oxygen evolution. Also, the materials must be chemically stable to prevent corrosion. A variety of semiconductors materials have been studied as CdS, SiC, GaP, Cu_2O, ZnO, $SrTiO_3$, $NaTaO_3$, $BiVO_4$, WO_3, etc.[28] However, the most extensively studied and used material is TiO_2.[29]

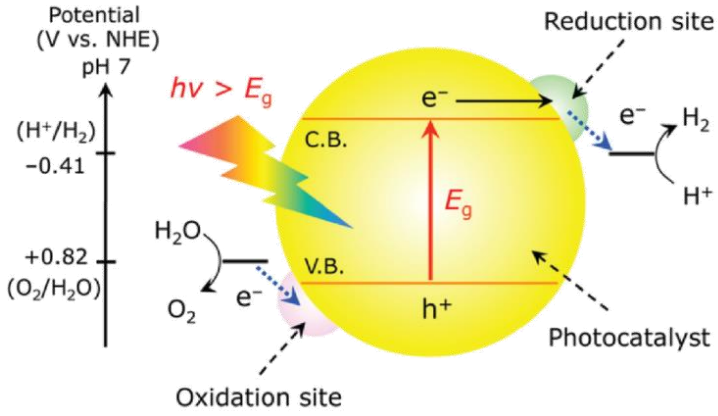

Figure 1. 10 Single band gap photolysis system based on a photo-absorber and a catalyst.[30,31]

TiO_2 has three different polymorphs i.e. anatase, brookite and rutile, but the last is the most stable form. In all cases, (Ti^{4+}) is co-ordinated to six oxygen anions (O^{2-}), producing networks of octahedra, *Figure 1. 11*. When Ti^{4+} reduces to Ti^{3+}, this causes oxygen deficiency and hence becomes an n-type semiconductor. The anatase and brookite band gap is 3.2 eV and 3.0 for rutile.[32] Nevertheless, a disadvantage of titanium oxide is the absorption limitation to the UV range. For this reason, over the past few years, research advances have been focused in extending its absorption spectra via doping or coupling with other semiconductors, for example metal-based materials, which could improve the electrical conductivity. However, it is still a big challenge.[33,34]

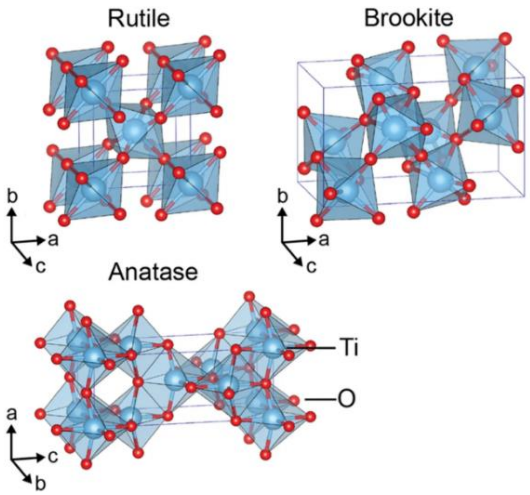

Figure 1. 11 Crystal structures of TiO_2 rutile (tetragonal), brookite (orthorhombic) and anatase (tetragonal) polymorphs [32]

1.2.3 Water decontamination

For many years, several human activities such as industry, agriculture, deforestation, urbanisation, transport, etc, have demonstrated an important impact on human health or the environment. One of the most important consequences is water contamination. There is a high variety of chemicals that have been spilled to water such as nutrients, leachates, oil, sludge, non-biodegradable materials, etc.[35]

Statistics published by EUROSTAT in 2019, *Figure 1. 12*, reveal that over 80 million tonnes of chemicals hazardous to the environment have been produced for last decade,[36] many of which are thrown to water. Even so, all these common wastewater treatments are not designed to remove low concentration or trace level chemical pollutants, called emerging pollutants (EPs), emerging contaminants (ECs) or contaminants emerging concern (CECs).

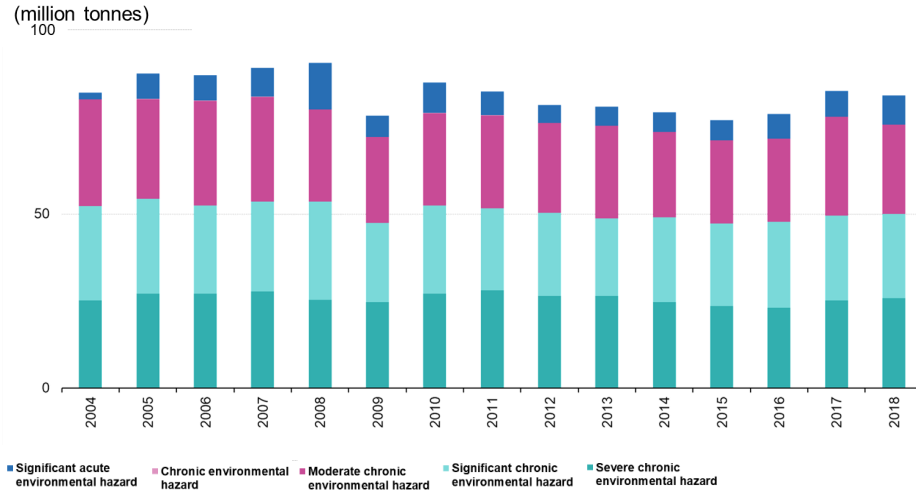

Figure 1. 12 Production of chemical hazardous to the environment, EU-28, 2004-2018[36]

For this reason, wastewater treatment is the key to improve this issue. Traditionally, there are three treatments for wastewater: primary, secondary, etc. The main goal of primary treatment is to reduce suspended particles via some physical-chemical processes, including sedimentation, flotation, neutralization, or other processes such as using filters, oxidation reactions, or even ion exchange. In the second treatment, organic compounds must be removed. To achieve that, aerobic and anaerobic processes are carried out, as the classic active sludge, bacterial beds, green filters, anaerobic digestion, electrocoagulation, electrooxidation, biological membrane reactor, etc. Finally, in the third treatment the goal is to remove pathogens, through UV radiation, ion exchange, inverse osmosis, filtration, chlorine treatment.[37]

ECs are defined as pollutants, which are chemical substances, that have been introduced in the environment years ago, but they have not been investigated until recently. Most ECs are industrial products, pesticides, personal-care products, textile compounds, pharmaceuticals (as antibiotics, anticonvulsant, antipyretics, cytostatic drugs, hormone, etc.).[38] The list of ECs is extremely large, and it will expand with time.[39] The problem is that the toxicity level, quantity and exposure of ECs are not defined to evaluate environmental risk. For this reason, the European Commission funded the NORMAN project to predict the effects in the mid- and long-term and monitor them.[40,41] It is necessary to remember that ECs are resistant to conventional wastewater treatments, hence latest research has been focused on determining their presence and eradicating them by other chemical methods. One extensive study found innovative processes suggested a solution for this environmental problem via the use of advanced oxidation processes as photocatalysis, membrane-based devices as micro/ultra/nanofiltration or adsorption/ion exchange systems. In

this thesis, only photo-catalytical processes will be considered. Photocatalysis is a heterogeneous process that is based on the oxidation of some chemical pollutant substances through a reaction between a catalyst and the contaminant, specifically when the surface of a semiconductor is irradiated as described in a previous section. Thus, it is not surprising that titanium oxide was extensively used in many research works.[38,42–50] A number of studies have postulated its use to remove (i) pharmaceuticals compound as paracetamol,[38,49] ibuprofen,[48] lorazepam and other pharmaceuticals;[42] (ii) textile dye as methyl orange,[46] methylene blue[44] or azo dye;[45] (iii) industrial contaminants as octane,[43] caffeine,[48] or rare-earth,[47] (iv) or even micro-organisms.[51]

In the last section, the activity of the titanium oxide was described, now the mechanism will be explained regarding contaminant removal. When the light with energy higher than 3.2 eV ($\lambda \leq 387nm$) hits the catalyst surface, a photon is absorbed and a valence electron is excited to the conduction band, producing a positive hole in the valence band, *Equation (1.6).* Then, positive holes oxidize hydroxyl anions (OH^-) or water (H_2O) at the catalyst surface generating hydroxyl radicals ($OH^\bullet$) and protons, *Equation (1.7)*. These hydroxyl radicals can oxidize organics compounds that are mineralized rendering minerals salts, carbon dioxide and water, *Equation (1.8)*. Simultaneously, the molecular oxygen absorbed on the titania surface traps the electrons produced in *Equation (1.6)*, forming a superoxide radical anion, *Equation (1.9)*. Then, this superoxide radical anion reacts with a proton producing hydroperoxyl radicals, *Equation (1.10)*, and afterwards reacts with other similar radicals to produce hydrogen peroxide, *Equation (1.11)*, or reacting with pollutant contributing to the oxidation process, *Equation (1.12)*. In addition, superoxide radical anion can react directly with the contaminant too, causing its degradation, *Equation (1.13)*.[32] As most of CEs are organic species, the mechanism is the same for all of them, just changing the salt of the pollutant produced.

Regarding the presence of the catalyst in the sample, it could be suspended in wastewater, supported in porous solid, or forming itself a structure three-dimensional. Depending on whether the catalyst is in contact with the contaminated solution or not, there would be some advantages or disadvantages. Independently the goal is to achieve; (i) the largest active area (the support/catalyst must be very porous, or the structure must be complex respectively), (ii) good mechanical properties, (iii) stability in aqueous solutions, (iv) and easy to separate from the solution. For all these reasons, 3D structures are better than powder suspensions, which will be a key aspect in this thesis.

$$TiO_2 + hv \rightarrow h^+ + e^- \quad \textit{Equation (1.6)}$$

$$h^+ + H_2O \rightarrow OH^\bullet + H^+ \quad \textit{Equation (1.7)}$$

$$OH^\bullet + pollutant \rightarrow H_2O + CO_2 + salts \quad \textit{Equation (1.8)}$$

$$e^- + O_2 \rightarrow {O_2}^{\bullet -} \quad \textit{Equation (1.9)}$$

$${O_2}^{\bullet -} + H^+ \rightarrow OOH^\bullet \quad \textit{Equation (1.10)}$$

$$OOH^\bullet + OOH^\bullet \rightarrow H_2O_2 + O_2 \quad \textit{Equation (1.11)}$$

$$OOH^\bullet + pollutant \rightarrow H_2O + CO_2 \quad \textit{Equation (1.12)}$$

$${O_2}^{\bullet -} + pollutant \rightarrow H_2O + CO_2 + salts \quad \textit{Equation (1.13)}$$

1.2.4 Biofuels synthesis

To reduce the fossil fuel consumption, some alternative fuels have emerged such as hydrogen, natural gas, syngas and biofuel. In the previous section, the role of hydrogen has been highlighted, though this section will focus on the synthesis of biofuels due to the relevance of renewable materials and eco-friendly environmental processes. Hence, biofuels may help to reduce both the dependence on fossil fuels and waste generation, as waste can be used as starting material during biofuel synthesis. Among all types of biofuels, liquids are the most likely for application in internal combustion engines in automobile engineering. Even biofuel are being studied jet fuel in aeronautics industry.[52] Fortunately, biodiesel can be used in diesel engines of cars without any variation, it is a biodegradable material, the combustion is better because of the controlled chemical composition and also reduces the emission of hydrocarbons, particles and carbon monoxide.[53]

Biodiesel is made by the transesterification of animal fats or vegetables oils with an alcohol in order to produce esters and therefore can be synthetized from a large diversity of raw materials that are composed by triglycerides.

There exist three types of biofuels depending on the raw material used during the synthesis: first, second and third generation. First generation biofuels come from agricultural crops for human consumption (sunflower, soya bean, corn, etc.). Second generation biofuels come from inedible crops and, finally, third generation biofuel come from algae. So, evidently, the ideal route is from agricultural waste or cooking oils waste, that is second generation biodiesel, because first generation biodiesel would involve a lot of lands to cultivate these crops. [53,54]

In transesterification, triglycerides react with an alcohol with low molar weight to produce fatty acid alkyl esters and a large amount of glycerol, via catalyst, which can be homogeneous or heterogeneous, *Figure 1. 13*.[55] During homogeneous transesterification reactions with basic

catalysts, hydrolysis and saponification can go on due to the presence of water and free fatty acids in the media. This can be improved by using acid catalysts.

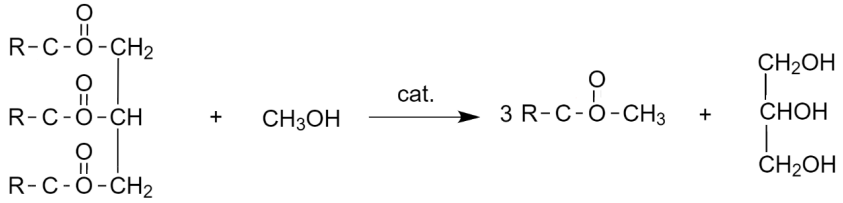

Figure 1. 13 Biodiesel production reaction from methanol and triglycerides

However, homogeneous catalysts show some disadvantages including product purification, residue generation and undesirable reactions as saponification. In contrast, heterogeneous catalysts offer great advantages to substitute biodiesel production via homogeneous pathway and consequently, it has been more extensively studied and used. Some of the major advantages are the following: less corrosive, the catalyst can be recycled and reused several times, it is cheaper because the process is simpler than the homogeneous method. Also, it improves the separation and recovery of the solid catalyst, it shows high yields and does not require a washing step for the crude ester. In summary, the heterogenous process is safer, and more environmentally friendly.[56–59]

Thus, the catalyst is a solid and its performance can be improved by controlling the (i) pore size and shape, especially when reaction involve external surface, (ii) diffusion process, (iii) acidity, (iv) specific area, (v) type of catalyst patterning.[60,61] Therefore, most of the catalysts used nowadays are ceramics. According with the phase of the catalyst, it can be produced by different ways, for example impregnation, sol-gel, precipitation/co-precipitation, conversion by thermal treatment, mechanical mixing, self-assembly or chemical vapour deposition (CVD). As a result, slurry and fixed/packed bed reactors are the most used configurations. A clear example of this is the work led by M. E. Borges,[60] based on a catalyst with high mechanical strength that uses pumice as stirrer.

Some materials normally used are metals, metal oxides (TiO_2, Al_2O_3, SiO_2, ZrO_2, CeO_2, etc.), zeolites, carbons (activated carbon, nanofibers, nanotubes, etc.), due to both their chemical physical properties as support.[60] Overall, the catalyst porosity is the most important parameter for biodiesel production. However, the combination of parameters is the reason why a large variety of ceramics are used in this field. Thence most of the studies utilize mesoporous based-zeolites materials due to the porosity presented, and the starting product is waste cooking oil. In *Table 1. 2*, it can be observed the variety of materials used in heterogeneous catalyst from waste oil. Thus, once again, the important role of ceramics to progress in the energy and environmental field is proved.

Table 1. 2 Heterogeneous base catalysts and heterogeneous acid catalysts used in transesterification of waste cooking oil [58]

Heterogeneous base catalysts	Heterogeneous acid catalysts
- Calcium oxide (CaO) - Basic solid Mg-Al-CO_3 hydrotalcite catalysts in powder form - CaO and ZrO_2 mixed oxides with various Ca-to-Zr - Barium meliorated construction site waste marble - Potassium-loaded pumice material (K-Pumice) - Strontium/zirconia (Sr/ZrO_2) catalyst - Palm ash from empty fruit bunches - Calcium oxide supported on activated carbon (CaO/AC) - Calcium ethoxide - An agglomerated Zr-SBA-15/bentonite catalyst - Calcined waste coral fragments	- WO_3/ZrO_2. WO_3/ZrO_2–Al_2O_3. MoO_3/ZrO_2 - MoO_3/SiO_2 TPA/ZrO_2 Zinc stearate/SiO_2. Zinc ethanoate/SiO_2 - Tri-potassium phosphate - Carbohydrate-derived catalysts from various carbohydrates such as D-glucose, - sucrose, cellulose and starch - Zinc aluminate catalyst - Mg MCM-41, Mg-Al hydrotalcite, and K+ impregnated zirconia - Aminophosphonic acid resin D418 - Solid acid resins: Amberlyst ®15 and Amberlyst®46 and Purolite®D5081 - Sulfonating pyrolyzed rice husk with concentrated sulphuric acid - Y-type zeolites with Al_2O_3 and Na_2O - Mixed oxides of TiO_2–MgO - Zirconiumdodecatungstophosphate $Zr_{0.7}H_{0.2}PW_{12}O_{40}$ (ZrHPW)

1.2.2 Solar fuels

In previous sections, it has been mentioned the solar energy relevance for hydrogen generation, water splitting and pollutant removal. This section is focused on extending the photocatalytic response of semiconductor materials for application in solar fuel production, especially using carbon dioxide as starting material.

The consequences of carbon dioxide emission to the atmosphere have been mentioned along this introduction and some strategies have been described in order to decrease this emission following an environmentally friendly energy process. However, CO_2 conversion is another possibility to reduce its concentration in the atmosphere, or rather, reducing the emissions and converting CO_2 into useful chemical fuels. Industrially, there are three main pathways: (i) electrochemical

reduction, (ii) thermal reduction giving monoxide carbon and oxygen as products, (iii) and chemical reduction producing hydrogen or hydrocarbon as methane, via solar energy.[62] Thus, solar energy would be converted and stored into fuels. This last section will emphasise the carbon dioxide recycling into a hydrocarbon fuel such as methane via using a semiconductor and sunlight. The reaction mechanism is the next:[63]

$$H_2O + 2h^+ \rightarrow \frac{1}{2} O_2 + 2H^+ \qquad \textit{Equation (1.14)}$$

$$CO_{2\,(aq.)} + 2H^+ + 2e^- \rightarrow HCOOH \qquad \textit{Equation (1.15)}$$

$$HCOOH + 2H^+ + 2e^- \rightarrow HCHO + H_2O \qquad \textit{Equation (1.16)}$$

$$HCHO + 2H^+ + 2e^- \rightarrow CH_3OH \qquad \textit{Equation (1.17)}$$

$$CH_3OH + 2H^+ + 2e^- \rightarrow CH_4 + H_2O \qquad \textit{Equation (1.18)}$$

Some physico-chemical processes will determine the performance such as light absorption, charge separations, charge migration, surface redox reactions, chemical composition, porosity and particle size, crystal structure, architecture and electronic band structure. The photocatalytic configurations can be as a particular system (suspended or packed-bed reactor), or as photoelectrochemical cell (PEC) where the semiconductor material is supported on a conductive substrate forming a photoelectrode. For the last four decades, many semiconductors have been selected or developed for this application. The most common have already been mentioned in this work, as metal oxides, metal chalcogenides, metal nitrides, carbon nitrides, and III-V compounds, such as TiO_2, Fe_2O_3, $BiVO_4$, CdS, CdSe, ZrO_2, Ga_2O_3, NiO, WO_3, CuO, carbonaceous compounds, etc. One of the innovative aspects regarding materials is the architecture, and, for this reason, semiconductors with different dimensions have been investigated, *Figure 1. 14*. Zero dimension, 0D, corresponds with free-standing nanoparticles, that is, particles in suspension. 1D. 2D and 3D is related to how the material is built, i.e. along one direction (1D), a plane (2D) or in the three dimensions (3D). In the *Figure 1. 14*, one-dimension particles are as nanowires, nanorods, nanotubes, nanofibers, etc. Two-dimension particles are associated with film electrodes (photoanode/cathode) or planar films deposited on a substrate. Finally, three-dimension structures are be made assembling two-dimension films. It is important to underline that 3D structures have excellent properties such is the case of optical features. For this reason, these types of architectures have been explored over the last years. However, they can be used not only as a single material but also can be combined in heterojunctions, co-catalyst, composites, etc., in order to achieve a better conversion efficiency, selectivity and/or harvesting visible light.[64,65]

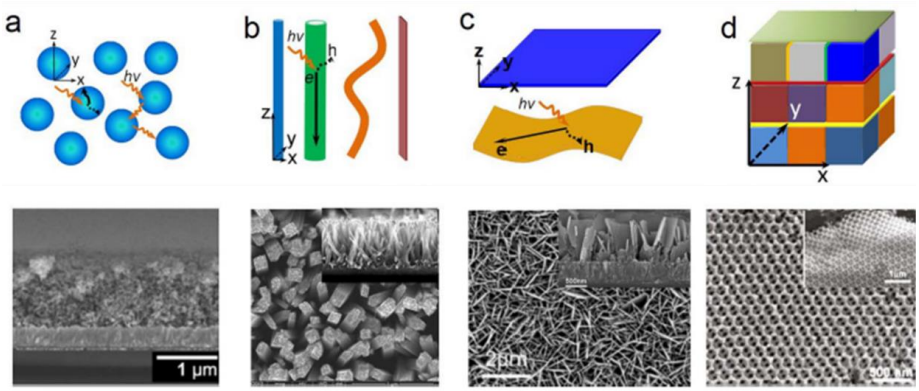

Figure 1. 14 Different dimensional architectures (a) 0D nanocrystals, (b) 1D nanostructures, (c) 2D nanosheets and films, and (d) 3D nanostructures constructed with 0D, 1D and 2D building block units [64]

1.3 Shaping technologies for advanced ceramics

1.3.1 Current fabrication methods

Several methods can be used to fabricate ceramic materials. The usual goal is the production of a solid product with specific shape/geometry (film, fiber or monolith) and functionality. Traditional processing uses a bulky block as starting material, which is then carved to get a specific structure. However, this process has some disadvantages as the large amount of waste, the difficulty of achieving certain geometries and the high cost of the process.[19,66] Contrary to the subtractive fabrication strategies, additive manufacturing consists on building up an object by adding raw material layer by layer (see next section).

Despite the growing number of examples using additive manufacturing in ceramics, there is still a long road to implement these technologies at industrial level.[67,68] Therefore, this work is focused on the possibilities of 3D printing for implementing material and functional complexity to precisely engineer ceramics microstructures required for the highly demanding applications in energy[22] and environmental sector.

Additive manufacturing (AM) is a promising candidate due to the advantages that presents in terms of fabrication flexibility, simple design for manufacturing, reduction of the time-to-market, low waste material and reduced manufacturing steps, cost and environmental impact.

The different additive manufacturing processes and their classification will be presented in the next section.

1.3.2 3D Printing Technologies

Additive processes have more than thirty years of history. The history of 3D printing begins in 1981 with Dr. Hideo Kodoma, who was the first person to describe a rapid prototyping system to build up a solid model using photopolymers and a laser beam to cure them.[69] Three years later, Charles Hull invented the stereolithography 3D printer.[70] Since then, 3D printing processes have become extremely popular continuously decreasing their cost. Additive manufacturing is the process to achieve a three-dimensional object using an additive process that works adding layer-upon-layer of a certain material (in contrast to traditional manufacturing techniques where material is removed from starting bulk by subtractive processes). Commonly it is called 3D printing. The shape of each printed layer is defined by a model, which is normally made by a CAD modelling software (Computer-Aided Design),[22] able of slicing the shape model into layered cross sections, *Figure 1. 15*.

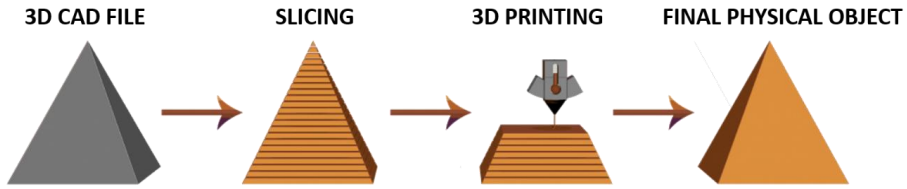

Figure 1. 15 Slicing process of the digital design [71]

According to ISO/ASTM standard, two categories of AM processes can be defined: direct process and indirect process.[72] In a direct process, the geometrical shape and material properties are achieved simultaneously. While the indirect processes are multi step processes where first geometric shape is provided and then the parts are consolidated to get the material properties. On the basis of this classification, there are only two direct printing processes for ceramic materials: Selective Laser Melting (SLM) and Selective Laser Sintering (SLS). The others are multi-step process as it is necessary to use a binder as sacrificial material in order to shape the ceramic which finally has to be removed.[73] The main indirect AM processes are Direct Inkjet Printing (DIP), Binder Jetting (BJ), Fused Deposition Modelling (FDM), Robocasting, Stereolithography (SLA), Digital Light Processing (DLP) and Laminated Object Manufacture (LOM). In the next section we will briefly present all these 3D printing technologies.

According to their dimensional order there are three different AM processes: 0D (point-by-point), 1D (line-by-line) and 2D (layer-by-layer). All the previously aforementioned 3D printing techniques can be classified accordingly, *Figure 1. 16*. Depending on the starting material and the building process, the final object will have some specific properties, for example, powder bed process deposition will build porous structure (BJ, SLM, SLS). On the other hand, slurry bases

techniques (SLA, DLP) build dense ceramic structures. Other techniques, e.g. FDM, can fabricate both type of structures adding only the material (dense structure) or adding pore former too (porous structures).

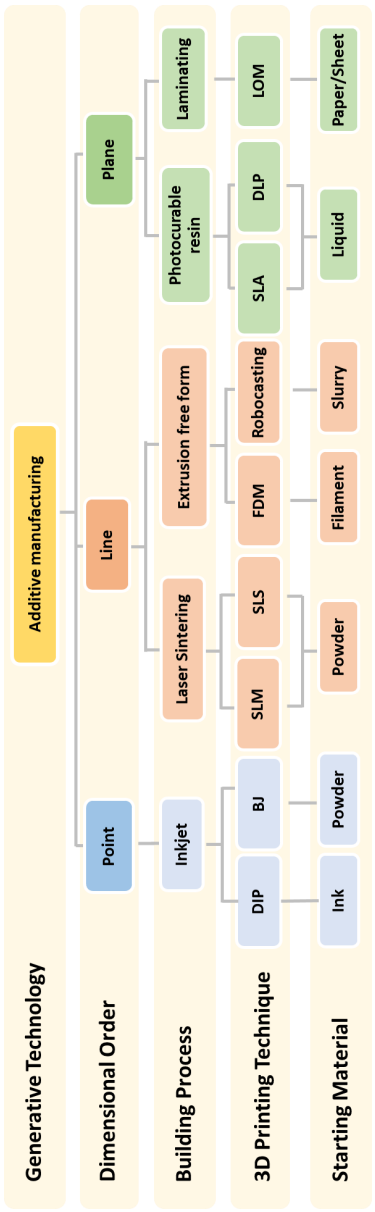

Figure 1. 16 Classification of the commercially available additive manufacturing

1.3.2.1 Direct Inkjet Printing (DIP)

Inkjet printing is a powerful fabrication tool classified as 0D (point dimensional order) because it creates the object by depositing droplets of a well-dispersed suspension. This technique consists on the accurate deposition of small amounts of ink onto a substrate, through a nozzle whose diameter is in the 20 – 75 µm range. Typical droplet volumes are in the picoliter range (10^{-12} – 10^{-9} L), which allows a local deposition of thin layers eventually different materials. Finally, the printed ink solidifies by solvent evaporation, temperature induced solidification, gelation or chemical reaction, *Figure 1. 17*.

Direct inkjet printing has also been applied to ceramic manufacturing by suspending ceramic powder into an organic ink. The success of direct ceramic jet printing depends on the dispersion of the fine ceramic powder in the media. And, for this reason, ceramic particles size must be very fine in order to avoid nozzle clogging (D100 < 0.50 Ø nozzle). Although some classic reports in ceramic inkjet mention a 1/20 ratio.[74] The small size of the particles practically limits the thickness of the printed layers to few micrometres.

On the other hand, it should be pointed out that it is possible to make components with different composition and microstructure due to the fact that the ink composition can be easily changed at each point using matrix of nozzles. This makes this process very attractive for functionally graded materials.[22,75–81]

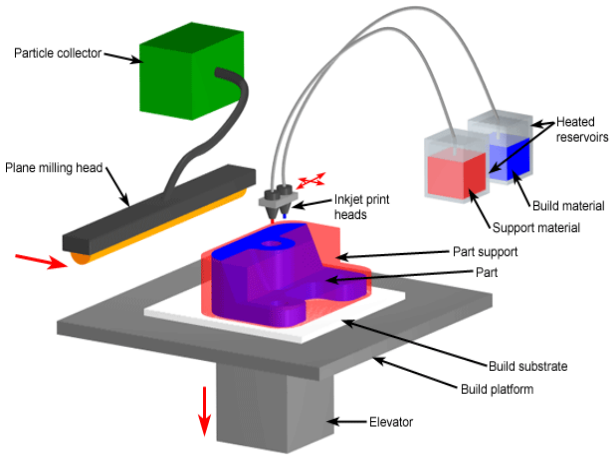

Figure 1. 17 Scheme of direct inkjet printer [82]

1.3.2.2 Binder jetting (BJ)

Binder jetting (BJ) is one of the additive manufacturing techniques with higher capability to print different materials, specially metals and ceramics. This 3D printing method is based on a powder bed system over which a print head selectively deposits a binder onto each powder layer. The

binder is a liquid bonding agent, usually a sacrificial polymer or aqueous solution, that joins the powder particles. This binder will be pyrolyzed after printing, during the debinding and sintering treatments.

The BJ printing system consists of a print bed, a feed bed, a roller, a drying unit and a printhead, *Figure 1. 18*. The printing process starts by depositing a thin layer of the powder in the bed by the roller. Once the powder bed is uniformly deposited, the printhead injects binder material onto the powder bed following the specific pattern of the first layer object design. The printhead is made by a common commercial inkjet cartridge, which can be opened, cleaned and filled with a new binder solution. In this step, there may be differences in the process depending on the printer type. Some printers use an infrared heater to dry the binder. On the other hand, other printers continue printing the next layer without drying the previous one. After the binder is sprayed, the powder bed platform goes down and the roller spreads a new powder layer over the printed layer. Thus, binder is injected again, and the process is repeated until the 3D object is completed. Finally, the green body (object recent printed without thermal treatment) is obtained.

Post-printing processes involve removing the green body from the powder bed, cleaning unbound powder using pressurized air and, ultimately, infiltrating the part to improve its mechanical resistance, or sintering the piece at high temperature.

The advantages of binder jetting technique include (i) free of support (the printed object is self-supported in the powder bed), (ii) design freedom, (it is possible to print assemblies of part and kinematic joints), (iii) large building volume, (iv) high print speed, (v) relatively low cost (due to the very little amount of waste) and (vi) several application fields due to the variety of materials that can be printed such as ceramics, metals, glasses, polymers and even sand. However, the critical point of this process is the selection of a proper binder because of the good surface finish, dimensional accuracy and high resolution strongly depend on this. For this reason, the binder must meet strict requirements. First, the binder must penetrate into the powder pores to provide enough strength. Also, it is necessary a specific surface tension, viscosity, molecular weight, conductivity and material compatibility. If not, the nozzle may clog and in turn, this may lead to a non-uniform distribution of material in the final piece.

This technique was first used in the ceramic field in the early 1990s when some powder mixtures were explored in order to produce porous ceramic hot-gas filters, investment casting shells/cores, rapid tooling (including metal materials) and drug delivery devices. Originally, coarse dry powder was used. However, modified submicrometric ceramic powders (< 20 μm) were required to achieve full density after firing. Then, the powder bed was changed by slurry-based beds, where each powder bed layer is created by jetting the slurry of ceramic material onto a substrate. Next, the layer is dried and finally the binder is deposited.[73,83–88]

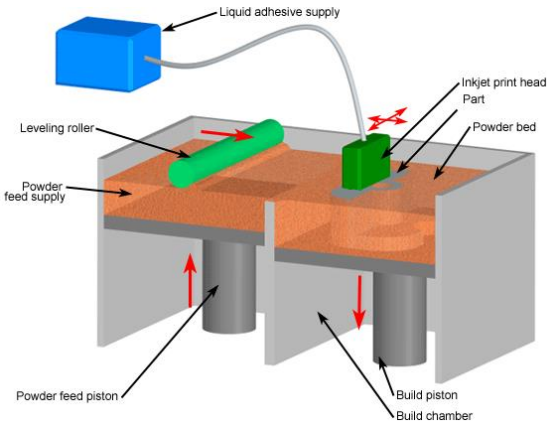

Figure 1. 18 Scheme of a binder jetting printer (adapted from reference [89])

1.3.2.3 Selective Laser Sintering (SLS) and Selective Laser Melting (SLM)

These techniques have been used for prototyping and for the fabrication of products that fit a wide range of applications. SLS and SLM are pretty similar processes that differ primarily in the binding mechanism between powder particles, being both powder-based AM techniques.

First, a thin powder layer (typically of 20-150 μm in thickness) is deposited via a roller onto the building platform. Then, a laser (usually of CO_2) traces the pattern to melt (SLM) or sinter (SLS) the powder particles following the CAD file information. After that, the building platform goes down and another powder layer is added. The steps are repeated until the piece is completed, *Figure 1. 19*. It should be pointed out that there are some differences from one instrument to another. For example, the way the powder is deposited could be by roller or scraper and also, the laser type can change (CO_2, Nd:YAG, disk or fibre laser).

In summary, in SLS the particles are compacted while in SLM they are fully melted. The production of sintered products without further post-treatment distinguishes SLS and SLM from other AM techniques. However, strong limitations appear in ceramics due to their high melting points and low thermal shock resistance. Among others, densification problems, crack formation and local stress have been a challenge. For this reason, the application of these processes has been limited. [90–99]

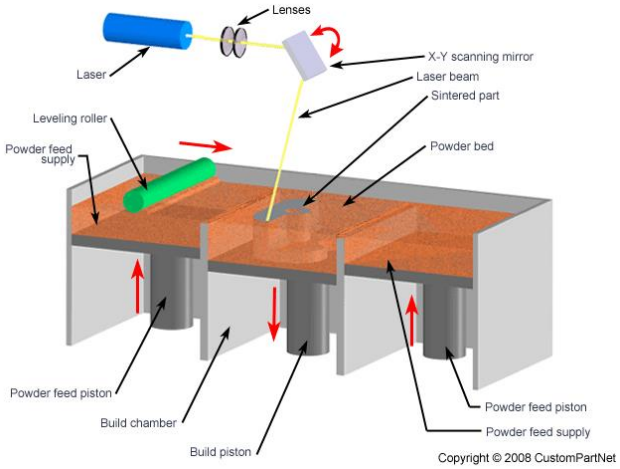

Figure 1. 19 Scheme of SLM and SLM printers [89]

1.3.2.4 Fused deposition modelling (FDM)

Fused deposition modelling (FDM) is a technique based on extrusion processes to manufacture 3D models. As other 3D printing techniques, FDM allows to build 3D parts directly from 3D CAD data. In this case, the printing material is supplied as a filament, which is extruded through a nozzle that moves in the horizontal x-y plane to produce the layers. Inside the nozzle, there are two gears that feed the filament. Also, there are resistive heaters, so while the filament is going inside the nozzle, it is warmed up at temperatures slightly above the melting point, facilitating flowing and is deposited onto the building platform following the pattern design. Once the first layer is built, the platform goes down in z-direction and the nozzle deposits another layer. The layer thickness is determined by the resolution *z* axis motor, by the diameter of the nozzle and the type of material and may vary typically from 25 µm to 1mm. The process is repeated until getting the final 3D part, *Figure 1. 20*.

A range of materials are available for this process, including polylactic acid (PLA), acrylonitrile butadiene styrene (ABS), polyamide, polycarbonate (PC), polyethylene and polypropylene, which are thermoplastics. However, other materials, as ceramics or metals, are available too.[100,101] Thermoplastics are used in automotive, electronics and telecommunications applications due to their good strength and rigidity with toughness and temperature tolerance.

In the case of ceramics, their applicability is still limited in many sectors mainly due to extrusion issues. The difficulty of ceramic fused deposition is that the printable material (ceramic embedded in a thermoplastic) must have an adequate flexibility, stiffness and viscosity to be formed as a filament, spooled and to be extruded by the nozzle, which is the key to be successful in this process. Finally, the fabricated ceramic green parts need a post-treatment processing to burnout the binder and are subjected to a final sintering in order to get the desired densification of the ceramic part.

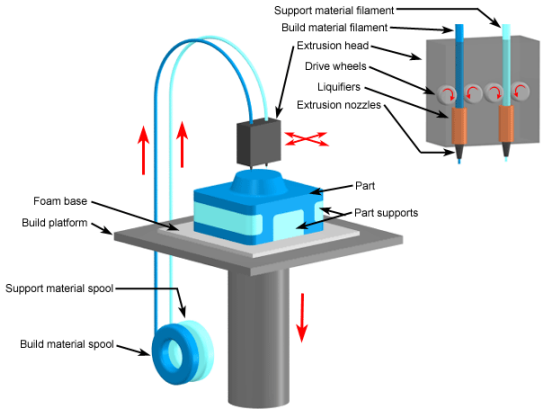

Figure 1. 20 Scheme of FDM printer [104]

The main advantage of FDM is the reduction in the processing time, minimizing the process costs too and producing minimum waste. In contrast, it has a limited accuracy due to the shape of the filament form of the material. [22,101–103]

1.3.2.5 Robocasting or Direct Ink Writing (DIW)

Robocasting is a 3D printing technique that can produce complex ceramic parts, which have low porosity and high strength, or with a large porosity including pore former. It builds the objects layer-by-layer via extruding a line of pseudoplastic slurry. The slurry is stored in a syringe connected to a dispensing nozzle on the printhead. Also, the syringe is connected to a piston that applies pressure and the slurry starts to move inside the syringe until flowing through the nozzle. Thus, the slurry is deposited in a filamentary form and undergo fast solidification to maintain the shape. Solidification may be carried out via (i) heat (the solvent evaporates), (ii) or using UV/IR light (the resin photo-cures). After the first layer is deposited, the build platform goes down and the process is repeated until getting the 3D part. Finally, the resulting green body needs a debinding process to burn the organic components, and subsequently a sintering process in order to densify the object, *Figure 1. 21*.

Obviously, robocasting is a very flexible technique in the types of materials that can be printed, including metals, polymers, bioactive polymers, ferroelectric composites and a wide range of ceramics slurries. Moreover, printing multi-ceramic structures is also possible using several nozzles with different materials. For this reason, it is possible to use this system for various applications such as (i) biocompatible scaffold material for biomedical applications, (ii) electro ceramics for energy storage, (iii) photonic crystals for optoelectronic applications, (iv) catalyst

support material for water splitting or heterogeneous catalyst supports for environmental applications.

For robocasting it is essential that slurries have adequate rheological and shear thinning properties. The mixtures have to (i) easily and fast be gelated, (ii) easily flow by the thin nozzle with low resistance, (iii) maintain the structure, (iv) prevent the collapse when is wet (a high yield stress and quickly recover elasticity), (v) support a high solid load to prevent cracks after frying, (vi) fast cure in case of thermal or UV induced curing was necessary, (vii) be homogeneous and free of air bubbles. [105–112]

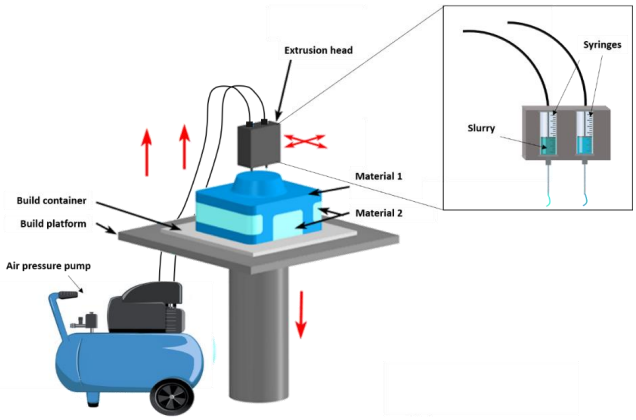

Figure 1. 21 Scheme of a robocasting printer (adapted from reference [104])

1.3.2.6 Stereolithography (SLA)

Stereolithography (SLA) was the first 3D technique introduced by Charles W. Hull as mentioned in Section 1.3.2. This process is basis in the photopolymerization process of the acrylate monomer. It occurs in three steps: initiation, propagations and termination.

Initiation in the first stage where the monomer is active by photoinitiator (PA). UV light decomposes it in PA* and generates two free radical $R°_1$ and $R°_2$:

$$PA + h\nu \rightarrow PA^* \rightarrow {R^o}_1 + {R^o}_2 \qquad \textit{Equation (1.19)}$$

After that, radicals will combine with the monomer (M) and will generate its radical RM°:

$$R^o + M \rightarrow RM^o \qquad \textit{Equation (1.20)}$$

Next stage is the propagation where some successive additions of monomer in order to create a larger radical:

$$RM^o + M \rightarrow {RM^o}_{n+1} \qquad \textit{Equation (1.21)}$$

Finally, in the termination stage the process finishes, and it is the end of the chain growth. In summary, it involves the mobility of reactive species and the rheology changes, hence is a critical step.

Thus, in relation to the components, the mixture would have (i) a photoinitiator chosen as function of the laser wavelength, (ii) a monomer, (iii) and a low viscosity solvent to improve the flow of the mixture.

According to the photo-polymerization process, SLA method is based on layer-by-layer fabrication, which uses an ultraviolet curable material. For that, this method uses an equipment with the next components: computer, a laser, an optical system, a vat and a building platform.

First, the vat is filled with the liquid monomer or commonly known as photocurable resin. The printing process starts when the object design is sliced by CAD software. The elevator platform immerses in the vat with the liquid and then the laser beam draws the first layer design. Where laser pass the resin solidifies and keeps touching the platform, which is called curing process. After that, the platform goes up but drops enough to cover the solid polymer with another layer of the photocurable suspension. A levelling blade moves across the vat surface to recoat the next layer of resin, and then, the laser draws the next layer. The process continues printing the object form until the 3D object is completely made.

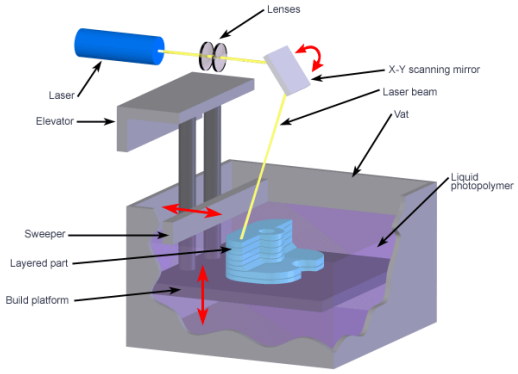

Figure 1. 22 Scheme of a SLA printer [116]

Finally, the part is taken off and the polymer excess must be cleaned. The resolution depends on both the laser and the z axis of the building platform, which defines the layer thickness, *Figure 1. 22*.

Regarding the process system, there are two types of equipment, bottom-up and top-down. In bottom-up printers, the resin is cured through a window in the bottom of the vat by a light source from below. In a top-down printer, resin is cured by a light source above the vat and the build platform is lowered down into the resin vat.

One of the parameters of the stereolithography method is the velocity in building a 3D object from a photopolymerization process. It depends on the energy per unit area of the focused spot in the resin surface, the wavelength, the type of laser used, and, of course, of the mixture composition. Other printing parameters are time, depth curing and scattering process. However, a few materials allow a control of them. For this reason, this technique is more restricted than others regarding the type of materials than can be used, even though recently, variety of available resins has been increasing. In addition, in the photosensitive resin it is possible to introduce solid

powders that may remain in the structure after curing, so the goal is to extend this technique to fabricate ceramics. To achieve that, it is necessary to introduce a highly loaded suspension of ceramic particles into polymer binder, which requires the use of a dispersant to ensure that the mixture is homogeneous. In this case, when the laser beam falls upon the surface slurry, the mixture solidifies, and the ceramic particles will be anchored in the cross-linked polymer. Lastly, a debinding and sintering process must be done in order to obtain dense ceramic parts.

Following this procedure, it is possible to fabricate high quality ceramics with smooth surfaces that can be used as microelectronics devices or biomedical implants due the precision and spatial resolution of the technique. However, it has some disadvantages, including (i) the most resins could be toxic, (ii) the long printing time in comparation with other AM techniques, due to the curing time by the laser and (iii) the high cost because of the resin and the laser. [105,113–115]

1.3.2.7 Digital Light Processing (DLP)

Digital Light Processing (DLP) can be catalogued as an SLA subtype. Both use resin and a UV light source to produce 3D parts, but the main difference resides in the type of light source used to cure the resin. While SLA uses a laser as light source, DLP uses a UV projector. In addition, as described before, SLA uses an optical system to focus a laser, while it is going through the surface of the resin, causing solidification. On the other hand, DLP uses a digital light projector screen (either UV or white light). Thus, while SLA cures the resin in a point to point way, DLP flashes the mask of a single layer (plane *xy*) all at once and all points of a layer are cured at the same time. In conclusion, DLP increases the printing speed, *Figure 1. 23*. However, DLP has some limitations too and the most important is the resolution. The resolution of a DLP printer is determined by the number of micromirrors existing in the digital micromirrors device (DMD) which is inside the projector (similar to the pixel concept). Then, in case to print large objects it is necessary to have a good resolution image. Moreover, another limitation is that curved sections do not have a very smooth and refined surface. For this reason, it a surface polishing post-treatment after printing may be required.

The material range and field of applications are the same in both techniques. It only changes the photo-initiator whose choice will be influenced by the light wavelength, although last DLP models use LED/LCD screens where wavelength can be regulated.[117–120]

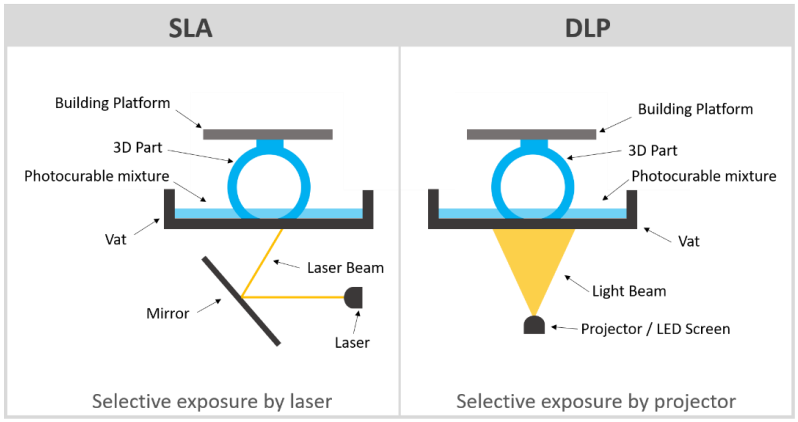

Figure 1. 23 Comparation between SLA and SLP processes (adapted from reference[121])

1.3.2.8 Laminated object Manufacture (LOM)

Laminated object manufacturing is the rapid prototyping process that combines additive and subtractive techniques in order to build a 3D object. In this process the material comes as an adhesive-coated sheet form. Four simple steps are followed to manufacture the object, (i) 3D-CAD part design, (ii) Slicing, (iii) layer attachment (iv) and production of the laminated body. For that, first a sheet of material is expended across a substrate, *Figure 1.24*. Then a carbon dioxide laser beam cuts the sheet depending on the cross-section design determined by the CAD model. Speed and focus of the laser must be adjusted in order to control the cutting depth, which must be exactly the thickness of each sheet layer. After that, the platform moves down and the second feed sheet advances and is cut as well. Then, the layers are attached by applying pressure and heat using a hot roller. The sequence is repeated, and, at the end of the process, the excess material is removed manually, *Figure 1. 24*. Finally, sometimes a post-processing treatment is required, usually polishing or resin infiltration, in order to improve the surface quality.

The advantages of this additive manufacturing process are the high fabrication speed, low cost, no supporting structures are required, no deformation or phase change taking place during the process and the possibility of building large parts. On the contrary, it presents some disadvantages as the wasted material that was subtracted, the loss of surface definition, geometrical limitations and that the printed part presents directional/anisotropic machinability and mechanical properties. A variety of materials can be used in LOM, including metals, paper, plastics, synthetic materials, ceramics and composites. Specially, ceramic tapes, which have high powder load (>40 wt. %), require the use of a strong adhesive agent such a double side adhesive or a binder solution, to improve the interconnection between consecutive tapes.

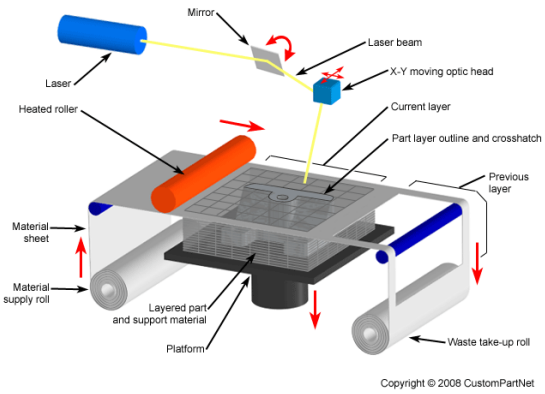

In conclusion, this technique is used extensively for tooling and manufacturing for sand casting, mould casting, car applications and tools for thermal forming and prototype stamping.[105,122–127]

Figure 1. 24 Scheme of LOM printer

1.4 State-of-the-art of 3D printing ceramics for energy and environmental applications

1.4.1 Solid oxide fuel/electrolysis cells

As mentioned in *Section 1.2.1*, fuel cells have three essential components (i) electrolyte, (ii) cathode and (iii) anode. In the case of SOFCs, the electrolyte is a ceramic oxide, *Table 1. 1*, and the cathode and anode are ceramic composites. Therefore, each component could be obtained by ceramic 3D printing, using novel techniques described in *Section 1.3.2*. Furthermore, the whole device could be printed in a single step. This can be considered a great advantage because, according to the report *Cost Study for Manufacturing of SOFC Power Systems*[128] more than one hundred steps are required to fabricate a complete SOFC via traditional methods, which highlights how difficult their manufacturing is and raises the cost and timeline. Therefore, using 3D printing technologies, it will be possible to simplify and reduce the number of steps during SOFC fabrication, while reducing the waste material and energy consumption.

Recent works have reported the use of 3D printing technologies for the fabrication of the electrolyte or electrodes of a SOFC.[118,126-136]

Regarding the electrolyte, 3D printing technologies including direct inkjet printing (DIP), selective laser sintering (SLS), robocasting and stereolithography (SLA) have been used. Most of the reported research works have employed DIP. Sukeshini *et at.*[129,130] were pioneers in this field using this technique to fabricate electrolytes and electrodes in cells exhibiting maximum power of densities of 430-460 mW/cm^2 at 850°C. Recently, previous knowledge on inkjet and SLA 3D printing has been applied in order to get thin YSZ electrolytes. Esposito *et al.*[131] have produced 1.2µm-thick YSZ electrolyte deposited on NiO-YSZ tape casted anode supports by DIP, which led

to ASR values below 0.5 Ω cm² at 750°C with an open circuit voltage (OCV) of 1.07-1.15 V for the full cell with a LSM/YSZ cathode (under dry hydrogen conditions), *Figure 1. 25*.

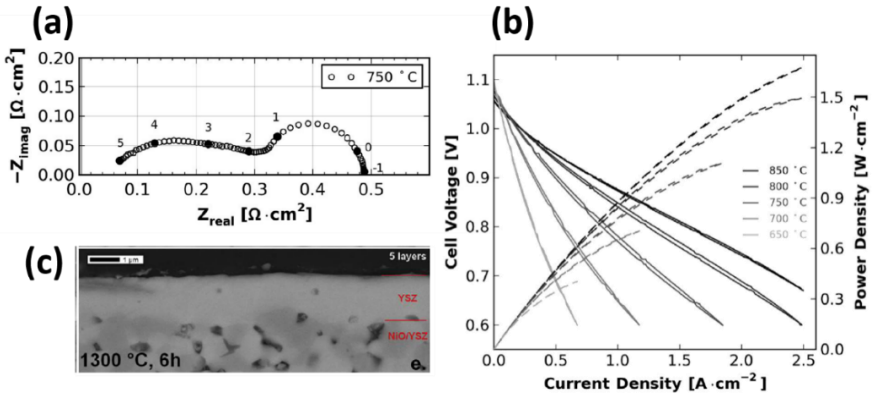

Figure 1. 25 (a) Nyquist plot of the electrochemical impedance spectrum of 1.2 µm-thick 8YSZ electrolyte at 750°C and 96% de H_2 + 4% H_2O as the fuel and air as the oxidant. (b) Polarization curves obtained for the 5-layer electrolyte SOFC with a composite LSM-YSZ cathode. Using 96% de H_2 + 4% H_2O as the fuel. (c) 1.2 µm-thick 8YSZ sintered electrolyte.[131]

The inkjet printing technique was also used by Farandos *et al.*[132] in order to print planar and 3D YSZ electrolyte structures, printing micro-pillars and square lattices subsequently, *Figure 1. 26*. The planar 23 µm-thick YSZ electrolyte was used to measure the performance of a Ni-YSZ|YSZ|YSZ-LSM|LSM electrolysis cell using CO_2/CO, achieving a remarkable current density of -0.78A cm^{-2} at 1.5V.

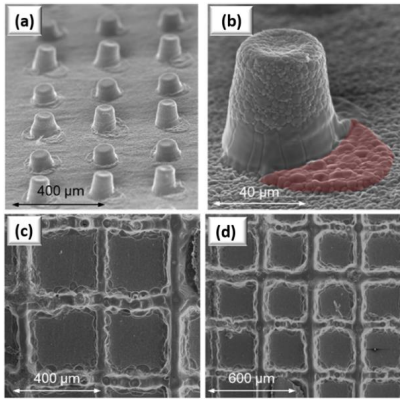

Figure 1. 26 (a,b) Array of 50 layer YSZ pillars (c,d) YSZ square scaffolds [132]

Using a different approach, Wei *et al.*[118] also fabricated 8 YSZ electrolytes of 500 µm-thickness via SLA-DLP using UV emitted light at 355-400 nm for curing each layer. Overall, this electrolyte present 10 layers of 50 µm each one. After that, it was sintered at 1550°C and Ag and GDC ($Ce_{0.8}Gd_{0.2}O_{1.9}$, Gadolinium Doped Ceria) were used as electrode, rendering an OCV of 1.04 V and a maximun power density of 176 mW cm^{-2} under hydrogen at 850°C. Similarly, Masciandaro *et al.*[133] obtained 3 YSZ electrolytes with planar and honeycomb structures, reaching SOFC performances

of 100 mW cm^{-2} and 115 mW cm^{-2}, respectively, at 900°C. This result shows that fuel cell performance may be boosted via 3D printing by producing non-conventional geometries.

Regarding the electrodes, as porous microstructures are mandatory, the techniques with this purpose are robocasting, laser sintering or powder bed. Alternatively, inkjet is employed to deposit functional layers or infiltrate already existing porous scaffolds fabricated by other means. In these cases, 3D printing is used to carry out a functionalization rather than a proper shaping step.

Interestingly, the possibility of controlling the microstructure by simply tuning 3D printing parameters has been studied by Yi. *et al.* [134], who obtained dense parts of NiO-YSZ (60-40 %wt) anode by SLS and SLM when using a CO_2 lasers while porous structures when employing a fiber laser. Regarding the infiltration of existing porous scaffolds with complementary materials to increase the electrochemical performance, Mitchell-Williams *et al.*[135] infiltrated CGO by DIP on a porous NiO-YSZ anode to increase the oxidation capability of the anode, whilst Tomov *et al.*[136] fabricated multi-component cermet anodes of Cu-Ni-YSZ for direct carbon fuel cells and reported an increase of 25% in the cell performance.

Similar to anodes, most of the studies on cathode 3D printing were focused on the use of inkjet printing, covering the optimization of the necessary inks and the printing process. Han *et al.*[137] optimized different parameters, such as deposition rate, viscosity and porosity of the LSCF (Lanthanum Strontium Cobalt Ferrite) sintered layer to obtain power densities of 377 mW/cm^2 at 600°C. More specifically, Yashiro *et al.*[138] studied the advantages of using inkjet printing technology by comparing the performance of cells based on stand-alone air-brushed cathodes and cathodes combining inkjet printed and air-brushed layers, using LSCF-GDC composites deposited on GDC dense electrolytes. The cells presented enhanced performances with maximum power densities of 710 mW/cm^2 at 600°C (compared to 540 mW/cm^2 measured for the conventional cell). This work claims that the improvement is due to an induced higher number of TPBs available for the electrochemical reaction. Due to the excellent results obtained for infiltrated cells, 3D printing is also considered a promising candidate to scale up such type of functionalization processes giving them the required level of homogeneity, reproducibility and velocity. In addition, *Li et al.*[139] introduced pore formers to produce cathode layers. Although the use of pore formers yielded an improved performance of the cells fabricated, i.e. maximum power of 950 mW/cm^2 vs. 550 mW/cm^2 at 750°C in NiO-8YSZ/YSZ/SDC/SSC-SDC, even higher performances were obtained when using conventional techniques, which stresses the need for improving the current strategies to generate porosity by inkjet printing.

In summary, technical advances have allowed to fabricate SOFC components by 3D printing techniques. These results promise a cost reduction due to a reduction in the number of steps upon

manufacturing which is better to penetrate commercial markets and becoming SOFC more competitive with alternative generating systems. However, for implementation in industrial processes, it will be necessary to achieve high specific power per unit mass and volume, which implies the fabrication of high spec ratio architectures. This will complicate the use of direct inkjet printing, hence stereolithography and extrusion processes may be considered as alternative 3D printing technologies for this application niche. Nevertheless, SLA cannot be used for multi-material fabrication, and extrusion methods have low resolutions, so it will be necessary to develop a hybrid 3D printing processes that combine different techniques in order to print a complete fuel cell (electrolyte, cathode and anode).

1.4.2 Batteries and supercapacitors

The most popular batteries to power portable systems are based on Li-ion and dominate the market due to their electrochemical performance, lightweight and cyclability. This is one of the hottest research topics in the energy field for the last 3 decades, and consequently the 2019 Nobel Prize in Chemistry has been rewarded to John Goodenough, M. Stanley Whittingham and Akira Yoshino for their pioneering work in this technology.

In recent years, 3D structures have been applied in the battery field, in order to maximize energy density and power, minimising the ionic path. For example, Notten *et al.*[140] suggest intercalating Li in Si thin films in order to increase the energy density of planar batteries, resulting in micro-fabricated 3D-integrated rechargeable batteries. Chi *et al.*[141] achieved a 3D solid-state lithium battery with a stable voltage over 700h at 0.2 mA/cm^2 current of density at 90°C. This was possible because 3D Li metal anodes were fabricated by thermal infusion strategy, in order to assemble 3D Li | SPE-LLZTO-SPE | 3D Li cells, producing ($Li_{6.4}La_3Zr_{1.4}Ta_{0.6}O_{12}$) electrolyte disks by the solid-state method.

Nevertheless, 3D components are not 3D devices, which could take further advantage towards a new generation of batteries and capacitors. Nevertheless, to date, some AM techniques have been applied in this research field: direct melting laser sintering, holographic lithography, micro-extrusion or ink-jet printing.

Concerning the direct melting laser sintering process, Liu *et al.*[142] have fabricated metallic scaffolds which could be used as pseudo-capacitors after functionalisation. Pikul *et al.*[143] used a process similar to holographic lithography, where nickel scaffolds act as outline for electrodes deposition, in order to achieve better results for Li micro-batteries than for supercapacitors. In the same group, a similar strategy was adopted to produce a 3D structure that was further infiltrated with battery materials. Furthermore, a lithographic method has been used to fabricate carbon electrodes devices too. This is the case of Ranganathan *et al.*[144] where photoresistive films

are pyrolyzed. Another technique is robocasting (also called micro-extrusion), used by Sun *et al.*[145] to fabricate graphene planar micro-supercapacitors employing a syringe-pump coupled to an XYZ system. The well-known ink-jet printing technique has been also used to fabricate batteries and capacitors components, as is the case of Kohlmeyer *et al.*[146] They printed 3D free-standing electrodes (Li_4TiO_{12}, $LiFePO_4$ or $LiCoO_2$ with nanofiber of carbon and poly(vinylidene fluoride)) with current collectors for Li-ion batteries. Using the same 3D printing process, Sun *et al.*[147] made $La_4Ti_5O_{14}$ (LTO) and $LiFePO_4$ (LFP) electrodes obtaining an entire power system, *Figure 1. 27*. Although modest performances were obtained, this can be considered as a pioneering proof of concept, which showed that ink-jet printing may successfully be applied to the energy storage research field.

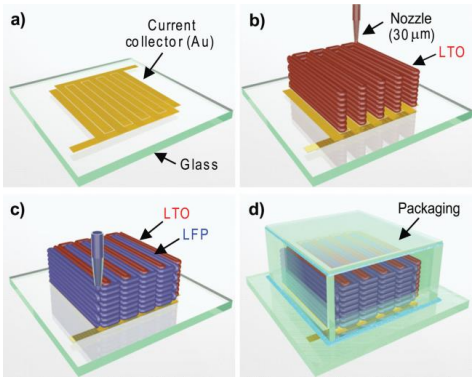

Figure 1. 27 (a) Schematic illustration of a 3D interdigitated micro-battery fabricated on (a) a gold current collector by printing $Li_4Ti_5O_{12}$ (b) and (c) $LiFePO_4$ inks through 30 mm nozzles, followed by sintering. (d) SEM image of the 3D microbattery.[147]

1.4.3 Solar energy applications

In the solar energy field, researchers have been working on 3D printing, with the goal of improving the efficiency and reducing manufacturing cost of light and flexible solar panels. These solar panels will be used in different applications, for example, portable electronics, houses and buildings or in the innovative wearable electronics. Krebs *et al.*[148] reviewed more than ten coating and printing techniques that were relevant for the case of polymer solar cells. In this work, it is established that ink-jet printing is the most conventional choice to produce complex patterns and devices. More advanced manufacturing techniques include knife-over-edge, gravure coating and slot-die methods. This last technique was used by Vak *et al.*[149] who changed a commercial 3D printer and coupled a slot-die coater to print electroactive materials. At first, they used robocasting process with a point nozzle to print patterned poly(3-hexylthiphene) (P3HT) films on ITO (indium tin oxide) glass substrate, *Figure 1. 28,* though it was not ideal for printing a uniform coating. Consequently, the nozzle was changed by a mini slot-die head, which rendered P3HT thin films. This strategy can be used to print out multilayer structures to produce a complete solar cell.

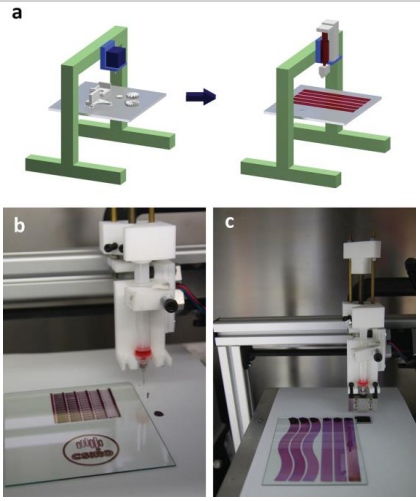

Figure 1. 28 3D printer for solution processing. a) Schematic illustration of this work. A 3D printer was modified for solution processing for the fabrication of solar cells by printing new parts for modification of function of the printer. Demonstration of capabilities of the modified 3D printer: b) in printing mode with a point nozzle and c) in coating mode with a slot nozzle.[149]

In a later work, the same research group[150] produced all the layers of a fully perovskite solar cell made by the same technique. Meanwhile, Di Giacomo *et al.*[151] applied an additive manufacturing process to fabrication flexible substrates, required to produce flexible interconnects.[152] An example would be silver electrodes, which have been deposited by some research teams using ink-jet printing[153,154] and robocasting [155] process. An efficiency of 17% was finally achieved with 40 µm of electrode line width, proving efficiency of Si solar cell when decreasing the electrode thickness. Ahn *et al.*[156] also generated flexible silver microelectrodes via robocasting. Firstly, silver nanoparticle ink was deposited onto a silicon wafer to prove the printing process. Later, flexible, spanning, stretchable, metallic and 3D printed microelectrodes were obtained on a polyimide substrate. Therefore, 3D printing opens the possibility of producing flexible components, which is a turning point to design solar cells with complex structures and high efficiencies (up to a factor of 20 higher).[157,158]

1.4.4 Catalytic reactors for fuel production and CO_2 capture

Over the last decade, one of the goals in this field has been the development of new and innovative reactor structures in order to increase chemical reactions, heat and mass transport, and obviously, at the same time reducing the environmental impact. This goal is directly related to the reactor design. In this reaction, 3D printing opens the door to produce intentionally complex packed beds, monoliths and foam structures as a support. Apart from this, 3D printing processes are a good strategy to obtain directly heterogeneous catalyst materials with a high loading of catalyst.

Traditionally, synthetizing materials for heterogeneous catalysis has been carried out by some methods where the catalyst is made or added into a support, such as: sol-gel, impregnation, atomic layer and chemical vapor deposition (CVD, ALD), co-precipitation, electrophoretic deposition, etc. However, all these processes involve a low loading of catalyst. On the other hand, a high loading

is pursued to reach a good mechanical strength, uniform catalytic distribution in the structure and a great chemical activity.

The most popular 3D printing techniques in this field is robocasting, but there are some reported works using FDM. With regard to support fabrication, Hazan *et al.*[159] reported α-Al_2O_3 and hydroxyapatite (HA) architectures via robocasting, using UV light as ink solidification method. In both cases, inks have a high solid loading (75wt. % and 59wt. %, respectively), achieving 2D printed and flexible nanocomposites, *Figure 1. 29*. Finally, Al_2O_3 structures were functionalized with TiO_2 nanoparticles to photocatalytic activity. Tubío *et al.*[160] reported the direct 3D printing of Cu/Al_2O_3 (51 vol.%) as catalytic system by robocasting. Thanks to this method, porosity, loading, interconnectivity and design could be controlled. This architecture was tested in Ullmann reactions, resulting in high efficiency and a great recyclability validated. Nevertheless, one point is clearly related to printed catalytic reactors, the majority of structures obtained are based on zeolites via robocasting.[161–165] Thakkar *et al.*[162] described as 13X and 5A zeolites (80-90 wt. %) monoliths were obtained for CO_2 removal from air. They proved that increasing the zeolite load, a better CO_2 adsorption is obtained being equivalent to the powder material. Analogously, Lefevere *et al.*[163,164] produced ZSM-5 zeolitic monolith for CO_2, N_2 and CH_4 gas separation, resulting CO_2 the strongest adsorbed gas.[163] One year later, they reported some progress with the same material, achieving a zigzag channelled structure that enhances both the stability and the activity. This last is also improved by decreasing the fiber diameter.[164] Some other materials such as 13X zeolite have been used, as is the case of Middelkoop *et al.*[165] and Regufe *et al.*[161] for CO_2 adsorption. Finally, fused deposition modelling has been also studied to fabricate reactors. Skorski *et al.*[166] produced TiO_2 constructions by dispersing the active powder (1-10 wt. %) in ABS, one typical material for FDM. This work proposes printing of titanium oxide as catalyst for removal of different pollutants.

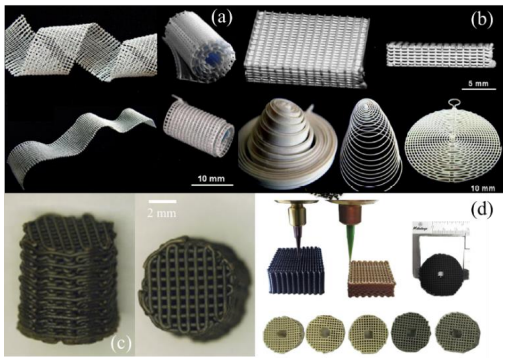

All these results show that 3D printed reactors are a currently an interesting approach for gases capture due to the stability of the porous structure and active area apart from the optimization achieved regarding heat and mass transfer and performance of the conversion reaction.

Figure 1. 29 (a) Sintered bent and rolled HA structures (1250°C).[159] *(b) Top: Sintered Al_2O_3 periodic multilayer printed. Bottom: Cured periodic multilayers, simple and multi-layered spiral architectures.*[159] *(c) Cu/Al_2O_3 sintered structure.*[160] *(d) Black samples are carbon and lighter coloured samples are 13X zeolite material; 13X zeolite samples in darker shades on the right in the bottom row are calcined samples at 470–500°C* [165]

1.5 Thesis scope

The present thesis describes the implementation of additive manufacturing processes, known as 3D printing methods, of advanced ceramic materials for energy and environmental applications. The thesis complements the current state-of-the-art of rapid prototyping of ceramics, covering the key aspect of microstructural control to improve the performance of different devices, such as Solid Oxide Fuel Cells (SOFCs) and catalytic reactors for wastewater cleaning and for solar fuels generation.

Moreover, it increases the knowledge in 3D printing technology by developing a cost-effective DLP printer, the optimization of printing parameters of different techniques such as DLP, SLA, FDM, binder jetting and robocasting for fabrication of new design concepts for electrolyte and catalytic reactors and the development of starting materials for some of these techniques and applications.

More specifically, **Chapter 2** describes the experimental aspects of this thesis: the synthesis and preparation of the different printable materials developed, the 3D printing procedures optimized, functionalization methodology used, and the whole set of characterization techniques employed (structural, chemical and electrochemical).

The following chapters are devoted to the presentation and discussion of result for each device (reactors and SOFCs) by a specific additive manufacturing process:

Chapter 3 presents a study of wastewater filters based on TiO_2 catalytic functionalization of $CaSO_4$ support reactors printed by Binder Jetting (BJ). The chapter discusses the photocatalyst degradation of methylene blue in water as a model system.

Chapter 4 is focused on the fabrication of TiO_2 filaments printed by Fused Deposition Modelling (FDM), for the same applications in wastewater filters as in Chapter 3.

Chapter 5 shows the development of a Digital Light Processing (DLP) prototype printer and its use to fabricate YSZ electrolytes for Solid Oxide Fuel Cells. The chapter also present the optimization of the printable slurry and the optimization printing parameters. In addition, the chapter describes the functionalization and characterization of such electrolytes and the device performances.

Chapter 6 summarizes all the conclusions derived from the thesis.

Finally, **Appendix I** presents preliminary results of tests realized for LSM-YSZ electrode deposition on a printed electrolyte via robocasting. This study intends to further develop fully printed SOFC devices. And **Appendix II** present preliminary results of test done for biodiesel production using 3D printing technology to manufacture the mould of the catalyst structure.

1.6 References

[1] Nuvolari, A. Collective Invention during the British Industrial Revolution: The Case of the Cornish Pumping Engine. Cambridge J. Econ. (2004), 28 (3), 347–363, doi:10.1093/cje/28.3.347.

[2] Allen, R. C. The British Industrial Revolution in Global Perspective: How Commerce Created the Industrial Revolution and Modern Economic Growth. Cambridge Univ. Press (2009), 1–41.

[3] Musson, A.; Robinson, E. Science and Technology in the Industrial Revolution; Gordon and Breach, (1989).

[4] Ruiz-Morales, J. C.; J, P.-M.; P, M. L.; Romero, D. P. C. Dn. C. Pb. P. Bc. V. Jg. Pilas de Combustible de Óxidos Sólidos (SOFC), 2nd ed.; Centro de la Cultura Popular Canaria, Ed.; Santa Cruz de Tenerife, (2008).

[5] US Department of Commerce, NOAA, E. S. R. L. ESRL Global Monitoring Division - Global Greenhouse Gas Reference Network https://www.esrl.noaa.gov/gmd/ccgg/trends/index.html (accessed Feb 28, 2020).

[6] El observatorio de Izaña confirma la entrada del ser humano en territorio inexplorado: 415 ppm de CO2 http://www.aemet.es/es/noticias/2019/05/415_ppm_umbral_dioxido_de_carbono_izana (accessed Mar 20, 2020).

[7] Carbon Dioxide measured by AEMET https://www.epdata.es/buscador?texto=AEMET CO2 (accessed Mar 20, 2020).

[8] US Department of Commerce, N. E. S. R. L. ESRL Global Monitoring Division - Global Greenhouse Gas Reference Network https://www.esrl.noaa.gov/gmd/ccgg/trends/ (accessed Feb 28, 2020).

[9] NOAA National Centers for Environmental information, Climate at a Glance: Global Time Series https://www.ncdc.noaa.gov/cag/global/time-series/globe/land_ocean/ytd/12/1880-2019 (accessed Feb 28, 2020).

[10] Halkos, G. E. Sulphur Abatement Policy: Implications of Cost Differentials. Energy Policy (1993), 21 (10), 1035–1043, doi:10.1016/S0301-4215(06)80006-6.

[11] Marrakech Climate Change Conference - November 2016 | UNFCCC https://unfccc.int/process-and-meetings/conferences/past-conferences/marrakech-climate-change-conference-november-2016/marrakech-climate-change-conference-november-2016 (accessed Feb 28, 2020).

[12] Lüthi, D.; Le Floch, M.; Bereiter, B.; Blunier, T.; Barnola, J. M.; Siegenthaler, U.; Raynaud, D.; Jouzel, J.; Fischer, H.; Kawamura, K.; et al. High-Resolution Carbon Dioxide Concentration Record 650,000-800,000 Years before Present. Nature (2008), 453 (7193), 379–382, doi:10.1038/nature06949.

[13] Kuehr, R. Towards a Sustainable Society: United Nations University's Zero Emissions Approach. J. Clean. Prod. (2007), 15 (13–14), 1198–1204, doi:10.1016/j.jclepro.2006.07.020.

[14] Groenevelt, H. The Just-in-Time System. In Handbooks in Operations Research and Management Science; Elsevier, (1993); Vol. 4, pp 629–670 doi:10.1016/S0927-0507(05)80192-6.

[15] International Energy Agency (IEA) Energy efficiency indicators. https://www.iea.org/data-and-statistics?country=WORLD&fuel=Energy supply&indicator=Coal production by type (accessed Feb 28, 2020).

[16] Renewables in electricity oroduction; Global Energy Satistical Yearbook 2019; Enerdata https://yearbook.enerdata.net/renewables/renewable-in-electricity-production-share.html (accessed Oct 5, 2019).

[17] Antonucci, V.; Antonucci, P. L.; Gullo, L.; La Rosa, D.; Siracusano, S. Advanced (Electro) Ceramics and Innovative Energy Technologies. J. Eur. Ceram. Soc. (2004), 24 (6), 1337–1342, doi:10.1016/S0955-2219(03)00560-0.

[18] Rödel, J.; Kounga, A. B. N.; Weissenberger-Eibl, M.; Koch, D.; Bierwisch, A.; Rossner, W.; Hoffmann, M. J.; Danzer, R.; Schneider, G. Development of a Roadmap for Advanced Ceramics: 2010-2025. J. Eur. Ceram. Soc. (2009), 29 (9), 1549–1560, doi:10.1016/j.jeurceramsoc.2008.10.015.

[19] Rice, R. W. Ceramic Fabrication Technology; Marcel Dekker Inc, Ed.; New York, (2003) doi:10.1201/9780203911020.

[20] Ruiz-Morales, J. C.; Marrero-López, D.; Canales-Vázquez, J.; Irvine, J. T. S. Symmetric and Reversible Solid Oxide Fuel Cells. RSC Adv. (2011), 1 (8), 1403–1414, doi:10.1039/c1ra00284h.

[21] EG&G Technical Services, I. U. Fuel Cell Handbook, Seventh.; EG&G Technical Services, I., Ed.; Morgantown, West Virginia, (2004).

[22] Ruiz-Morales, J. C.; Tarancón, A.; Canales-Vázquez, J.; Méndez-Ramos, J.; Hernández-Afonso, L.; Acosta-Mora, P.; Marín Rueda, J. R.; Fernández-González, R. Three Dimensional Printing of Components and Functional Devices for Energy and Environmental Applications. Energy Environ. Sci. (2017), 10, 846–859, doi:10.1039/C6EE03526D.

[23] Fernández-González, R. Synthesis , Assembling and Validation of Solid Oxide Fuel Cell Units., University of La Laguna, (2014).

[24] Mahato, N.; Banerjee, A.; Gupta, A.; Omar, S.; Balani, K. Progress in Material Selection for Solid Oxide Fuel Cell Technology: A Review. Prog. Mater. Sci. (2015), 72, 141–337, doi:10.1016/j.pmatsci.2015.01.001.

[25] Derek Fray, Á. V. S. M. and J. C. T. Fuel Cell. DoITPoMS, University of Cambridge https://www.doitpoms.ac.uk/tlplib/fuel-cells/printall.php (accessed Feb 28, 2020).

[26] Han, Y.; Zhu, J. Surface Science Studies on the Zirconia-Based Model Catalysts. Top. Catal. (2013), 56 (15–17), 1525–1541, doi:10.1007/s11244-013-0156-5.

[27] Abdin, Z.; Zafaranloo, A.; Rafiee, A.; Mérida, W.; Lipiński, W.; Khalilpour, K. R. Hydrogen as an Energy Vector. Renew. Sustain. Energy Rev. (2020), 120, 32, doi:10.1016/j.rser.2019.109620.

[28] Tarancón, A.; Fábrega, C.; Morata, A.; Torrell, M.; Andreu, T. Power-to-Fuel and Artificial Photosynthesis for Chemical Energy Storage. In Materials for Sustainable Energy Applications: Conversion, Storage, Transmission, and Consumption; Moya, X., Muñoz-Rojas, D., Eds.; Pan Standford Plublishing, (2016); pp 493–566 doi:10.4032/9789814411820.

[29] Fujishima, A.; Honda, K. Electrochemical Photolysis of Water at a Semiconductor Electrode. Nature (1972), 37–38, doi:10.1038/238037a0.

[30] Maeda, K. Z-Scheme Water Splitting Using Two Different Semiconductor Photocatalysts. ACS Catal. (2013), 3, 1486–1503, doi:10.1021/cs4002089.

[31] Maeda, K.; Domen, K. Photocatalytic Water Splitting: Recent Progress and Future Challenges. J. Phys. Chem. Lett. (2010), 1, 2655–2661, doi:10.1021/jz1007966.

[32] Pelaez, M.; Nolan, N. T.; Pillai, S. C.; Seery, M. K.; Falaras, P.; Kontos, A. G.; Dunlop, P. S. M.; Hamilton, J. W. J.; Byrne, J. A.; O'Shea, K.; et al. A Review on the Visible Light Active Titanium

Dioxide Photocatalysts for Environmental Applications. Appl. Catal. B Environ. (2012), 125, 331–349, doi:10.1016/j.apcatb.2012.05.036.

[33] Ma, X. X.; Chen, L.; Zhang, Z.; Tang, J. L. _CuO@Cu2O Nanowires Array on Cu Foam as Bifunctional Electrocatalyst for Efficient Water Pplitting. Chinese J. Anal. Chem. (2020), 48, 20001–20012, doi:10.1016/S1872-2040(19)61211-9.

[34] Méndez-Ramos, J.; Acosta-Mora, P.; Ruiz-Morales, J. C.; Hernández, T.; Borges, M. E.; Esparza, P. Turning into the Blue: Materials for Enhancing TiO_2 Photocatalysis by up-Conversion Photonics. RSC Adv. (2013), 3 (45), 23028–23034, doi:10.1039/c3ra44342f.

[35] Gavrilescu, M.; Demnerová, K.; Aamand, J.; Agathos, S.; Fava, F. Emerging Pollutants in the Environment: Present and Future Challenges in Biomonitoring, Ecological Risks and Bioremediation. N. Biotechnol. (2015), 32, 147–156, doi:10.1016/j.nbt.2014.01.001.

[36] Eurostat. Chemicals production and consumption statistics https://ec.europa.eu/eurostat/statistics-explained/index.php?title=Chemicals_production_and_consumption_statistics#Total_production_of_chemicals (accessed Jan 29, 2020).

[37] Belzona. Tratamiento de Aguas Residuales, 1 st.; Belzona, Ed.; (2010).

[38] Yang, L.; Yu, L. E.; Ray, M. B. Degradation of Paracetamol in Aqueous Solutions by TiO_2 Photocatalysis. Water Res. (2008), 42, 3480–3488, doi:10.1016/j.watres.2008.04.023.

[39] Loos, R.; Marinov, D.; Sanseverino, I.; Napierska, D.; Lettieri, T. Review of the 1st Watch List under the Water Framework Directive and Recommendations for the 2nd Watch List. Jorunal Tech. Reports (2018), No. April, 265, doi:10.2760/614367.

[40] Dulio, V.; van Bavel, B.; Brorström-Lundén, E.; Harmsen, J.; Hollender, J.; Schlabach, M.; Slobodnik, J.; Thomas, K.; Koschorreck, J. Emerging Pollutants in the EU: 10 Years of NORMAN in Support of Environmental Policies and Regulations. Environ. Sci. Eur. (2018), 30 doi:10.1186/s12302-018-0135-3.

[41] Alphenaar, P. A.; van Houten, M. Insight in Emerging Contaminants in Europe. The Netherlands Public Waste Agency of Flandershe Netherlands Public Waste Agency of Flanders (2016), 159.

[42] Sousa, M. A.; Gonçalves, C.; Vilar, V. J. P.; Boaventura, R. A. R.; Alpendurada, M. F. Suspended TiO_2-Assisted Photocatalytic Degradation of Emerging Contaminants in a Municipal WWTP Effluent Using a Solar Pilot Plant with CPCs. Chem. Eng. J. (2012), 198–199, 301–309, doi:10.1016/j.cej.2012.05.060.

[43] Xing, Z.; Zhou, W.; Du, F.; Qu, Y.; Tian, G.; Pan, K.; Tian, C.; Fu, H. A Floating Macro/Mesoporous Crystalline Anatase TiO 2 Ceramic with Enhanced Photocatalytic Performance for Recalcitrant Wastewater Degradation. Dalt. Trans. (2014), 43, 790–798, doi:10.1039/c3dt52433g.

[44] Hernández-Afonso, L.; Fernández-González, R.; Esparza, P.; Borges, M. E.; González, S. Dí.; Canales-Vázquez, J.; Ruiz-Morales, J. C. Ceramic-Based 3D Printed Supports for Photocatalytic Treatment of Wastewater. J. Chem. (2017), 9, doi:10.1155/2017/7602985.

[45] Soutsas, K.; Karayannis, V.; Poulios, I.; Riga, A.; Ntampegliotis, K.; Spiliotis, X.; Papapolymerou, G. Decolorization and Degradation of Reactive Azo Dyes via Heterogeneous Photocatalytic Processes. Desalination (2010), 250, 345–350, doi:10.1016/j.desal.2009.09.054.

[46] Sangiorgi, A.; Gonzalez, Z.; Ferrandez-Montero, A.; Yus, J.; Sanchez-Herencia, A. J.; Galassi, C.; Sanson, A.; Ferrari, B. 3D Printing of Photocatalytic Filters Using a Biopolymer to Immobilize TiO_2 Nanoparticles. J. Electrochem. Soc. (2019), 166, H3239–H3248, doi:10.1149/2.0341905jes.

[47] Borges, M. E.; Sierra, M.; Méndez-Ramos, J.; Acosta-Mora, P.; Ruiz-Morales, J. C.; Esparza, P. Solar Degradation of Contaminants in Water: TiO_2 Solar Photocatalysis Assisted by up-Conversion Luminescent Materials. Sol. Energy Mater. Sol. Cells (2016), 155, 194–201, doi:10.1016/j.solmat.2016.06.010.

[48] Miranda-García, N.; Suárez, S.; Sánchez, B.; Coronado, J. M.; Malato, S.; Maldonado, M. I. Photocatalytic Degradation of Emerging Contaminants in Municipal Wastewater Treatment Plant Effluents Using Immobilized TiO_2 in a Solar Pilot Plant. Appl. Catal. B Environ. (2011), 103, 294–301, doi:10.1016/j.apcatb.2011.01.030.

[49] Borges, M. E.; García, D. M.; Hernández, T.; Ruiz-Morales, J. C.; Esparza, P. Supported Photocatalyst for Removal of Emerging Contaminants from Wastewater in a Continuous Packed-Bed Photoreactor Configuration. Catalysts (2015), 5, 77–87, doi:10.3390/catal5010077.

[50] Pozzo, R. L.; Baltanás, M. A.; Cassano, A. E. Supported Titanium Oxide as Photocatalyst in Water Decontamination: State of the Art. Catal. Today (1997), 39, 219–231, doi:10.1016/S0920-5861(97)00103-X.

[51] Murugan, R.; Ganesh Ram, C. Energy Efficient Drinking Water Purification System Using TiO_2 Solar Reactor with Traditional Methods. Mater. Today Proc. (2018), 5, 415–421, doi:10.1016/j.matpr.2017.11.100.

[52] Li, T.; Cheng, J.; Huang, R.; Zhou, J.; Cen, K. Conversion of Waste Cooking Oil to Jet Biofuel with Nickel-Based Mesoporous Zeolite Y Catalyst. Bioresour. Technol. (2015), 197, 289–294, doi:10.1016/j.biortech.2015.08.115.

[53] Laura Díaz Rodríguez. Procesos de Catálisis Heterogénea Para La Obtención de Biodiésel. Utilización de Aceite de Jatropha Curcas y Aceite de Fritura Como Materias Primas., Universidad de La Laguna, (2017).

[54] Ooi, X. Y.; Gao, W.; Ong, H. C.; Lee, H. V.; Juan, J. C.; Chen, W. H.; Lee, K. T. Overview on Catalytic Deoxygenation for Biofuel Synthesis Using Metal Oxide Supported Catalysts. Renew. Sustain. Energy Rev. (2019), 112, 834–852, doi:10.1016/j.rser.2019.06.031.

[55] Yazdani, S. S.; Gonzalez, R. Anaerobic Fermentation of Glycerol: A Path to Economic Viability for the Biofuels Industry. Curr. Opin. Biotechnol. (2007), 18, 213–219, doi:10.1016/j.copbio.2007.05.002.

[56] Brito, A.; Borges, M. E.; Garín, M.; Hernández, A. Biodiesel Production from Waste Oil Using Mg - Al Layered Double Hydroxide Catalysts. Energy and Fuels (2009), 23, 2952–2958, doi:10.1021/ef801086p.

[57] Borges, M. E.; Díaz, L. Catalytic Packed-Bed Reactor Configuration for Biodiesel Production Using Waste Oil as Feedstock. Bioenergy Res. (2013), 6, 222–228, doi:10.1007/s12155-012-9246-7.

[58] Said, N. H.; Ani, F. N.; Said, M. F. M. Review of the Production of Biodiesel from Waste Cooking Oil Using Solid Catalysts. J. Mech. Eng. Sci. (2015), 8, 1302–1311, doi:10.15282/jmes.8.2015.5.0127.

[59] Borges, M. E.; Díaz, L.; Alvarez-Galván, M. C.; Brito, A. High Performance Heterogeneous Catalyst for Biodiesel Production from Vegetal and Waste Oil at Low Temperature. Appl. Catal. B Environ. (2011), 102, 310–315, doi:10.1016/j.apcatb.2010.12.018.

[60] Borges, M. E.; Hernández, L.; Ruiz-Morales, J. C.; Martín-Zarza, P. F.; Fierro, J. L. G.; Esparza, P. Use of 3D Printing for Biofuel Production: Efficient Catalyst for Sustainable Biodiesel Production from Wastes. Clean Technol. Environ. Policy (2017), 19 (8), 2113–2127, doi:10.1007/s10098-017-1399-9.

[61] Taufiqurrahmi, N.; Mohamed, A. R.; Bhatia, S. Production of Biofuel from Waste Cooking Palm Oil Using Nanocrystalline Zeolite as Catalyst: Process Optimization Studies. Bioresour. Technol. (2011), 102 (22), 10686–10694, doi:10.1016/j.biortech.2011.08.068.

[62] Buelens, L. C.; Galvita, V. V.; Poelman, H.; Detavernier, C.; Marin, G. B. Super-Dry Reforming of Methane Intensifies CO_2 Utilization via Le Chatelier's Principle. Science. (2016), 354, 449–452, doi:10.1126/science.aah7161.

[63] Roy, S. C.; Varghese, O. K.; Paulose, M.; Grimes, C. A. Toward Solar Fuels: Photocatalytic Conversion of Carbon Dioxide to Hydrocarbons. ACS Nano (2010), 4 (3), 1259–1278, doi:10.1021/nn9015423.

[64] Jiangtian Li, N. W. Semiconductor-Based Photocatalysts and Photoelectrochemical Cells for Solar Fuel Generation: A Review. Catal. Sci. Technol. (2015), 5, 1360–1384, doi:DOI: 10.1039/C4CY00974F.

[65] Liu, L.; Li, Y. Understanding the Reaction Mechanism of Photocatalytic Reduction of CO_2 with H_2O on TiO_2-Based Photocatalysts: A Review. Aerosol Air Qual. Res. (2014), 14 (2), 453–469, doi:10.4209/aaqr.2013.06.0186.

[66] Rahaman, M., N. Ceramic Processing and Sintering. Int. Mater. Rev. (1996), 41, 36–37, doi:10.1179/095066096790151286.

[67] Tay, B. Y.; Evans, J. R. G.; Edirisinghe, M. J. Solid Freeform Fabrication of Ceramics. Int. Mater. Rev. (2003), 48 (6), 341–370, doi:10.1179/095066003225010263.

[68] Travitzky, N.; Bonet, A.; Dermeik, B.; Fey, T.; Filbert-Demut, I.; Schlier, L.; Schlordt, T.; Greil, P. Additive Manufacturing of Ceramic-Based Materials. Adv. Eng. Mater. (2014), 16, 729–754, doi:10.1002/adem.201400097.

[69] Kodama, H. Automatic Method for Fabricating a Three-Dimensional Plastic Model with Photo-Hardening Polymer. Rev. Sci. Instrum. (1981), 52, 1770–1773, doi:10.1063/1.1136492.

[70] Hull, C. W.; Arcadia, C. Apparatus for production of three-dmensonal objects by stereolithography. US4575330A, August 8, 1984.

[71] Redwood, B.; Schöffer, F.; Garret, B. The 3D Printing Handbook: Technologies, Design and Applications, 1st ed.; Hubs, 3D, Ed.; (2017).

[72] ISO - ISO/ASTM 52900:2015 - Additive manufacturing — General principles — Terminology https://www.iso.org/standard/69669.html (accessed Mar 11, 2020).

[73] Deckers, J.; Vleugels, J.; Kruth, J. P. Additive Manufacturing of Ceramics: A Review. J. Ceram. Sci. Technol. (2014), 5, 245–260, doi:10.4416/JCST2014-00032.

[74] Derby, B.; Reis, N. Inkjet Printing of Highly Loaded Particulate Suspensions. MRS Bulletin. Materials Research Society 2003, pp 815–818 doi:10.1557/mrs2003.230.

[75] Lewis, J. A.; Smay, J. E.; Stuecker, J.; Cesarano, J. Direct Ink Writing of Three-Dimensional Ceramic Structures. J. Am. Ceram. Soc. (2006), 89, 3599–3609, doi:10.1111/j.1551-2916.2006.01382.x.

[76] Teng, W. D.; Edirisinghe, M. J.; Evans, J. R. G. Optimization of Dispersion and Viscosity of a Ceramic Jet Printing Ink. J. Am. Ceram. Soc. (2005), 80, 486–494, doi:10.1111/j.1151-2916.1997.tb02855.x.

[77] Song, J. H.; Edirisinghe, M. J.; Evans, J. R. G. Formulation and Multilayer Jet Printing of Ceramic Inks. J. Am. Ceram. Soc. (2004), 82, 3374–3380, doi:10.1111/j.1151-2916.1999.tb02253.x.

[78] Zhao, X.; Evans, J. R. G.; Edirisinghe, M. J.; Song, J. H. Direct Ink-Jet Printing of Vertical Walls. J. Am. Ceram. Soc. (2002), 85, 2113–2115, doi:10.1111/j.1151-2916.2002.tb00414.x.

[79] Rosa, M.; Gooden, P. N.; Butterworth, S.; Zielke, P.; Kiebach, R.; Xu, Y.; Gadea, C.; Esposito, V. Zirconia Nano-Colloids Transfer from Continuous Hydrothermal Synthesis to Inkjet Printing. J. Eur. Ceram. Soc. (2019), 39, 2–8, doi:10.1016/j.jeurceramsoc.2017.11.035.

[80] Rosa, M.; Barou, C.; Esposito, V. Zirconia UV-Curable Colloids for Additive Manufacturing via Hybrid Inkjet Printing-Stereolithography. Mater. Lett. (2018), 215, 214–217, doi:10.1016/j.matlet.2017.12.096.

[81] Derby, B. Inkjet Printing Ceramics: From Drops to Solid. J. Eur. Ceram. Soc. (2011), 31, 2543–2550, doi:10.1016/j.jeurceramsoc.2011.01.016.

[82] Custompart.net. Inkjet Printing Process http://www.custompartnet.com/wu/ink-jet-printing (accessed Mar 2, 2020).

[83] Han, C.; Yaoyao Fiona, Z. Process Parameters Optimization for Improving Surface Quality and Manufacturing Accuracy of Binder Jetting Additive Manufacturing Process. Rapid Prototyp. J. (2016), 22 (3), 527–538, doi:10.1108/RPJ-11-2014-0149.

[84] Gibson, I.; Rosen, D.; Stucker, B. Additive Manufacturing Technologies: 3D Printing, Rapid Prototyping, and Direct Digital Manufacturing, Second Edition. Addit. Manuf. Technol. 3D Printing, Rapid Prototyping, Direct Digit. Manuf. Second Ed. (2015), 1–498, doi:10.1007/978-1-4939-2113-3.

[85] Lee, J. Y.; An, J.; Chua, C. K. Fundamentals and Applications of 3D Printing for Novel Materials. Appl. Mater. Today (2017), 7, 120–133, doi:10.1016/j.apmt.2017.02.004.

[86] Gonzalez, J. A.; Mireles, J.; Lin, Y.; Wicker, R. B. Characterization of Ceramic Components Fabricated Using Binder Jetting Additive Manufacturing Technology. Ceram. Int. (2016), 42, 10559–10564, doi:10.1016/j.ceramint.2016.03.079.

[87] Miyanaji, H.; Zhang, S.; Lassell, A.; Zandinejad, A.; Yang, L. Process Development of Porcelain Ceramic Material with Binder Jetting Process for Dental Applications. J. Miner. Met. Mater. Soc. (2016), 68, 831–841, doi:10.1007/s11837-015-1771-3.

[88] Trombetta, R.; Inzana, J. A.; Schwarz, E. M.; Kates, S. L.; Awad, H. A. 3D Printing of Calcium Phosphate Ceramics for Bone Tissue Engineering and Drug Delivery. Ann. Biomed. Eng. (2017), 45, 23–44, doi:10.1007/s10439-016-1678-3.

[89] Custompart.net. DMLS - Direct Metal Laser Sintering http://www.custompartnet.com/wu/direct-metal-laser-sintering (accessed Mar 2, 2020).

[90] Kruth, J. P.; Froyen, L.; Van Vaerenbergh, J.; Mercelis, P.; Rombouts, M.; Lauwers, B. Selective Laser Melting of Iron-Based Powder. J. Mater. Process. Technol. (2004), 149, 616–622, doi:10.1016/j.jmatprotec.2003.11.051.

[91] Bertrand, P.; Bayle, F.; Combe, C.; Goeuriot, P.; Smurov, I. Ceramic Components Manufacturing by Selective Laser Sintering. Appl. Surf. Sci. (2007), 254, 989–992, doi:10.1016/j.apsusc.2007.08.085.

[92] Mercelis, P.; Kruth, J. P. Residual Stresses in Selective Laser Sintering and Selective Laser Melting. Rapid Prototyp. J. (2006), 12, 254–265, doi:10.1108/13552540610707013.

[93] Yves-Christian, H.; Jan, W.; Wilhelm, M.; Konrad, W.; Reinhart, P. Net Shaped High Performance Oxide Ceramic Parts by Selective Laser Melting. Phys. Procedia (2010), 5, 587–594, doi:10.1016/j.phpro.2010.08.086.

[94] Kruth, J. P.; Mercelis, P.; Van Vaerenbergh, J.; Froyen, L.; Rombouts, M. Binding Mechanisms in Selective Laser Sintering and Selective Laser Melting. Rapid Prototyp. J. (2005), 11, 26–36, doi:10.1108/13552540510573365.

[95] J.P. Kruth, X. Wang, T. L. & L. F. Lasers and Materials in Selective Laser Sintering. Int. J. Assem. Technol. Manag. (2006), 23, 357–371.

[96] Agarwala, M.; Bourell, D.; Beaman, J.; Marcus, H.; Barlow, J. Emerald Article: Direct Selective Laser Sintering of Metals Direct Selective Laser Sintering of Metals. Rapid Prototyp. J. (1995), 1, 26–36.

[97] Kumar, S. Selective Laser Sintering: A Qualitative and Objective Approach. J. Miner. Met. Mater. Soc. (2003), 55(10), 43–47.

[98] Shishkovsky, I.; Yadroitsev, I.; Bertrand, P.; Smurov, I. Alumina-Zirconium Ceramics Synthesis by Selective Laser Sintering/Melting. Appl. Surf. Sci. (2007), 254, 966–970, doi:10.1016/j.apsusc.2007.09.001.

[99] Kuscer, D.; Shen, J. Z. Selective Laser Sintering Learn More about Selective Laser Sintering Advanced Direct Forming Processes for the Future. In Additive Manufacturing; (2018).

[100] Chen, Z.; Li, Z.; Li, J.; Liu, C.; Lao, C.; Fu, Y.; Liu, C.; Li, Y.; Wang, P.; He, Y. 3D Printing of Ceramics: A Review. J. Eur. Ceram. Soc. (2019), 39, 661–687, doi:10.1016/j.jeurceramsoc.2018.11.013.

[101] Mohammadi, F. A Novel System for Fused Deposition of Advanced Multiple Ceramics. Rapid Prototyp. J. (2006), 6, 161–175, doi:10.1108/13552540010337047.

[102] Schantz, J. T.; Brandwood, A.; Hutmacher, D. W.; Khor, H. L.; Bittner, K. Osteogenic Differentiation of Mesenchymal Progenitor Cells in Computer Designed Fibrin-Polymer-Ceramic Scaffolds Manufactured by Fused Deposition Modeling. J. Mater. Sci. Mater. Med. (2005), 16 (9), 807–819, doi:10.1007/s10856-005-3584-3.

[103] Barna, J.; Torok, J.; Novakova-Marcincinova, L.; Kuric, I. Basic and Advanced Materials for Fused Deposition Modeling Rapid Prototyping Technology. Manuf. Ind. Eng (2012), 11 (1), 1338–6549,.

[104] Custompart.net. Fused Deposition Modeling (FDM) http://www.custompartnet.com/wu/fused-deposition-modeling (accessed Mar 2, 2020).

[105] Weinmann, M.; Aldinger, F. Rapid Prototyping of Ceramics. In Handbook of Advanced Ceramics: Materials, Applications, Processing and Properties; Elsevier, Ed.; (2013); pp 489–524 doi:10.1016/B978-012654640-8/50007-9.

[106] Feilden, E. Additive Manufacturing of Ceramics and Ceramic Composites via Robocasting., Centre for Advanced Structural Ceramics Department of Materials Imperial College London, (2017).

[107] Peng, E.; Zhang, D.; Ding, J. Ceramic Robocasting: Recent Achievements, Potential, and Future Developments. Adv. Mater. (2018), 30, 1–14, doi:10.1002/adma.201802404.

[108] Feilden, E. Robocasting of Structural Ceramic Parts with Hydrogel Inks., Imperial College London, (2016).

[109] Ren, X.; Shao, H.; Lin, T.; Zheng, H. 3D Gel-Printing-An Additive Manufacturing Method for Producing Complex Shape Parts. Mater. Des. (2016), 101, 80–87, doi:10.1016/j.matdes.2016.03.152.

[110] Xu, W.; Wang, X.; Sandler, N.; Willför, S.; Xu, C. Three-Dimensional Printing of Wood-Derived Biopolymers: A Review Focused on Biomedical Applications. ACS Sustain. Chem. Eng. (2018), 6, 5663–5680, doi:10.1021/acssuschemeng.7b03924.

[111] Franchin, G.; Scanferla, P.; Zeffiro, L.; Elsayed, H.; Baliello, A.; Giacomello, G.; Pasetto, M.; Colombo, P. Direct Ink Writing of Geopolymeric Inks. J. Eur. Ceram. Soc. (2017), 37, 2481–2489, doi:10.1016/j.jeurceramsoc.2017.01.030.

[112] Shao, H.; Zhao, D.; Lin, T.; He, J.; Wu, J. 3D Gel-Printing of Zirconia Ceramic Parts. Ceram. Int. (2017), 43, 13938–13942, doi:10.1016/j.ceramint.2017.07.124.

[113] Chartier, T.; Badev, A.; Abouliatim, Y.; Lebaudy, P.; Lecamp, L. Stereolithography Process: Influence of the Rheology of Silica Suspensions and of the Medium on Polymerization Kinetics - Cured Depth and Width. J. Eur. Ceram. Soc. (2012), 32, 1625–1634, doi:10.1016/j.jeurceramsoc.2012.01.010.

[114] Stansbury, J. W.; Idacavage, M. J. 3D Printing with Polymers: Challenges among Expanding Options and Opportunities. Dent. Mater. (2016), 32, 54–64, doi:10.1016/j.dental.2015.09.018.

[115] Griffith, M. L.; Halloran, J. W. Ultraviolet Curing of Highly Loaded Ceramic Suspensions for Stereolithography of Ceramics. In International Solid Freeform Fabrication Symposium; (1994); pp 396–403.

[116] Custompart.net. Rapid Prototyping - Stereolithography (SLA) http://www.custompartnet.com/wu/stereolithography (accessed Mar 2, 2020).

[117] Varghese, G.; Moral, M.; Castro-García, M.; López-López, J. J.; Marín-Rueda, J. R.; Yagüe-Alcaraz, V.; Hernández-Afonso, L.; Ruiz-Morales, J. C.; Canales-Vázquez, J. Fabricación y Caracterización de Cerámicas Mediante Impresión 3D DLP de Bajo Coste. Bol. la Soc. Esp. Ceram. y Vidr. (2018), 57, 9–18, doi:10.1016/j.bsecv.2017.09.004.

[118] Wei, L.; Zhang, J.; Yu, F.; Zhang, W.; Meng, X.; Yang, N.; Liu, S. A Novel Fabrication of Yttria-Stabilized-Zirconia Dense Electrolyte for Solid Oxide Fuel Cells by 3D Printing Technique. Int. J. Hydrogen Energy (2019), 44, 6182–6191, doi:10.1016/j.ijhydene.2019.01.071.

[119] Ge, L.; Dong, L.; Wang, D.; Ge, Q.; Gu, G. A Digital Light Processing 3D Printer for Fast and High-Precision Fabrication of Soft Pneumatic Actuators. Sensors Actuators, A Phys. (2018), 273, 285–292, doi:10.1016/j.sna.2018.02.041.

[120] Mu, Q.; Wang, L.; Dunn, C. K.; Kuang, X.; Duan, F.; Zhang, Z.; Qi, H. J.; Wang, T. Digital Light Processing 3D Printing of Conductive Complex Structures. Addit. Manuf. (2017), 18, 74–83, doi:10.1016/j.addma.2017.08.011.

[121] Scott Frey. Laser SLA vs DLP vs Masked SLA 3D Printing Technology - The Ortho Cosmos https://theorthocosmos.com/laser-sla-vs-dlp-vs-masked-sla-3d-printing-technology-compared/ (accessed Mar 2, 2020).

[122] Guo, N.; Leu, M. C. Additive Manufacturing: Technology, Applications and Research Needs. Front. Mech. Eng. (2013), 8, 215–243, doi:10.1007/s11465-013-0248-8.

[123] Park, J.; Tari, M. J.; Hahn, H. T. Characterization of the Laminated Object Manufacturing (LOM) Process. Rapid Prototyp. J. (2002), 6, 36–50, doi:10.1108/13552540010309868.

[124] Wang, W.; Conley, J. G.; Stoll, H. W. Rapid Tooling for Sand Casting Using Laminated Object Manufacturing Process. Rapid Prototyp. J. (1999), 5, 134–141, doi:10.1108/13552549910278964.

[125] Huang, S. H.; Liu, P.; Mokasdar, A.; Hou, L. Additive Manufacturing and Its Societal Impact: A Literature Review. Int. J. Adv. Manuf. Technol. (2013), 67, 1191–1203, doi:10.1007/s00170-012-4558-5.

[126] Wong, K. V.; Hernandez, A. A Review of Additive Manufacturing. ISRN Mech. Eng. (2012), 2012, 1–10, doi:10.5402/2012/208760.

[127] Windsheimer, H.; Travitzky, N.; Hofenauer, A.; Greil, P. Laminated Object Manufacturing of Preceramic-Paper-Derived Si-SiC Composites. Adv. Mater. (2007), 19, 4515–4519, doi:10.1002/adma.200700789.

[128] Weimar, M.; Gotthold, D.; Chick, L.; Whyatt, G. Cost Study for Manufacturing of Solid Oxide Fuel Cell Power Systems. Pacific Northwest Natl. Lab. (2013), 50.

[129] Sukeshini, A. M.; Cummins, R.; Reitz, T. L.; Miller, R. M. Inkjet Printing of Anode Supported SOFC: Comparison of Slurry Pasted Cathode and Printed Cathode. Electrochem. Solid-State Lett. (2009), 12 (12) doi:10.1149/1.3243468.

[130] Sukeshini, M. A.; Cummins, R.; Reitz, T. L.; Miller, R. M. Ink-Jet Printing: A Versatile Method for Multilayer Solid Oxide Fuel Cells Fabrication. J. Am. Ceram. Soc. (2009), 92 (12), 2913–2919, doi:10.1111/j.1551-2916.2009.03349.x.

[131] Esposito, V.; Gadea, C.; Hjelm, J.; Marani, D.; Hu, Q.; Agersted, K.; Ramousse, S.; Jensen, S. H. Fabrication of Thin Yttria-Stabilized-Zirconia Dense Electrolyte Layers by Inkjet Printing for High Performing Solid Oxide Fuel Cells. J. Power Sources (2015), 273, 89–95, doi:10.1016/j.jpowsour.2014.09.085.

[132] Farandos, N. M.; Kleiminger, L.; Li, T.; Hankin, A.; Kelsall, G. H. Three-Dimensional Inkjet Printed Solid Oxide Electrochemical Reactors. I. Yttria-Stabilized Zirconia Electrolyte. Electrochim. Acta (2016), 213, 324–331, doi:10.1016/j.electacta.2016.07.103.

[133] Masciandaro, S.; Torrell, M.; Leone, P.; Tarancón, A. Three-Dimensional Printed Yttria-Stabilized Zirconia Self-Supported Electrolytes for Solid Oxide Fuel Cell Applications. J. Eur. Ceram. Soc. (2019), 39, 9–16, doi:10.1016/j.jeurceramsoc.2017.11.033.

[134] Hong, T.; Kenneth, Y. I.; Pei-Chen, S. U.; Chen-Nan, S.; Jun, W. EFFECTS OF LASER PROCESSING ON NICKEL OXIDE-YTTRIA STABILIZED ZIRCONIA. Proc. 2nd Intl. Conf. Prog. Addit. Manuf. (2016), 367–373, doi:10.3850/2424-8967.

[135] Mitchell-Williams, T. B.; Tomov, R. I.; Saadabadi, S. A.; Krauz, M.; Aravind, P. V.; Glowacki, B. A.; Kumar, R. V. Infiltration of Commercially Available, Anode Supported SOFC's via Inkjet Printing. Mater. Renew. Sustain. Energy (2017), 6 (2) doi:10.1007/s40243-017-0096-2.

[136] Tomov, R. I.; Dudek, M.; Hopkins, S. C.; Krauz, M.; Wang, H.; Wang, C.; Shi, Y.; Tomczyk, P.; Glowacki, B. A. Inkjet Printing of Direct Carbon Solid Oxide Fuel Cell Components. doi:10.1149/05701.1359ecst.

[137] Han, G. D.; Neoh, K. C.; Bae, K.; Choi, H. J.; Park, S. W.; Son, J. W.; Shim, J. H. Fabrication of Lanthanum Strontium Cobalt Ferrite (LSCF) Cathodes for High Performance Solid Oxide Fuel Cells Using a Low Price Commercial Inkjet Printer. J. Power Sources (2016), 306, 503–509, doi:10.1016/j.jpowsour.2015.12.067.

[138] Yashiro, N.; Usui, T.; Kikuta, K. Application of a Thin Intermediate Cathode Layer Prepared by Inkjet Printing for SOFCs. J. Eur. Ceram. Soc. (2010), 30 (10), 2093–2098, doi:10.1016/j.jeurceramsoc.2010.04.012.

[139] Li, C.; Chen, H.; Shi, H.; Tade, M. O.; Shao, Z. Green Fabrication of Composite Cathode with Attractive Performance for Solid Oxide Fuel Cells through Facile Inkjet Printing. J. Power Sources (2015), 273, 465–471, doi:10.1016/j.jpowsour.2014.09.143.

[140] Notten, P. H. L.; Roozeboom, F.; Niessen, R. A. H.; Baggetto, L. 3-D Integrated All-Solid-State Rechargeable Batteries. Adv. Mater. (2007), 19, 4564–4567, doi:10.1002/adma.200702398.

[141] Chi, S. Sen; Liu, Y.; Zhao, N.; Guo, X.; Nan, C. W.; Fan, L. Z. Solid Polymer Electrolyte Soft Interface Layer with 3D Lithium Anode for All-Solid-State Lithium Batteries. Energy Storage Mater. (2019), 17 (May 2018), 309–316, doi:10.1016/j.ensm.2018.07.004.

[142] Liu, X.; Jervis, R.; Maher, R. C.; Villar-Garcia, I. J.; Naylor-Marlow, M.; Shearing, P. R.; Ouyang, M.; Cohen, L.; Brandon, N. P.; Wu, B. 3D-Printed Structural Pseudocapacitors. Adv. Mater. Technol. (2016), 1 (9) doi:10.1002/admt.201600167.

[143] Pikul, J. H.; Gang Zhang, H.; Cho, J.; Braun, P. V.; King, W. P. High-Power Lithium Ion Microbatteries from Interdigitated Three-Dimensional Bicontinuous Nanoporous Electrodes. Nat. Commun. (2013), 4, 1–5, doi:10.1038/ncomms2747.

[144] Ranganathan, S.; Mccreery, R.; Majji, S. M.; Madou, M. Photoresist-Derived Carbon for Microelectromechanical Systems and Electrochemical Applications. J. Eeectrochemical Soc. (2000), 147, 277–282, doi:10.1149/1.1393188.

[145] Sun, G.; An, J.; Chua, C. K.; Pang, H.; Zhang, J.; Chen, P. Layer-by-Layer Printing of Laminated Graphene-Based Interdigitated Microelectrodes for Flexible Planar Micro-Supercapacitors. Electrochem. commun. (2015), 51, 33–36, doi:10.1016/j.elecom.2014.11.023.

[146] Kohlmeyer, R. R.; Blake, A. J.; Hardin, J. O.; Carmona, E. A.; Carpena-Núñez, J.; Maruyama, B.; Daniel Berrigan, J.; Huang, H.; Durstock, M. F. Composite Batteries: A Simple yet Universal Approach to 3D Printable Lithium-Ion Battery Electrodes. J. Mater. Chem. A (2016), 4 (43), 16856–16864, doi:10.1039/c6ta07610f.

[147] Sun, K.; Wei, T. S.; Ahn, B. Y.; Seo, J. Y.; Dillon, S. J.; Lewis, J. A. 3D Printing of Interdigitated Li-Ion Microbattery Architectures. Adv. Mater. (2013), 25 (33), 4539–4543, doi:10.1002/adma.201301036.

[148] Krebs, F. C. Fabrication and Processing of Polymer Solar Cells: A Review of Printing and Coating Techniques. Sol. Energy Mater. Sol. Cells (2009), 93, 394–412, doi:10.1016/j.solmat.2008.10.004.

[149] Vak, D.; Hwang, K.; Faulks, A.; Jung, Y. S.; Clark, N.; Kim, D. Y.; Wilson, G. J.; Watkins, S. E. 3D Printer Based Slot-Die Coater as a Lab-to-Fab Translation Tool for Solution-Processed Solar Cells. Adv. Energy Mater. (2015), 5, 1–8, doi:10.1002/aenm.201401539.

[150] Hwang, K.; Jung, Y. S.; Heo, Y. J.; Scholes, F. H.; Watkins, S. E.; Subbiah, J.; Jones, D. J.; Kim, D. Y.; Vak, D. Toward Large Scale Roll-to-Roll Production of Fully Printed Perovskite Solar Cells. Adv. Mater. (2015), 27, 1241–1247, doi:10.1002/adma.201404598.

[151] Di Giacomo, F.; Fakharuddin, A.; Jose, R.; Brown, T. M. Progress, Challenges and Perspectives in Flexible Perovskite Solar Cells. Energy Environ. Sci. (2016), 9, 3007–3035, doi:10.1039/c6ee01137c.

[152] Yoon, J.; Baca, A. J.; Park, S. Il; Elvikis, P.; Geddes, J. B.; Li, L.; Kim, R. H.; Xiao, J.; Wang, S.; Kim, T. H.; et al. Ultrathin Silicon Solar Microcells for Semitransparent, Mechanically Flexible and Microconcentrator Module Designs. Nat. Mater. (2008), 7, 907–915, doi:10.1038/nmat2287.

[153] Galagan, Y.; Coenen, E. W. C.; Sabik, S.; Gorter, H. H.; Barink, M.; Veenstra, S. C.; Kroon, J. M.; Andriessen, R.; Blom, P. W. M. Evaluation of Ink-Jet Printed Current Collecting Grids and Busbars for ITO-Free Organic Solar Cells. Sol. Energy Mater. Sol. Cells (2012), 104, 32–38, doi:10.1016/j.solmat.2012.04.039.

[154] Gizachew, Y. T.; Escoubas, L.; Simon, J. J.; Pasquinelli, M.; Loiret, J.; Leguen, P. Y.; Jimeno, J. C.; Martin, J.; Apraiz, A.; Aguerre, J. P. Towards Ink-Jet Printed Fine Line Front Side Metallization of Crystalline Silicon Solar Cells. Sol. Energy Mater. Sol. Cells (2011), 95, S70–S82, doi:10.1016/j.solmat.2010.12.031.

[155] Jiang, Y.; Chen, Y.; Zhang, M.; Qiu, Y.; Lin, Y.; Pan, F. 3D-Printing Ag-Line of Front-Electrodes with Optimized Size and Interface to Enhance Performance of Si Solar Cells. RSC Adv. (2016), 6, 51871–51876, doi:10.1039/c6ra08985b.

[156] Ahn, B. Y.; Duoss, E. B.; Motala, M. J.; Guo, X.; Park, S. Il; Xiong, Y.; Yoon, J.; Nuzzo, R. G.; Rogers, J. A.; Lewis, J. A. Omnidirectional Printing of Flexible, Stretchable, and Spanning Silver Microelectrodes. Science. (2009), 323, 1590–1593, doi:10.1126/science.1168375.

[157] Bernardi, M.; Ferralis, N.; Wan, J. H.; Villalon, R.; Grossman, J. C. Solar Energy Generation in Three Dimensions. Energy Environ. Sci. (2012), 5 (5), 6880–6884, doi:10.1039/c2ee21170j.

[158] Myers, B.; Bernardi, M.; Grossman, J. C. Three-Dimensional Photovoltaics. Appl. Phys. Lett. (2010), 96, 0719021–0719023, doi:10.1063/1.3308490.

[159] de Hazan, Y.; Thänert, M.; Trunec, M.; Misak, J. Robotic Deposition of 3d Nanocomposite and Ceramic Fiber Architectures via UV Curable Colloidal Inks. J. Eur. Ceram. Soc. (2012), 32, 1187–1198, doi:10.1016/j.jeurceramsoc.2011.12.007.

[160] Tubío, C. R.; Azuaje, J.; Escalante, L.; Coelho, A.; Guitián, F.; Sotelo, E.; Gil, A. 3D Printing of a Heterogeneous Copper-Based Catalyst. J. Catal. (2016), 334, 110–115, doi:10.1016/j.jcat.2015.11.019.

[161] Regufe, M. J.; Ferreira, A. F. P.; Loureiro, J. M.; Rodrigues, A.; Ribeiro, A. M. Electrical Conductive 3D-Printed Monolith Adsorbent for CO_2 Capture. Microporous Mesoporous Mater. (2019), 278 (January), 403–413, doi:10.1016/j.micromeso.2019.01.009.

[162] Thakkar, H.; Eastman, S.; Hajari, A.; Rownaghi, A. A.; Knox, J. C.; Rezaei, F. 3D-Printed Zeolite Monoliths for CO_2 Removal from Enclosed Environments. ACS Appl. Mater. Interfaces (2016), 8 (41), 27753–27761, doi:10.1021/acsami.6b09647.

[163] Couck, S.; Lefevere, J.; Mullens, S.; Protasova, L.; Meynen, V.; Desmet, G.; Baron, G. V.; Denayer, J. F. M. CO_2, CH4 and N2 Separation with a 3DFD-Printed ZSM-5 Monolith. Chem. Eng. J. (2017), 308, 719–726, doi:10.1016/j.cej.2016.09.046.

[164] Lefevere, J.; Mullens, S.; Meynen, V. The Impact of Formulation and 3D-Printing on the Catalytic Properties of ZSM-5 Zeolite. Chem. Eng. J. (2018), 349 (April), 260–268, doi:10.1016/j.cej.2018.05.058.

[165] Middelkoop, V.; Coenen, K.; Schalck, J.; Van Sint Annaland, M.; Gallucci, F. 3D Printed versus Spherical Adsorbents for Gas Sweetening. Chem. Eng. J. (2019), 357 (2019), 309–319, doi:10.1016/j.cej.2018.09.130.

[166] Skorski, M. R.; Esenther, J. M.; Ahmed, Z.; Miller, A. E.; Hartings, M. R. The Chemical, Mechanical, and Physical Properties of 3D Printed Materials Composed of TiO_2-ABS Nanocomposites. Sci. Technol. Adv. Mater. (2016), 17 (1), 89–97, doi:10.1080/14686996.2016.1152879.

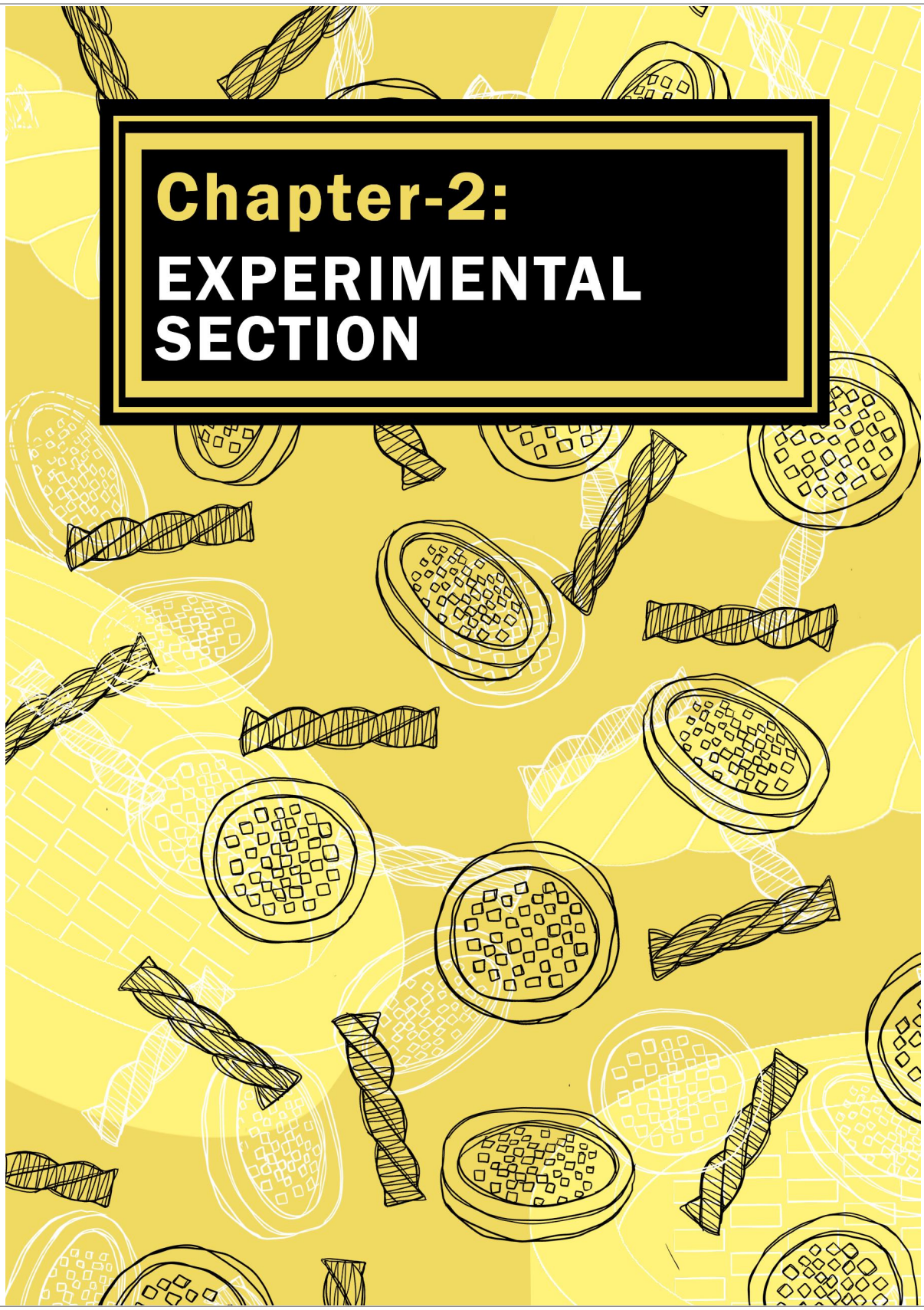

2.1 3D Printing technologies & Materials

In this chapter, the basis, the printing parameters and the procedures to prepare the starting materials for each 3D printing process will be described. Therefore, this experimental chapter has been divided into several subsections, which correspond to each additive manufacturing process.

2.1.1 Ceramic Fused Deposition Modelling (FDM) printing

In this section, ceramic FDM printing will be specifically described, detailing the materials used, the printing parameters and the most common issues.

2.1.1.1 Printer

Ceramic Fused Deposition was carried out on a desktop printer developed by 3DPrinted Solutions and based on a Prusa model, *Figure 2. 1*. As the ceramic-loaded filaments are not commercial, the temperature at the hot-end must be the first parameter studied. The same occurs with several other relevant parameters such as flow printing, nozzle size, layer and shell thickness, filling density, speed printing and bed temperature and therefore the 3D printing system must allow a complete control of the printing parameters for each composition.

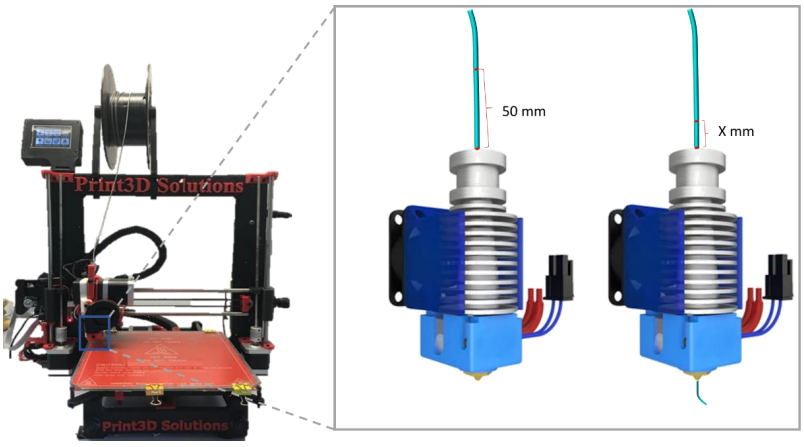

Figure 2. 1 Ceramic fused deposition modelling printer of Print3D Solution

After printing, a green body is obtained, therefore a thermal treatment must be done to remove organics and promote sintering of the ceramic structures. This is a very important step as the 3D printed ceramics will be applied as catalysts for water decontamination. In the case of titanium oxide ceramics, a multistep temperature profile and changes in the atmospheric conditions i.e. argon and air, were required to produce high quality ceramics as depicted in *Table 2. 1*. Usually,

inert atmospheres, as argon, are employed during debinding process in order to burn the organic compounds in a controlled way. While reducing or oxidant atmospheres, as air, are employed during the sintering process depending of the studied material.

Table 2. 1 Thermal treatments for 3D printed structures via ceramic FDM

A	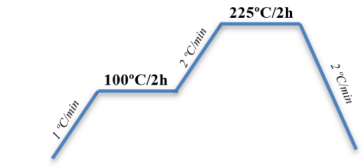
B	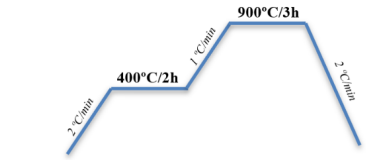
C	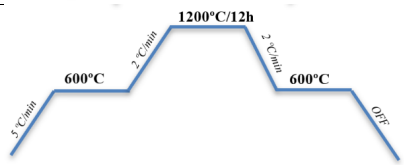
D	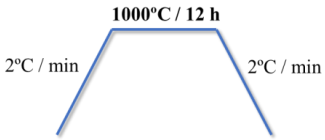
E	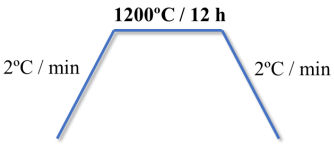

2.1.1.2 Printing parameters

In the present work, the printing temperature was set in the 180-240°C temperature range. Lower temperatures do not guarantee the adequate rheological properties of the softened filament to flow through the nozzle and may cause clogging problems. Higher temperatures may also cause problems as the viscosity may be too low and therefore not adequate to reproduce correctly the geometry of the 3D object.

As the filament manufacturing process was home-made, the printing flow must be measured for each filament used as the diameter may exhibit certain variations and this affects largely the FDM 3D printing process. To optimize this parameter, 50 mm of the filament were measured and

marked. After that, the printer was set to extrude 50 mm. When the extrusion is done, the distance between the initial and final point of the process is measured and using equation 2.4., the filling percentage is calculated.

$$flow\ printing\ (\%) = 100 + \frac{X\ mm * 100}{50\ mm} \qquad \textit{Equation 2.1}$$

Regarding other printing parameters, are shown in *Table 2. 2*.

Table 2. 2 Printing parameters of the ceramic FDM printer

Parameters	Data
Nozzle size (mm)	0.4 - 0.6
Thickness layer (mm)	0.05 – 0.1 – 0.2
Speed printing (mm/s)	25 – 30 – 40 – 50 – 70
Shell thickness (mm)	3.5 (fixed)
Fill density (%)	100 (fixed)

2.1.1.3 Filament composition

FDM technology uses filaments of the target material for the printing process. As ceramic materials are not commercially available, they must be produced considering several critical parameters such as thermoplastic behaviour (filament must soften upon arrival to the extrusion printing head), flexibility (storage) and relatively high hardness to ensure the filament pushes the mass into the hot zone of the printhead. During this research work, ceramic-loaded filaments were produced following the procedure described in [1], therefore some specific details cannot be provided. The first step is choosing the raw material, which must be a powder with a relatively narrow particle size distribution. Then, a combination of organic compounds is mixed with the raw material to generate a green body that can be extruded. During extrusion, the green body is introduced and heated into a worm drive at the melting temperature of the mixture, *Figure 2. 2*. As the green body softens, it is pushed towards the nozzle giving rise to a cylindrical shape or filament. The diameter of the filament will be determined by the nozzle size. Immediately after extrusion, the filament is cooled down to room temperature and wrapped. In a final stage, the filament undergoes a drying process in an oven to remove the volatile compounds still present after extrusion.

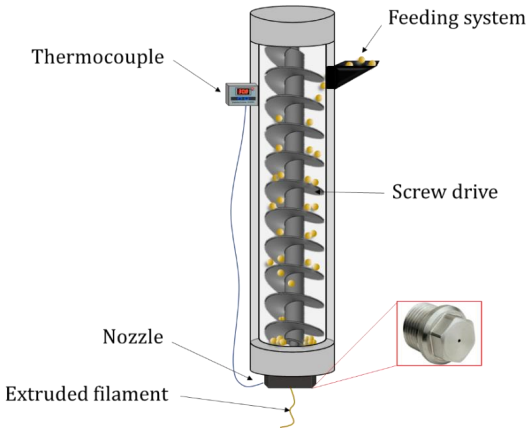

Figure 2. 2 Filament extrusion system

2.1.1.3.1 Ceramic solid load

In this work, filaments based on titanium oxide powder were considered due to the application mentioned in *Chapter 1*, *Section 1.2.3*, that is water decontamination. As mentioned above, the ceramic powder (TiO_2 in this case) must be mixed with an organic binder and other organic compounds (e.g. plasticizer, solvent, thermoplastic resin, etc.) in order to ensure adequate properties for FDM 3D printing.

As the organic compounds must be removed after 3D printing, one of the initial main aims is to obtain a very high ceramic load to retain the geometries produced upon printing. However, a too high ceramic load can be risky, due to the lower flexibility and the plastic deformation characteristics of the material are lost, hence the nozzle could clog. In this work, some different material loads were used, all of them over 50 wt. % After that, the material is cut into pellets (<5mm) and extruded. The extrusion temperature was in the 55-120 °C temperature range using 1.75 mm nozzles. Finally, the rolled filament is kept into a vacuum desiccator before printing.

2.1.1.3.2 Pore former

A thermal treatment must be performed after printing the structures to sinter them. However, as sintering takes place, the porosity of the ceramic is reduced which is negative considering the potential application in photocatalysis. Therefore, a pore former agent is added to the initial mixture, in order to leave a certain degree of porosity after the thermal treatment. In the present case, glassy carbon microspheres were used. Thus, from this point on, two inorganic powders compound the mixture. Some different compositions were tested, modifying weight percentage of powder and changing the ratio $TiO_2 - C_{spheres}$, *Table 2. 3*.

Table 2. 3 Compositional ratio of the mixture to the solid components

Inorganic powder wt. %	Ceramic : Pore former
70	80 : 20
70	70 : 30
75	80 : 20
82	80 : 20

2.1.2 Ceramic Binder Jetting (BJ) printing

In this section, the commercial ceramic BJ system will be specifically described in addition to the material used and the printing parameters.

2.1.2.1 Printer

The binder jetting printer used in this thesis is a Project CJP 360 from 3D Systems. This commercial printer allows faster printings than other technologies, making a 3D structure in hours instead of days. Another advantage is the low cost due to elimination of waste and reduction of the processing time because supports are not necessary during printing, as a consequence of the power bed-based method previously described in *Chapter 1*.

The printer is divided in two different chambers, *Figure 2. 3*: printing chamber and cleaning chamber. The first is constituted by the building platform, raw material tank, a roller with binder extrusion head and the vacuum system. The second chamber consists of a perforated platform and a compressed air system to blow the excess powder from the printed structures. That powder goes through holes on the platform and is collected to be used as raw material for future work.

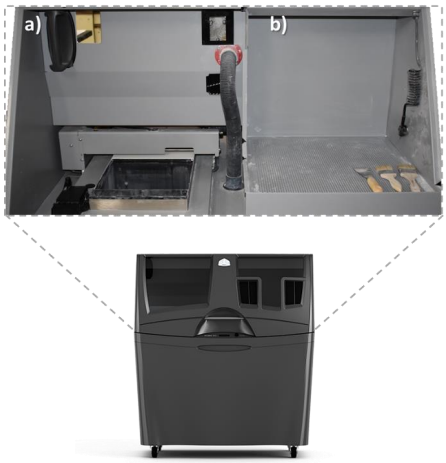

Figure 2. 3 Ceramic Binder Jetting printer of 3D System a) Printing chamber b) Cleaning chamber

2.1.2.2 Printing parameters

The BJ printer does not allow controlled changes in the printing parameters and the user may select the final resolution by choosing the process to be fine, medium or low. Each option implies an automatic adjustment of the printing parameters. *Table 2. 4* shows some of the printing parameters of the system.

Table 2. 4 Printing parameters of binder jetting printer

Parameters	Data
XY accuracy (mm)	0.15
Min. layer thickness (mm)	0.089 – 0.102
Max. Speed printing (layer/min)	2 – 4

2.1.2.3 Material

Regarding materials, the company offers a range of printable materials, for example, ceramic materials, VisiJet® PXL™ Core™, but their detailed composition is not specified. On suspicion a thermogravimetric analysis study (TGA) using equipment describe in this chapter, *Section 2.2.3*.

The analysis was performed under flowing oxygen using temperature rates of 2°C/min between 25-300°C, and 10°C/min between 300-1100°C. The results confirmed that the powder was $CaSO_4$ as X-Ray diffraction suggested.

The aim is to use this ceramic material, $CaSO_4$, as support for photocatalysis applications. In this situation, the digital design is uploaded to the printer software, the printer starts to print the object layer by layer until producing the 3D object. After printing, it is necessary to wait for 2 hours to let the binder consolidate the ceramic powder particles. Finally, the object can be extracted and cleaned.

2.1.2.4 Functionalization printed substrates with TiO_2

As the so-fabricated monoliths will be used in water decontamination, they must be mechanically stable in this media. However, this is not the case. None of the 3D printed monoliths of calcium sulphate show any catalytic activity due to their chemical composition. Thus, it is necessary to carry out the functionalization of the monoliths to achieve catalytic activity and a better mechanical strength too. To achieve this, functionalization with titanium oxide was studied employing different methods, including (i) dip coating in TiO_2-ethanol dispersions and Ludox® TiO_2 solutions, (ii) spraying of ethanolic TiO_2 suspensions and (iii) in situ TiO_2 synthesis.

Regarding the dip coating method, two processes were carried out. On one hand, Ludox® treatment under vacuum was carried out to provide greater resistance to the supports. Then, they

were dried at 600 °C for 2 hours. Next, the monoliths were dipped on a Ludox®, Triton X and TiO_2 solution and finally, they were dried at 70 °C for 1 hour and fired at 300 °C for 2 hours. On the other hand, dip coating in TiO_2 ethanolic solution was made under vacuum too and then dried at 80 °C for 24 hours. Concerning spraying, the same TiO_2 ethanolic solution was used. Finally, *in situ* synthesis of the catalyst onto the supports was carried out by immersing the monoliths into $TiCl_4$ under vacuum to guarantee the solution getting into the porous structure. Next, hydrolysis is made using distilled water, and finally drying at 80°C for 1 hour and firing at 150 °C for 2 hours. The overall process may be summarised in *Equation 2.2*:

$$TiCl_{4_{aq.}} + 2\,H_2O_{aq.} \rightarrow TiO_{2_{sol.}} + 4\,HCl_g \qquad \textit{Equation 2.2}$$

Different results were obtained, and the optimum method was employed to measure their photocatalytic activity as discussed in *Chapter 3*.

2.1.3 Ceramic stereolithography (SLA) printing

Stereolithography was the first technique developed in the rapid prototyping field four decades ago,[2–5] therefore it is one of the most developed techniques. Ceramic stereolithography and digital light processing have been developed lately, although most of the studies are focused on structural ceramics and not so much in advanced ceramics. Ceramic processing via SLA or DLP is based on the addition of ceramic powders to a photosensitive resin, causing important changes in the rheology of the slurry and stability becomes a key issue. Moreover, the effect of ceramic particles causing light scattering and hence modifying crucial printing parameters implies a very important research effort towards optimisation. Consequently, conventional printers must be modified to operate correctly under the constraints imposed by these ceramic-based photosensitive slurries. In the context of this thesis, two different resin-based 3D printers were used. On one hand, a digital light process prototype printer and on the other hand, a stereolithography commercial printer. Both will be presented in the next sections.

2.1.3.1 Printer

The commercial stereolithography system is a CERAMAKER printer by 3D CERAM operating at IREC, Barcelona (Catalonia Institute for Energy Research), *Figure 2. 4*.

The light source is a laser that cures point by point, so the resolution will be better than DLP, however a disadvantage is that the printing process will be slower. The building process is not the commonly used in stereolithography and in this case is top down, which means that the laser passes over the building platform and cures each layer while the platform descends after curing. That is due to the viscosity of the slurry, which prevents from using bottom up.

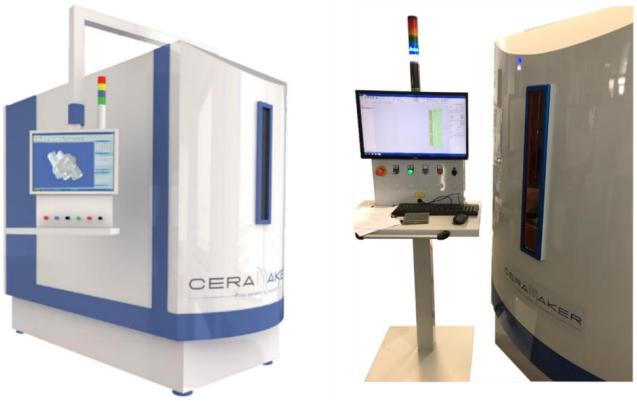

Figure 2. 4 SLA commercial printer Made by 3D Ceram located at IREC.

This printer has a doctor blade system, *Figure 2. 5.* that must be calibrated with micrometres tapes to fix the height of the sample layer to be deposited. There are two blades, *Figure 2. 5 (c)*, one to pull the slurry and the other to smooth the slurry and remove the excess. They are adjusted at 150 µm and another at 50 µm respectively. When the printing process starts, the blades sweep the slurry along one direction to deposit it into the platform and sweep a second time in order to define the thickness. Next, the laser starts to cure the profile of the layer design. Then, the platform, *Figure 2. 5 (b),* goes down and the process is repeated until finishing the 3D object. It is important to have a good attachment/adherence of the cured layer with the platform to avoid being pulled by the blades in the following stages. To achieve this, a magnet tape is put on the aluminium platform to facilitate removal of 3D printed object, and on top of it, an adhesive paper is placed to obtain a perfect attachment.

Figure 2. 5 Doctor Blade of the SLA printer a) Paste deposit b) Printing platform c) Blades

The manufacturer gives some recommendations to print successfully, such is the design of supports. Despite the slurry shows very high viscosity, the design must include supports to ensure adherence to the printing platform and avoid deformation during printing.

It should be noted that the surface is sometimes too small to be self-supported, and the friction force caused by the blades will remove the cured part modifying the rest of process. Supports can be very difficult to make, but sometimes it is enough with a grip layer to promote the bonding with the building plate. Also, they advise that scrapping tests must be done before printing, to verify the laser intensity and securing that the blade system is working correctly.

When the printing process is finished, the platform is completely covered with excess slurry, *Figure 2. 6*. Removing samples from the platform is a meticulous process, and care must be taken to avoid breaking them down. With a brush and a spatula, excess slurry can be removed. Then, the resulting pieces are dipped into a cleaning solution (given by the company) under stirring. Finally, clean structures are introduced into the furnace for debinding and sintering thermal treatments.

Figure 2. 6 Printing platform when the printing has finished

One of the goals of this thesis is to compare the electrolytes obtained with this printer [6] with the electrolytes made via the DLP[7] prototype printer explained below and conventionally fabricated electrolytes.

2.1.3.2 Printing parameters

The selected printing parameters are shown in the following *Table 2. 5*. Regarding the laser, the intensity must be confirmed before printing. Therefore, a polymerization test is made before printing to ensure that the UV light cures a determined thickness layer.

Table 2. 5 Printing parameters of the Ceramaker printer to print 8 YSZ electrolytes

Parameters	Data
Laser wavelength (nm)	355
Intensity laser (%)	93
Blade 1 height (paste deposition) (µm)	200
Blade 2 height [thickness layer] (µm)	100
Thickness layer printed (µm)	100
Speed rastering (mm/s)	5000

2.1.3.3 Commercial material

This system can print a range of materials, including alumina [Al_2O_3], zirconia [3 & 8% YSZ], hydroxyapatite [HA; $Ca_5(PO_4)_3(OH)$], tricalcium phosphate [TCP; $Ca_3(PO_4)_2$], etc. In this work, 8% mol YSZ (~40% vol. ceramic load) was chosen to fabricate SOFC electrolytes.

An important consideration is that the type of paste must be defined in the software before printing, as the sintering contraction in the three axes is already known and is considered when creating the model. Hence, the structures will be increased by this factor in order to get the correct dimensions after the thermal treatments.

Due to the intellectual property of the company, debinding and sintering process cannot be described in detail. Debinding for 8 YSZ was made at 1150°C (in total ~ 72 h.) and sintering at 1450°C (in total ~ 17 h.), both in air.

2.1.3.4 Functionalization of electrolytes with electrodes

Three dimensional printed 8-YSZ electrolytes by SLA and DLP require electrode deposition for testing in either symmetrical or complete cells. Symmetrical cells are those using the same material as anode and cathode, whereas a complete cell uses different anode and cathode materials.

As the electrolyte has been made by 3D printing and one of the goals is to compare the resulting properties with the state-of-the-art processing technologies, it is necessary to measure the electrochemical performance. A rather simple and common preliminary test can be performed by attaching the same electrode on both faces of the electrolyte to produce a symmetrical cell.

First, a YSZ roughness layer (RL) was sprayed on both electrolyte sides to improve the electrode attachment and avoid cracking after thermal treatment due to the different thermal expansion coefficients of the electrolyte and the electrodes. To achieve this, a YSZ suspension was prepared as described in *Table 2. 6*, under stirring for 12 hours. Then, a spray-coater by Print3D Solutions was used to deposit the roughness layer, followed by a thermal treatment at 1150°C for 1 hour.

Table 2. 6 Roughness layer solution composition

Material	wt. %
8 YSZ	90.83
PVP (Polyvinylpyrrolidone)	0.09
Ethanol	9.08

Regarding the electrodes, they were painted in order to achieve a thickness of 35 µm at least using the compositions and thermal treatments indicated in *Table 2. 7*. As the cathode deposition must

be optimised, a range of temperatures were tested to determine which gives the best conductivity, lowest resistance and best area specific resistance (ASR). Finally, a gold ink, was painted on top of the electrodes and fired at 800 °C for 1 hour. The schematic representation of the so-fabricated cells made can be observed in *Figure 2. 7*.

With these cell configurations, it is possible to study important parameters such as conductivity, polarization resistances (R_s and R_p), area specific resistance (ASR) and cell performance. For symmetric cells, an oxidising atmosphere was used and for the complete cells, both oxidizing and reducing atmosphere were employed in separate chambers (anode and cathode chamber). In all experiments, a gold layer was deposited on both sides to act as current collector.

Table 2. 7 Composition inks for electrodes and current collector

Ink	Composition (wt. %)	Solid load (wt. %)	Temperature (°C)	Time (h)
LSM – YSZ	50 – 50	60 – 70	1100 1150 1200	3
Au	100	≥ 70	800	1

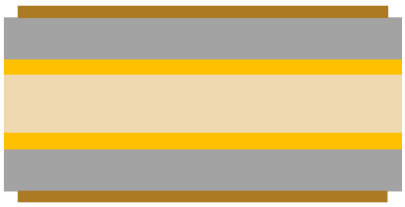

Figure 2. 7 Schematic composition for a cathodic symmetric SOFC

2.1.4 Ceramic digital light processing (DLP)

In this section, ceramic digital light processing (DLP) system will be specifically described, providing details of the components used and the printing parameters.

This technique shares the same basis and issues that ceramic SLA. Consequently, the main goal is to achieve the highest ceramic loading in the slurry, solving the typical issues mentioned in the previous section.

2.1.4.1 Printer

The prototype DLP printer was designed and fabricated in collaboration between University of La Laguna, University of Castilla-La Mancha and Print3D Solutions. It was called Spid3R since it

physically looks like a spider. The system is divided in two fundamental parts: light source and the printer itself. The light source is a commercial projector, 1080p Acer H6510BD DLP Projector located over the printer, *Figure 2. 8*. It has a high-pressured mercury discharge lamp with tungsten electrodes (Osram P-VIP lamp), with a rated power of 210 Watts and wavelength of 380 nm (UV-Visible), so the lamp power pulse on a specific colour improves the brightness as the colour wheel spins inside the projector.

Regarding the printer, it is a methacrylate frame with four adjustable legs, which contains the main components of the printer such as building platform, slurry vat, axis motors, information screen, electronic board and power supply, *Figure 2. 9*. Firstly, the tank must be filled with the photosensitive slurry and closed to avoid exposure to ambient light. Then, when the printing process starts, the *xz* axes go to the origin reference position. The slurry deposit/doctor blade moves along the printer (*x* axis) placing the first layer of slurry with a controlled thickness. Once deposited, a specific mask is projected solidifying the mixture. The second layer is made when the building platform descends (*z* axis) and deposits the slurry again. The process is repeated until all layers have been deposited and subsequently cured.

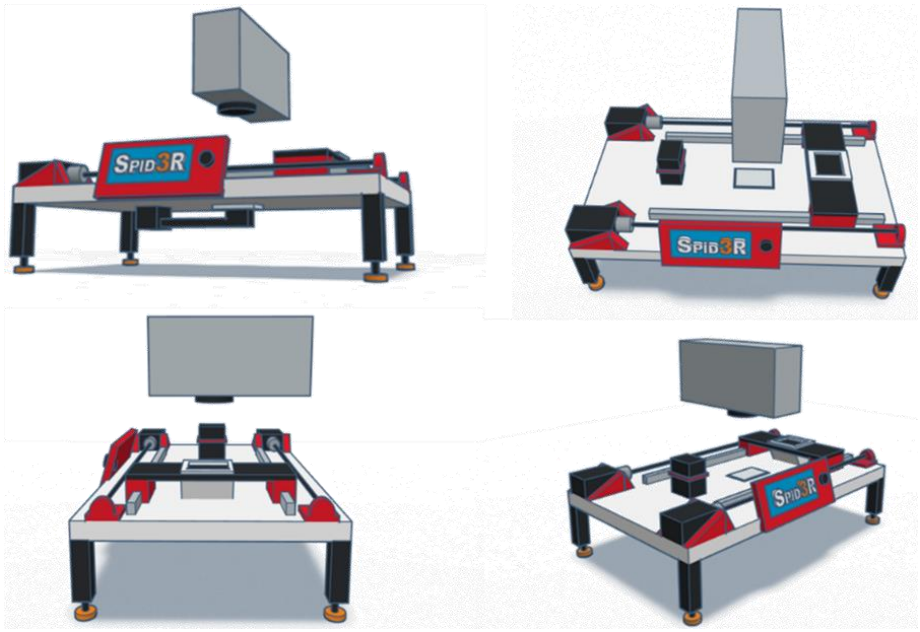

Figure 2. 8 SPID3R, digital design of the DLP prototype printer

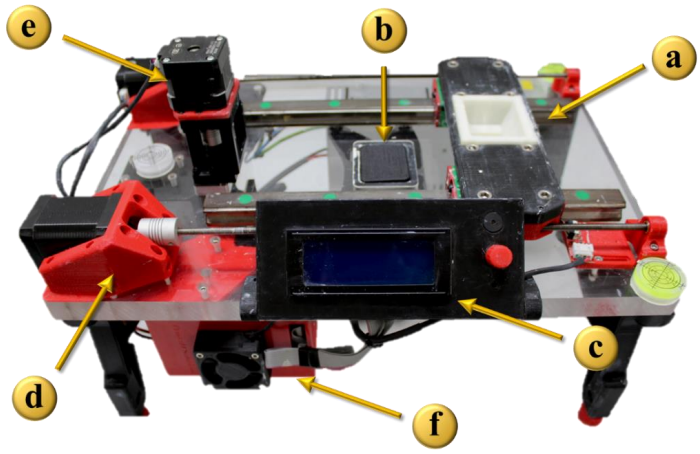

Figure 2. 9 SPID3R DLP Printer a) Slurry deposit b) Building platform c) Screen information d) X axis e) Z axis f) Arduino board

One of the most interesting features of the Spid3r printing system is the modularity and therefore it is possible to modify parts, fabricate them by FDM and repair them when necessary. Indeed, the digital design of the vat may be modified, hence the width and length of slot may be changed, *Figure 2. 10*, depending on the amount of material or geometry of the printing platform. Similarly, the platform design can be adapted to ease the printing, structure removal and cleaning processes. Diverse designs (flat surface, scratched, square patterns) and materials such as PLA, ABS or aluminium were used, *Figure 2. 11*.

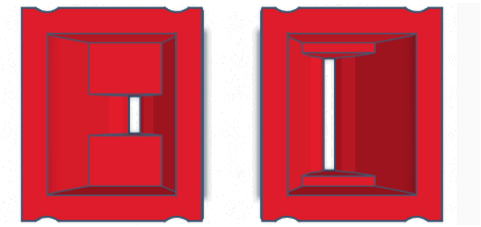

Figure 2. 10 Digital design for slurry deposit of SPID3R

Figure 2. 11 Different types of platforms for SPID3R printer

2.1.4.2 Printing parameters

Some aspects must be considered when operating with this printer. Essentially, the thickness and quality of the slurry layer deposited will depend on (i) deposit travel speed (*x* axis), (ii) deposit slot size, (iii) building platform initial height, (iv) thickness layer fixed in the software and (v) slurry viscosity. During the entire process, the scan speed and slot size were not changed.

A common issue with this machine is achieving a good attachment between the first printed layer and the platform and also to ensure that the layers show good adherence between them. If not, the layers will move with every pass of the deposit, giving rise to the formation of bubbles. For this reason, it is necessary to study the curing depth to select correctly the layer thickness in the printer software.[8]

Consequently, it is essential to optimize the printing parameters and, as occurs in all 3D printing technologies to produce ceramic materials, a thermal treatment must be carried out in the green body to remove the organics and complete sintering. However, if any problem related to curing happens, the final body may show defects such as cracks, delamination, etc, after processing.

2.1.4.2.1 Curing parameters: time and depth

As previously described, DLP and SLA of ceramics require photosensitive resins containing a high load of inorganic solid (typically > 60%) as otherwise, the structure/microstructure may collapse partially or totally after debinding and sintering, thus affecting the final properties.

A low content of organics will (i) help to avoid crack formation during the debinding process, *Figure 2. 12*, (ii) and will facilitate the production of dense (pore free) ceramic structures too.[9]

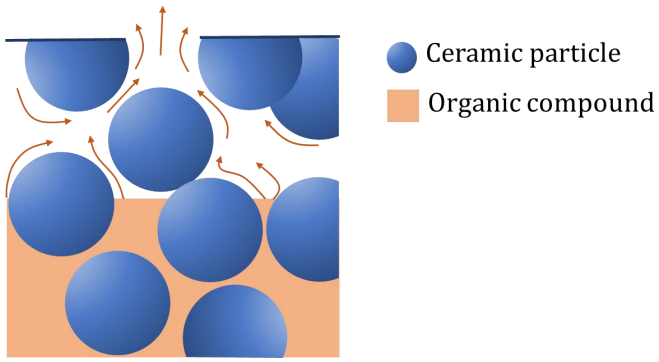

Figure 2. 12 Debinding process (adapted from reference [9])

However, as photopolymerization depends on UV light interacting with the resin monomers, the presence of ceramic particles has a very large impact on light scattering, *Figure 2. 13,* which in turn is related to the quality of the printing process/resolution. Thus, monitoring the ceramic particles via their refractive index, could be helpful to control the curing process. In summary, the curing process depends on the absorption and curing properties of the monomer solution as well as the scattering due to the ceramic particles.[10]

Scattering describes the interaction between light, the ceramic particles and the liquids organic compounds. This process could be explained by Mie scattering theory which describes the scattering of an electromagnetic plane wave by a homogeneous sphere, *Section 2.2.4*. However, this is not valid for the rather complex situation found in a typical highly loaded ceramic suspension. Ideally, the refractive index of the solution matched the refractive index of the powder, hence the solution reduces refraction effects. However, most of times this is not possible because ceramic materials have refractive indexes larger than organic liquids. For this reason, in this work the role of the curing process according to the viscosity of the slurry (mass fraction of ceramic powder in the suspension) has been studied, which will be related to the amount of dispersant added as described in the next sections.[11]

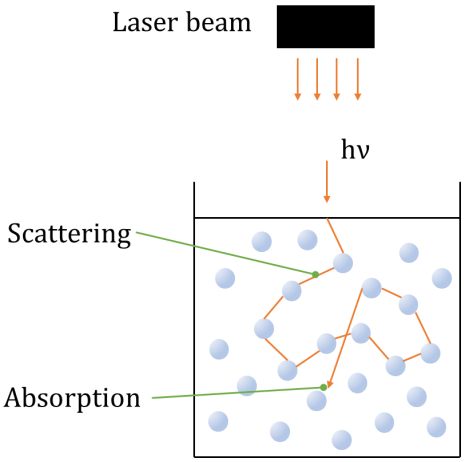

Figure 2. 13 Scattering process between ceramic particles and organic liquid [11]

Regarding the curing process, there are two crucial parameters that must be under control: curing time and curing depth, and both are correlated.[12] The higher the curing time, the larger the curing depth will be. In addition, depending on the curing time, the process will be faster or slower. But also, it affects to achieve a good adherence between layers, which is called formability.[13]

The problem is particularly relevant in highly loaded slurries, as light scattering will affect the penetration distance of the light in the mixture, and this, in turn, will decrease the curing depth.

Nonetheless, depth curing can be approximately calculated by the following equations:[14]

$$D_{curing} \approx \left[\frac{d}{Q}\right]\left(\frac{1}{\phi}\right) ln\left[\frac{I_0}{I_{cure}}\right] \qquad \textit{Equation 2.3}$$

$$Q = \left[\frac{\Delta n}{n_0}\right]^2 \left(\frac{d}{\lambda}\right)^2 \qquad \textit{Equation 2.4}$$

- d: particle size
- I_0: incident intensity light
- I_{cure}: minimum intensity required for photocuring (given by photo-initiator)
- ϕ: volume fraction of ceramic
- Q: efficiency factor for extinction coefficient for ceramic-resin system
- Δn: refractive index between ceramic and resin
- n_0: refractive index curable resin
- λ: wavelength

As shown in *Equation 2.3*, the curing depth is strongly related with a lot of parameters. In this work the volume fraction of ceramic, ceramic and resin refractive indexes and wavelength are parameters that will not change, as the volume fraction of ceramic will be fixed, and the compounds and the light source will always be the same.

In the present work, DLP 3D Printing will be carried out using a commercial DLP projector, which uses UV lamps that do not guarantee the same intensity during their lifetime. Thus, as the intensity projector lamp may be altered with time, and the intensity of the lamp cannot be modified manually, depth curing tests will be carried out to correlate it with the exposure time.

To determinate the optimum conditions for the photopolymerization of the ceramic slurries, two different masks were used, i.e. a rectangular mask for curing depth and an arrow for curing time, *Figure 2.14.* In both cases, the slurry was exposed to 3, 5, 7.5, 10, 13 and 15 seconds curing a single layer in order to monitor resolution differences.

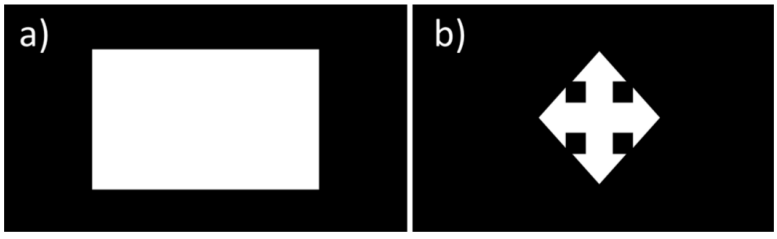

Figure 2. 14 a) Rectangular mask used to curing depth, b) Arrows mask used to curing time

2.1.4.2.2 Light dispersion and resolution

As discussed above, scattering directly affects the resolution in the printing process. However, in addition to high resolution, a good adherence between layers is necessary. For this reason, the best curing time is chosen in the *z* axis resolution (thickness layer) rather than in the *x-y* axes.

Light dispersion was evaluated by printing a symmetrical geometry, i.e. a cube and the thickness layer is measured in the 4 faces of the cube along the z-direction. If the thickness is the same in all the faces, then there is no dispersion, although this is a very common issue in DLP technology. Thus, by knowing this issue future designs could be controlled. The chosen curing time was several seconds per layer as discussed in *Chapter 5*.

2.1.4.2.3 Slurry composition

In this subsection, the preparation of the YSZ slurries for DLP-3D Printing of SOFC electrolytes will be described.

DLP uses a photosensitive slurry as starting material which polymerises/solidifies upon interaction with UV light. As there are not commercially available YSZ-based inks for DLP Printing, an adequate slurry must be developed and will include the next main ingredients: monomer resin, photo-initiator, solvent, dispersant and ceramic powders. Also, a commercial resin that directly contains the photo-initiator can be used. In all cases, the ratio of the slurry components, the procedure and the printing parameters must be optimized.

During the preparation of the slurry, all compounds are mixed and, finally, the paste is left still for 15 minutes to remove bubbles. Sometimes an ultra-sonic bath is used to facilitate this process. A Thinky ARE-250 planetary was used to mix the compounds. Firstly, liquid substances were added to the tank of the planetary mixer, then the powders were added and finally they were mixed at 2000 rpm for 30 minutes.

2.1.4.2.3.1 Resin

Some different commercial resins were used as the basis of the slurry, including Clear Resin (FSL3D), Black, Red and un-pigmented Resin (Standard Bled). All these resins already contain photoinitiator. In addition, a home-made resin based on a monomer (polyethylene glycol diacrylate, PEGDA), a photo-initiator (Irgacure 819 or Sudan I) and a solvent (as ethanol) was studied.

Once resin is made, the curing times are studied in order to choose the best option to ensure a good final resolution and a good attachment between cured layers.

2.1.4.2.3.2 Dispersant

The resin used in SLA or DLP technologies should have a viscosity preferably below 3000 mPa*s, to make easier the recoating of a fresh new resin layer after each successive printed layer.[15] However, nowadays it is still a challenge due to the high ceramic loads necessary for some applications.

Usually, more than 50wt. % of ceramic powder suspended is demanded to get this goal. For this reason, it is very important the dispersant role in DLP slurries, to prevent sedimentation, particles agglomeration and helping to keep the slurry homogeneous. The slurry viscosity can be calculated by the next equation:[14]

$$\eta = \eta_0 \left(1 - \frac{\beta_\phi}{\phi_o}\right)^{-2,5\phi_0} \qquad \textit{Equation 2.5}$$

- ϕ_o: volume fraction solids at maximum packing
- η_0=viscosity of resin
- β_ϕ: effective volume fraction of the suspended solid

A good dispersion has always an important role as the interactions between compounds allow incorporating high ceramic loadings. Two different processes may be adopted: (i) use of a dispersant or gelling agent (ii) amplify the inter-particles interactions.

Regarding the first strategy, the dispersant role is based on solid particles interaction with the solvent. Inter-particle electrostatic interactions come from the distribution of charges around the particle and understanding how they occur is essential to comprehend the colloidal stability. Depending on the functional groups on the surface of the particle, there will be some specific interactions between the liquid and the solid when the particle is submerged into a liquid. Depending on these charges, there may appear interactions between particles, causing attraction among them. These interactions could be supressed by steric stabilization, using large molecules (of the dispersants) that difficult the interactions between particles via sterically repulsion.[16] If the steric stabilization combines with the charges around the particles, it is an electrosteric stabilization, *Figure 2.15*.

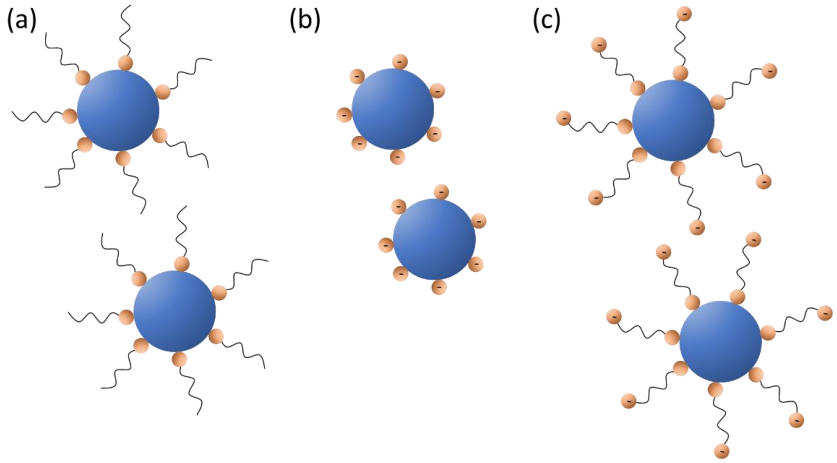

Figure 2. 15 a) Steric stabilization b) Electrostatic stabilization c) Electrosteric stabilization

In this work, Triton™ X-100 (t-Octylphenoxypolyethoxyethanol) dispersant was used. It is a non-ionic surfactant which has a hydrophobic (tail) and hydrophilic parts. In this case, the head group has no charge, for this reason is called non-ionic. Thus, it coincides with *Figure 2.15 (a).*

Specifically, in this thesis fine ceramic powder were used, so for this reason, different amounts of Triton™ X-100 dispersant were tested (0, 0.5, 1.0, 1.5, 2.0, 2.5, 2.85, 3.0 wt. %) to study the particle size distribution to predict if there are or not particles agglomeration. The goal is the production of a 70wt. % 8 YSZ slurry.

2.1.4.2.3.3 Ceramic powders

In this work, YSZ 8% mol (TOSOH and Kceracell) powder to produce the 3D-printed electrolytes. Their properties are shown in *Table 2. 8*. As mentioned in chapter before, this is the state-of-the-art electrolyte material for SOFCs.

Table 2. 8 Theoretical data of YSZ commercial powders [17,18]

Material	Parameters	Data
8 YSZ (Kceracell)	Specific Surface area [S_{BET}] (m^2/g)	14.636
	Particle Size Distribution (PSD) (μm)	0.1870
	Composition	$(Y_2O_3)_{0.08}(ZrO_2)_{0.92}$

Debinding procedure removes most of organic compound, while sintering results in the powder particles (YSZ) compacting via interdiffusion. The optimized process employed in this work is shown in *Table 2. 9*.

Table 2. 9 Debinding and Sintering program for printed electrolytes obtained in SPID3R printer

Debinding (5% H_2-Ar)	**Sintering** (airtight)
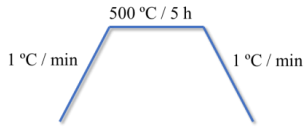	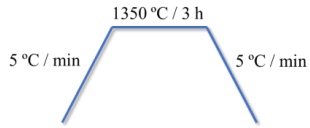

2.1.4.4 Functionalization of electrolytes with electrodes

The same procedure described in *Section 2.1.3.4* was carried out.

2.1.5 Ceramic robocasting

Robocasting, or direct ink printing, is the last method used for ceramic materials in this thesis. Among the advantages of this system, it could be highlighted that it is possible to print a pattern avoiding material waste, the potential use of high solid load and even multi-material printing. Although that printer is fundamentally focused to biomaterial printing, it is also convenient for thick electrodes deposition with customized geometries for SOFCs. Thus, the slurry optimization allowed taking advantage of this printer for the production of LSM-YSZ electrodes.

2.1.5.1 Printer

In this case a commercial printer, BioX Cellink was selected, *Figure 2. 16*. There are a lot of models of Cellink brand. BioX model have some advantages with reference to its specifications. The maximum pressure that can achieve is 200 kPa, a resolution of 1 µm and the temperature at the cartridge and printing bed can be modified up to 250°C for the printhead and between 7°C and 60°C for the platform. Another advantage is the multi-head printing, in this case three different cartridge can be used helping to implement multi-material printing.

The printer works with a pump that applies a precise pressure in the cartridge (a syringe) to extrude the mixture through the needle. The nozzle will be selected depending on the viscosity and the target resolution, so if the slurry is viscous and the needle is thin, the pressure would be greater. However, there is a limit, if the viscosity is very high, the material cannot be extruded in spite of the applied pressure.

The most important aspect in this method is controlling the printability, i.e. the capability of paste extrusion while maintaining the shape once printed. This concept is strongly correlated with paste rheology, being the goal to achieve a balance between viscosity, gravity and surface tension.

Consequently, in this thesis, the study will be dedicated to develop ceramic pastes (LSM-YSZ) for 3D printable SOFCs electrodes. To achieve this, some parameters were studied: ceramic load charge, achieve a good gelling mechanism using different methods and optimization of the printing parameters such as needle size, pressure, speed printing and filling percentage.

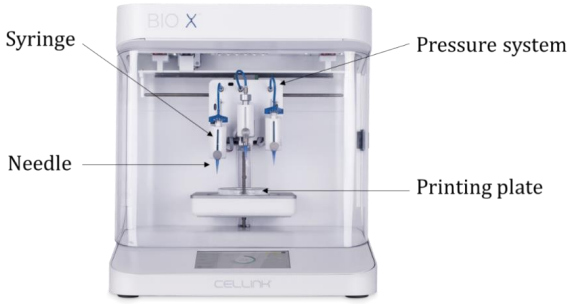

Figure 2. 16 Robocasting BioX Cellink printer

2.1.5.2 Printing parameters

The printing parameters studied in this work in order to extrude different slurries are shown in *Table 2. 10*.

Table 2. 10 Robocasting printing parameters

Parameters	Data
Pressure (kPa)	5; 20; 30; 40; 45; 50; 70
Filled (%)	60; 80; 90; 100
Speed printing (mm/s)	10; 15; 20
Initial high (mm)	0.4

2.1.5.3 Slurry composition

As described in Chapter 1, robocasting is a 3D direct ink printing technique, where the machine is fed with inks. Inks undergo stress inside the nozzle due to the syringe piston or plunger, causing modifications in the ink viscosity down through the barrel.[18,19] For this reason, adequate rheological and shear-thinning properties of the ink are required to produce good quality 3D printing structures such as (i) easy and quick solidification, (ii) easy flow through thinner nozzles, (iii) specific viscosity allowing mechanical stability after extrusion, (iv) can recover elasticity to avoid the collapse of the 3D structure, (v) have a high solid load to prevent deformation after drying (vi) and must be cured without difficulties by thermal or UV-light application.[20]

In this work, robocasting is used as an attractive technique for fabrication of ceramic electrodes for SOFCs.

2.1.5.3.1 Ceramic powders

As mentioned above, the manufacturing process to produce ceramic slurries for electrodes via robocasting will be described. All ceramic powders must be well-dispersed in an aqueous solution and then the suspension is left to dry at room temperature until water evaporates to avoid crack formation. Nevertheless, crack formation may be hindered by using high ceramic loadings, around ≥ 40 wt. % and low organics contents, e.g. ≤ 30 wt. %[18]

Lanthanum Strontium Manganite (LSM) as-received and LSM calcined at 800°C for 2h. (Kceracell, ≥ 150 μm), and Yttria-Stabilized Zirconia (YSZ) 8% mol (TOSOH) were employed for three different mixtures, pure YSZ, pure LSM and YSZ-LSM (50-50). These mixtures were suggested as electrolyte (YSZ) and as cathode (LSM, LSM-YSZ) for SOFCs. Solid loadings higher than 70 wt. % were tested.

Firstly, sedimentation tests were performed to evaluate powder dispersion. The procedure is as follows: ceramic powders were added to aqueous solutions and sonicated (200 W, 26 kHz) at different basic pH controlled by KOH addition (10^{-2}, 10^{-3}, 10^{-4}, 10^{-5}, 10^{-6} M). The suspension was left for 15 minutes in the case of LSM and 2 hours for YSZ slurries and the results were evaluated via visual inspection. Besides solid and solvent, a dispersant was added which is the key compound in this technique.

For the printing tests, solvent, dispersant and powders were added and ball-milled for ten minutes at 200 rpm. In the case of two powders (LSM-YSZ composites), the addition was stepwise, i.e. first ceramic is added and ball-milled, and then the second material is added to the slurry and mixed for further ten minutes

2.1.5.3.2 Solvent

Some compounds are crucial if a high solid load want to be manufactured, such as appropriate solvent, suitable binder, plasticizer, dispersant, and/ or a great flocculant, a specific cross-linker and finally a possible catalyst and initiator to cure after printing, which will be specified later.

The use of some compounds or others will depend on the type of dispersion desired. When a high ceramic load is made, solvent easily evaporates. If there is a high amount of solvent it is necessary to use a catalyst and an initiator in order to consolidate the slurry after to be extruded, via temperature or radiation.

Regarding the solvent, different types as water and Propylene Glycol (PG) were employed.

2.1.5.3.3 Dispersant

As explained in *Section 2.1.4.2.3.2*, two different processes may be adopted in order to achieve a good dispersion: (i) use of a dispersant or gelling agent (ii) amplify the inter-particles interactions.

Regarding the first approach, in this work Pluronic F-127 was studied, *Figure 2. 17*. Pluronic F-127 is a copolymer of polyethylene oxide (PEO) and polypropylene oxide (PPO) (ratio 2:1), which shows relatively low viscosity at low temperatures, whilst is highly viscous at room temperature.

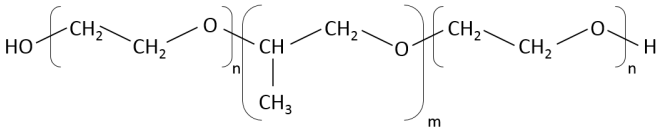

Figure 2. 17 Pluronic structure

It is usually added in 20 – 30 wt. % to aqueous solutions forming a hydrogel at room temperature. But at low temperature it flows.[21] Consequently, in this work some different compositions with Pluronic were tested.

Several tests were made changing the dispersant proportion to obtain a printable slurry. The slurries tested in the present work are collected in the Robocasting Appendix.

Regarding the second strategy, an inter-particle interaction study was performed using different solvents and dispersants. The slurries developed in this section were made using water or propylene glycol as solvents and studying the effects of five different dispersants in the slurry such as Dispex® A40 (ammonium salt solution of an acrylic polymer in water) (Ciba-BASF, UK), Darvan® (an ammonium polymethacrylate solution) (R.T. Vanderbilt), Dolapix CE64 ($C_4H_6O_2NH_4^+$) (Zschimmer & Schwarz), Polyethylene glycol (PEG) (Aldrich), and Pluronic F-127 ($(C_3H_6O{\cdot}C_2H_4O)_x$) (Sigma Aldrich). PEG and Pluronic to achieve a stabilization mechanism steric. In the case of Dispex®, Darvan® and Dolapix, steric stabilization was studied, *Figure 2.15*.

2.1.5.3.4 Monomer and initiator

When a good slurry was obtained with a specific viscosity to be extruded by the syringe nozzle, acrylamide (Am) as main monomer, N-N'-Methylenebisacrylamide (BisA) as crosslinker and sodium persulfate ($Na_2S_2O_8$) as initiator and tetramethylethylenediamine (TEMED) were added in order to print a 3D structure. These two last compounds are the key to cure the slurry using temperatures ≈ 40°C. Chemical mechanism is initiated by sodium persulfate followed by TEMED in order to solidify acrylamide monomer.[23] All of them were studied at different proportions in order to achieve a good slurry, with a fast solvent evaporation, leaving a rigid object after printing

and easily printable and avoiding nozzle stuck during printing process. The results will be discussed in detail in Appendix 7.

2.1.5.3.4 Pore former

Finally, pore former was added too, to increase structure porosity after thermal treatment. Graphite with diameter > 1 µm was employed with this purpose adding increasing amount of it: 8.7, 10.7, 12.6, 14.4 and 16.1 wt. % in the slurry.

2.1.5.4 Thermal treatment

The debinding and sintering process were proposed in the same program, going until 600ºC with a low rate. Then, sintering was got at 1100ºC for 6h.

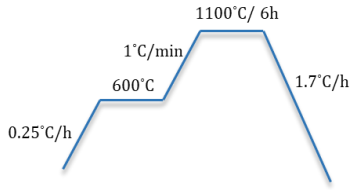

Figure 2. 18 Thermal treatment for LSM structures printed with robocasting technique

2.2 Structural characterization

The techniques used along this thesis will be describe below, specifying for what purpose have been applied.

2.2.1 Scanning electron microscopy

Scanning electron microscopy (SEM) in one of the most popular techniques used for microstructural characterization of thin and microstructures samples, due to the high-resolution images that can be obtained from any specimen in a rather quick and simple process.

In SEM, the surface of the samples is scanned with an electron beam and the result of this interaction produces surface images. Electrons can be generated via current or a field, by using a thermionic emission source or a field emission source, respectively. Then the electrons go through condenser and objective lenses that accelerate and focus the beam electrons to a spot. Next, the sample interacts with the electron beam, giving rise to energy exchanges, which results in the reflection of high-energy electrons, emission on secondary electrons or/and emission of electromagnetic radiation, *Figure 2. 19*, where each signal is recognized by particular detector.

Depending of the signal and the detector there are some types of images, which are usually recorded from Secondary Electrons (SE). The number of emitted SE depends of the incident angle, for example in the borders more secondary electrons are emitted, so the image will be brighter than in a plane surface, which yields high definition, producing topography information. In the case of backscattered electrons (BSE) being used, the image contrast depends on the chemical composition, allowing the identification of areas with various compositions. Lastly, the electromagnetic radiation (both X-Rays and visible light) generated upon interaction with the beam may be used for elemental analysis (X-Ray) or may cause fluorescence (visible light).[23–25]

In this thesis different SEM models were employed in various institutions, including Jeol JSM 6300 (SEGAI, ULL), Jeol JSM 6490 LV (UCLM) and Zeiss Auriga (IREC). SEM was used to analyse the morphology, density and porosity of printed devices (electrolytes, electrodes, catalyst and supports). SEM was also used to measure the cross-section thickness of these devices and to check the resolution of the printed pieces.

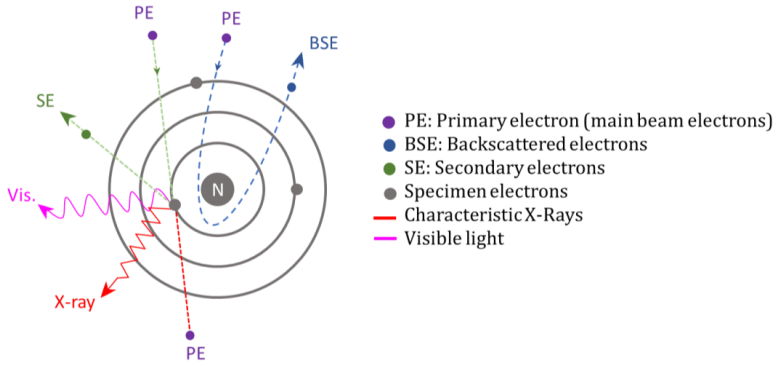

Figure 2. 19 Electron process when beam electrons inside in the sample

2.2.2 X-Ray Diffraction

X-Ray diffraction (XDR) is a technique used to study and analyse sample composition and to identify crystalline phase of materials. The principle of this technique is based on the sample exposure to X-Rays. The sample atomic nuclei diffracts the radiation with particular direction and intensities according to Bragg's Law[20] as the wavelength of X-Rays is in the same order of magnitude of the atomic radii, *Figure 2. 20*. Emerging diffracted X-Rays provide information regarding position and type of atom. Thus, a pattern characteristic of each crystalline structure is produced, which allows resolving the position of atoms in the crystal, the chemical bonds and their crystallographic disorder, among other parameters.

In this work, this technique played a major role on phase identification of titanium oxide structures printed by FDM after thermal treatment. The XRD equipment used were located at SEGAI, ULL and UCLM (Panalytical Empyrean). Experiments were carried out with mono-chromatic copper radiation (Kalpha$_1$= 1.5406 Å) in both cases.

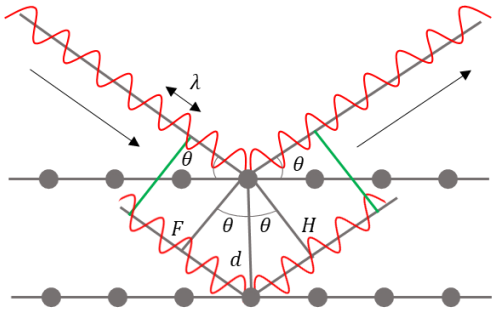

Figure 2. 20 Interaction of X-rays and crystal lattice (adapted from reference [20])

2.2.3 Thermal gravimetric analysis

Thermal analysis techniques detect physical and chemical changes of the sample, according to temperature and time. These analyses are made by controlling the heating and cooling program and the atmosphere, producing a thermal analysis curve (thermogram).

The most common and used thermal analysis technique is thermogravimetry (TG or TGA), that measures the mass variation of the sample when exposed to a thermal treatment, *Figure 2. 21*. The atmosphere must be controlled, and can be inert or oxidising, i.e. nitrogen or air / oxygen respectively. While the sample is heated, mass variations are recorded by a highly sensitive balance. In this way, any change in the sample information is provided with respect to the temperature.[26]

In this thesis, TG analysis was employed for the compositional study of commercial powder of the 3D System Binder Jetting Printer, in order to ensure that commercial ceramic powder was pure and only contained crystallization water molecules. Thus, it was possible to look for a correct application of this compound, either as support or catalyst. The TG equipment used was a PYRIS Diamond TG/DTA High Temp VA, Perkin Elmer Instruments, located at SEGAI, ULL.

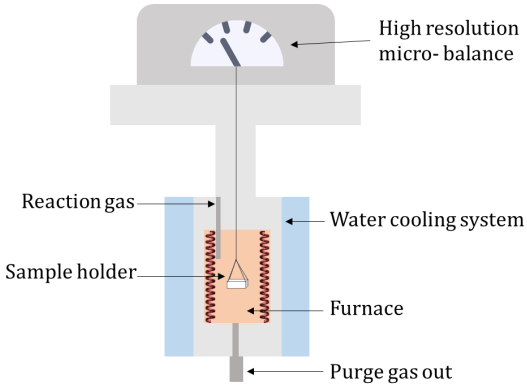

Figure 2. 21 Scheme of TG analyser

2.2.4 Particle Size

The particle size distribution (PSD) analyser allows to analyse between a range of 20 nm and 2000 µm. This technique uses a laser diffraction which evaluates the intensity of the scattered light as a function of the angle when a laser beam passes through a sample of scattered particles. Thus, the angular dispersion intensity data is used to calculate the size distribution model of the particles responsible for creating the experimental dispersion pattern, using the Mie theory of light scattering, *Figure 2. 22*.[27] The equipment always obtains particle size as the diameter of a sphere equivalent in volume. When there is small amount of sample measuring accessory via wet, Hydro 2000 SM, is employed. Usually, 400 mg of sample are added to 50 – 150 mL of water, approximately, which ensures that no sample is lost during the measurement.

The main goal of this work was to measure the particle size distribution of slurry for DLP printing according with different amount of dispersant added. The PSD analyser used was the model Mastersizer 2000, Malvern Instruments, located at SEGAI, ULL.

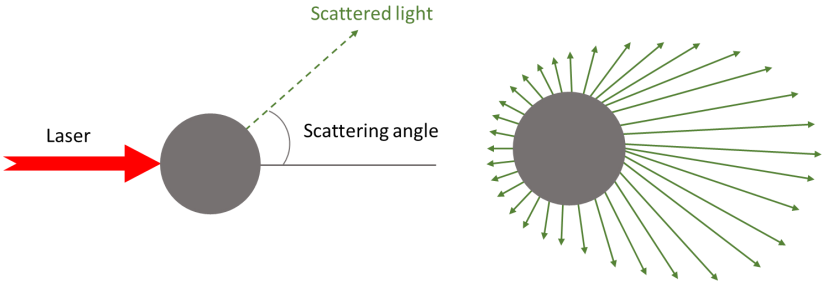

Figure 2. 22 Scattering process when laser inside on the sample

2.2.5 Viscosity

Viscosity is measured by a rotary rheometer, which can apply force to a sample in different ways. The pressure can be controlled, enabling a progressive and continuous shear stress, or the performance of controlled oscillation tests. Alternatively, the tension can be controlled, to allow a continuous shear strain rate or controlled oscillation. The most appropriate operation mode is in a continuous and regular shear mode, either with speed or effort control. That generates information to study material behaviour as a function of time and the forces applied, which allows the study of the viscoelastic nature of the material.[28]

In this thesis, this technique was employed to measure the different viscosity of slurry for DLP printing according with different amount of dispersant added. The rheometer used was the model CVO-100-901, Malvern Instruments, located at SEGAI, ULL.

2.2.6 Porosimetry

Mercury Intrusion Porosimetry (MIP) is a technique used in the characterization of porosity in solid materials by applying various levels of pressure on a sample immersed in mercury. The pressure required to force the entry of mercury into the porous of the material is inversely proportional to the opening of the pores. The data provided is the volume of mercury injected as a function of the pressure applied, which indicates some characteristics of the porous space and can be correlated with different physical properties of the sample, such as the distribution of pore size, total pore volume, area total pore surface, average pore diameter and sample densities.[29] In addition, the pressure required to get mercury to enter the pores of the sample is inversely proportional to their size, that means, when smaller is the pore size higher must be the pressure. The pores according to their size are classified as shown in *Table 2. 11*.

In this thesis, porous samples are required for heterogeneous catalyst applications. Thus, this technique was used to study the porosity of the printed devices such as supports via binder jetting and catalyst via FDM MIP equipment used was the model AutoPore IV 9520, Micrometics, located at SEGAI, ULL.

Table 2. 11 Sample classification according pores sizes

Pore size	Radio (nm)	Diameter (nm)
Macro-porous	> 25	> 50
Meso-porous	25 > x > 1	50 > x > 2
Micro-porous	< 1	< 2

2.3 Functional characterization of materials and printed parts

The functional characterization of the printed devices must be done to measure their performance and evaluate the impact of the 3D structure. In the present work, two different tests were carried out: a) electrochemical performance of the 3D printed electrolytes fabricated by SLA and DLP and b) photocatalytic activity for directly printed catalyst via FDM and impregnated catalyst on printed monoliths.

2.3.1 Performance measurement for SOFCs

Performance of printed YSZ electrolytes by SLA and DLP must be characterized. One of the most important parameters of this type of device is the conductivity and electrocatalytic activity. This is a characteristic magnitude of each material. In this case the material is the same (8 YSZ), but with a determined geometry conductivity can be measured knowing the electrical resistance to the passage of a current, using for that Ohm's law, *Equation 2.6*. Where the conductivity is inversely proportional to resistance. At the same time, resistivity is directly proportional to the sample thickness (L), and inversely proportional to the surface (S) and the resistance (R). Therefore, for a sample with a given geometry it is possible to determine the thickness and the surface. Thus, by measuring the resistance when current passes through the specimen, the conductivity can be calculated.

Impedance spectroscopy (EIS) is one of the most common technique to measure the electrical conductivity of materials as it is possible to separate the different contributions (of the material or device) among other applications. This technique applies an alternating current of variable frequency and very small amplitude on the sample.

The potential applied to the sample is given by the *Equation 2.7*, where E_o is amplitude of the applied voltage and ω the variable angular frequency. The current measured through the sample is also a function of the frequency, as shown in *Equation 2.8*, being θ the phase shift between the applied potential and the current

Keeping in mind that the impedance is the resistance of the material under alternating current, the impedance can be expressed as in *Equation 2.9*, hence it can be expressed in terms of real and imaginary components.

$$\sigma = \frac{L}{S*R} \qquad \textit{Equation 2.6}$$

$$\tilde{E}(t) = E_O e^{i\omega t} \qquad \textit{Equation 2.7}$$

$$\tilde{I}(t) = I_O e^{i(\omega t+\theta)} \qquad \textit{Equation 2.8}$$

$$\tilde{Z}(\omega) = \frac{\tilde{E}(t)}{\tilde{I}(t)} = |Z|e^{-i\theta} = |Z|cos\ \theta - i|Z|sen\ \theta = Z' - iZ'' \qquad \textit{Equation 2.9}$$

$$RC = \frac{1}{2*\pi f_{max}} \qquad \textit{Equation 2.10}$$

The representation of the imaginary term $Z''(\omega)$ versus the real term $Z'(\omega)$ is known as Nyquist plot, *Figure 2.22*. The maximum point of the semicircle is the maximum frequency, which is related with the capacitance (Z'') and the resistances (Z') of the material, *Equation 2.10*. The experiment is carried out in a frequency interval and depending on the relaxation frequencies of the electrochemical processes taking place, the response will result in the appearance of different semicircles in the impedance spectra. This is a consequence of applying a perturbation on polycrystalline materials, hence the conductive species must move through the interior of the grains and through the grain borders, and the ion/electron mobility in the grain boundaries is different to that from the bulk, etc.

When analysing the data, it must be noted that the capacitance value (relaxation frequency) of the semicircle is related to the electrochemical process going on, *Table 2. 12*. Processes in the in the high frequency range appear in the left side of the Nyquist plot and are typically related to the bulk, while processes in the lowest frequency range appear on the right and may be ascribed to electrode responses.

In the case of measuring cells (symmetrical cells and full cells), some info can be extracted out of the Nyquist plots. The first intercept (lowest impedance) is usually related to series resistance (Rs), which includes the ohmic contributions of the electrolyte and the electronic resistance of the electrodes when not negligible. On the other hand, the intercepts in the lower frequency range are usually related to parallel resistance (Rp), typically associated to electrode processes.[31,32]

Table 2. 12 Classification of processes depending its capacity

Process	Capacity (F)
Bulk	10^{-12}
Grain boundary	10^{-8} - 10^{-11}
Interface electrolyte/electrode	10^{-5} - 10^{-7}
Electrochemical reactions	10^{-4}

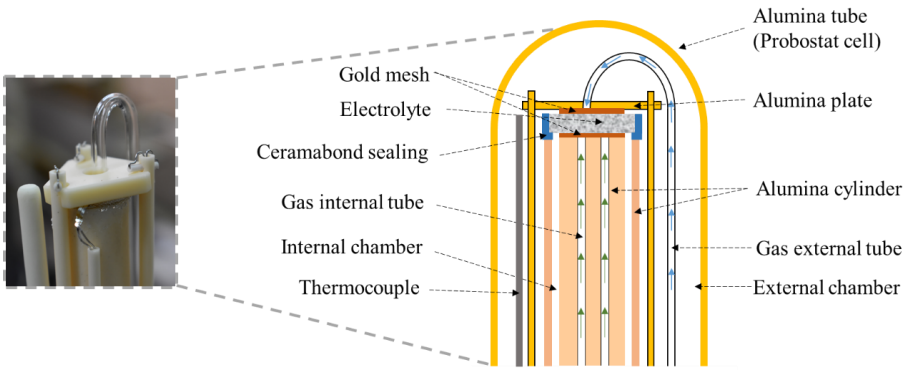

Figure 2. 23 Scheme of Probostat cell

In this work, EIS was used to study plain and structured YSZ electrolytes, which were obtained by traditional methods, SLA and DLP in order to compare them. To carry out the tests, cylindrical electrolytes were made with different thickness and geometries. Also, different cathode fixing temperatures were studied.

These studies were done at IREC and ULL, using in both cases Probostat cells, *Figure 2.23*, between 500-900°C, using a frequency of 100mHz – 1MHz and perturbation of 0.05 V. In addition, measurements were done using either a Novocontrol (Alpha-A High performance frequency analyser) or a Parstat (2273 Advance Electrochemical System) equipment located at IREC. While the equipment located at ULL was an Autolab (PGSTAT204) potentiostat / galvanostat. The data were analysed in all cases with Z-View software.

2.3.2 Catalytic Tests

Photocatalytic tests were carried out in this work due to the potential application of 3D printed monoliths in contaminant degradation in water. Spiral-shaped monoliths were printed via FDM for direct catalyst production and binder jetting for catalyst support fabrication. In both cases, the structure is the same and the catalyst used is TiO_2, as previously mentioned. Considering the mechanism described in *Equations 1. 4 - 1. 11*, solar light is necessary to trigger all reactions in order to remove the contaminant, methylene blue and ciprofloxacin in the present work.

The photocatalytic equipment used is home-made setup with the following components, *Figure 2. 24*.

- Fixed bed reactor: quartz tube (18 cm length and 0,6 cm internal diameter)
- UV-Vis lamp: high pressure sodium vapor 50 cm away from the reactor (model 400-WG / 92/2, Philips)

- Air extractor system to cooling lamp
- Parabolic cylindrical light concentrator
- Thermostatic solution deposit (100 mL) with mercury thermometer
- Thermostat
- Magnetic stirring system
- Peristaltic pump to propel the solution through the circuit system with flow controller (model 302 S, Watson Marlow)
- Air bubbling system which maintain the solution oxygenated

The 3D printed catalysts were placed in the fixed bed reactor, which is placed at a distance of 50 cm from the lamp and surrounded by a cylindrical parabolic concentrator capable of concentrating the radiation from the lamp (Philips, model 400-WG/92/2). Inside the lamp, the discharge tube is filled with sodium amalgam, so that the lamp emits in the UV-Vis, reproducing solar radiation. It is also placed in a system with air extraction for cooling. The contaminant solution was introduced into the tank. The tank has five entries for (i) thermometer, (ii) entry of solution, (iii) exit of solution, (iv) bubbling system accoupling and (v) a free joint to take samples to measure. This tank is based on a double wall cell, so that the temperature can be controlled during the experiment. One of the deposit mouths is connected to the peristaltic pump (Watson-Marlow, model 302S), which absorbs the solution feeding the photoreactor. Another mouth is connected to the reactor to receive the solution that has circulated through the circuit, generating a continuous flow. Another of the entries has a thermometer inserted to control that the temperature remains constant throughout the experience. The fourth hole is linked to an air bubbling system, which comes from a gas scrubber bottle where the air is saturated in water. This ensures that system remains closed, preventing losses due to evaporation. It also ensures that the solution remains oxygenated, which is necessary for contaminant photochemical degradation. The amount of hydroxyl radicals responsible for the oxidation process will increase in presence of O_2. The last entry remains closed with a lid, except when necessary for taking an aliquot. Finally, it should be pointed out that the solution is under stirring to homogenize in the tank and avoiding concentration gradients when a piece of sample is taken.[29]

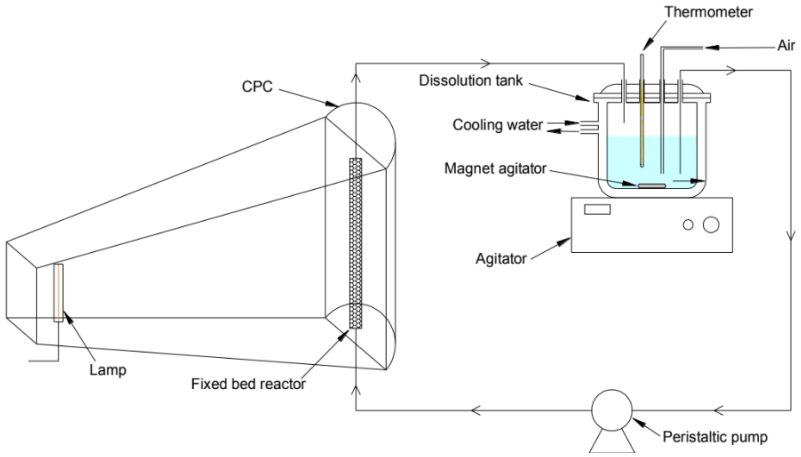

Figure 2. 24 Photocatalytic system [33]

2.4 References

[1] J. Canales-Vázquez, G. B. S. B. J. R. M.-R. V. Y.-A. and J. J. L.-L. Method for Obtaining Ceramic Barbotine for the Production of Filaments for 3D-FDM Printing, Barbotine Obtained Using Said Method, and Ceramic Filaments. WO2017191340A1, 2017.

[2] Hull, C. W.; Arcadia, C. AAPPARATUS FOR PRODUCTION OF THREE-DMENSONAL OBJECTS BY STEREO THOGRAPHY. US4575330A, August 8, 1984.

[3] Griffith, M. L. Stereolithography of Ceramics., University of Michigan, (1995).

[4] Griffith, M. L.; Halloran, J. W. Freeform Fabrication of Ceramics via Stereolithography. J. Am. Ceram. Soc. (2005), 79 (10), 2601–2608, doi:10.1111/j.1151-2916.1996.tb09022.x.

[5] Halloran, J. W. Ceramic Stereolithography: Additive Manufacturing for Ceramics by Photopolymerization. Annu. Rev. Mater. Res. (2016), 46, 19–40, doi:10.1146/annurev-matsci-070115-031841.

[6] Masciandaro, S.; Torrell, M.; Leone, P.; Tarancón, A. Three-Dimensional Printed Yttria-Stabilized Zirconia Self-Supported Electrolytes for Solid Oxide Fuel Cell Applications. J. Eur. Ceram. Soc. (2019), 39, 9–16, doi:10.1016/j.jeurceramsoc.2017.11.033.

[7] Wei, L.; Zhang, J.; Yu, F.; Zhang, W.; Meng, X.; Yang, N.; Liu, S. A Novel Fabrication of Yttria-Stabilized-Zirconia Dense Electrolyte for Solid Oxide Fuel Cells by 3D Printing Technique. Int. J. Hydrogen Energy (2019), 44 (12), 6182–6191, doi:10.1016/j.ijhydene.2019.01.071.

[8] Ibrahim, A.; Ibrahim, M.; Sa'ude, N. Optimization of Process Parameter for Digital Light Processing (DLP) 3D Printing. (2017), 19–22, ISBN: 978-93-86291-88-2.

[9] Becker, F. H.; Gmbh, R. Debinding Processes. Physical and Chemical Conclusions and Their Practical Realisations. 1–21.

[10] Gentry, S. P.; Halloran, J. W. Light Scattering in Absorbing Ceramic Suspensions: Effect on the Width and Depth of Photopolymerized Features. J. Eur. Ceram. Soc. (2015), 35, 1895–1904, doi:10.1016/j.jeurceramsoc.2014.12.006.

[11] Delhote, N.; Bila, S.; Baillargeat, D.; Chartier, T.; Verdeyme, S. Advanced Design and Fabrication of Microwave Components Based on Shape Optimization and 3D Ceramic

Stereolithography Process. In Advances in Ceramics - Synthesis and Characterization, Processing and Specific Applications; InTech, (2011) doi:10.5772/18322.

[12] Mitteramskogler, G.; Gmeiner, R.; Felzmann, R.; Gruber, S.; Hofstetter, C.; Stampfl, J.; Ebert, J.; Wachter, W.; Laubersheimer, J. Light Curing Strategies for Lithography-Based Additive Manufacturing of Customized Ceramics. Addit. Manuf. (2014), 1, 110–118, doi:10.1016/j.addma.2014.08.003.

[13] Lu, X.; Zhou, Y. F.; Xing, X. L.; Shao, L. Y.; Yang, Q. X.; Gao, S. Y. Open-Source Wire and Arc Additive Manufacturing System: Formability, Microstructures, and Mechanical Properties. doi:10.1007/s00170-017-0636-z.

[14] Griffith, M. L.; Halloran, J. W. Ultraviolet Curable Ceramic Suspensions for Stereolithography of Ceramics. Am. Soc. Mech. Eng. Prod. Eng. Div. PED (1994), 68–2 (January 1994), 529–534,.

[15] Halloran, J. W.; Griffith, M.; Chu, T.-M. Stereolithography Resin for Rapid Prototyping of Ceramics and Metals. US6117612A, September 12, 2000.

[16] Tan, T. B.; Yussof, N. S.; Abas, F.; Mirhosseini, H.; Nehdi, I. A.; Tan, C. P. Stability Evaluation of Lutein Nanodispersions Prepared via Solvent Displacement Method: The Effect of Emulsifiers with Different Stabilizing Mechanisms. Food Chem. (2016), 205, 155–162, doi:10.1016/j.foodchem.2016.03.008.

[17] Kceracell. Electrolyte Materials http://www.kceracell.com/electrolyte.html (accessed Mar 6, 2020).

[18] Feilden, E.; Blanca, E. G. T.; Giuliani, F.; Saiz, E.; Vandeperre, L. Robocasting of Structural Ceramic Parts with Hydrogel Inks. J. Eur. Ceram. Soc. (2016), 36 (10), 2525–2533, doi:10.1016/j.jeurceramsoc.2016.03.001.

[19] M'barki, A.; Bocquet, L.; Stevenson, A. Linking Rheology and Printability for Dense and Strong Ceramics by Direct Ink Writing OPEN. (2017), 7, 10, doi:10.1038/s41598-017-06115-0.

[20] Rosa, M. Development of Printing Media for Digital Manufacturing of Fuel Cells., Technical Univeristy of Denmkar (DTU), (2019).

[21] Feilden, E. Additive Manufacturing of Ceramics and Ceramic Composites via Robocasting., Imperial College London, (2017).

[22] Liu, K.; Zhang, K.; Bourell, D. L.; Chen, F.; Sun, H.; Shi, Y.; Wang, J.; He, M.; Chen, J. Gelcasting of Zirconia-Based All-Ceramic Teeth Combined with Stereolithography. Ceram. Int. (2018), 44 (17), 21556–21563, doi:10.1016/j.ceramint.2018.08.219.

[23] Ackermann, H. W. Basic Phage Electron Microscopy. Methods Mol. Biol. (2009), 501, 113–126, doi:10.1007/978-1-60327-164-6_12.

[24] McMullan, D. Scanning Electron Microscopy. Scanning (1995), 17 (3), 175–185, doi:10.1002/sca.4950170309.

[25] Kuo, J. Electron Microscopy: Methods and Protocols, 2nd ed.; Press, H., Ed.; (2007), ISBN: 978-1-58829-573-6.

[26] W.M. Groenewoud. Thermogavimetry. In Characterisation of Polymers by Thermal Analysis; Elsevier: The Netherlands, (2001); pp 61–76 doi:10.1016/b978-0-444-50604-7.x5000-6.

[27] Malvern Panalytical. Basic principles of particle size analysis. https://www.malvernpanalytical.com/es/learn/events-and-training/webinars/W170216BasicsParticleSize.

[28] Barnes, H. A Handbook of Elementary Rheology; Institute of Non-Newtonian Fluid Mechanics, University of Wales, Eds.; (2000).

[29] Borges, M. E.; García, D. M.; Hernández, T.; Ruiz-Morales, J. C.; Esparza, P. Supported Photocatalyst for Removal of Emerging Contaminants from Wastewater in a Continuous Packed-Bed Photoreactor Configuration. Catalysts (2015), 5 (1), 77–87, doi:10.3390/catal5010077.

[30] Irvine, J. T. S.; Sinclair, D. C.; West, A. R. Electroceramics: Characterization by Impedance Spectroscopy. Adv. Mater. (1990), 2, 132–138, doi:10.1002/adma.19900020304.

[31] West, A. R.; Sinclair, D. C.; Hirose, N. Characterization of Electrical Materials, Especially Ferroelectrics, by Impedance Spectroscopy. J. Electroceramics (1997), 1 (1), 65–71, doi:10.1023/A:1009950415758.

[32] Borges, M. E.; Sierra, M.; Esparza, P. Solar Photocatalysis at Semi-Pilot Scale: Wastewater Decontamination in a Packed-Bed Photocatalytic Reactor System with a Visible-Solar-Light-Driven Photocatalyst. Clean Technol. Environ. Policy (2017), 19 (4), 1239–1245, doi:10.1007/s10098-016-1312-y.

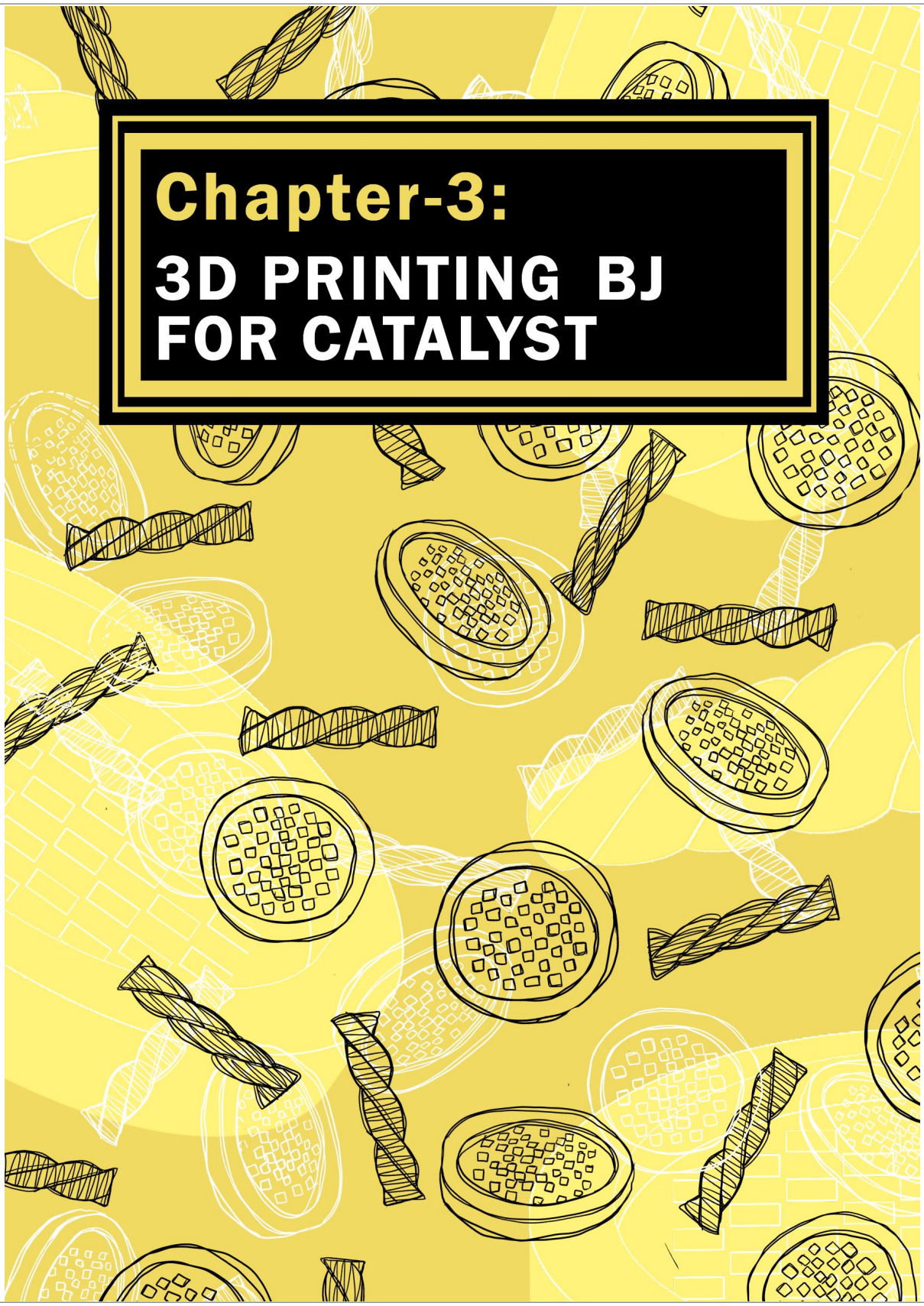

3.1 Monolith Architecture

As discussed in previous chapters, one of the highlights of 3D printing techniques is the possibility of improving the performance of different devices by the control of materials microstructure allowing the fabrication of complex architectures that could not be obtained using traditional manufacturing processes.

On the other hand, catalytic processes largely depend on the active area and therefore catalysts are designed to enhance the contact with reagents, while taking into consideration parameters such is the reactor geometry. Consequently, 3D printing technologies may find a niche of applications to take advantage of non-conventional geometries to boost the overall performance as previously discussed. In this work, photo-catalysis is used to remove emerging contaminants in water, as mentioned in *Chapter 1, Section 1.2.3*, following previous work in this field of the research team.[1–3]

Several different designs were considered in order to manufacture these devices, *Figure 3. 1.* However, in this thesis, the design of the catalyst is conditioned by the catalytic reactor, which is a 10 cm long quartz tube with 6 mm of internal diameter. Consequently, the designs collected in *Figure 3. 1* are not compatible and other geometries must be explored.

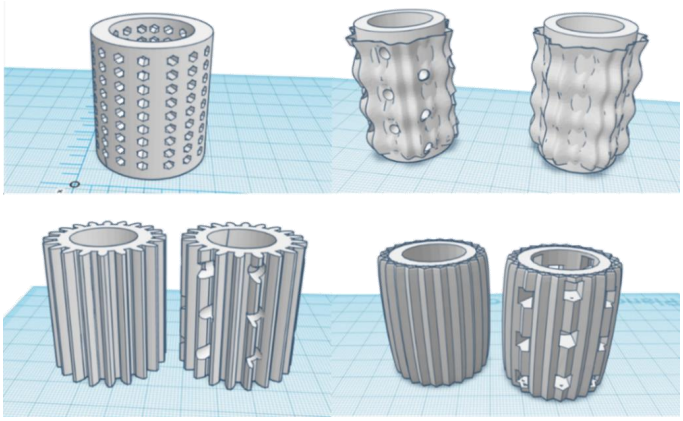

Figure 3. 1 Different digital designs for catalyst supports

As the catalyst was in a fixed-bed rector, the solution containing contaminants must pass through the sample, hence it was necessary using an adequate design of the catalyst that could facilitate the flow of the solution. Thus, the chosen design was a spiral that facilitated the flow of methylene blue solution on the system counteracting the effect of gravity inside the reactor.[4] In addition, the spiral geometry allows a more efficient irradiation of the fluid while passing through the catalyst into the reactor.

Considering all the above in addition to the dimensions of the quartz tube reactor, the resulting design is a 40 mm long and 6 mm wide spiral, *Figure 3. 2*, whose CAD model was carried out on Thinkercad, a free online tool for 3D modelling.[5] After completed, the *stl* file was downloaded for printing.

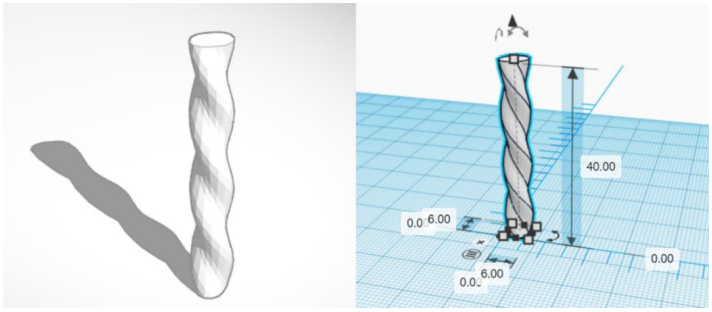

Figure 3. 2 Spiral designs of the catalyst and its dimensions expressed in millimetres

3.2 Binder Jetting Process

The specific objective of this chapter is to use binder jetting (BJ) printing for the fabrication of the catalyst supports. BJ technique offers potential advantages compared to other ceramic 3D printing techniques, for example, the use of the powder as raw material, which is simpler to handle than ceramic slurries for SLA or DLP or ceramic filaments for FDM. This is a key issue and explains why BJ is the 3D manufacturing technique with the largest catalogue of ceramics commercially available.[6–8] A further advantage is the possibility of achieving a good porosity in the final structure, which will give an advantage with respect to functionalizing via infiltration proccesses.[9,10]

The printer used was a ProJet® 360, the described in *Chapter 2, Section 2.1.2.1*. The printing parameters and the characterization of the raw materials will be described below.

3.1.1 Feedstock powder and binder

The starting material is a commercial powder (VisiJet PXL Core, from S.A.T.ÉLITE) which requires a water-based binder (VisiJet Clear, from S.A.T.ÉLITE) for the consolidation of the powder particles. As the composition is unknown, X-ray diffraction of the powders and TGA were carried out to obtain some information regarding phase, composition, etc The experiments were performed for (i) the raw material (VisiJet PXL Core, from S.A.T.ÉLITE.), (ii) the printed material to ensure that the binder does not cause changes in the ceramic powders.

The XRD pattern of the **raw material**, *Figure 3. 3,* **shows the characteristic peaks of calcium sulphate hemihydrate, $CaSO_4 \cdot ½\ H_2O$ (basanite)**, with a 95% match, while if it is compared with $CaSO_4$, matching goes down to 5%.

These results are in good agreement with previous studies,[11] corroborating that calcium sulphate hemihydrate ($CaSO_4 \cdot ½H_2O$) is one of the most used materials for 3D printing via binder jetting.

Regarding the printed support, there is a clear similarity between both phases, besides some additional wide peaks ($2\theta_1$=11.7 , $2\theta_2$=20.9 , $2\theta_3$=23.3 , $2\theta_4$=29.1 , $2\theta_5$=31.1, $2\theta_6$=33.5) that may be perfectly attributed to the organic binder, *Figure 3. 4*.

Thus, it can be concluded that the **printed support retains the unit cell of the raw material, $CaSO_4 \cdot ½\ H_2O$**.

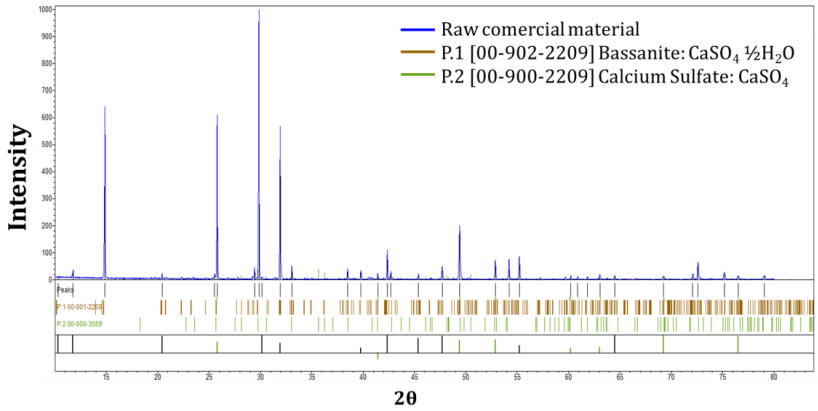

Figure 3. 3 XRD patterns for commercial raw material compared with patterns of $CaSO_4 \cdot ½H_2O$ and $CaSO_4$

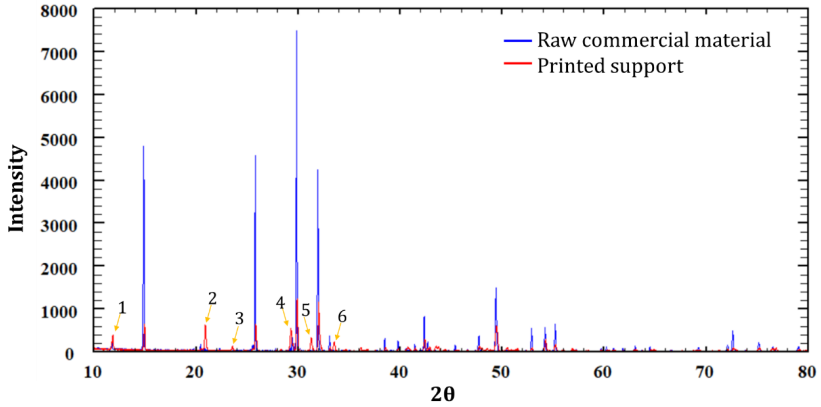

Figure 3. 4 XDR patterns corresponding to the raw commercial material (blue) and the printed support (red)

XRD analysis indicates that the main phase was $CaSO_4 \cdot ½H_2O$. However, dehydrated $CaSO_4$ was present as well. Therefore, TGA was performed in order to determine the number of water molecules in the raw material composition.

As mentioned before, previous studies suggest that calcium sulphate hemihydrate ($CaSO_4 \cdot ½H_2O$) is one of the most used materials for 3D printing via binder jetting[11] because when the commercially binder (98% content water) is jetted, gypsum paste ($CaSO_4 \cdot 2H_2O$) forms according to *Equation 3. 1*,[12] transforming the powder into a paste.

$$CaSO_4 \cdot \frac{1}{2}H_2O + \frac{3}{2}H_2O \rightarrow CaSO_4 \cdot 2\,H_2O \qquad \textit{Equation 3. 1}$$

TGA of the commercial powder was carried out under flowing air atmosphere (50ml/min) in the 25 - 1000°C temperature range using ramp rates of 10°C/min, *Figure 3. 5*, displays the TGA results.

Simplifying the data expressed in percentage of mass fraction, there are three main processes of mass loss at 150ºC, 300ºC and 500ºC. Comparing with the initial mass, it is possible to estimate the mass loss at each step, using the *Equation 3. 2*.

$$\%_{H_2O\ theoretical} = \frac{MW_{H_2O}}{MW_{\mathrm{CaSO4 \cdot ½H2O}}} \times 100 \qquad \textit{Equation 3. 2}$$

The molar weight of the suggested compound ($CaSO_4 \cdot ½H_2O$) is 145.25 g/mol, where 9.0 g/mol corresponds to half a water molecule. Replacing these values in *Equation 3. 2*, **this corresponds to 6.21%**. After the first step, at 150˚C, there is 94% of compound. This means **6.38% of mass loss, which is fairly close to half a water molecule in the compound**. Consequently, the first step may be ascribed to dehydration.

The effects of the thermal treatments on $CaSO_4$ dehydration have been reported by Zhou *et al.*[11], which happens in the first step regarding, regarding the DSC data with an endothermic decomposition at 150°C. These authors suggested that the sample suffers several transformations into other phases. The $CaSO_4$-system is characterized by five solid phases, four of them present at room temperature: calcium sulphate dihydrate (gypsum), calcium sulphate hemihydrate, soluble calcium sulphate anhydrite III and insoluble calcium sulphate anhydrite II. The fifth phase is calcium sulphate anhydrite I, which is only chemically stable at temperatures above 1180°C.

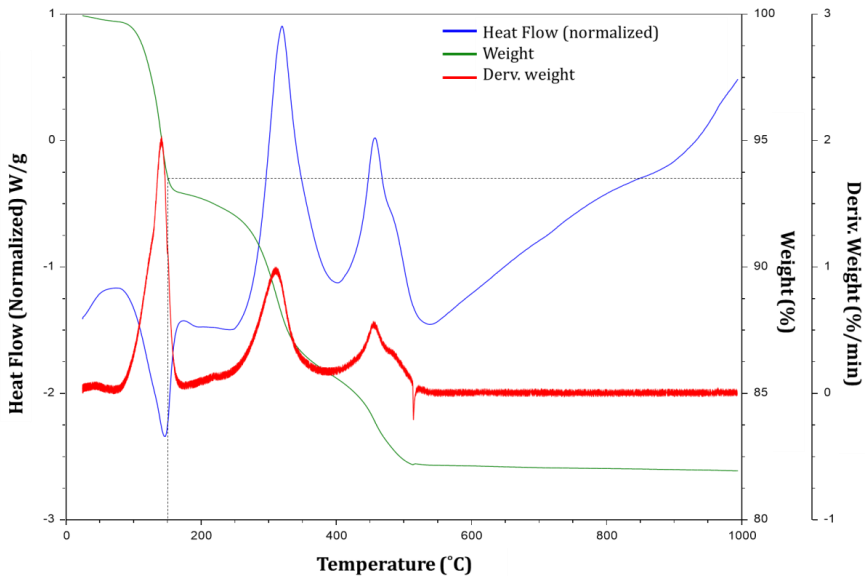

Figure 3. 5 TGA of the commercial powder (VisiJet PXL Core, from S.A.T.ÉLITE)

According to reported results in literature and the XRD analysis performed in this work, *Figure 3. 6 and 3. 7*, the second step at 300ºC, is associated to an exothermic decomposition due to γ-$CaSO_4$ transformation to other anhydrous species, including calcium hydroxide (CaOH) (12% mass loss). And the third step at 500ºC, that is associated to an exothermic decomposition due too according with DSC data, could be related with the decomposition of the organics present in the 3D commercial powder (18% mass loss).

Therefore these results suggest that the commercial powder (VisiJet PXL Core, from S.A.T.ÉLITE.) used as raw material for BJ printed is $CaSO_4 \cdot ½H_2O$.

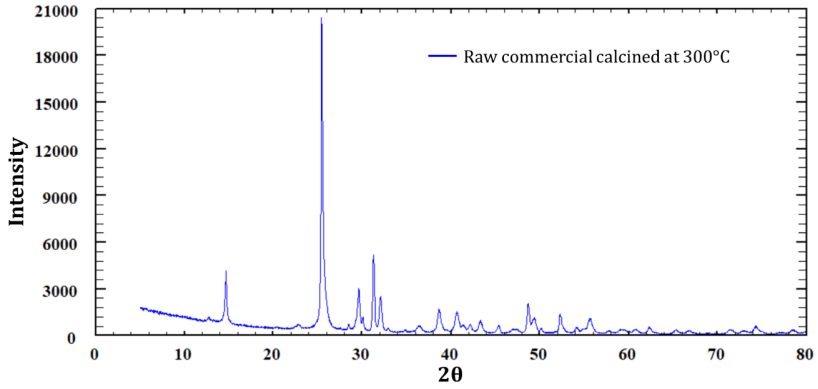

Figure 3. 6 XDR patterns corresponding to the raw commercial material calcined at 300°C

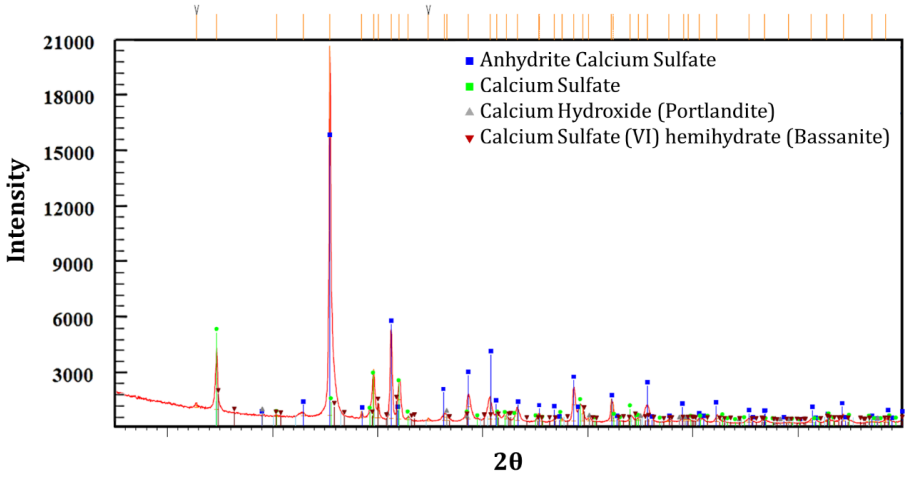

Figure 3. 7 XDR patterns corresponding identified peaks of the raw commercial material calcined at 300°C

3.1.2 Printing process

As the printer is commercial, the parameters for the process are pre-defined. It has 300×450 dpi resolution and layer thickness of 0.1 mm, which is the height of the powder layer deposited when the platform goes down.

As the process is automatic, the construction area is completely filled with the starting powder. Therefore, the *stl* files will be placed maximizing the space in the *xy* plane, in order to save material. If more space was necessary, the digital designs would be stacked creating different layers with the designs on the *z* axis. As shown in *Figure 3. 8,* there are three lines of files in the *xy* plane, and only one layer of file in the *zx* plane. The green area corresponds to free space to add more *stl* files if necessary.

Before starting the printing process, the software provides the user with a report containing information about it, *Figure 3. 9*. In this work, four monoliths will be used in the catalytic reaction test. To obtain these four structures, the process takes 18 minutes using 6.9 mL of binder. In addition, it gives information about the area and volume of one design: 691.22 mm^2. From this info, one may calculate **the total active area exposed during the photo-catalytic test, i.e. 2764.88 mm^2**.

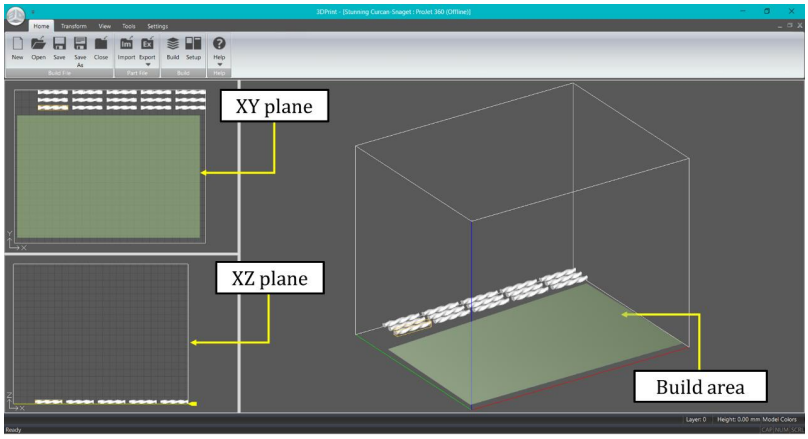

Figure 3. 8 Printer software with stl file uploaded

Doing the simulation for one hundred monoliths, the process would take 30 minutes, and it would use 24.7 mL of binder. This confirms that **it is worthwhile printing as many objects as possible in the same plane of the building platform**.

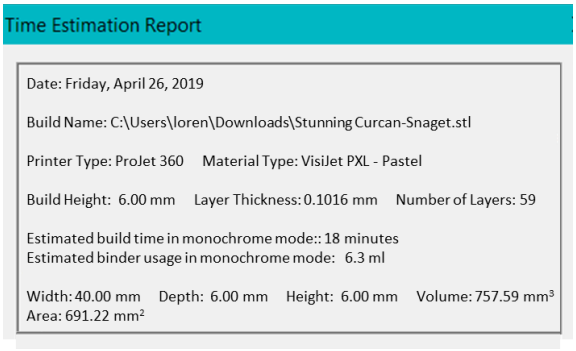

Figure 3. 9 Printing report for one piece

Figure 3. 10 shows the aspect of the spirals after the printing process. After a quick glance, it can be appreciated that the green body exhibits superficial porosity, which must be considered in order to support the catalyst on the surface and inside the pores.

However, this work is focused in the use of these architectures in aqueous solution for wastewater cleaning applications. Hence, it is crucial to carry out some previous treatments (i) for achieving a good mechanical stability into aqueous solutions (ii) and for functionalization with the photo-catalyst active material.

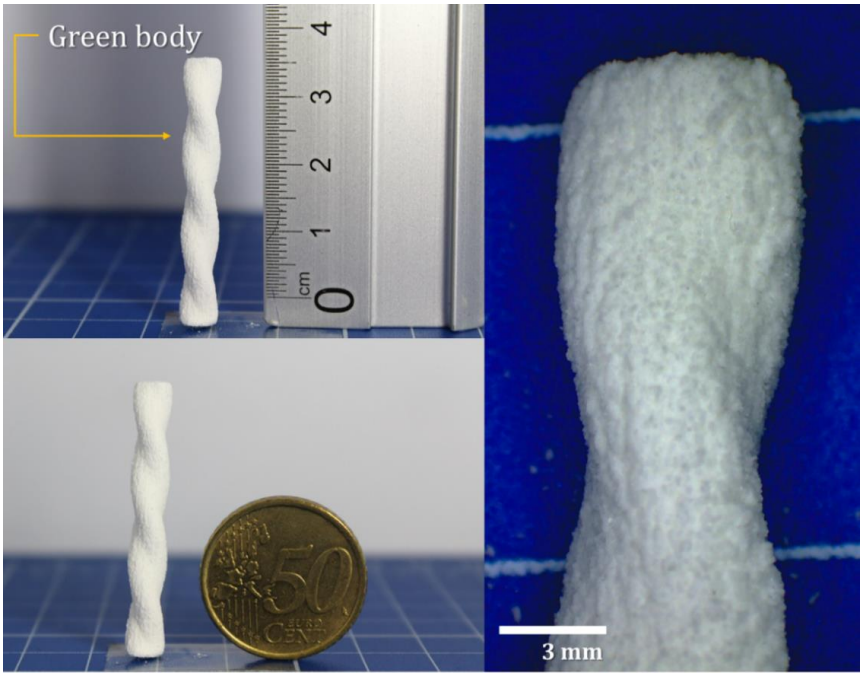

Figure 3. 10 3D printed support of $CaSO_4$ manufactured via BJ

3.1.3 Functionalization

Prior to functionalization, the monoliths must exhibit adequate mechanical properties, which were obtained via thermal treatments.

In this work, 3D printed monoliths were fired in a range of temperatures, i.e. 150°C, 250°C and 350°C, for 2 hours to improve the mechanical stability in aqueous solutions needed for the functionalization. *Figure 3. 11*. From that picture, it is clear that the scaffold colour changes as a function of the temperature, which highlights the presence of organic components in the green body coming from the binder. After 350°C the black colour of the sample suggests the carbonisation of the organic compound, which implied that sample was very fragile due to the binder decomposition. Thus, the qualitative best results corresponded to monoliths fired at 150°C, as they could be manipulated without mechanical damage.

Figure 3. 12 shows the SEM images of the cross section and the surface of the green body of 3D printed ceramic support. The as-printed support exhibited a large degree of porosity, with particle sizes in the 10 – 40 µm range. In the cross-section images, 4 µm long and 1.5 µm wide orthogonal shapes can be observed. This is due to binder impregnation being more important in the cross

section than in the surface, causing powder particle agglomeration. Even so, cross sectional and superficial images are fairly similar, showing a good homogeneity which means that the 3D printing process does not cause significant changes along the different directions, which is always a concern in additive manufacturing.

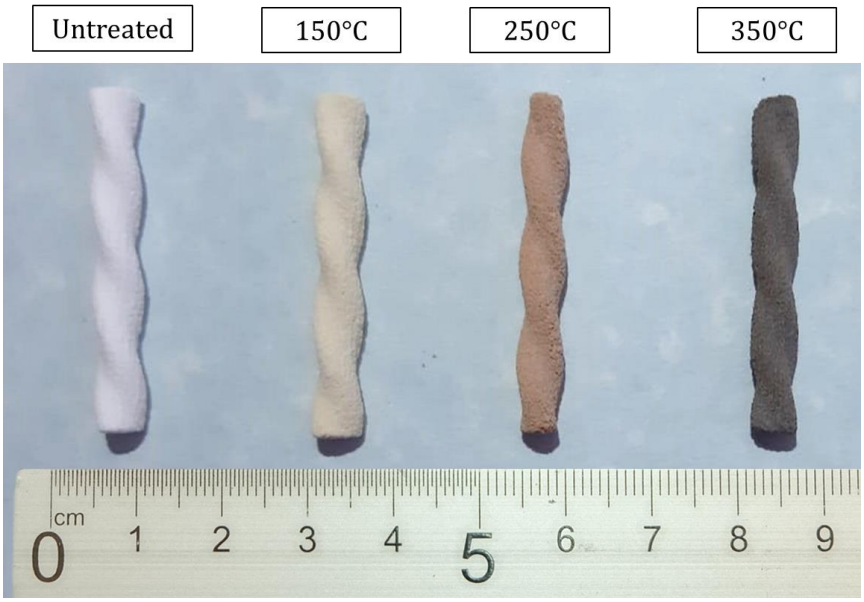

Figure 3. 11 3D printed support fired at different temperatures

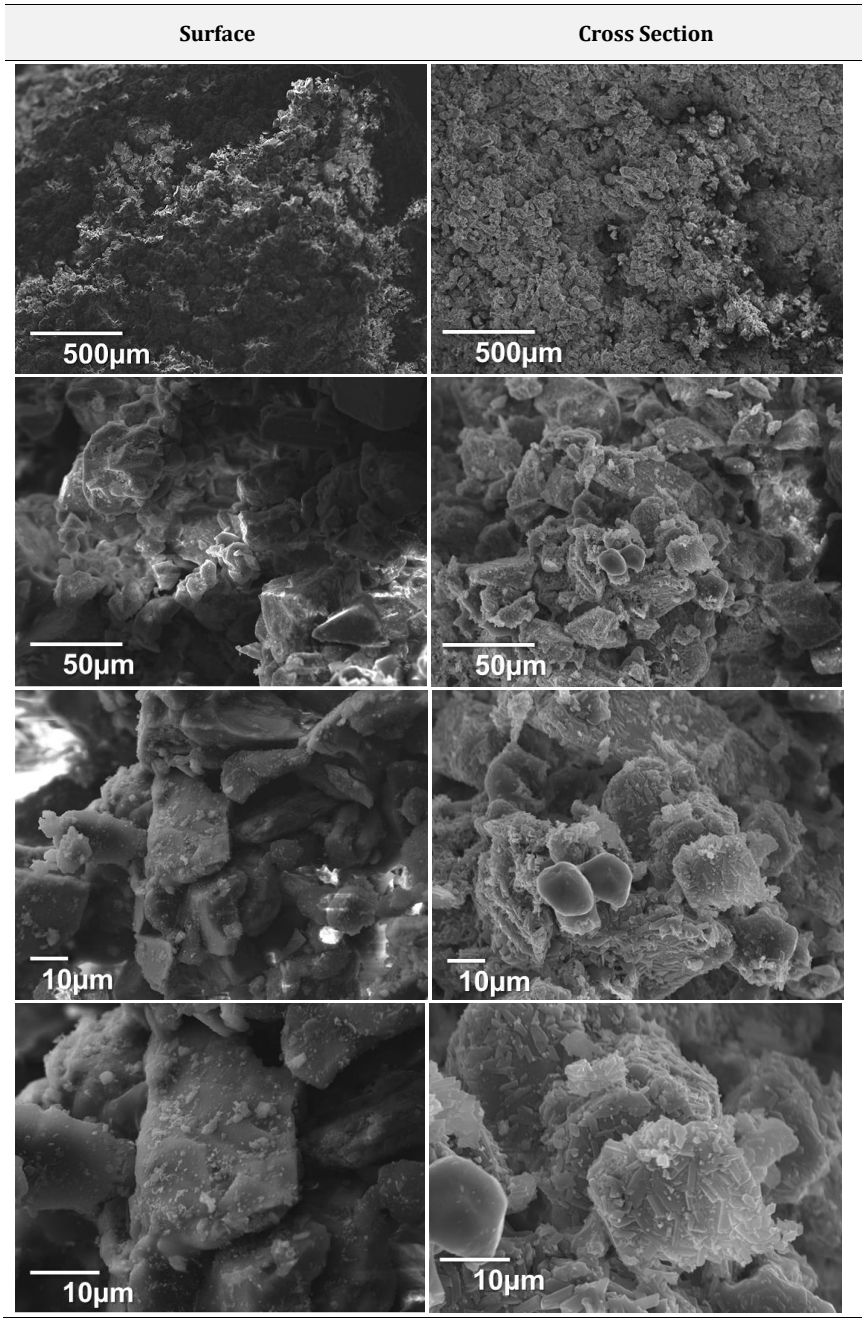

Figure 3. 12 SEM images showing different magnifications of the 3D printed $CaSO4·½H_2O$ support, corresponding to the surface (left) and the cross section (right)

Once the monoliths show certain degree of mechanical resistance, functionalization can be carried out. Several routes were explored. The first route consisted in impregnating the monoliths with TiO_2, because the raw material for the printing process ($CaSO_4$) is not photo-catalytically active, so its only function is as support.

As the impregnation must be done in a TiO_2 solution, the specimens were previously dip coated in Ludox® (colloidal silica, 1.1g) to obtain a better mechanical resistance and preventing the structure deformations when in contact with water. The Ludox® coating was carried out under vacuum and then fired at 300°C for 2h, with heating and cooling ramp rates of 5°C/min. This step is performed twice to ensure high mechanical resistance of the sample during the impregnation with the catalyst solution.[13] After that, the structures were dip coated under vacuum too, with a suspension of TiO_2 (Degussa P25) in a Ludox® and Triton X-100 (2wt. %) mixture, then dried at 70°C for 1h and finally fired at 150°C for 2h. However, following this procedure the porosity of structures decreased and the introduction of the catalyst was somewhat impeded. The final result was a superficial non-homogeneous layer of TiO_2, *Figure 3. 13*. Consequently, other options were tested maintaining the thermal process applied in the beginning.

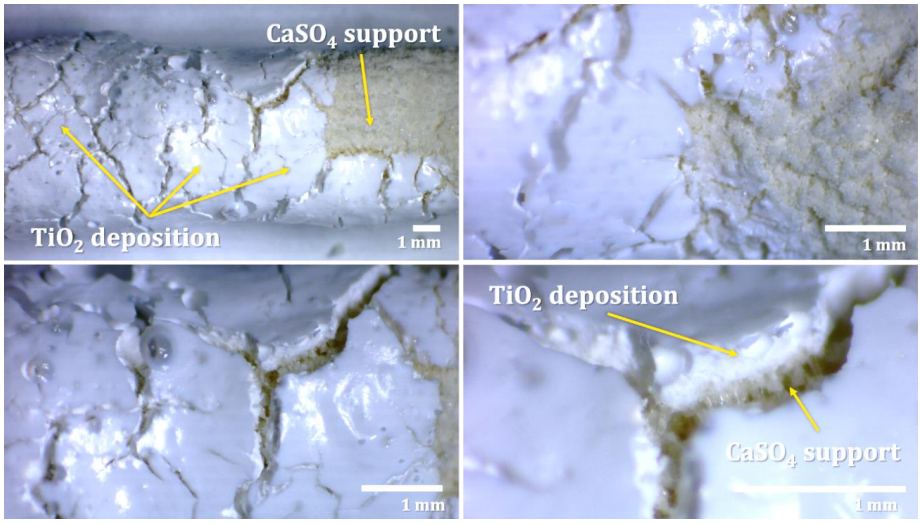

Figure 3. 13 Functionalised 3D printed ceramic support via Ludox-TiO_2 dip-coating under vacuum

The second strategy was based on the same 2-step process, but with TiO_2 suspended in an ethanolic solution to avoid the final treatment at 150°C. After dip-coating, the assembly was dried at 80°C for 2 h, though the result was negative too, *Figure 3. 14*.

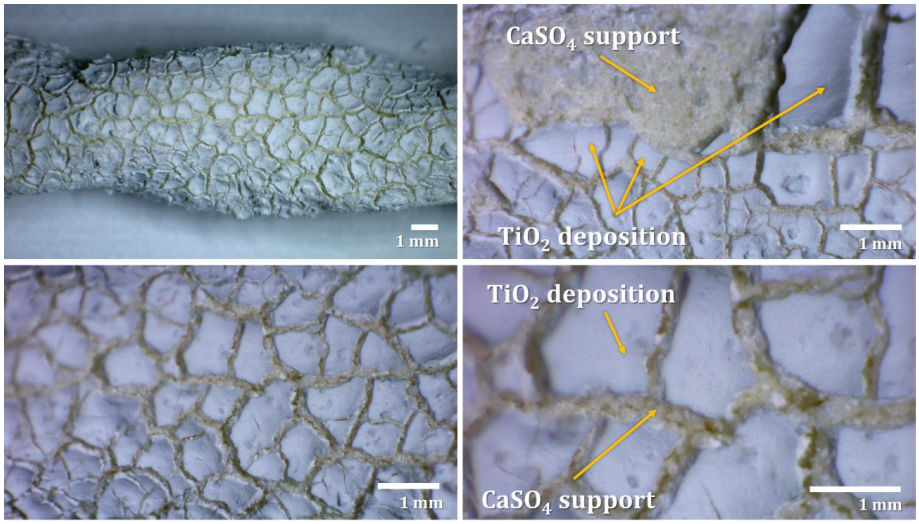

Figure 3. 14 Functionalised 3D printed ceramic support via dip-coating in TiO_2 ethanolic suspension under vacuum

As an alternative, TiO_2 was deposited via spray coating and further thermal treatment at 150°C for 2h, however the result was pretty similar to *Figure 3. 13*.

Therefore, the strategy was completely changed. As adding the TiO_2 particles was not effective, we evaluated the *in-situ* generation of the catalyst particles while preserving the porosity of the 3D ceramic green support.

In order to achieve this goal, the porosity of the support was measured via porosimetry, where the sample is submerged into mercury and pressure is applied in order to introduce it into the pores. According to the pressure required to Hg getting inside the pores, the pore size distribution can be determined. Regarding this experiment, the graphs shown in *Figure 3.15* were obtained. *Figure 3. 15 (a)* shows as at 8.91 psia of mercury filling pressure there is a peak associated with a median pore diameter volume of 25 µm, *Figure 3. 15 (b)*. Therefore, it may be concluded that 3D printed support possesses macro-porosity, which is appropriate to synthesise TiO_2 *in situ* via $TiCl_4$ hydrolysis.

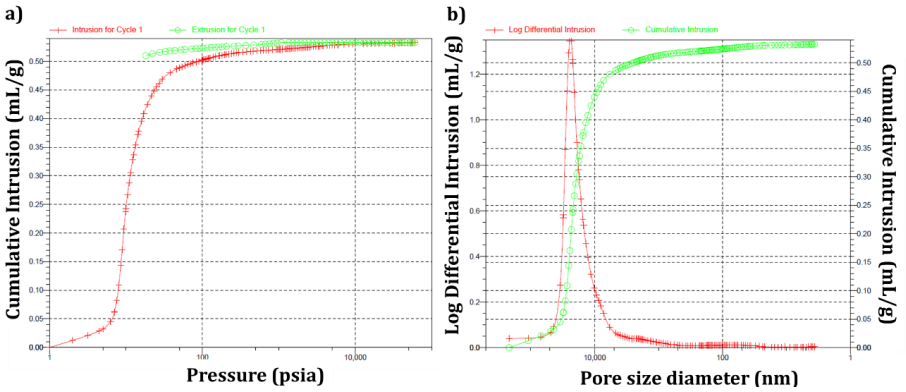

Figure 3. 15 Porosimetry tests performed in the 3D printed support. (a) Hg cumulative intrusion according to the pressure and (b) differential intrusion according to the pore size diameter

This was achieved by using $TiCl_4$ as starting material that upon hydrolysis allows the production of TiO_2 according to *Equation 3. 3*.

$$TiCl_4 + 2\,H_2O \rightarrow TiO_2 + 4\,HCl \qquad \textit{Equation 3. 3}$$

The 3D printed spirals were immersed in $TiCl_4$ under vacuum to ensure impregnation of all the pores of the support. When bubbling stopped, the excess titanium tetrachloride was removed, and the structures were covered in distilled water to promote the hydrolysis reaction. After that, samples were extracted from water and fired at 100°C for 2h and later at 350°C for further 2h, in order to ensure good adherence between the catalyst and the support *Figure 3. 16*. In addition, by using this process smaller particle size of TiO_2 were produced compared to the impregnation-based strategies described before. This is a relevant result as the smaller particle size and their integration into the porous support will lead to larger active surfaces.

Surprisingly, this process provided greater mechanical stability to the spirals. In order to ensure that the compound synthesised was TiO_2, EDS analyses were performed in particles scraped-off the support. *Figure 3. 17* shows the results, *Figure 3. 17 (a).* Particle size could be measured from the SEM images *Figure 3. 17 (a)* that show the presence of the 100-300 nm TiO_2 particles synthesised via $TiCl_4$ hydrolysis. The EDS analyses confirmed that the composition of these particles is TiO_2. *Figure 3. 17 (b)* shows particles of commercial TiO_2 employed in the other strategies with fairly similar diameters in the 200-240 nm range. Thus, it can be concluded that this route of synthesise was optimum for the functionalisation of the support.

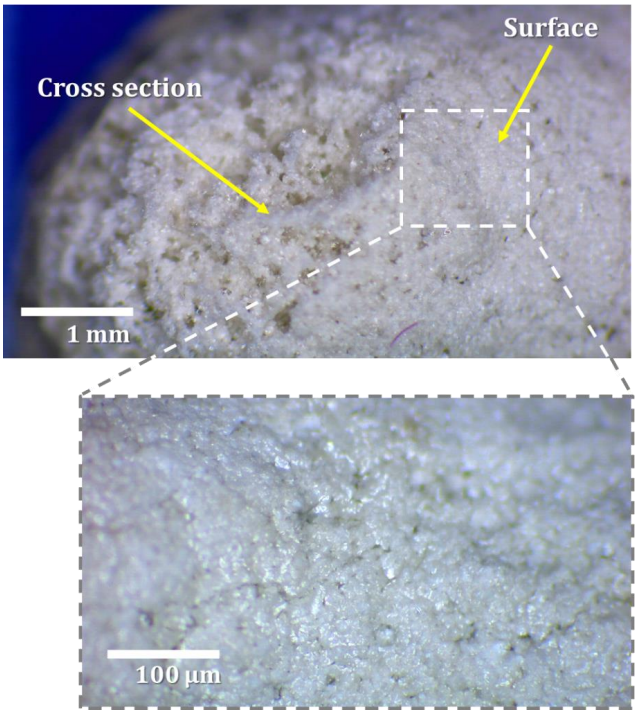

Figure 3. 16 Functionalised 3D printed ceramic support with TiO_2 synthesised in situ

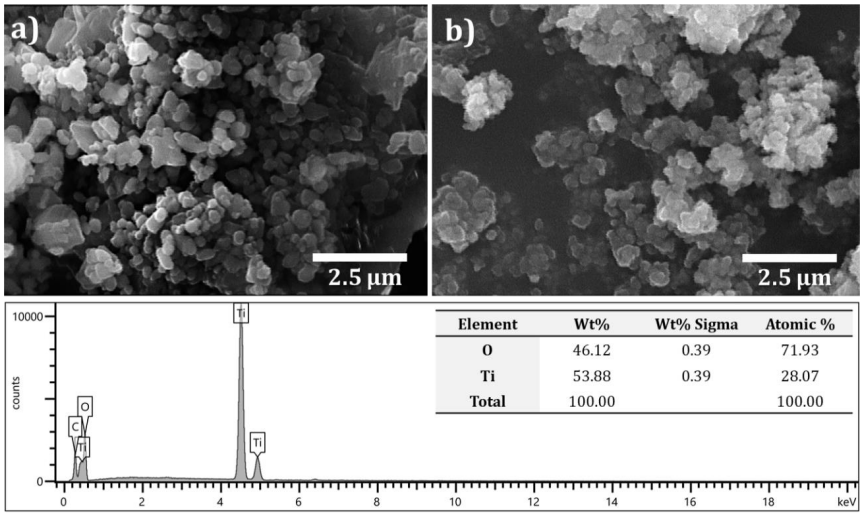

Element	Wt%	Wt% Sigma	Atomic %
O	46.12	0.39	71.93
Ti	53.88	0.39	28.07
Total	100.00		100.00

Figure 3. 17 (a) SEM images of TiO_2 particles synthesised via $TiCl_4$ hydrolysis, (b) SEM images of the commercial TiO_2 (c) EDS results for the TiO_2 particles obtained via $TiCl_4$ hydrolysis

To sum up, these results suggest that the **strategy based on $TiCl_4$ hydrolysis for the *in-situ* generation of TiO_2 showing good adherence to the BJ 3D printed ceramic porous support exhibits adequate mechanical strength to the assembly** that will be used for photo-catalytic experiments.

At this point, the microstructure of TiO_2-functionalised ceramic support was studied via SEM too. *Figure 3. 18* shows smoother surface in the TiO_2 functionalised support as a consequence of the TiO_2 layer formation upon dipping and further thermal treatment. Nevertheless, at higher magnification one can observe that the layer is not fully homogeneous and, apart from the cracks formed during $TiCl_4$ hydrolysis, the TiO_2 layer exhibits a mosaic-like microstructure, which indicates that a large number of TiO_2 particles agglomerate on top of the 3D printed support.

Surface images, in *Figure 3. 18 (left)* a cracked layer can be seen that could be caused by the fast kinetics of $TiCl_4$ hydrolysis reaction. On the other hand, the microstructure of cross section, *Figure 3. 18 (right),* reveals that porosity remains mostly unchanged and, in some regions, the TiO_2 layer covering the support can be clearly observed, revealing different microstructures. Indeed, the support shows a columnar/fibrous structure, while the 1µmTiO_2 coating exhibits particulate texture.

Thus, it can be concluded that this process provided greater mechanical stability to the spirals since titanium oxide was integrated into the ceramic porous support.

Nevertheless, this process may be optimised and, in future work, experimental conditions such as dipping time into titanium tetrachloride or distilled water and firing temperature and time could be screened.

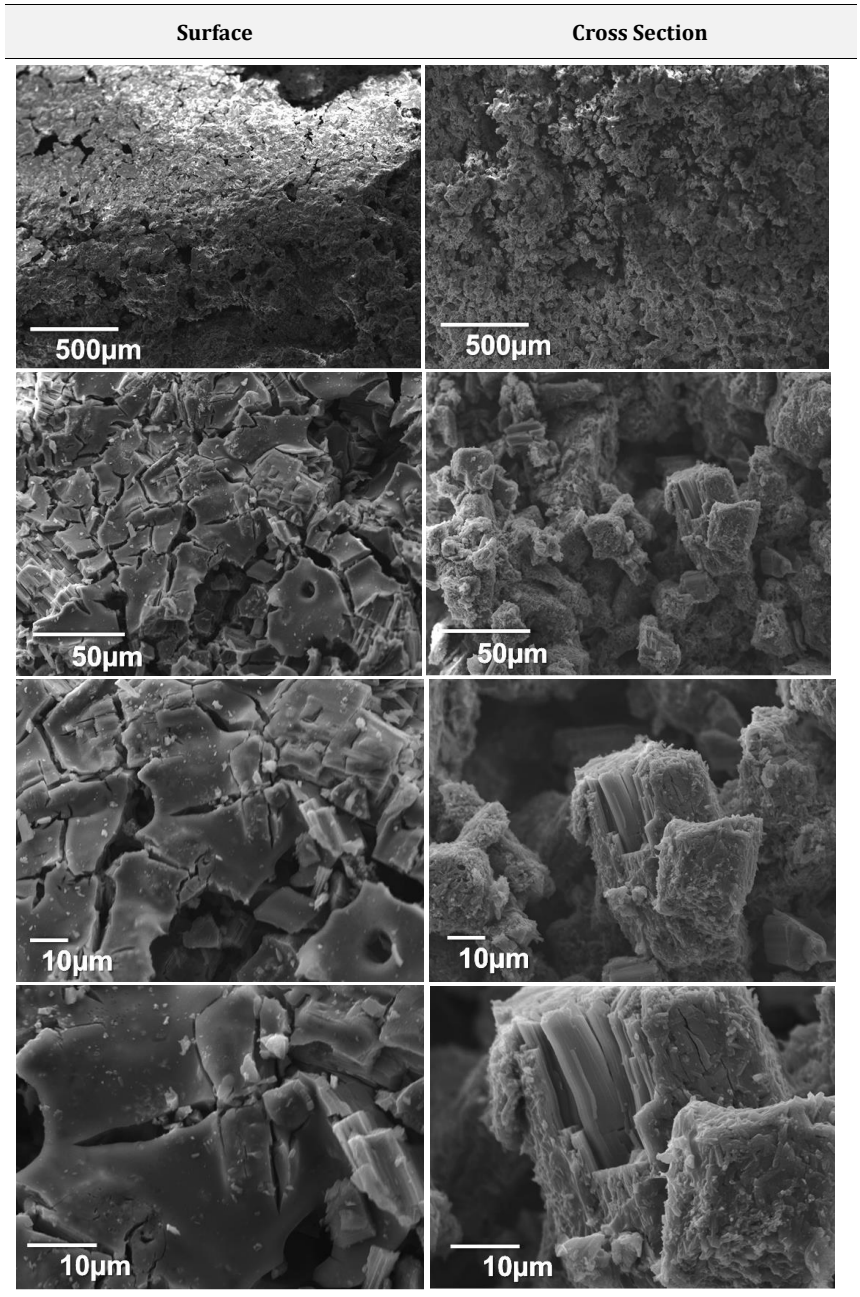

Figure 3. 18 SEM images of TiO_2-activated printed supports. Images corresponding to the surface (left) and the cross section (right)

EDS was performed on the surface areas of both the green body support and the functionalised support. The results for the superficial area of the green body support and of the functionalised support are shown in *Table 3. 1*.

Table 3. 1 Percentages of elements measured via EDS on the surface of the green body and functionalised body via $TiCl_4$ hydrolysis

Element	Green body	Functionalised body
Calcium	52 %	25 %
Sulphur	48 %	26 %
Titanium	0 %	49 %

These results can be graphically observed in the mapping plot in *Figure 3. 19*, where titanium is the blue area which represents most of the monolith surface. This suggests that the TiO_2 functionalisation via $TiCl_4$ hydrolysis was successful as most of the monolith surface is covered with a rather homogeneous layer that shows good adherence and the pre-existing porosity does not collapse.

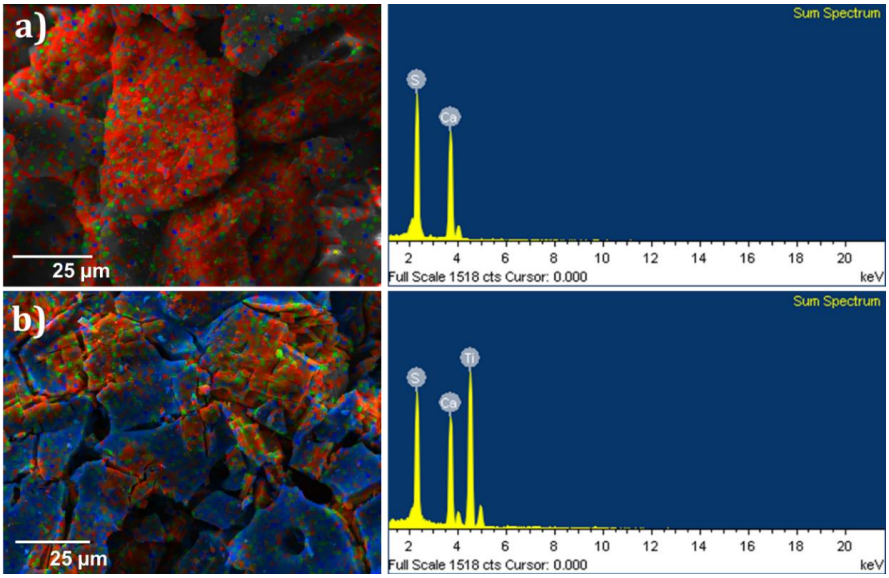

Figure 3. 19 SEM mapping and EDS spectra of (a) printed green body support and (b) functionalised support. In the SEM coloured images, three elements are represented: calcium (red), sulphur (green) and titanium (blue)

Finally, the TiO_2-functionalised support was analysed by XRD as well. As can be observed in *Figure 3. 20* a new phase is detected compared with printed support and confirmed with Qualx

software, *Figure 3. 21*, shows the pattern matching of this specimen for $CaSO_4$, $CaSO_4 \cdot ½H_2O$ and 20-30wt. % TiO_2.

Thus, it can be concluded that the **activation procedure carried out via $TiCl_4$ hydrolysis to obtain TiO_2 was successfully achieved, allowing the deposition of 20 – 30wt. % of TiO_2.**

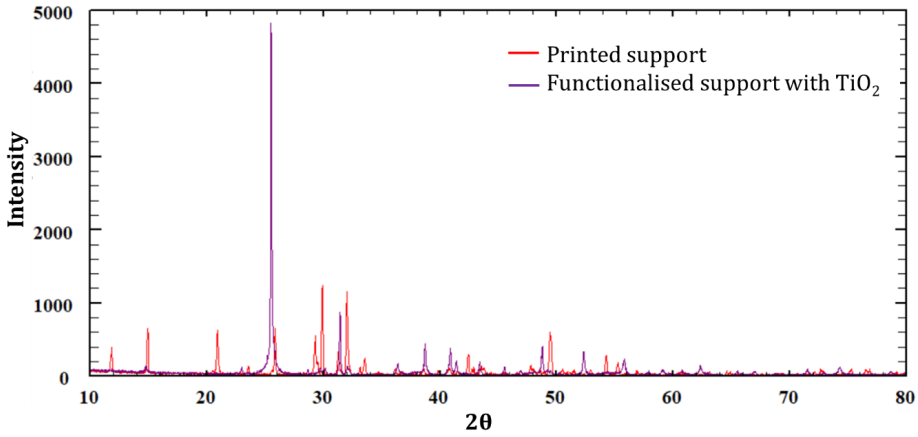

Figure 3. 20 XRD patterns of the printed (red) and functionalised supports (purple)

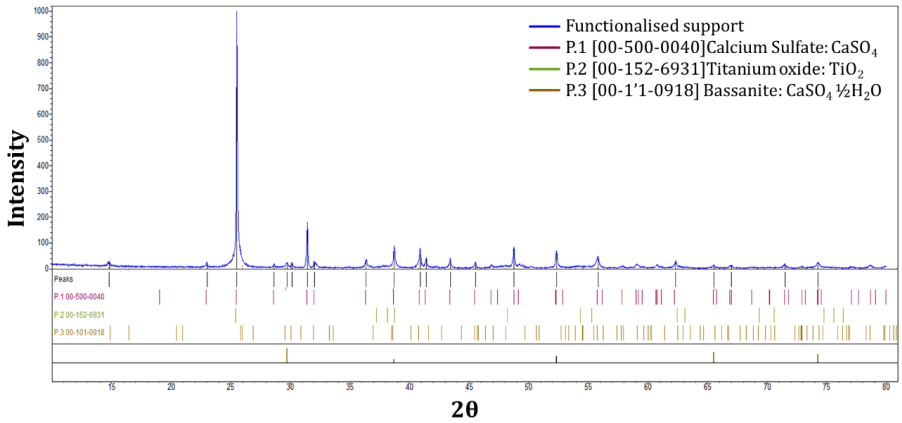

Figure 3. 21 XRD patterns for functionalised support with TiO_2 showing the pattern matching with TiO_2, $CaSO_4 \cdot ½H_2O$ and $CaSO_4$

3.3 Photo-catalyst performance

3,7-Bis(Dimethylamine)pheno-5-thiazinium chloride, commonly known as methylene blue (Panreac, C.I. 52015, $C_{16}H_{18}C|N_3S{\cdot}x\ H_2O$) was the model molecule as emergent contaminant, *Figure 3. 22*, to measure the photocatalytic activity of the printed helicoidal monoliths.

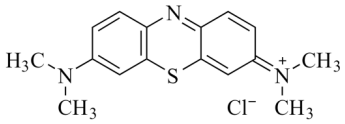

Figure 3. 22 Methylene blue (MB) molecule

The photodegradation of the MB tests were carried out in a system, described in *Chapter 2, Section 2.3.2,* where the catalyst is in a fix-bed reactor and the solution goes through it. In addition, photodegradation is done due to the reactor is irradiated with artificial UV light.

At different times, a fraction of the solution was taken, and the absorbance was measured at 664 nm using a UV/Vis spectrophotometer (Cary 50, 530-710nm). Thus, via the Lambert-Beer law it is possible to know the concentration of each fraction of solution. Finally, this concentration is expressed as percentage of contaminant conversion, using *Equation 3. 4.*

$$Conversion\ (\%) = \frac{C_0 - C_t}{C_0} * 100 \qquad \textit{Equation 3.4}$$

Degradation of the methylene blue was reported in literature by *Lached et al.*[14] who showed mineralization by the photocatalyst action, *Equation 3. 5*.

$$C_{16}H_{18}N_3S^+ + \frac{51}{2}O_2 \rightarrow 16\ CO_2 + 3\ NO_3{}^- + SO_4{}^{2-} + 6H^+ + 6H_2O \qquad \textit{Equation 3. 5}$$

First of all, the calibration curve of MB must be done, where the absorbances of the different concentration solutions can be obtained, *Figure 3. 23*. Afterwards, the A_{max} (664 nm) vs concentration is represented. In this calibration curve, the concentrations were in the 0.8 and 13.1 ppm range. All samples were run using distilled water as solvent and they were measured at room temperature, 25°C.

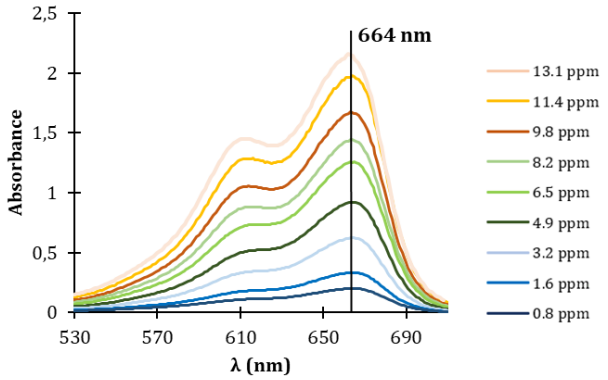

Figure 3. 23 Calibration curve absorbances of the MB solutions

Regarding the adsorption on the catalyst active surface, the tests were carried out with the catalyst inside the reactor, but with no irradiation. Therefore, four 3D printed helicoidal active supports were into the packed bed reactor, through which passed a solution of methylene blue, keeping the lamp switched off to operate with no UV-Vis light. Consequently, the adsorbed amount on the surface catalyst can be measured as a function of time, rendering useful values to compare with the surface-active area of the 3D printed supports.

While the adsorption process happens, there is no photo-degradation of pollutant molecules, hence there will be a saturation point when pollutant cannot be adsorbed anymore. In the present case, this is achieved at 22% of MB after 0.5 – 1.5 h, *Figure 3. 24*.

These results are fairly similar to those obtained for FDM 3D-printed catalysts (see *Chapter 4*). Despite both structures were printed using different 3D printing techniques, the adsorption values in both cases are the same, *Figure 4. 42*, which may be considered as an advantage because when fabricating catalysts, one potential strategy would be to print a support/backbone of a cheap material and then functionalise it with the active material, instead of printing directly the catalyst. Considering that in both situations the catalyst is TiO_2, this result implies that the monoliths exhibit the same active surface and therefore the adsorbed contaminant is the same. This is further evidence of the geometry being a key parameter on these processes.

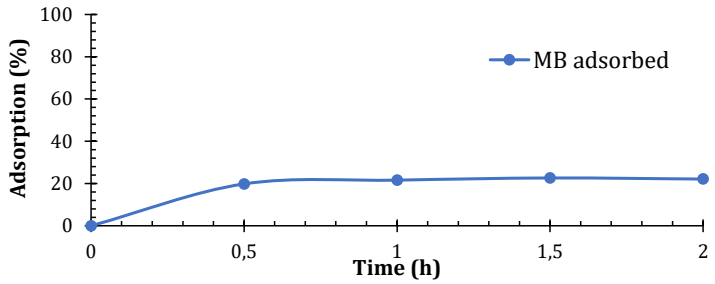

Figure 3. 24 Adsorption test of MB using monolithic structures obtained via BJ technique

After defining the calibration curve, a photolysis test was done to compare the percentage of MB converted when the catalyst is in the solution. After that, a degradation test was carried out using four 3D printed ceramic supports, which were functionalised via titanium tetrachloride as described before. The data resulted are collected in *Table 3. 2* and represented in *Figure 3. 25*.

Table 3. 2 MB photo-degradation data, using activated 3D printed ceramic support

Time (h)	Absorbance	[C] ppm	Conversion (%)
0	2,615	16,4	0
0,5	2,326	14,6	10,8
1	2,155	13,6	17,1
1,5	2,090	13,2	19,5
2	2,030	12,8	21,7
2,5	1,906	12,1	26,4
3	1,797	11,4	30,4
3,5	1,691	10,8	34,3
4,22	1,619	10,3	37,0
4,73	1,543	9,9	39,8
5	1,419	9,1	44,5
5,5	1,386	8,9	45,7
6	1,264	8,2	50,2
6,5	1,180	7,7	53,3
7	1,109	7,2	56,0
24,53	0,138	1,3	92,0
70	0,059	0,8	94,9

It must be highlighted that more than 50% of contaminant is photo-converted after 6 h, reaching almost complete conversion photo-conversion (92%) after 24 h, *Figure 3. 25*. Comparing these results with those obtained for FDM 3D-printed catalysts Chapter 4, it can be concluded that most of the contaminant is converted during the first six hours.

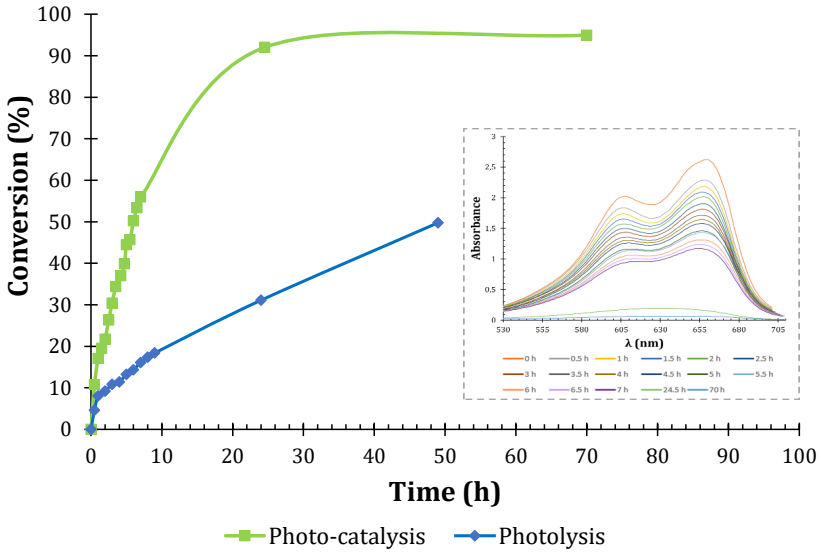

Figure 3. 25 MB Photo-conversion using functionalised 3D printed ceramic support and MB photolysis

Regarding the kinetics of the MB conversion compared with the photolysis effect, they were fitted by a pseudo-second-order kinetic model, obtaining $k_{conversion}$=1.71×10^{-4} mol^{-1}·L·min^{-1} and $k_{photolysis}$=2.34×10^{-5} mol^{-1}·L·min^{-1}, *Figure 3. 26*. Thus, it can be concluded that the photolysis effect is irrelevant compared with photoconversion of MB carried out by the functionalised support obtained via BJ 3D printing technique.

Regarding the photolysis effect, a comparison of the two results reveals an increase in the conversion upon catalyst introduction, hence, to remove emergent contaminants it is necessary the use of catalysts as the photolysis effect (natural removal) is not enough.

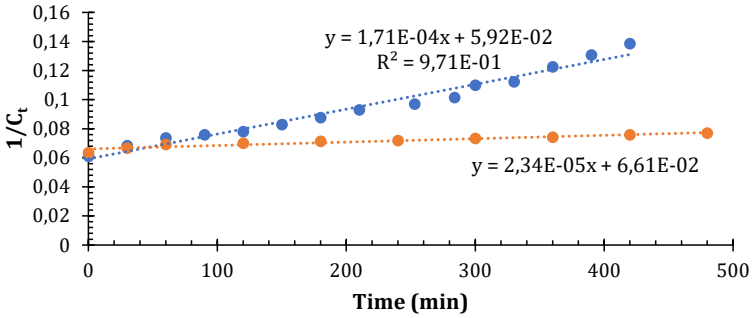

Figure 3. 26 Pseudo-second-order kinetics for the photodegradation of MB onto 3D printed supports functionalised with TiO_2 (circular blue line) and photolysis effect (squared orange line).

Finally, MB photo-degradation and adsorption results were combined in the same graph, *Figure 3. 27,* revealing that the photo-degradation process drives complete conversion of the contaminant when compared to the adsorption process, which is a typical technique used for removing organic pollutants from wastewater.[15]

Therefore, the **photo-degradation process is a better choice for contaminants removal and can be implemented in devices that work as water filters, thanks to the chemical reactions based on heterogeneous catalysis. Moreover, these devices could be produced at lower cost than the state-of-the-art via the use of BJ 3D printing technique.** However further data collection is required to determine exactly how post-thermal treatment affects to sample constitution to be reused.

Nowadays, MB is typically removed via adsorbent filters (filter paper), because they may retain emergent contaminants in a range of concentrations. An example of the state of the art is the commercial HMA-79 filter 0,32$ approximately (~0,27€). The costs of the 3D catalysts manufactured in this work would cost around 0.10€,[16]. Nevertheless, there are some issues that must be addressed as the TiO_2 loading and the microstructure of the $CaSO_4$ support may change upon operation in water.

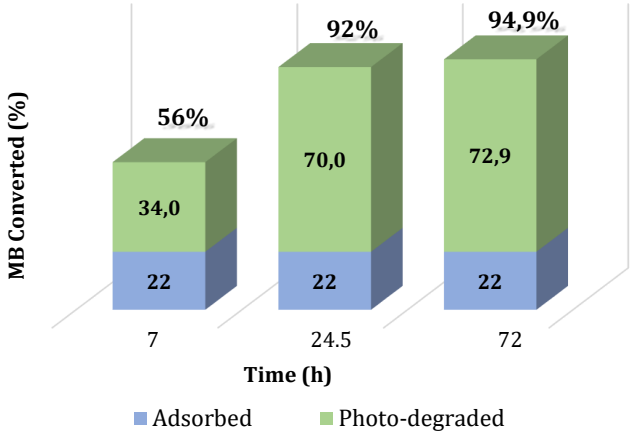

Figure 3. 27 MB adsorption and photo-degradation percentages

To sum up, on one hand, the **process developed for the functionalization of 3D printed ceramic support via $TiCl_4$ hydrolysis is completely viable to synthetize TiO_2 on the 3D printed support via BJ.**

On the other hand, the **activated supports photo-degrade completely to methylene blue solution after 24 h,** being an effective process to be employed on a large scale.

For future work, it would be interesting to study other catalyst designs involving the use of less material, i.e. roller or curly geometries. In addition, these tests can be made with real solar light in order to establish the real parameters than must be taken into account to apply these devices in industrial wastewater treatments.

3.4 References

[1] Méndez-Ramos, J.; Acosta-Mora, P.; Ruiz-Morales, J. C.; Hernández, T.; Borges, M. E.; Esparza, P. Turning into the Blue: Materials for Enhancing TiO_2 Photocatalysis by up-Conversion Photonics. RSC Adv. (2013), 3 (45), 23028–23034, doi:10.1039/c3ra44342f.

[2] Borges, M. E.; García, D. M.; Hernández, T.; Ruiz-Morales, J. C.; Esparza, P. Supported Photocatalyst for Removal of Emerging Contaminants from Wastewater in a Continuous Packed-Bed Photoreactor Configuration. Catalysts (2015), 5 (1), 77–87, doi:10.3390/catal5010077.

[3] Borges, M. E.; Sierra, M.; Méndez-Ramos, J.; Acosta-Mora, P.; Ruiz-Morales, J. C.; Esparza, P. Solar Degradation of Contaminants in Water: TiO_2 Solar Photocatalysis Assisted by up-Conversion Luminescent Materials. Sol. Energy Mater. Sol. Cells (2016), 155, 194–201, doi:10.1016/j.solmat.2016.06.010.

[4] Robert L. Mott. Mecanica de Fluidos, 6th ed.; Pablo Miguel Guerrera Rosas, Bernardino Gutiérrez Hernández, E. T. H., Ed.; México, (2006), ISBN: 970-26-0805-8.

[5] Tinkercad https://www.tinkercad.com/#/ (accessed Apr 19, 2020).

[6] Lv, X.; Ye, F.; Cheng, L.; Fan, S.; Liu, Y. Binder Jetting of Ceramics: Powders, Binders, Printing Parameters, Equipment, and Post-Treatment. (2019) doi:10.1016/j.ceramint.2019.04.012.

[7] Ziaee, M.; Crane, N. B. Binder Jetting: A Review of Process, Materials, and Methods. (2019) doi:10.1016/j.addma.2019.05.031.

[8] Du, W.; Ren, X.; Ma, C.; Pei, Z. Binder Jetting Additive Manufacturing of Ceramics: A Literature Review. In ASME International Mechanical Engineering Congress and Exposition, Proceedings (IMECE); American Society of Mechanical Engineers (ASME), (2017); Vol. 14 doi:10.1115/IMECE2017-70344.

[9] Paranthaman, M. P.; Shafer, C. S.; Elliott, A. M.; Siddel, D. H.; McGuire, M. A.; Springfield, R. M.; Martin, J.; Fredette, R.; Ormerod, J. Binder Jetting: A Novel NdFeB Bonded Magnet Fabrication Process. JOM (2016), 68 (7), 1978–1982, doi:10.1007/s11837-016-1883-4.

[10] Levy, A.; Miriyev, A.; Elliott, A.; Babu, S. S.; Frage, N. Additive Manufacturing of Complex-Shaped Graded TiC/Steel Composites. Mater. Des. (2017), 118, 198–203, doi:10.1016/j.matdes.2017.01.024.

[11] Zhou, Z.; Mitchell, C. A.; Buchanan, F. J.; Dunne, N. J. Effects of Heat Treatment on the Mechanical and Degradation Properties of 3D-Printed Calcium-Sulphate-Based Scaffolds. (2013), 1-10, doi:10.5402/2013/750720.

[12] Utela, B.; Storti, D.; Anderson, R.; Ganter, M. A Review of Process Development Steps for New Material Systems in Three Dimensional Printing (3DP). J. Manuf. Process. (2009), 10 (2), 96–104, doi:10.1016/j.jmapro.2009.03.002.

[13] Hernández-Afonso, L.; Fernández-González, R.; Esparza, P.; Borges, M. E.; González, S. Dí.; Canales-Vázquez, J.; Ruiz-Morales, J. C. Ceramic-Based 3D Printed Supports for Photocatalytic Treatment of Wastewater. J. Chem. (2017), 9, doi:10.1155/2017/7602985.

[14] Lachheb, H.; Puzenat, E.; Houas, A.; Ksibi, M.; Elaloui, E.; Guillard, C.; Herrmann, J. M. Photocatalytic Degradation of Various Types of Dyes (Alizarin S, Crocein Orange G, Methyl Red, Congo Red, Methylene Blue) in Water by UV-Irradiated Titania. Appl. Catal. B Environ. (2002), 39 (1), 75–90, doi:10.1016/S0926-3373(02)00078-4.

[15] Nageeb, M. Adsorption Technique for the Removal of Organic Pollutants from Water and Wastewater. In Organic Pollutants: Monitoring, Risk and Treatment; Rashed, M. N., Ed.; InTech: Rijeka, Croatia, (2013) doi:10.5772/54048.

[16] La ULL crea nuevas microestructuras impresas en 3D para purificar aguas contaminadas por medio de la energía del sol - ULL - Noticias https://www.ull.es/portal/noticias/2017/microestructuras-3d-purificar-aguas/ (accessed Jul 27, 2020).

Chapter-4:

3D PRINTING FDM FOR CATALYST

4.1 Device Architecture

As presented in *Chapters 1 and 2*, the key parameter of 3D printing is the capability to produce complex structures that cannot be produced by conventional manufacturing processes and provide unfair advantages regarding performance. In this thesis, the design of the catalyst is conditioned by the catalytic reactor, which is a 10 cm long quartz tube with 6 mm of internal diameter.

Also, the design of the catalyst depends on the application. In this work, the photo-catalytic process is used to remove emerging contaminants in water, as mentioned in *Chapter 1, Section 1.2.3*, following the previous work in this field by our research team.[1–3]

As the aqueous solution passes through the sample, the chosen design is a spiral that facilitates the flow of the solution through the fixed-bed photoreactor. The blue-methylene solution is forced through the reactor tube against gravity by using a peristaltic pump.[4] As the flux goes up through the reactor, the helicoidal shape of the catalyst will facilitate the fluid path in the reactor.

As described in *Chapter 3*, the resulting design is a 40 mm long and 6 mm wide spiral, *Figure 4. 1*. The CAD model modifications were carried out using Thinkercad, a free online tool for 3D designing.[5] After completed, the *stl* file was downloaded for printing.

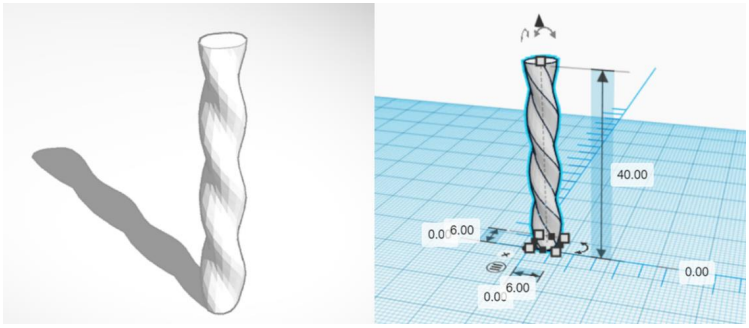

Figure 4. 1 Spiral design of the catalyst and its dimensions expressed in millimetres

4.2 Filament fabrication

The process followed for the fabrication of the filament was described in *Chapter 2, Section 2.1.1.3*.[6] The principal idea is to use this device as a photo-catalyst, therefore the material must be chemically active for this application (TiO_2). However, a key property of the device is the porosity as this will be used as heterogeneous catalyst. Thus, the more porous the structure, the more active sites there will be for the reactions showed in *Chapter 1, Equation 1. 6 – 1. 13, to occur*.

As mentioned in previous chapters, porosity can be induced in ceramics via the introduction of pore formers such as PMMA or C microspheres, flour, starch, etc, in the green bodies. The thermal treatments required to debind and sinter the ceramic object will also cause the degradation of all organic agents including the pore formers, which will leave a certain degree of porosity after those processes. However, the high temperatures required for sintering will cause a reduction in the porosity too. In the present work, glassy carbon microspheres were added as pore formers in different ratios. In addition, a 100% TiO_2 filament was produced (without pore former) in order to evaluate the impact of the porosity upon the photo-catalytic performance.

Table 4. 1 Compositional ratio of the mixture to the solid components

Sample	Inorganic powder wt. %	Ceramic : Pore former
A	70	70 : 30
B	70	80 : 20
C	70	100 : 0
D	75	80 : 20
E	82	80 : 20

In the first tests, when the inorganic solid load was 70 % (Table 4. 1, Samples A, B and C, *Figure 4. 2)*, the extrusion was correct in all cases, due to the relation between the solid and the organic compound was perfect during the filament extrusion (~50-120°C) and the printing process (200-275°C). However, when the total amount of solid loading in the filament raised, there were problems in the extrusion process and the nozzle clogged.

The filament extrusion was correct with sample D, however during the printing process the structure was not well defined, *Figure 4. 2,* due to the lower amount of organic compound related to the temperature used throughout printing. The filament partially loses thermoplastic behaviour and the flowability at the nozzle is reduced, consequently the 3D printing process cannot be completed with high quality standards.

In the last case, sample E, the extrusion was not successful neither. Hence, it could be verified that the solid load is directly related with the temperature used for the extrusion and the printing process, suggesting that this must be optimised in both cases.

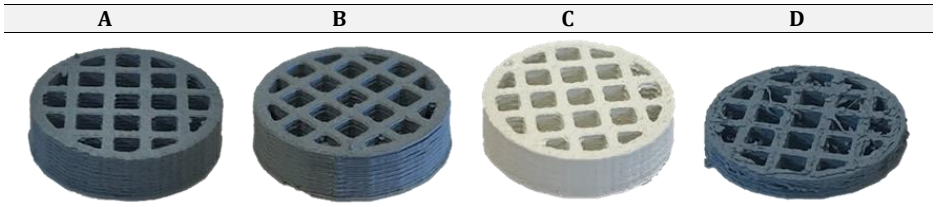

Figure 4. 2 Samples with different solid load: % solid load (TiO_2:C spheres) (A) 70% (70:30); (B) 70% (80:20); (C) 70% (100:0); (D) 75% (80:20)

We decided to work with compositions corresponding to A, B and C for the spiral design fabrication and to study the microstructure and the photo-catalyst activity because the optimization of the printing parameters for FDM processing, particularly the temperature, was beyond the scope of this thesis.

4.3 Printing process

As the filament is homemade and not commercial, the printing parameters must be optimised. Firstly, every time a new filament is used, the feeding parameter must be measured again, as described in *Chapter 2, Section 2.1.1.2*.

Once the filament flow is stabilised, printing temperature, shell thickness, density and bed temperature were defined, *Table 4. 2,* while the nozzle diameter, thickness layer and printing speed were optimized.

Table 4. 2 Fixed printing parameters

Printing parameters	Value
Printing temperature (°C)	215
Shell thickness (mm)	3.5
Density (%)	100
Bed temperature (°C)	Room temperature

For the laboratory tests performed during the parameter optimization, a grid pattern was envisaged as shown in *Figure 4. 2*.

The resolution of the printer is related with the nozzle diameter and the precision of the extruder (*xy* axes) and bed (*z* axis) movements.[7] For this reason, the first parameter optimised was the nozzle diameter. As the filament was made with ceramic powders, the smallest diameters were not tested, in order to avoid the ceramic getting stuck inside the nozzle. Consequently, two diameters were tested in this work: 0.6 and 0.4 mm. As shown in *Figure 4. 3*, with a larger nozzle diameter the squares of the grid are less defined, hence the design was modified, and the diameter reduced. Then, the structure with the 0.4 mm nozzle was better defined. After these results, **the nozzle size was fixed at 0.4 mm**.

0.6 mm	0.4 mm
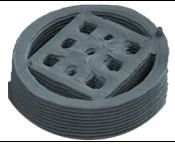	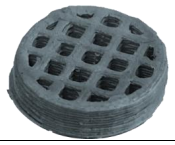

Figure 4. 3 Printed grilled design with different nozzle size

Another aspect to consider is the printing temperature. Initially, the temperature was set at 204°C, which was raised eleven degrees, 215°C, to facilitate melting of the filament in the search for resolution improvement. **215°C was the optimum temperature for the printing process.**

Next, the layer thickness was optimised using the 0.4 mm nozzle. The goal was to achieve the thinnest layers. Three different layer thicknesses were explored: 0.2, 0.1 and 0.05 mm, *Figure 4. 4*.

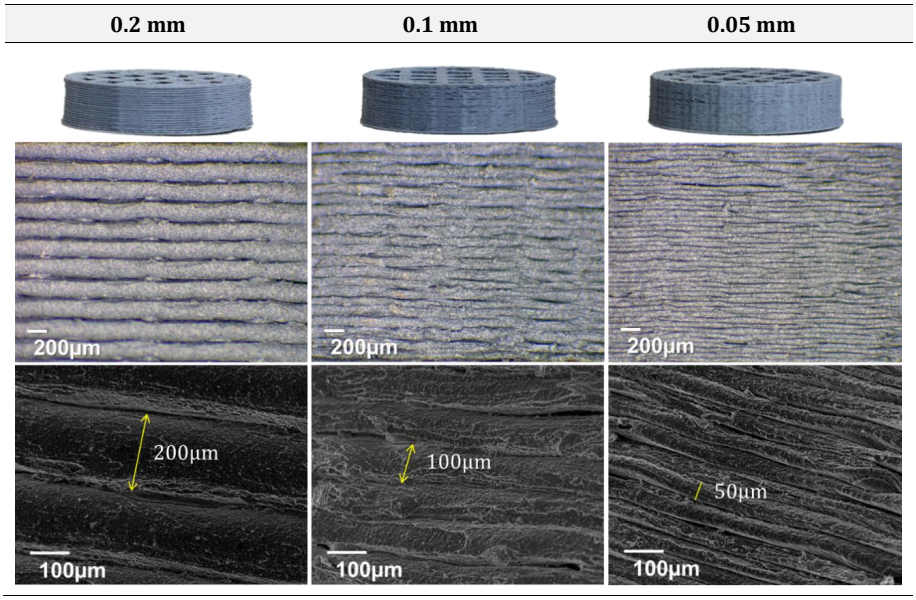

Figure 4. 4 Printed grilled design with different thickness layer

As can be observed in the SEM images shown in *Figure 4. 4.*, the micrographs reveal a good adherence between layers in all the specimens. The printed objects were free of defects and no cracks or delamination effects were observed. The layer thickness chosen for the spiral device fabrication was 0.1 mm, in order to save time during the printing process. This decision was made because, although the layer resolution is a key parameter in FDM, there is a trade-off between resolution, processing time (i.e. cost) and the final application. In this work, the resolution is not a limiting factor, especially due to the subsequent thermal treatment. Consequently, the **layer thickness was fixed at 0.1 mm** because it gives a good resolution and the printing process is faster than in the case of thinner layers and the performance of the ceramic will not be largely affected**.**

Finally, the printing speed was evaluated as well for time saving. In this work, five different printing speeds were tested: 25, 30, 40, 50 y 70 mm/s, using a 0.4 mm nozzle and 0.1 mm layer

thickness The results can be observed in *Figure 4. 5*. Regarding the resolution, there is not much difference between 25, 30 and 40 mm/s. However, there is a marked deleterious effect at speeds of 50 and 70 mm/s.

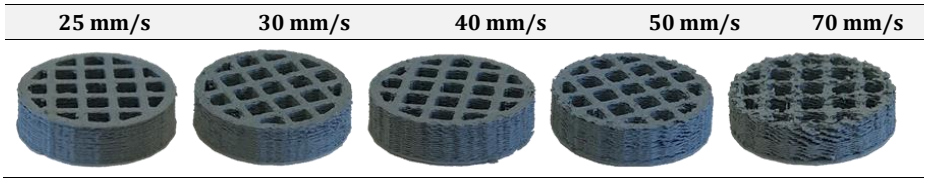

Figure 4. 5 Printed grilled design with different speeds printing

Regarding the processing time, it was 9'58'' for the lowest speed (25 mm/s) and 11'19'' for the fastest (70 mm/s). As there is not much difference regarding time, **the speed was set at 25 mm/s for the device fabrication**, avoiding resolution losses. Hence, the summary of parameters optimised is collected in *Table 4. 3*.

Table 4. 3 Optimised parameters for the devices printing

Optimised parameters	Value
Nozzle size (mm)	0.4
Thickness layer (mm)	0.1
Speed printing (mm/s)	25

4.4 Monolith printing

Using the parameters established in the previous section, some monoliths were fabricated with the spiral design in order to use them in the catalytic reactor and evaluate their performance in the degradation of emergent contaminants. Some monoliths were printed using 100% TiO_2 (Sample C, *Table 4. 1*) and some others using filaments containing TiO_2 and pore formers (Samples A and B, *Table 4. 1), Figure 4. 6.*

After printing, debinding and sintering treatments were carried out. Both thermal processes used are those described in *Chapter 2, Section 2.1.1.1*. The resulting green bodies and sintered monoliths are shown in *Figure 4. 7*. According to the measurements of the green and sintered bodies, **shrinkage could be measured for each of the printing axes: 21% (*z*), 25% (*y*) and 17% (*x*)**, approximately.

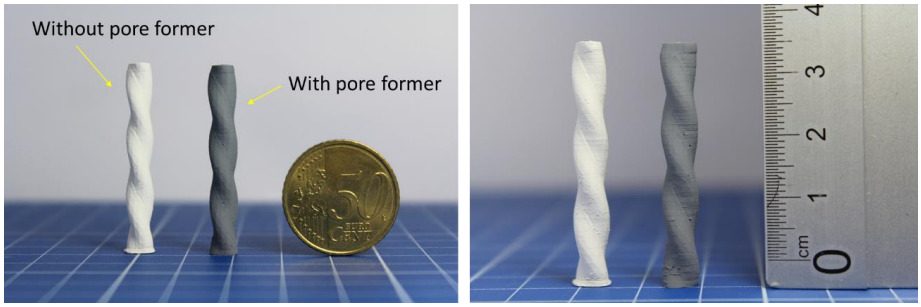

Figure 4. 6 Spiral structures printed by FDM without pore former (white structure) and with pore former (grey)

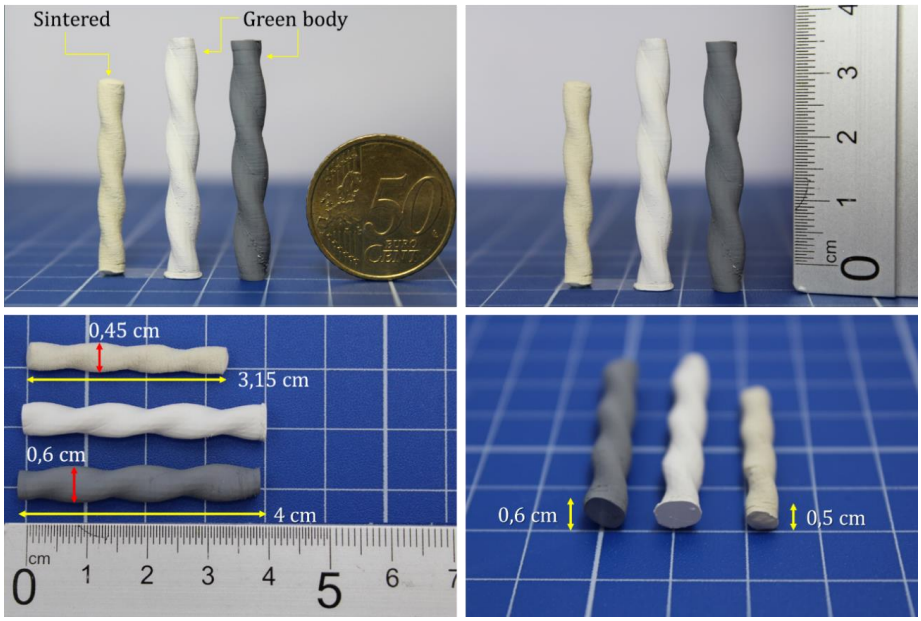

Figure 4. 7 Green and sintered spiral devices

4.5 Phase stability

As the printed items undergo thermal treatments at relatively high temperatures, a major concern is whether there occurs any phase transition upon sintering. Hence, XRD experiments were performed to study and analyse the composition of different printed and sintered monoliths.

According to the phase diagram of titania, over 600°C the predominant phase is rutile, independently if the starting raw material is anatase, *Figure 4. 8 (a)* or brookite, Figure 4.8 *(b)*.[8,9]

In this case, the raw material was anatase TiO_2, thus the final phase after sintering at 1200°C must have been rutile.

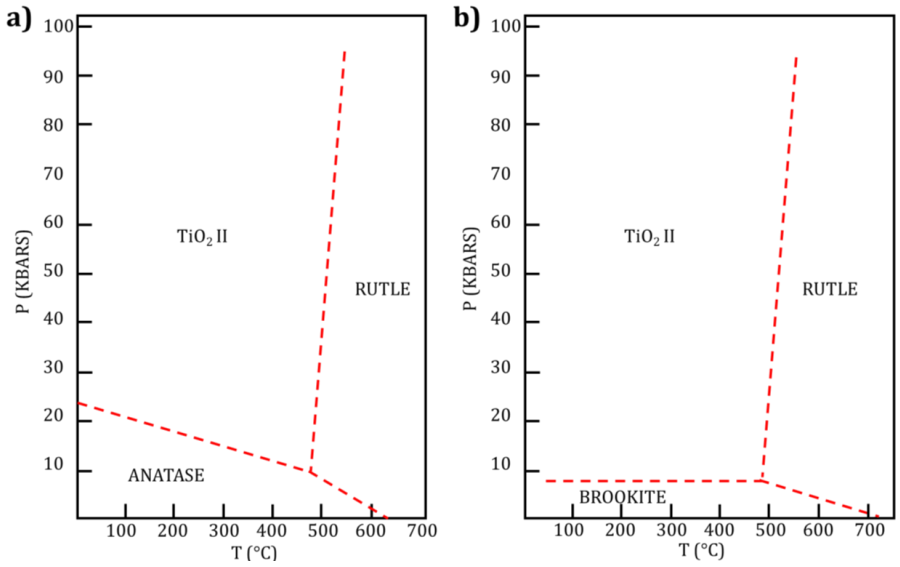

Figure 4. 8 Phase diagram for TiO_2 polymorphs [8,9] a) Anatase as starting material b) Brookite as starting material.

Along this work some thermal treatments were studied, *Chapter 2, Table 2. 1*, in order to avoid crack formation during the process.

The first thermal treatment test was done up to 225°C as drying process, *Table 2. 1 (A)*. Then, debinding was done at 400ºC and at 900ºC to burn the organic compounds in air, *Table 2. 1 (B).* Once the treatment was completed the absence of cracks was corroborated, and samples were completely white, but when they were manipulated, they broke down which would mean that the mechanical resistance was low, therefore this sintering route was not adequate, *Figure 4. 9*.

Figure 4. 9 Sintered structures at 900°C under air atmosphere

Then, the third thermal treatment was done at 1200°C, *Table 2. 1 (C),* which was successful as no cracks appeared and it could be summarised as a directly treatment, *Table 2. 1 (E).* Though the resulting samples had not the typical colour for rutile phases, *Figure 4. 8*. Usually, rutile and anatase have a white or yellowish white colour.[10,11] However, in these cases, in spite of being sintered at the same temperature and atmosphere, the results did not match with the initial expectations.

In the case of air atmosphere reddish brown, yellowish streaks in a reddish-brown structure and yellowish grey tonalities were observed, *Figure 4. 10 (a, b & c respectively).*

On the other hand, under argon atmospheres, darker colours were obtained. In addition, a colour gradient can be observed inside one of the monoliths, *Figure 4. 10 (e)* or in the bottom part of another, *Figure 4. 10 (f).*

Apart from rutile and anatase, there are several other TiO_2 polymorphs, including brookite. The role of brookite has not been extensively studied in photocatalysis. However, its photocatalytic activity for the degradation of hazardous organic compounds has been reported to be very superior to rutile and very similar to anatase, due to the similarity of both polymorphs regarding properties as particle size and shape, specific surface area, and band gap.[21] Considering all the above, it is important to know which phase is present in the fabricated device in order to analyse its activity removing contaminant via photocatalysis and the production of TiO_2 monoliths via FDM 3D printing and subsequent thermal treatments does not cause a major change in the structure.

As there were no reasons nor evidence to blame on cross-contamination, one hypothesis could be the formation of brookite phase in the structures that would explain the reddish brown colour.[12] In order to confirm this hypothesis, X-Ray diffraction was done to determine the phases present in the sintered monoliths.

	a	b	c
Air			
	d	**e**	**f**
Argon			

Figure 4. 10 Sintered structures at 1200°C using different atmospheres

Regarding the XRD pattern results, *Figure 4. 11*, the commercial TiO_2 coincides with anatase and the sintered specimens with rutile.[13,14] The presence of brookite could not be unambiguously confirmed, but as spectroscopic techniques ruled out the presence of chemical elements other than Ti and O, this result suggests that brookite appears as traces, very minor secondary phase, which can cause colour changes in the sintered sample despite the very small amount.[15] It should be noted that the limit of detection (LOD) in XRD is typically between 2-3 % of presence in the measured sample, which can be even higher if the phase does not have good crystallinity.

The presence of brookite after firing at 1200°C apparently contradicts the phase diagram showed above, but it could be due to the thermal treatment program combined with the presence of organics, which degrade at moderate temperatures. During the heating and cooling processes, the temperature program follows a very slow ramp rate to avoid the appearance of cracks that could compromise the structure. Under these working conditions, traces of brookite may form. Perhaps, by changing the conditions, the formation of brookite could be minimised. To corroborate that hypothesis, a quenching experiment was performed by removing the samples at 1200°C and immersing them in liquid nitrogen. After quenching, the reddish-brown sample became yellowish white. In order to confirm that the sintered sample (reddish brown) and the quenched sample (yellowish white) were the same phase, they both were analysed by XRD. The XRD pattern was the same for both samples, *Figure 4. 12*, which suggests that our hypothesis was correct.

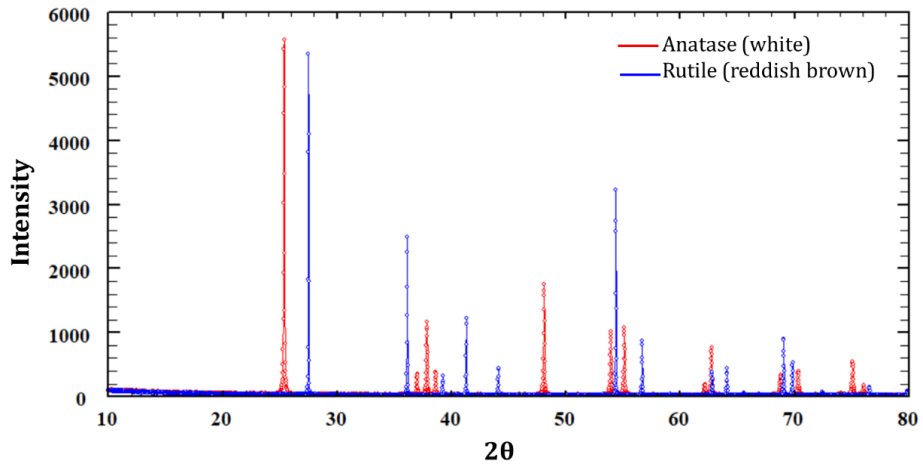

Figure 4. 11 XRD pattern of commercial TiO_2 (red) and sintered at 1200ºC (blue)

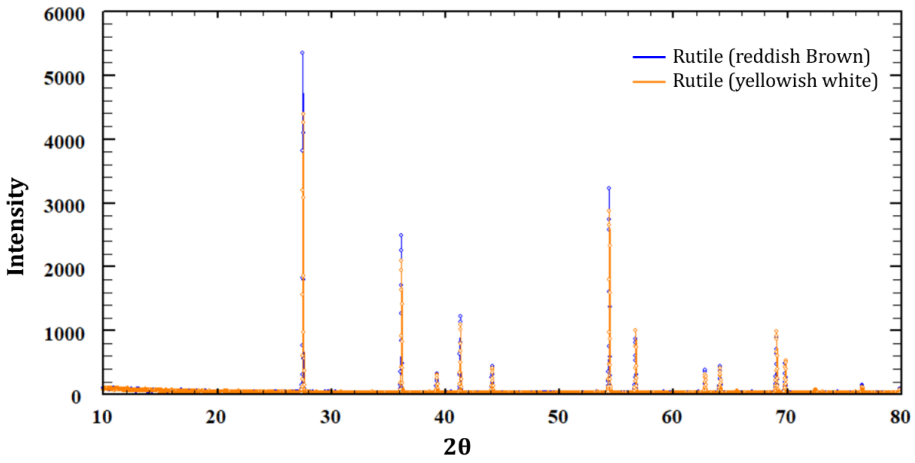

Figure 4. 12 XRD pattern of sintered (blue series) and quenched (orange series) titanium oxide samples.

For this reason, the presence of samples with the gradient colour, i.e. sintered under argon, is due to temperature gradients inside the furnace. *Figure 4. 13* shows the samples that were located in a row inside the furnace. In this case, it can be observed as some samples were exposed to higher temperatures (left samples) whilst some others could not complete of the degradation of the organics and hence, they remain grey (right samples). This issue was solved by putting less samples and locating them as centred in the hot-spot as possible, avoiding temperature gradients among them.

Figure 4. 13 Sintered samples at 1200°C under argon atmosphere (tubular furnace)

In conclusion, this study has found that after sintering at 1200ºC the phase of TiO_2 in the monoliths is mostly rutile, in spite of the colour differences. This is imperative as we need to know the composition before proceeding with any further work. Nevertheless, the relevance of identifying the phases present in the sample is important too, due to the different photocatalytic performance that exhibit each polymorph of titania. The photocatalytic reactions depend on the number of adsorbed radicals on the surface of catalyst, *Chapter 1, Section 1.2.3*. The higher the

surface area, the higher the density of localised states will be. However other parameters are relevant for a good photocatalytic performance, including band gap and the microstructure of the sample.[16] As mentioned *in Chapter 1, Section 1.2.2*, anatase has a larger experimental band gap compared with rutile (~3.2 eV and ~3.0 eV respectively), but despite this, it has been reported anatase has a superior photocatalytic performance. In contrast, other reports suggest that rutile can be beneficial for some applications due to acicular morphology, the combination of both phases or because of doping with a transition metal.[17–20]

4.6 Microstructure characterisation

At this point, the microstructure was studied via SEM to study the level of porosity and sintering. Therefore, the microstructure of 3D printed supports with different compositions were studied as well to evaluate the effect of the pore former in the slurry. In addition, as XRD did not show phase changes, SEM was employed to confirm whether the microstructural changes with the temperature and also to determine the optimum atmosphere for both the debinding and sintering processes, i.e. argon or air.

Firstly, the sintering program employed was under flowing argon atmosphere at 1000ºC as described in *Table 2.1 (D), Chapter 2*. Three different areas can be observed in the sample, *Figure 4. 14: (1) grey area, (2) yellowish white area and (3) reddish-brown area* (from the centre to outside). Regarding the microstructure, *Figure 4. 14 (c & d)* shows a similar degree of sintering between two different areas, with grain sizes in the 2-10µm range. The top region of the sample is fully dense, *Figure 4. 14 (a)*, with perfectly sintered microstructure. The bottom of the sample shows a somewhat different microstructure with a minor degree of porosity, *Figure 4. 14 (d)*, despite having a similar colour. Additionally, regarding the grey zone, *Figure 4. 14 (b)*, the corresponding SEM image clearly shows that organic compounds were not totally removed, because carbon spheres (3-6µm) can still be observed in the sample, which makes sense as the central zone is in contact with the alumina plate used as support during the thermal treatments, hence it is less exposed to the atmosphere and therefore organics burning off is more difficult.

In summary, it can be concluded that 1000°C is not enough to sinter the samples and at this temperature samples show different degrees of porosity. For this reason, the sintering temperature was set at 1200°C to remove all the organic compounds and the pore formers. Subsequently, the microstructure at 1200°C will be compared regarding both atmospheres: air and argon, *Table 2.1 (F), Chapter 2.*

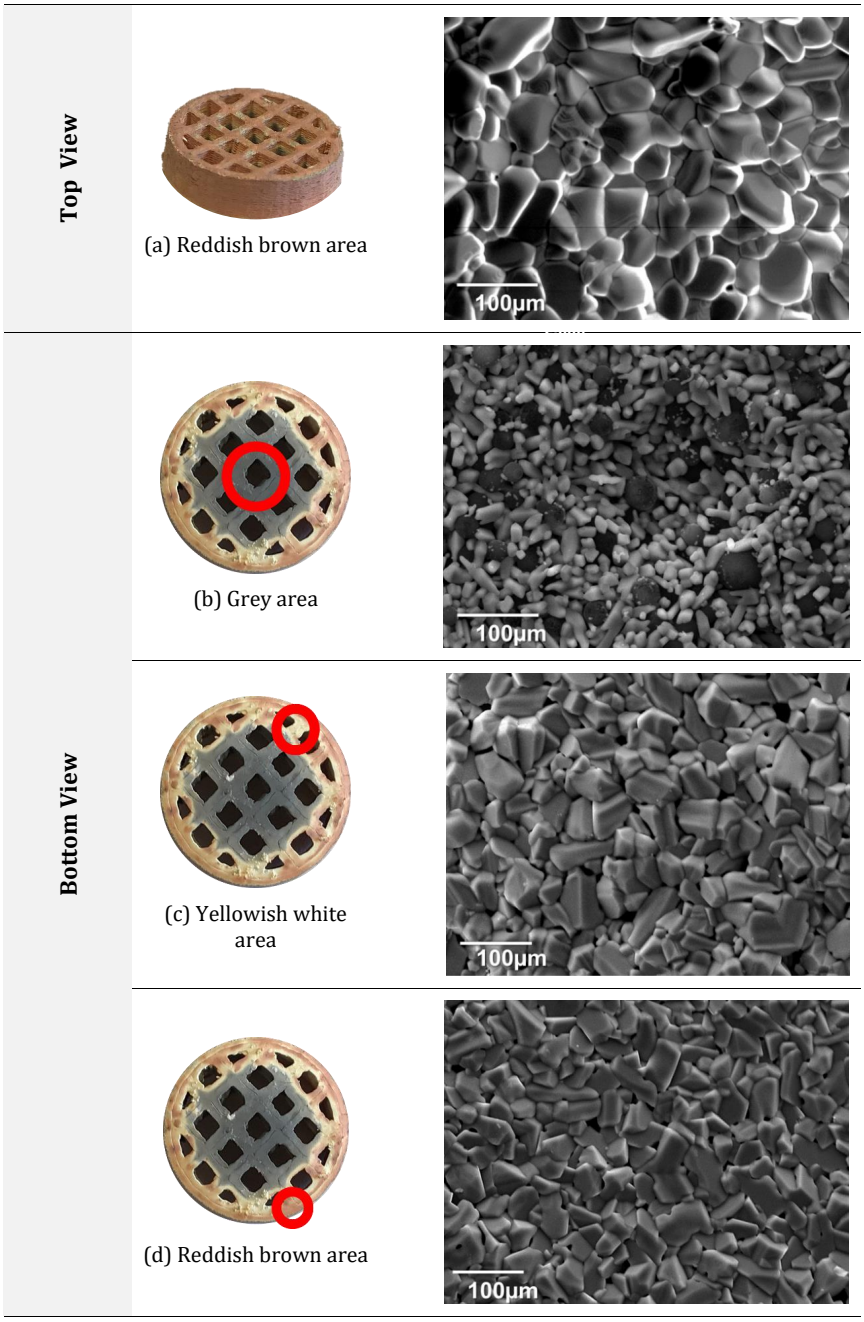

Figure 4. 14 SEM and digital images corresponding to sintered structure at 1000°C with different sintering levels

Most of the samples sintered under air at different temperatures (900°C and 1200°C) were yellowish white, despite some of them that were reddish brown. This issue was solved via temperature quenching as described before. When the samples had the typical colour for this phase, the microstructure was studied. *Figure 4. 15* shows 2-3 μm pores corresponding to the burnt carbon spheres and the posterior sintering process. Hence, it can be concluded that this program under air atmosphere does not lead to the complete densification, providing certain porosity to the sample that will be studied by mercury porosimetry.

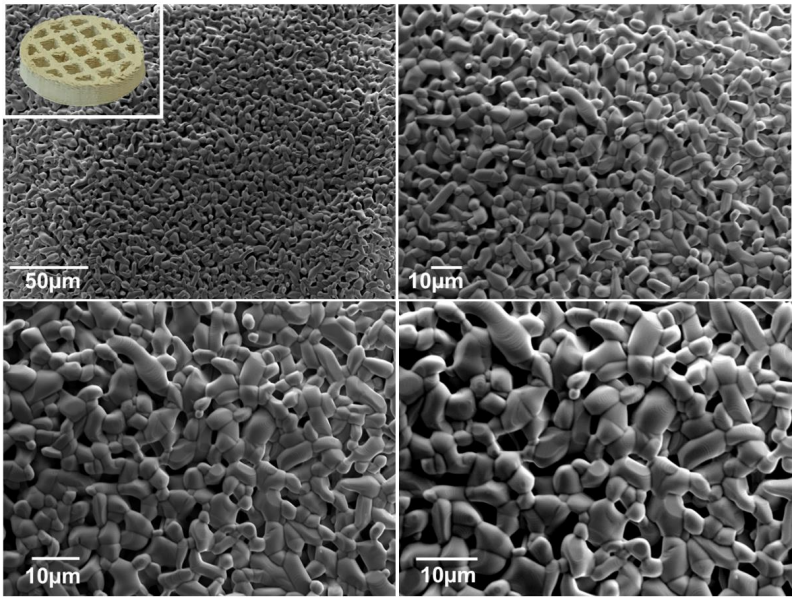

Figure 4. 15 SEM images corresponding to sintered structures at 1200°C under air

On the other hand, sintered samples under argon atmosphere show more complex results as three different microstructures could be observed. Firstly, a more porous microstructure was detected, showing larger pores than in samples sintered under air, *Figure 4. 16*. Also, unburnt structures can be noted as in the sample sintered at 1000°C, *Figure 4. 17*, which is due to glassy carbon being still stable under inert atmosphere.

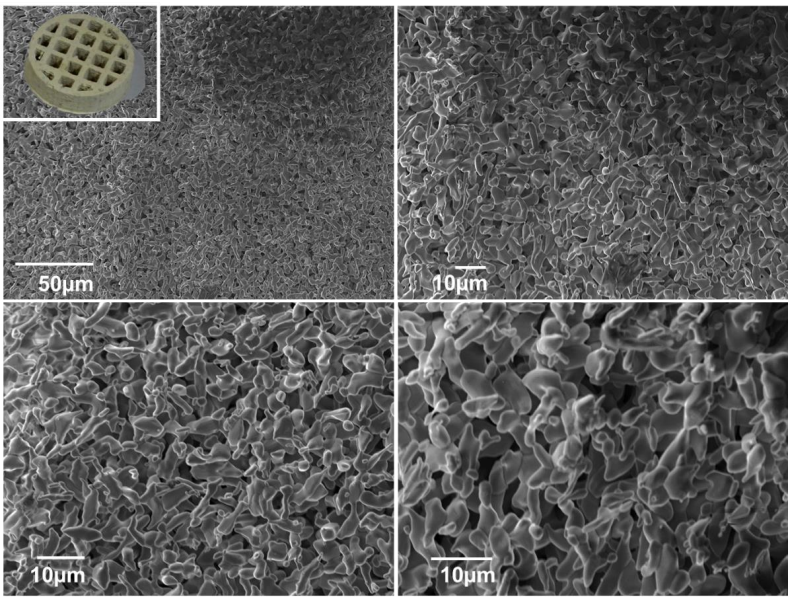

Figure 4. 16 SEM images corresponding to sintered structures at 1200°C under argon

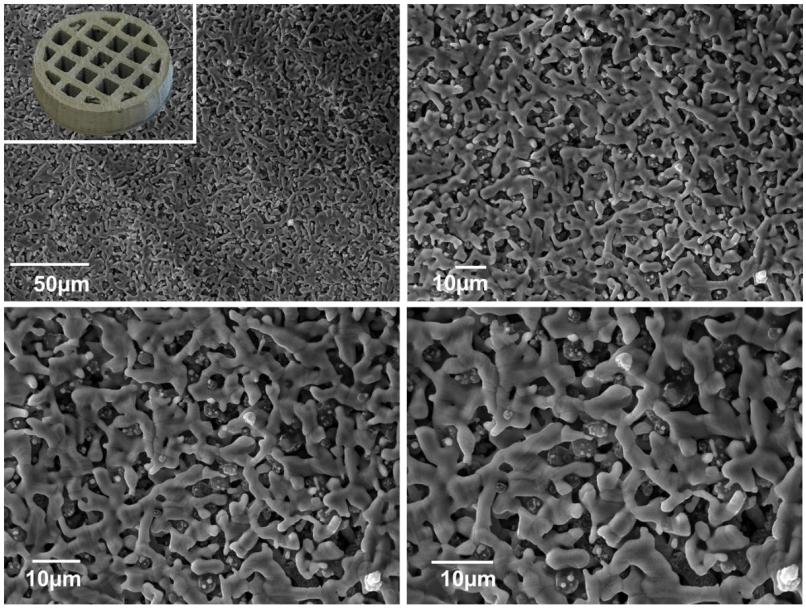

Figure 4. 17 SEM images corresponding to sintered structures at 1200°C under argon with remnants of unburnt pore formers

Finally, a surprising and unexpected acicular structure was achieved. The aggregated particles consist of many fine acicular or needle-shaped particles that measure 36µm long and 4µm wide on average, *Figure 4. 18*.

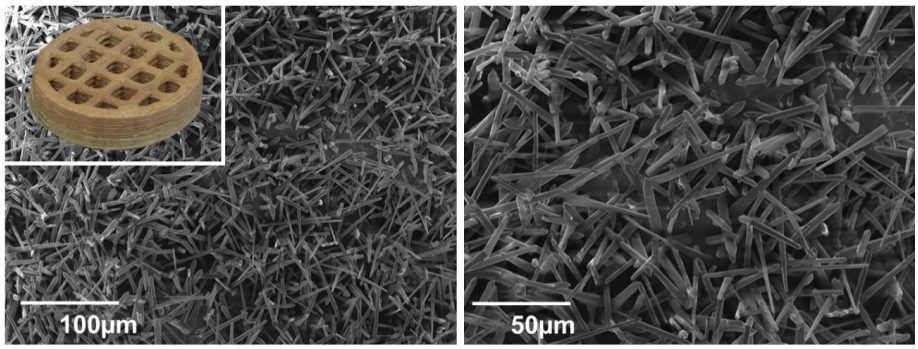

Figure 4. 18 SEM images corresponding to sintered structures at 1200°C under argon with acicular morphology

It is very interesting due to acicular morphology of rutile has the potential to improve the photocatalytic activity by increasing specific surface area, compared to spherical particles of anatase.[22,23] However, as the samples showed a gradient between the reddish brown and the grey colour, it is suspected that these acicular structures could be the result of carbon degradation. To corroborate the composition of the acicular shapes, EDS was carried in two different zones: (i) a general area*, Figure 4. 19*, and (ii) a specific needle, *Figure 4. 20*.

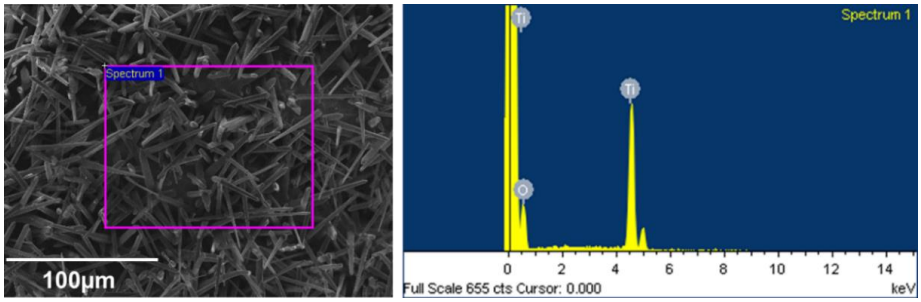

Figure 4. 19 SEM image and EDS spectra of a general acicular shaped zone

The program compared the EDS scan of the chosen area for study with stored standard scans to analyse the unknown composition. The results for the general area were 67% of oxygen and 33% of titanium, coinciding with the stoichiometry of TiO_2. The analysis of an isolated needle corresponds to 100% of TiO_2.

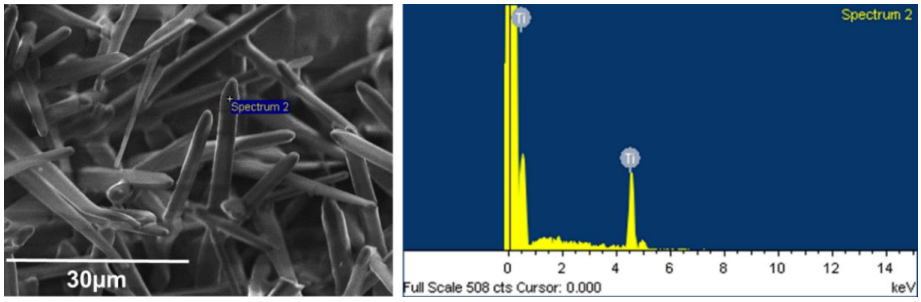

Figure 4. 20 SEM image and EDS spectra of a specific needle

Nevertheless, EDS is not a surface technique, so these signals may be from the TiO_2 background. To complete this study, the specimens were broken, and fragments were analysed by TGA, *Figure 4. 21*.

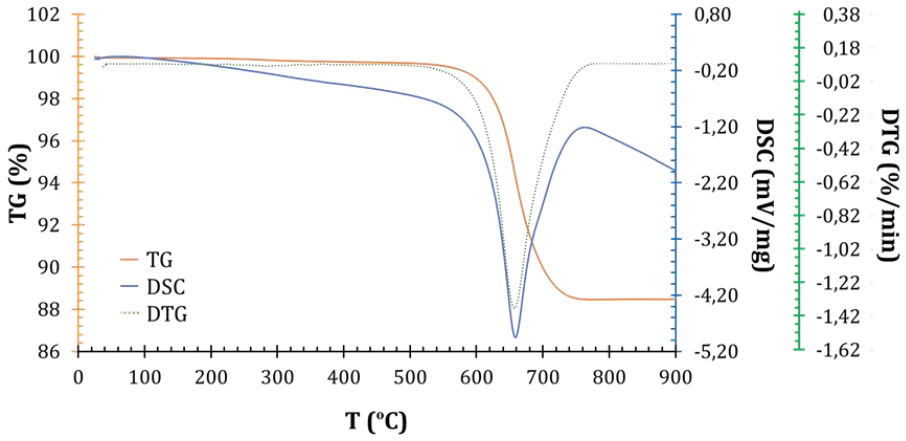

Figure 4. 21 TGA of TiO_2 structures with acicular shapes under oxidant conditions

Thermal gravimetry results show a mass loss above 660°C. This value is compatible with the oxidation of carbon residues. If fibres had been made of TiO_2, this loss of mass would have not been observed at this temperature. From this result, it can be concluded that **acicular shapes were due to the decomposition of carbon spheres**.

As the formation of this microstructure was unexpected, further thermal treatments under both atmospheres were performed *Table 2. 1 (F)* and the results were different. The SEM image of the sample sintered in air atmosphere, *Figure 4. 22*, shows a dense microstructure and thickness reduction of the layer printed at 0.1mm down to 83µm.

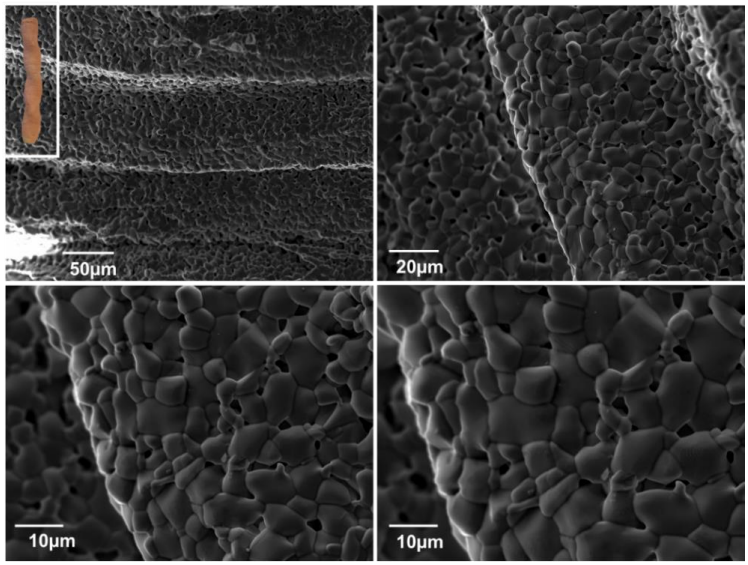

Figure 4. 22 SEM images corresponding to sintered spirals at 1200°C under air atmosphere

As occurred when sintering at 1200ºC, the spiral sintered under argon presents acicular particles, *Figure 4. 23*. The TGA was performed again with similar results to the previous case with acicular structures, i.e. weight loss above 610^{0}C, *Figure 4. 24*. In both cases the sintering program was carried out under argon atmosphere.

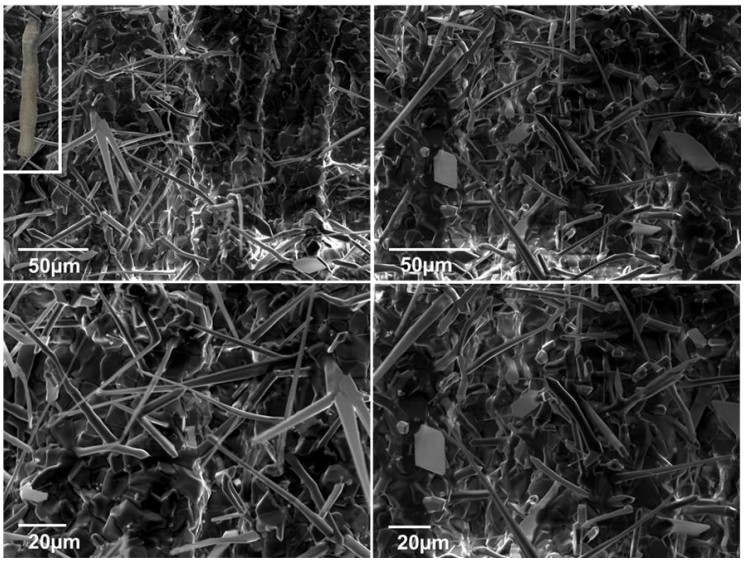

Figure 4. 23 SEM images corresponding to sintered spirals at 1200°C under argon atmosphere

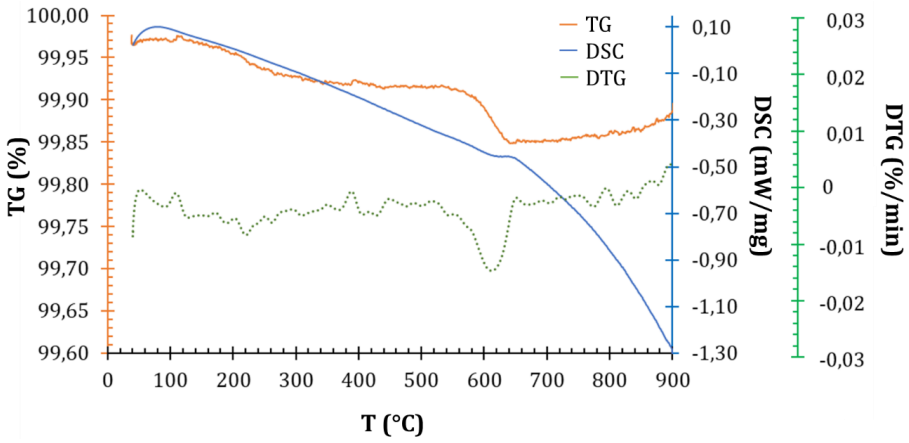

Figure 4. 24 TGA of TiO_2 spirals with acicular shapes under oxidant conditions

As the presence of acicular particles indicates that the degradation process of the pore formers was not finished, thermal conditions were changed to ensure a complete debinding and sintering. For that purpose, the thermal treatment was divided in two steps using different atmospheres. The new thermal treatment does not require stopping at an intermediate temperature to avoid cracks and achieve sintering for providing the device with enough mechanical resistance to support the water pressure during the photocatalysis experiment.

The **optimised thermal program consisted of debinding at 900°C for 12 hours under inert atmosphere followed by a sintering stage at 1200°C for 12 hours under air atmosphere, with a heating and cooling speed of 2°C/min**. This program was applied to the next samples whose microstructure was also studied to corroborate the results under these new conditions.

Besides, this microstructure was studied for the devices with two compositions: with and without pore former, both sintered with the ideal conditions just mentioned before. *Figure 4. 26* shows the microstructure of the surface for both compositions, while *Figure 4. 26,* reveals the microstructure of the cross section.

Regarding the surface of the sample without pore former, *Figure 4. 26 (right),* after the thermal treatment there is some residual porosity, although the cross section is fully dense, *Figure 4. 26 (right)* which indicates that it is a superficial phenomenon.

Concerning the sample with pore former, the porosity remains on the surface, *Figure 4. 26 (left)* and on the cross section too, *Figure 4. 25 (left).* **Thus, it can be concluded the successful use of the C microspheres in the composition as pore formers**.

The cross-sectional SEM images, *Figure 4. 26,* shows well-adhered layers without defects. The impact of the presence of pore formers in the filament composition is also quite clear, leading to

porous microstructures (left), with more disconnected grains, compared to the sample without pore formers (right) which is fully dense.

Summarising, it can be concluded that the main goal of this chapter was reached, i.e. the fabrication of good quality monoliths via FDM 3D printing, exhibiting good adherence between layers and with no defects. Moreover, the porosity of the sintered material can be controlled adding pore formers, which are burnt-off after printing via an optimised thermal treatment.

Despite these promising results, some aspects require further research, i.e. a complete porosity study including larger amounts of pore formers. That would imply changing the composition of the filaments, which could be explored to determine the maximum amount of pore formers that is viable to print and to study the photo-catalytic responses with highly porous monoliths.

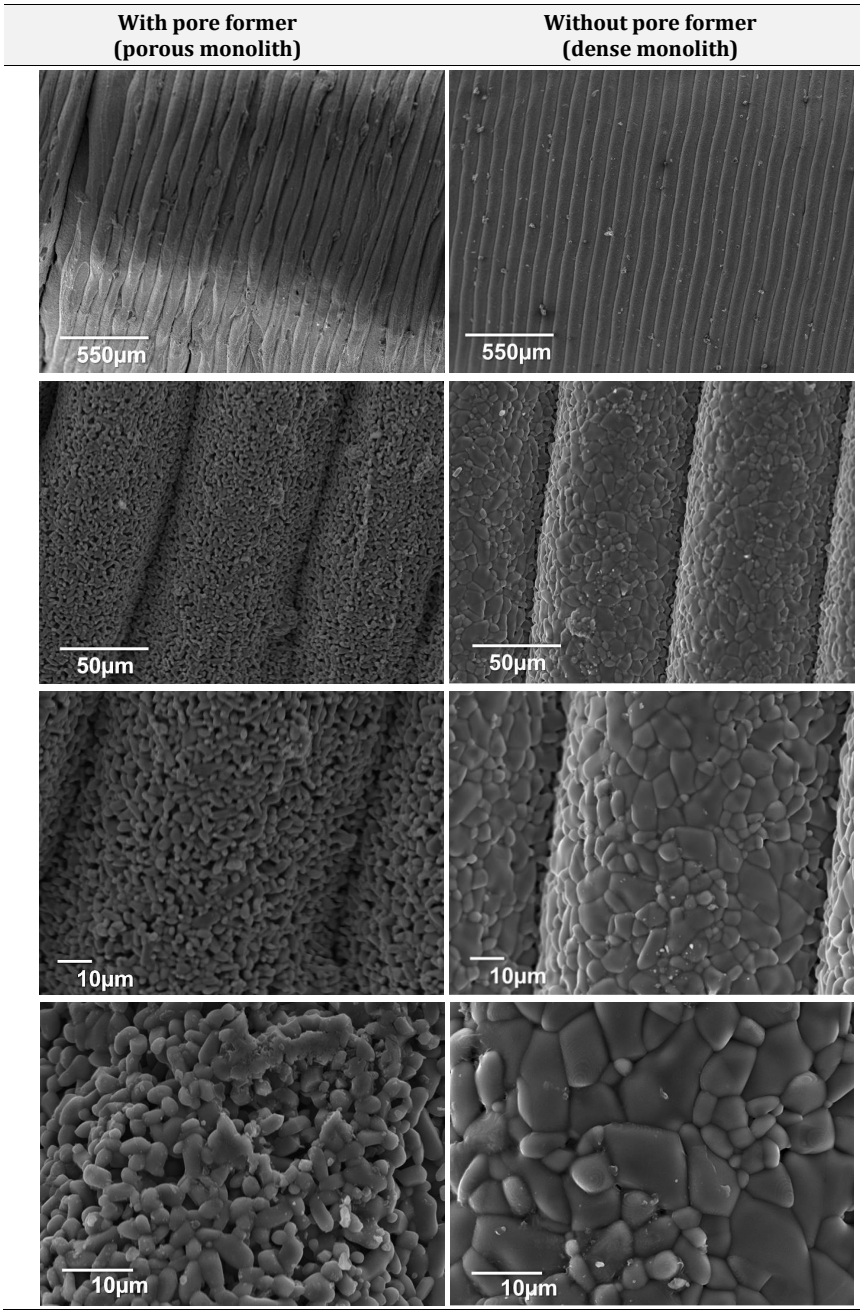

Figure 4. 25 SEM images corresponding to the surface microstructure of TiO_2 printed monoliths with pore formers and without pore formers (right)

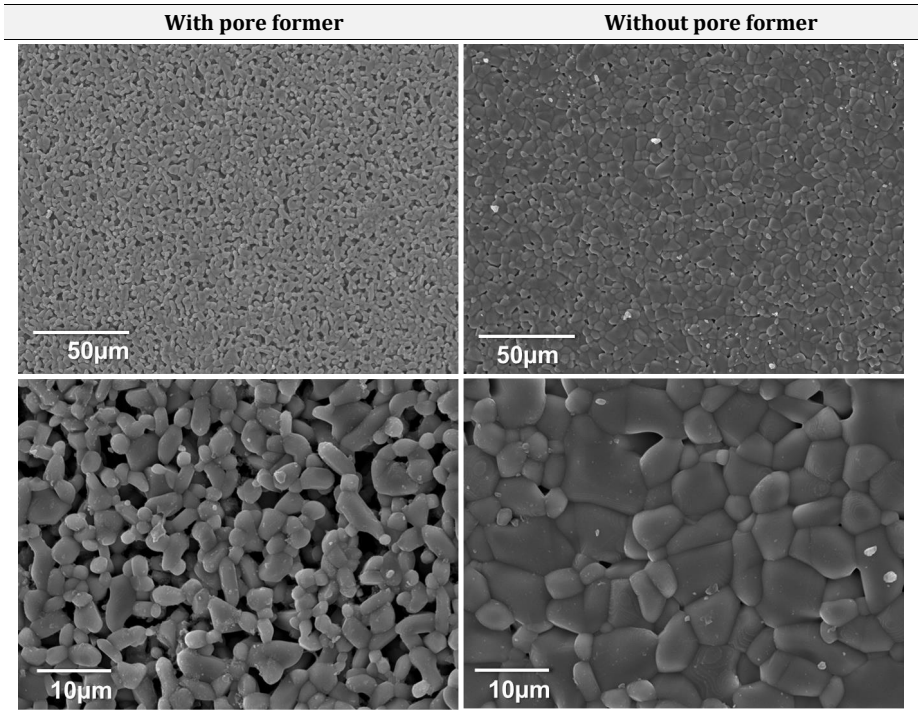

Figure 4. 26 SEM images corresponding to cross section microstructure of TiO_2 printed devices with pore formers (left) and without pore formers (right)

4.7 Catalyst studies on 3D printed monoliths

4.7.1 Methylene blue conversion

3,7-Bis(Dimethylamine)pheno-5-thiazinium chloride, commonly known as methylene blue (Panreac, C.I. 52015, $C_{16}H_{18}C|N_3S{\cdot}x\ H_2O$) was the model molecule used as emergent contaminant, *Figure 4. 27*, to measure the photocatalytic activity of the printed helicoidal monolith.

Regarding the catalytic tests, some different experiments were carried out: (i) photolysis, (ii) adsorption and (iii) degradation.

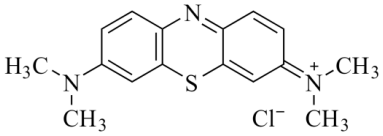

Figure 4. 27 Methylene blue molecule [24]

The photocatalytic tests were carried out in the system described in *Chapter 2, Section 2.3.2*. A solution containing the contaminant goes through the catalyst into a packed-bed reactor where artificial UV light strikes. The contaminant conversion will be measured at different times, as an aliquot is taken from the solution tank. Then, as methylene blue (MB) presents a maximum absorbance (A_{max}) the absorbance of the sample is measured at 664 nm, using a UV/Vis spectrophotometer (Cary 50, 530-710nm). Consequently, the concentration of the sample at different times can be determined using the Lambert-Beer law. Knowing the concentrations, the conversion equation, *Equation 4.1*, could be applied to obtain the percentage of contaminant conversion.

$$Conversion\ (\%) = \frac{C_0 - C_t}{C_0} * 100 \qquad \textit{Equation 4. 1}$$

With this goal, firstly a calibration curve must be obtained and, afterwards, representing the A_{max} *vs.* concentration. In this calibration curve, the concentrations were in the 0.8 and 13.1ppm range. All samples were run using distilled water as solvent and they were measured at room temperature.

Figure 4. 28 shows that the largest concentration (13.1 ppm) presents a somewhat saturated absorbance peak, being the oversaturation beyond 20ppm. For this reason, it is recommended that the photocatalytic tests are performed at lower concentrations.

After representing the curve calibration (R^2= 0.997), the concentration of future tests can be known by measuring their absorbance.

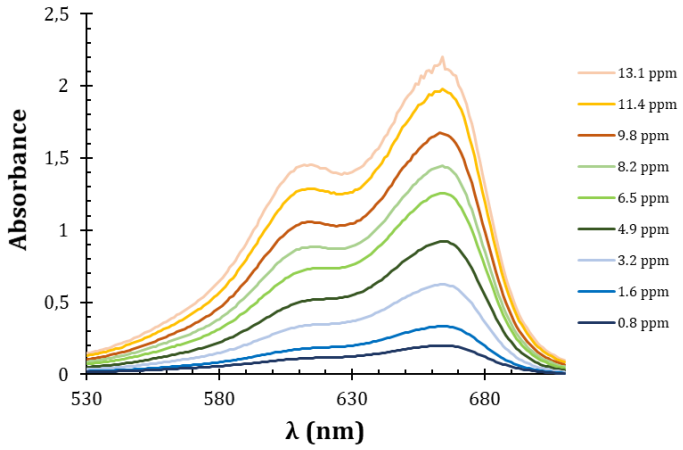

Figure 4. 28 Absorbance of methylene blue of the calibration curve solution

In previous studies, it has been suggested that MB can be degraded under solar light, this effect is known as photolysis.

Regarding the bibliography MB degradation occurs under solar light in basic media rather than acid, due to the presence of OH^-.[25,26] To illustrate this, photolysis effect showed a 15% conversion of the contaminant after 90 min, whereas the complete photolysis of the contaminant was obtained at pH=11.[25]

In this work, the MB solution has a pH=6.11. It is the limit where there could be a photolytic effect.[25] The experiment was carried out without the presence of catalyst, using an initial concentration of 15.7ppm.

The graph below shows the results of this work, *Figure 4. 29,* and illustrates that after 9h. (540 min) less than 20% of contaminant has been converted.

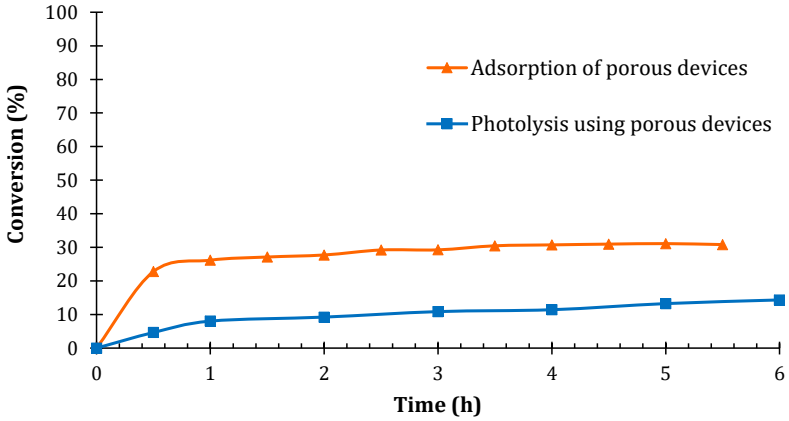

Figure 4. 29 Photolysis of methylene blue conversion curve (blue squares) and adsorption of TiO_2 porous printed devices

Thus, it can be concluded that there is an insignificant photolytic effect. For this reason, photolysis is not the best process to remove MB under these pH conditions, as the conversion value is very low to be applied to real wastewater treatments with this contaminant. However, in the same conditions, kinetics of the reaction could be improved by using catalysts with different: phases, geometries and porosities, which may lead to their use as water filters producing the highest conversion of pollutant in the shortest time.

During the degradation process, first, a part of the pollutant is adsorbed on to the TiO_2 catalyst surface, then light arrives, and radical reactions are triggered, *Chapter 1, Equations 1. 6 - 1. 13.* At

that point, the pollutant mineralised into salts, water and carbon dioxide, *Equation 4. 2*,[27] which did not absorb in the same range that MB, so it can be measured by UV-Vis spectrometry.

$$C_{16}H_{18}N_3S^+ + \frac{15}{2}O_2 \rightarrow 16\,CO_2 + 3\,NO_3^- + SO_4^{2-} + 6\,H^+ + 6\,H_2O \qquad \textit{Equation 4. 2}$$

The first experiment performed was related to the level of contaminant adsorption on the catalyst active surface. In this case, four porous 3D-printed monoliths were placed into the packed bed reactor, through which passed a solution of MB with no UV-Vis light, that is, the lamp of the system was switched off.

In this way, it is possible to know the level of the adsorbed contaminant, which is not converted, which will be useful to compare the porosity of the directly printed catalyst device with 3D printed catalyst support described in the previous chapter.

As can be seen in *Figure 4. 29*, the percentage of contaminant present in the solution decreases to 30% and then remains constant. This value is the amount of the contaminant adsorbed on to the total active area of the catalysts and it helps to understand how the degradation process takes place.

Then, degradation was studied in the next tests, where four catalytic monoliths were exposed to light, *Figure 4. 30*, and the reduction of the pollutant concentration as a function of time was monitored. To achieve this, porous and non-porous devices were studied to determine if porous structures show higher degree of adsorption, and whether the performance increases with the porosity, keeping the same experimental conditions.

Firstly, porous monoliths were tested. As shown in *Figure 4. 31*, after 48 hours, the sample absorption is close to the baseline, which implies that most of the pollutant has been transformed. These data are expressed as percentage of conversion versus time and reveal that 70% of pollutant is converted after 7 hours and after 24 hours 90% is converted. Therefore, it can be concluded that after 48 hours MB is almost completely removed.

Previous research works have reported several results on MB degradation. Many of them used TiO_2 as catalyst, but they combined the main reaction (i) with doped material;[28–33] (ii) or using different conformations as TiO_2 suspension,[34] nano-particles,[35] pellets,[36]coated,[37] or filmed,[38] (iii) or even assisting the UV photocatalyst with ultrasonic irradiation.[36,39] As the experimental parameters are rather scattered, it is very complicated to compare fairly the results. Furthermore, in this work, direct 3D printing of TiO_2 was employed for its manufacture, which is novel in this field. In the literature, higher conversion percentages were achieved in shorter periods of time. These cases report the use of TiO_2 powders that offer greater active surface, achieving even a

100% conversion in a few minutes. However, one should not forget that, although the kinetics of the reaction are faster, the method developed in this work render high conversion rates offers the possibility of reusing the catalyst and facilitates the separation between the solid and liquid phases, which is one of the main advantages compared to the catalyst suspensions. Lee *et al.*[39] reported one of the first studies evaluating MB degradation using TiO_2 suspensions as a function of a range of parameters such as pH, initial MB concentration, H_2O_2 presence, anions presence and varying of temperature. Using this study as reference, when TiO_2 suspensions are used (pH 5 – 7) a conversion of 50–60% was achieved after one hour. In this work, this was achieved after 2–7 hours. The difference may be due to the very different MB initial concentrations, i.e. 10 ppm vs. 10 µM in the literature. As described by Lee *et al*, the higher the initial concentration, the lower the kinetics of the reaction. Other research lines also achieve almost a complete degradation after 1 hour using suspended TiO_2.[34,40]

Thus, despite the slower conversions, the use of 3D printing technique provides advantages of heterogeneous catalysis as easy recovery and the capability of reusable the catalyst. A further advantage would be the possibility of producing more complex structures, which may enhance both the kinetics and the performance of the reaction. In this work spiral architectures were employed, though as future work, different more complex geometries that may maximise the catalyst irradiated/contact area could be tested.

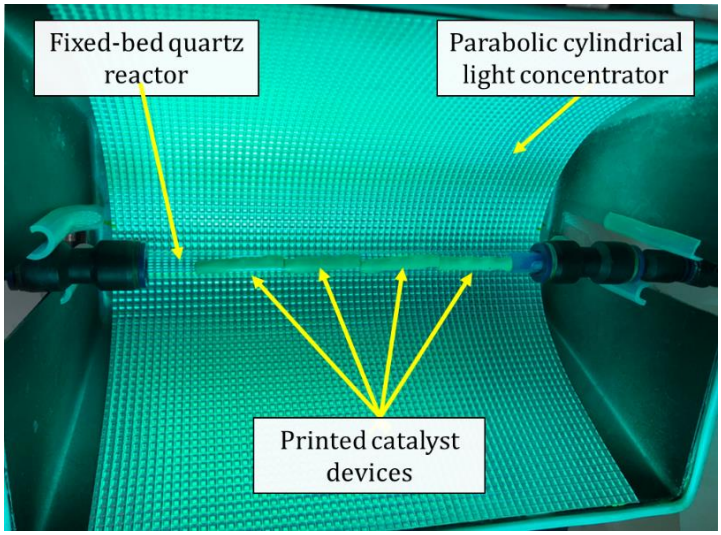

Figure 4. 30 Printed catalyst into the fixed-bed reactor under UV-Vis light

Table 4. 4 Data of MB conversion via photo-catalyst for 48h

Time (h)	Absorbance	[C] (ppm)	Conversion (%)
0	1.4956	8.5	0.0
0.5	1.1165	6.2	27.1
1	0.9419	5.2	39.5
1.5	0.8575	4.6	45.5
2	0.8171	4.4	48.4
2.5	0.7620	4.1	52.4
3.0	0.7113	3.8	56.0
3.5	0.6994	3.7	56.8
4.5	0.6298	3.3	61.8
5.5	0.5976	3.1	64.1
6.5	0.5504	2.8	67.5
7.5	0.5211	2.6	69.5
25	0.2482	0.9	89.0
48	0.1052	0.1	99.2

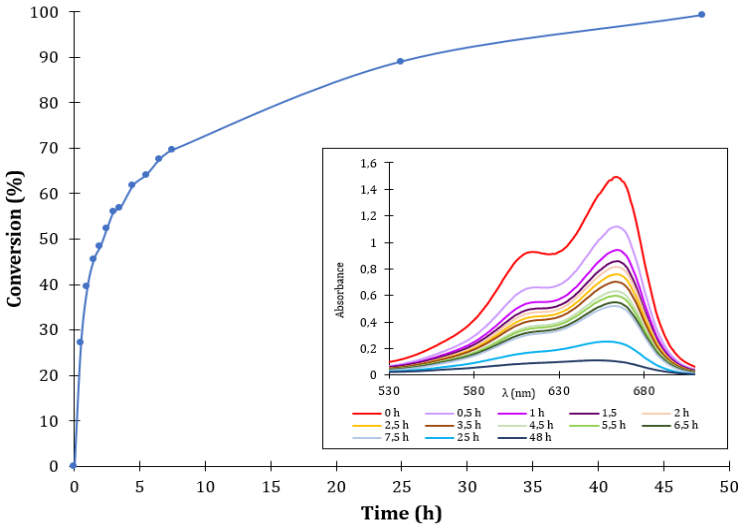

Figure 4. 31 Conversion of MB via photo-catalyst using FDM printed porous catalyst monoliths (data from Table 4. 4)

Among all the advantages of heterogeneous catalysis mentioned above, one of the most important is the easy separation of the catalyst from the study sample. According to the action plan of the European commission about circular economy, some sectors must be focused on potential resources with high circularity and ensuring less waste, such as: electronics, batteries, vehicles, packaging, plastics, textiles, construction, food; water, etc.[41] One of the general measures

established by European Commission, is aimed at product designs, emphasising their repairability, durability, and recyclability.[42]

Several studies reported that TiO_2 is a reusable catalyst for MB degradation or other dyes, although the activity decreased after several experimental runs.[43,44] Nevertheless, this loss of activity can be mitigated if the catalyst is immobilized.[45,46] Moreover, the catalyst could be reactivated by a thermal program to remove any organics remaining on the catalyst surface.[45]

In this context, after a first use, the 3D printed catalytic structures were re-activated via thermal treatment at 500°C for 3h under air atmosphere to remove pollutant traces that could have remained absorbed in the catalysts surface. After re-activation, the photo-catalyst tests were reproduced under the same conditions, *Figure 4. 32*.

The activity loss was 8 % after one cycle. To compare this result with the literature, more than 20% of activity loss has been reported when the catalyst is not reactivated[46], though this is reduced down to 2% when the catalyst is reactivated for the degradation of acid orange.[45] Although the contaminant is not MB, it is also a dye, hence it can be used for comparison. **Therefore, it can be concluded that the activity loss factor in the present work is very close to the values reported in the literature**. Finally, despite the kinetics of the reaction with the re-activated catalyst were higher during the first 5h., the overall performance was higher for the unused catalyst.

Overall, these results indicate that **printed catalysts convert more than 70% after 5h and complete transformation is achieved after 48h.** In addition, **TiO_2 printed monoliths can be re-used** with an 8% performance loss after the first cycle.

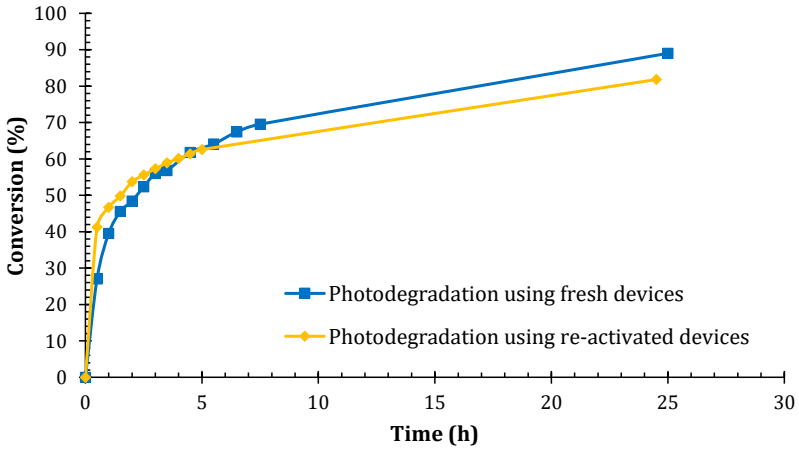

Figure 4. 32 MB degradation using fresh printed monoliths vs using re-activated supports.

Figure 4. 33 shows all measurements together. In summary, **the effect of catalyst photodegradation was higher than the photolysis effect**, corroborating the essential role of the 3D printed catalyst: **14.3 % of MB was photodegraded via photolysis after 6 hours, while the printed catalyst achieved a 67.5% conversion**.

Regarding the adsorption, **it is concluded that without light effect, the catalyst only adsorbs up to 30% of contaminant, being higher the catalyst activity**.

Finally, **the reusability of the printed monoliths was confirmed**, using a thermal reactivation. The result **was an 8% loss of catalyst efficiency after one cycle**.

Once the porous 3D printed monoliths were tested, their catalytic activity was compared with dense 3D printed devices (*Figure 4. 34)*, in order to study whether the achieved porosity caused changes in the catalytic activity.

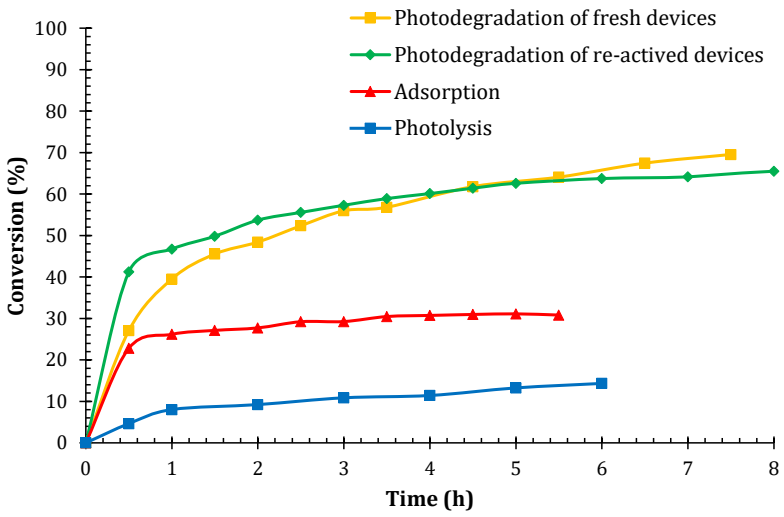

Figure 4. 33 Methylene blue conversion via different phenomenon using porous devices. Photodegradation of fresh 3D printed catalyst devices (rhomboid yellow line) tested under UV-Vis light. Photodegradation of re-activated 3D printed catalyst devices (squared green line) tested under UV-Vis light. Adsorption effect of the 3D printed catalyst devices (triangular red line) tested without light. Photolysis effect (circular blue lines).

Also, the photocatalysis of the dense structures was studied as well and they were re-activated via the thermal program described before.

Firstly, the adsorption was measured to compare the performance between porous and dense printed monoliths. Two different experiments were carried out. On one hand, both dense and

porous 3D printed structures were finely ground in an agate mortar to produce TiO_2 powders, hence their adsorption must be de same. *Figure 4. 34* shows that the result obtained was identical as expected. After 2 and 6 hours both powders present the same adsorption, which is strong evidence of the identical chemical nature of both monoliths.

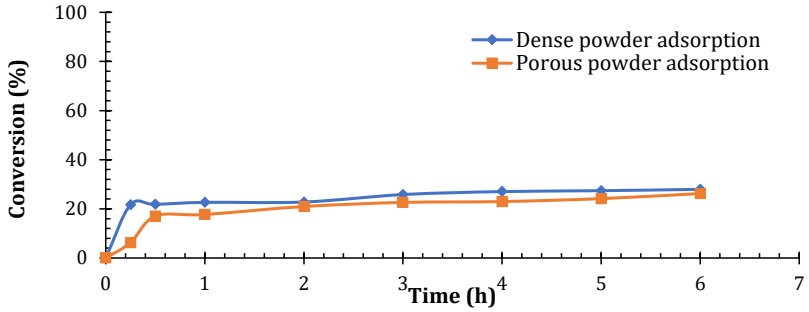

Figure 4. 34 Adsorption study of the TiO_2 powder proceeding from the milled porous and dense printed structures

On the other hand, the same experiment was carried out using coarser particles, i.e. between 1–2 mm. The results of the correlational analysis are presented in *Figure 4. 35*, where porous particles present higher adsorption values than in the case of dense particles. After 4 hours, porous particles were disaggregated, and this may explain the increase observed. As porous devices presented a higher surface area, a larger amount of contaminant can be adsorbed in order to carry out the photocatalysis reaction. Thus, these results suggest that the photodegradation of the porous monoliths will be higher due to the larger active surface.

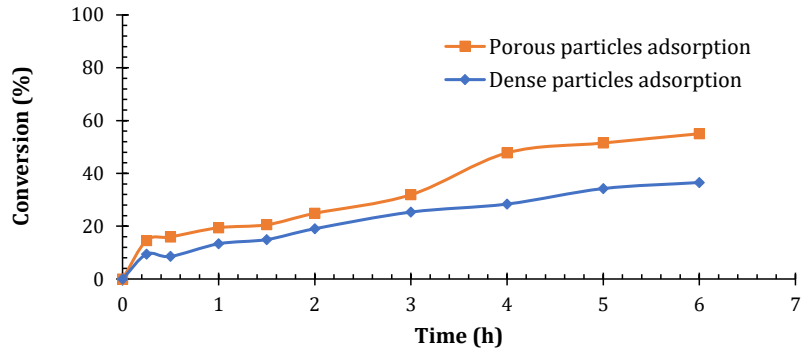

Figure 4. 35 Adsorption study of the TiO_2 particles (1-2 mm) proceeding from the milled porous and dense printed structures

Finally, the adsorption of the 3D printed structures (dense and porous) was also evaluated, *Figure 4. 36*, rendering very similar results. This implies that under these working conditions, the porosity generated in the 3D printed ceramic monoliths do not have an impact in the adsorption tests. Thus, it would be interesting to study in a future work a higher porosity grade or changing the thermal treatment to reduce the relative density to discern whether porosity may modulate pollutant adsorption.

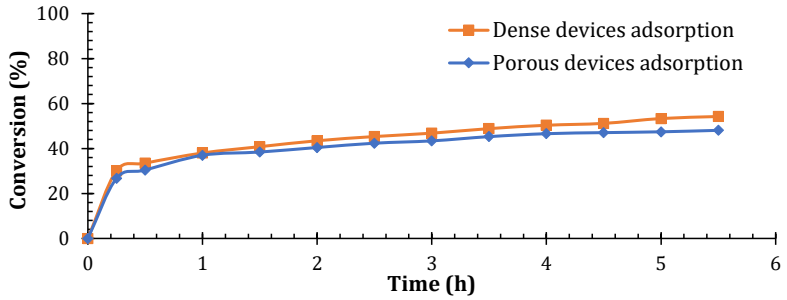

Figure 4. 36 Adsorption study of the dense and porous structured devices with helicoidal shape

The comparison between the photocatalytic activity of porous and dense monoliths is shown in *Figure 4. 37*. The **photocatalytic activity of dense devices is slightly lower than for porous catalyst,** which means that by increasing the porosity or achieving a nano-porosity, the fraction of photo-converted MB could be even higher.

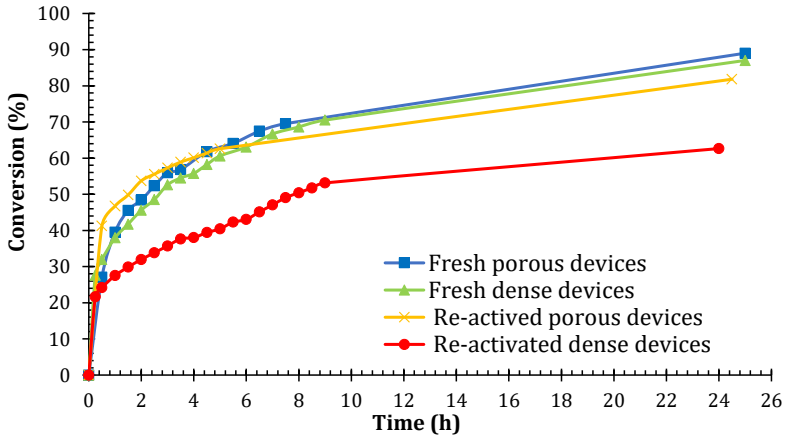

Figure 4. 37 Photo-catalytical activity for methylene blue conversion of porous devices compared with dense devices. Porous devices (squared blue line), dense devices (triangular green line), re-activated porous devices (crossed yellow line) and re-activated dense devices (circular red line).

As mentioned above, re-activating porous devices caused an 8% loss in their catalyst efficiency. However, when dense devices were re-activated using the same thermal program their catalyst efficiency is reduced by 72 %. In other words, **the loss of the photo-catalytical activity of re-activated devices for the dense printed catalyst is more significant than in the case of porous specimens,** because fresh dense devices converted 87.0 % of MB after 24 hours, while re-activated dense catalysts converted a 62.6 %, *Figure 4. 37*.

In addition, reusability of the porous catalyst was examined by employing it repeatedly for four times, after the thermal activation and observing the MB photodegradation during each test. Each photodegradation test repetition was taken for 24 hours, and then monoliths were reactivated following the thermal program before described. *Figure 4. 38* clearly exhibits that the photoconversion ratio remained above 50% even after 4 cycles. Some studies about TiO_2 recycling have been reported. Wang *et al.*[43] prepared polyalinile-TiO_2 composite for MB removing and studied its catalytic activity after 5 cycles of 3h. each one. They reached more than 60% conversion after the fifth cycle. Also, Dou *et al.*[44] studied the same effect after 5 cycles achieving successfully almost a 90% of conversion after the fifth cycle. However, these studies used TiO_2 suspensions and without any treatment in contrast to this work. Nevertheless, here it was necessary done a thermal treatment because catalyst was a monolith and not particles. So, it may retain MB into their porous being necessary the activation via a thermal program. In addition, in this thesis recycling experiments were carried out for 24 hours, much more than reported studies on literature, which probably it could affect at the efficiency. Regarding TiO_2 immobilised, Nawi *et al.*[46] reported a studio after 10 cycles, and they confirmed that when the catalyst is immobilised their activity is smaller than when it is on suspension due to the decrease of BET surface. And also, they reported more than 60% after ten cycles, but studying the conversion for 2 hours and cleaning the catalyst only with ultra-pure water under light irradiation. So, once again the photocatalyst time studio is lower than studied in this work and they do not use a temperature activation which in this case could decrease the BET surface of the printed catalyst too. Hence, the recyclability of the 3D printed TiO_2 catalyst in treating MB contaminated water is satisfactory but further studies could take these variables regarding the catalyst treatment into account for its recycling.

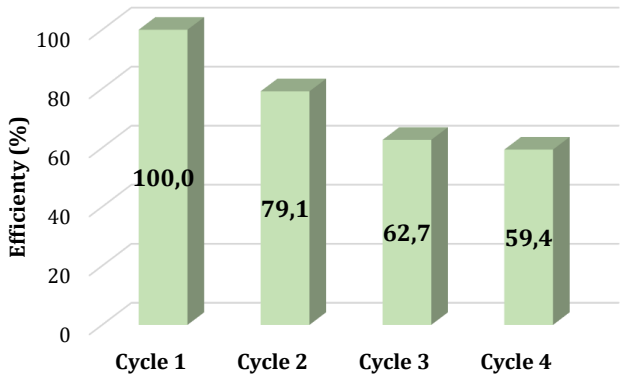

Figure 4. 38 The recycling of 3D printed porous TiO_2 monoliths for photodegradation of MB during four cycles

To corroborate the kinetics of the reaction, the results of the fresh monoliths (porous and dense) was better fitted by the pseudo-second-order kinetic model, k_{porous} =5.44×10^{-4} mol^{-1}·L·min^{-1} and k_{dense}=4.24×10^{-4} mol^{-1}·L·min^{-1}, *Figure 4. 39*

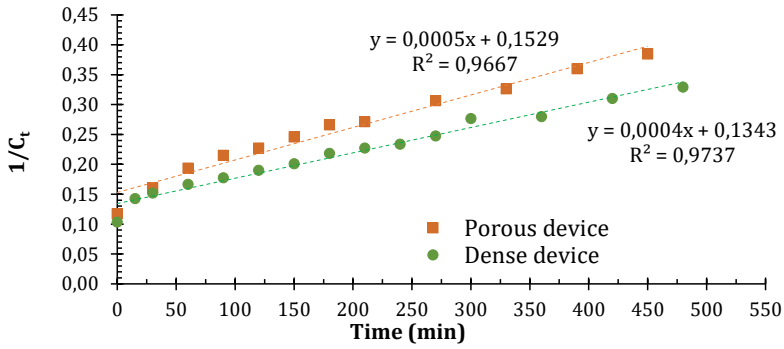

Figure 4. 39 Pseudo-second-order kinetics for photodegradations of methylene blue onto 3D printed TiO_2 porous (squared orange line) and dense devices (circular green line)

Lastly, a pack of nonstructured TiO_2 monoliths was studied in order to establish the relation between the catalytic activity and the geometry of the device. 5-6 mm diameter fragments of printed porous monolith were placed in the reactor taking up the same length exposed for the structured catalyst, *Figure 4. 40*.

Figure 4. 40 Unstructured catalyst devices placed into the reactor tube

Figure 4. 41 shows the MB conversion of structured and non-structured devices. As can be seen, during the first two hours the nonstructured catalyst had a higher conversion of contaminant than the structured monolith. However, thereafter, the conversion was lower for the nonstructured monolith, *Figure 4. 40 (magnification)*. This effect may be due to the macropores found in the cross section of the monoliths produced upon the debinding process. In those areas, the contaminant could be adsorbed preferentially.

This argument explains why after 2 hours the conversion is lower, as the light did not irradiate inside the macropores, therefore the contaminant was adsorbed on them, but not photodegraded. Consequently, it can be concluded that the phenomenon observed for the two first two hours in non-structured monoliths corresponded with the adsorption of the contaminant on the pores, while photodegradation prevails afterwards, and this process is higher for 3D printed structured monoliths.

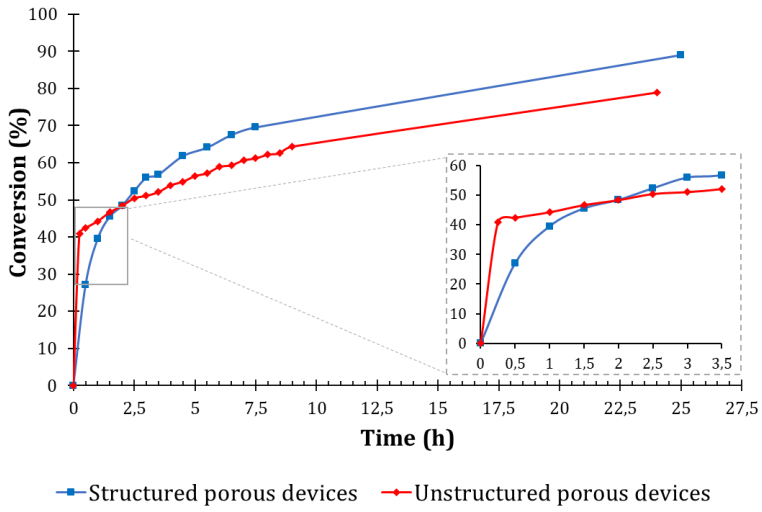

Figure 4. 41 Photodegradation of structured catalyst devices (squared blue line) vs unstructured catalyst devices (rhomboidal red line)

Therefore, the **catalyst conformation influences the performance of the photocatalytic reaction,** corroborating one of the main goals of this chapter, based on how 3D printing allows the fabrication of more complex structures that may enhance the material performance by increasing the active surface through its geometry.

4.7.1.1 3D printed catalysts or 3D printed supports?

As presented in this work, Chapter 3 and Chapter 4 are closely connected. While Chapter 3 studied 3D printing of ceramic support for their subsequent functionalisation with the catalyst, Chapter 4 studied the directly 3D printing of catalyst process.

In order to compare them, both studies used the same 3D structure geometry and the same emergent contaminant degradation. Thus, this section is focused on summarise all result exposed in both chapters to compare and conclude what process would be more adequate to be employed in a large scale. Consequently, the results obtained according to adsorption, photo-catalyst degradation and the kinetic of the MB conversion will be outlined.

Regarding to the MB adsorption, as mentioned in Chapter 3, the percentage of MB adsorbed using the functionalised 3D printed support is similar being around 20-30 %, *Figure 4. 42*. However, this difference comes from the direct 3D printed catalyst via FDM. Initially, it could be thought that ceramic supports obtained by BJ is more porous than the catalysts printed via FDM, which is confirmed by nitrogen adsorption analysis. *Table 4. 5* shows as the green body support manufactures via FDM has a S_{BET}= 1.3852 m^2/g, being almost the double of the porous catalyst fabricated via FDM, S_{BET}= 1.1446 m^2/g. Nevertheless, this support was functionalised via $TiCl_4$ hydrolysis, which caused a smother surface of TiO_2 on the support, reducing the porosity and consequently, a decreasing of the exposed surface. Therefore, the smallest values of adsorption of the contaminant were achieved for the functionalised support.

In addition, comparing both types of monoliths obtained via FDM, it is confirmed that the dense catalyst is much less porous than porous catalystas measured via nitrogen adsorption, being their S_{BET}= 0.2831 m^2/g and S_{BET}= 1.1446 m^2/g respectively. However, despite this big difference regarding their BET surface area, their MB adsorption is pretty similar. This may be due to the mechanism of absorption of methylene blue on the surface thereof, which can cause steric effects. Or even being able to collapse the pores of the catalyst, since methylene blue measures approximately 0.84 nm while monoliths have a pore size (PS) of PS_{dense}=7.8 nm and PS_{porous}=8.3 nm.

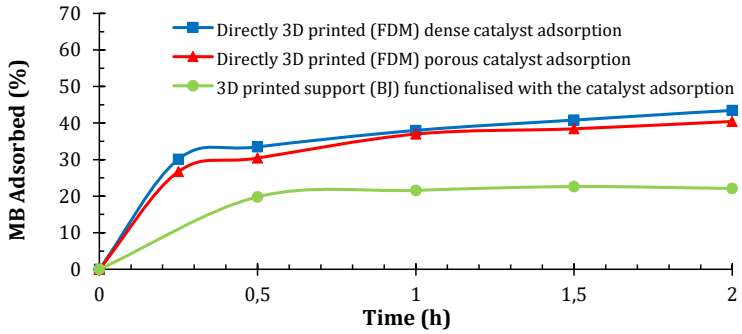

Figure 4. 42 Comparison according to the adsorption of MB between the catalyst obtained directly via FDM vs the printed support via BJ

Table 4. 5 BET Surface Area and pore size parameters of the tested materials via nitrogen adsorption test

	Micro-porosity		Macro-porosity	
Sample	**S_{bet} (m^2/g)**	**Pore Size (nm)**	**Pressure (psia)**	**Pore diameter (µm)**
FDM dense catalyst	0.2831	7.7869	10.0 139.2	21.82 1.567
FDM porous catalyst	1.1446	8.3032	5.01 8.91 14.68 23.33 90.69	43.53 24.49 14.86 9.353 2.406
BJ green body support	1.3852	27.5985	8.91	24.49

Macro-porosity was studied via mercury porosimetry, Figure 4. 43. In this case, the FDM dense catalyst, *Figure 4. 43 (a, b),* shows two pore dimeter volumes around 22 µm and 1.6 µm corresponding to 10.0 and 139.2 psia of mercury respectively. While, FDM porous catalyst, *Figure 4. 43 (c, d),* does not show two well defined pore size distribution. Firstly, it shows small peak at 43.53 µm; 24.49 µm; 14.86 µm and 9.353 µm corresponding with an interval of pressure between 5.01- 23.33 psia. But this sample shows a high defined peak at 90.69 psia associated with a pore diameter volume of 2.406 µm. All these results compared with the porosimetry of the ceramic support discussed in the previous chapter are reported in *Table 4. 5*. These results suggest that all samples exhibit mesoporosity as in all cases the pore diameter is between 2 – 50 nm.

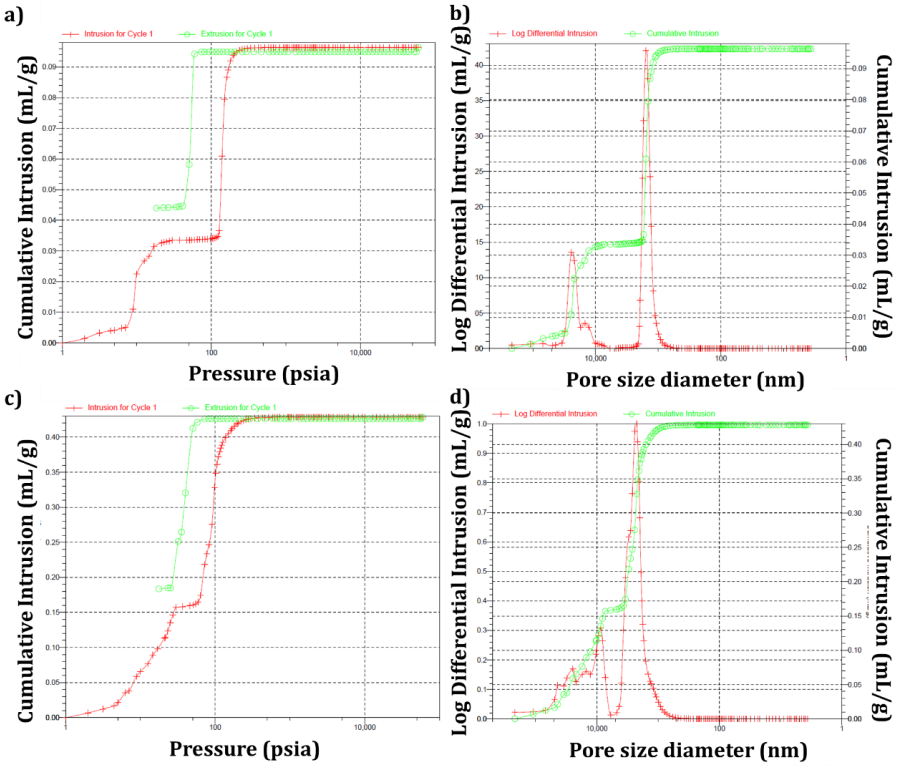

Figure 4. 43 Graph associated with porosimetry test of the (a, b) FDM dense catalyst and (c, d) FDM porous catalyst

As a reminder MB photodegradation depends on the amount of MB absorbed on the surface of the catalyst. Hence, the degradation of contaminant achieved for the functionalised support was smaller too than achieved for direct printed catalyst, *Figure 4. 44*. However, after 24 hours the percentage of MB converted is somewhat higher for the functionalised support, which means that the kinetics are different, but the overall performance after 24 hours is similar in both cases.

Consequently, if these results are analysed regarding the porosity of the samples, all of them show a similar porosity. Thus, the difference may be conditioned by the catalyst itself. This would explain that both catalysts obtained via FDM technique have a similar MB adsorption, while the catalyst manufactured via functionalisation of the BJ support shows a lower MB adsorption as the TiO_2 catalyst was synthesised via a different route.

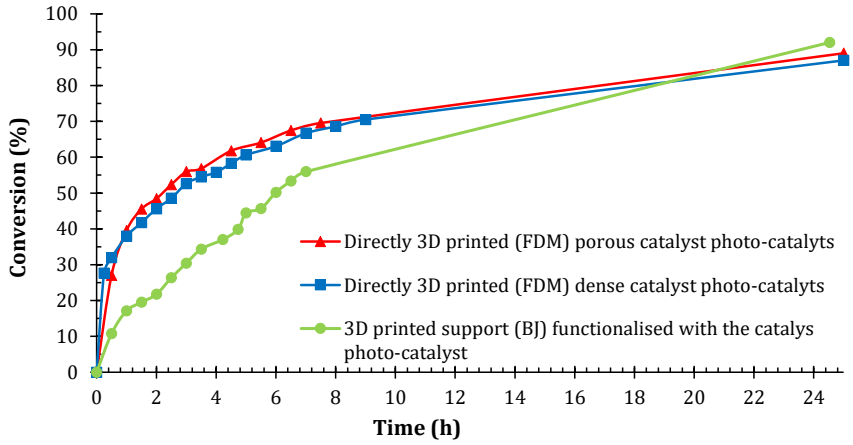

Figure 4. 44 Comparison according to the photodegradation of MB between the catalyst obtained directly via FDM vs the printed support via BJ which was posteriorly functionalised with TiO_2

This hypothesis was confirmed by comparing the kinetics in both cases, *Figure 4. 45*. The graph reveals that the kinetics for porous and dense FDM printed catalysts were higher, than for the functionalised support.

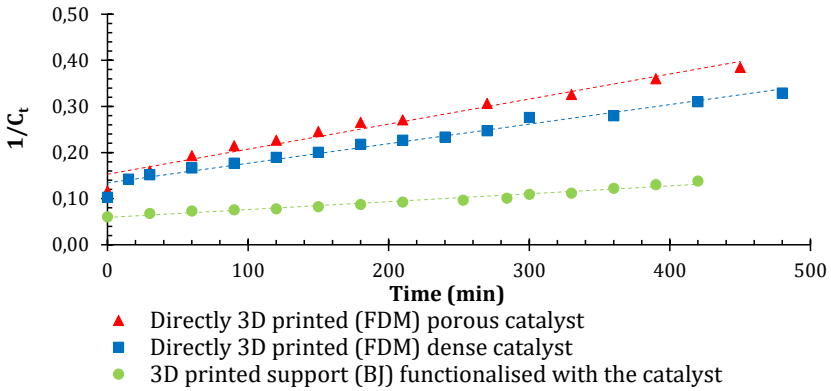

Figure 4. 45 Kinetic comparison between the FDM catalyst vs the printed support via BJ which was further functionalised with TiO_2 (Data reported in Table 4. 6)

Comparing the pseudo-second order kinetic constant in all cases, the **kinetics of photodegradation carried out by porous FDM printed catalysts is five times higher than BJ printed supports functionalised with TiO_2**.

Table 4. 6 Kinetic parameters extracted from graph showed in Figure 4. 45

Sample	Kinetic constant ($mol^{-1}\cdot L\cdot min^{-1}$)
Porous catalyst printed via FDM	5.44×10^{-4}
Dense catalyst printed via FDM	4.24×10^{-4}
Functionalised support printed via BJ	1.71×10^{-4}

However, **the performance after 24 hours is the same for all cases, even higher in BJ supports**.

Regarding the price, the cost of a piece a support was 0.10€ while the cost of a single piece of the direct printed catalyst is 5-10 €. However, despite the higher cost, printed catalysts can be easily reused as the supports lose their geometry in contact with solutions after a while, which could imply performance drops.

To sum up, it has been demonstrated that both routes are viable for contaminant removal and their application on large scale wastewater treatments must be focused on a deeper study about the relationship between performance and cost that both would entail.

4.7.2 Ciprofloxacin conversion

With the same goal, another emergent contaminant molecule was studied, that is a compound belonging to the drug field, specifically, ciprofloxacin (CIP), *Figure 4. 46.* CIP was chosen for degradation studies as is widely used as a third generation fluoroquinolone, i.e. an antibiotic used in infectious diarrhoea, respiratory tract infections, skin infections, typhoid fever, and urinary tract infections, etc.[47,48] The growth and extended use of this type of drug has caused a dramatic increase of its concentration in wastewater treatment plants effluents water, surface water, groundwater and soils which could favour the existence of microbial populations, i.e. fluoroquinolones resistant pathogens.[48,49] Hence, finding suitable catalysts accelerating the degradation of this contaminants can be considered as a hot topic in wastewater treatments.

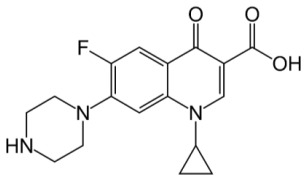

Figure 4. 46 Ciprofloxacin molecule

Previous research has established that TiO_2 is a good catalyst for ciprofloxacin.[50–52] with a well-known conversion mechanism rendering by-products with negligible toxicity.[51] Thus, in this work

the capability of the printed catalytic device for degradation of different types of molecules was evaluated, using the same system and parameters described before.

The degradation process occurs similar to that of MB. First, a part of the pollutant is adsorbed on to the catalyst surface, then light arrives, and then radical reactions are triggered, *Chapter 1, Equations 1.6 - 1.13*. *Paul et. Al*[53] reported a simplified description of the proposed mechanism for this drug photo-degradation, which had been reported in detail in the literature.[54–57] Thus, during photodegradation via TiO_2 catalyst, the pollutant undergoes piperazine ring cleavage, some nitrogen and fluorine loss, *Figure 4. 47*.[54]

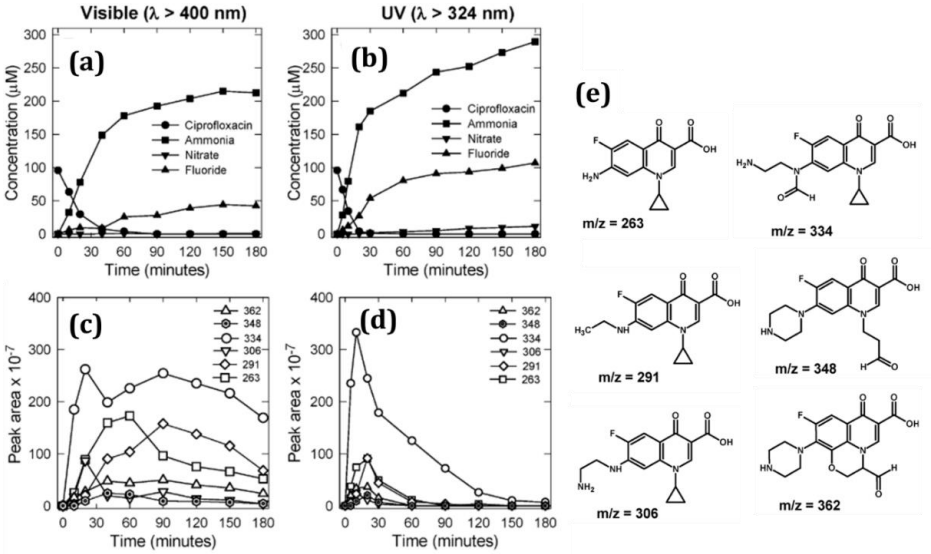

Figure 4. 47 Summary of the result reported by Paul et al.[54] Inorganic product formation under (a) visible light and (b) UV irradiation. Organic product formation under (c) visible light and (d) UV irradiation and (f) the proposed product structures

The experiment was carried out between 240-390 nm, where the pollutant has a maximum absorbance at 278 nm. The steps followed were the same to those of the MB experiment: (i) calibration curve, (ii) photolysis, (iii) adsorption and (iv) photo-degradation.

Figure 4. 48 shows the different absorbance values for a solution of ciprofloxacin (1-20 ppm). The largest concentration presents a somewhat saturated absorbance peak, being the oversaturation beyond 20ppm. For this reason, it is recommended that the photocatalytic tests are performed at lower concentrations.

The calibration curve was the result of representing the A_{max} (278nm) versus the concentration (ppm), (R^2= 0.9997). Consequently, the concentration of future tests can be known by measuring their absorbance.

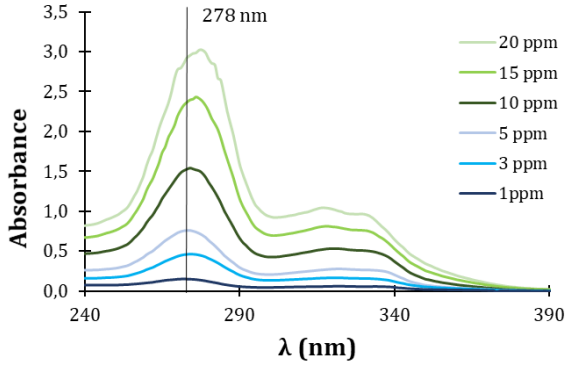

Figure 4. 48 Absorbance of ciprofloxacin in the corresponding calibration curve

Regarding the photolysis effect, an initial concentration of 15.7 ppm was employed to study whether this drug degrades only by the light action. *Figure 4. 49* shows as ciprofloxacin did not degrade under UV-Vis light without the presence of the catalyst. **Therefore, it can be concluded that ciprofloxacin does not undergo photodegradation by itself.**

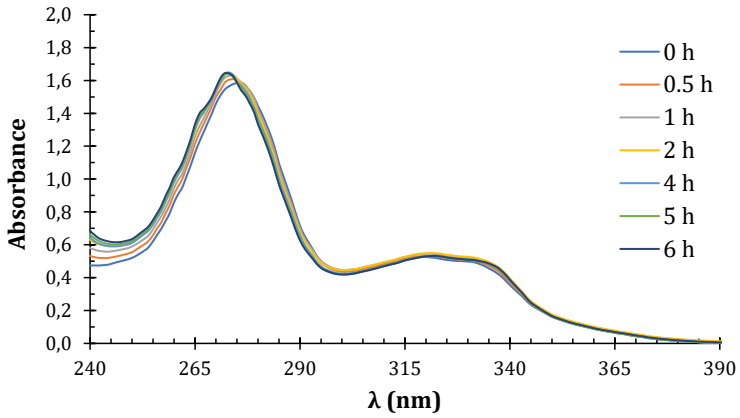

Figure 4. 49 Absorbances graph of ciprofloxacin solution during photolysis test

Photo-catalyst conversion was measured using four porous monoliths on the tube reactor, analogous to MB experiments done. Photodegradation data are collected in *Table 4. 7* and represented in *Figure 4. 50*. This graph shows that **34,8% of ciprofloxacin was converted after 5 h,** and **50,87% after 50 h**.

Table 4. 7 Data of ciprofloxacin conversion

Time (h)	Absorbance	[C] (ppm)	Conversion (%)
0	2,4799	15,7	0,0
0,5	1,8985	12,0	23,2
1	1,7760	11,3	28,1
1,5	1,7344	11,0	29,7
2	1,7113	10,9	30,6
2,5	1,6783	10,7	32,0
3	1,6672	10,6	32,4
4	1,6309	10,4	33,8
5	1,6800	10,7	34,9
6	1,5791	10,0	35,9
7	1,5844	10,1	35,7
25,5	1,4241	9,1	42,1
50	1,2037	7,7	50,9

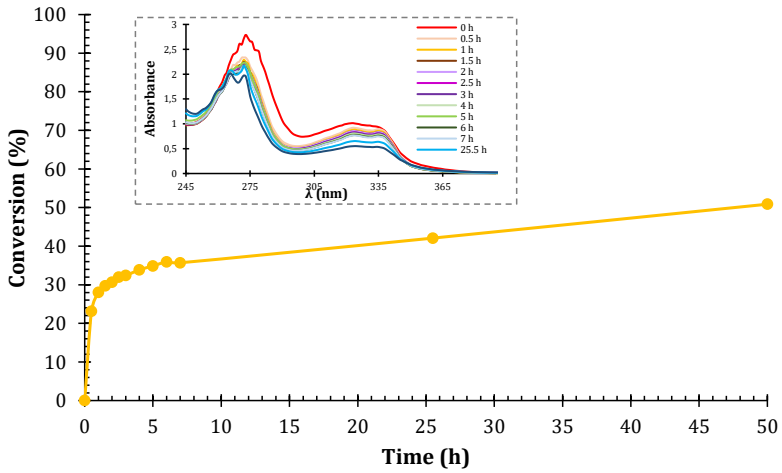

Figure 4. 50 Conversion of ciprofloxacin with porous printed catalyst from (data from Table 4. 7)

Also, the reusability of the catalyst monoliths was tested employing the same thermal program used in the case of MB experiments. *Figure 4. 51* **presents the loss of catalytic efficiency when the monolith is reactivated, which corresponds to 13.3 %.** This is somewhat higher than the obtained for MB, however they are different process so they could not be compared straightaway. Thus, it can be concluded that it is a good result regarding the reusability of the catalyst for this process.

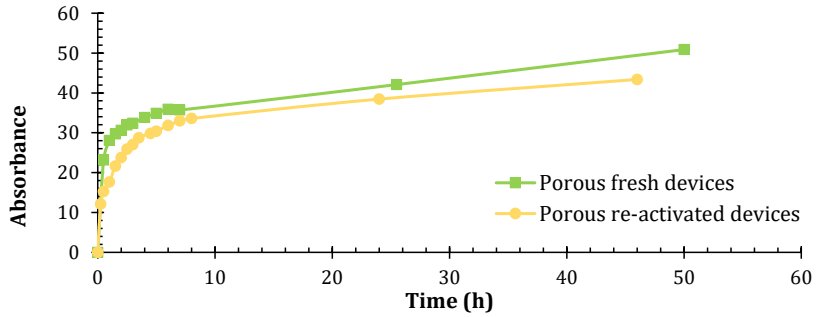

Figure 4. 51 Photodegradation graph of ciprofloxacin using fresh printed devices vs using re-activated devices

In summary, 3D printed TiO_2 monoliths exhibit catalytic activity for the degradation of different emergent contaminants, such as dyes and drugs. These results obtained provide important insights into the role of 3D printing process for the manufacturing of catalytical materials, saving material, time and money compared with the traditional manufacturing process. Thus, it would be possible to employ these monolithic catalysts for wastewater treatment to remove different types of molecules that can be dangerous for the environment and our health.

4.8 References

[1] Borges, M. E.; Díaz, L. Catalytic Packed-Bed Reactor Configuration for Biodiesel Production Using Waste Oil as Feedstock. Bioenergy Res. (2013), 6, 222–228, doi:10.1007/s12155-012-9246-7.

[2] Borges, M. E.; Sierra, M.; Méndez-Ramos, J.; Acosta-Mora, P.; Ruiz-Morales, J. C.; Esparza, P. Solar Degradation of Contaminants in Water: TiO_2 Solar Photocatalysis Assisted by up-Conversion Luminescent Materials. Sol. Energy Mater. Sol. Cells (2016), 155, 194–201, doi:10.1016/j.solmat.2016.06.010.

[3] Hernández-Afonso, L.; Fernández-González, R.; Esparza, P.; Borges, M. E.; González, S. Dí.; Canales-Vázquez, J.; Ruiz-Morales, J. C. Ceramic-Based 3D Printed Supports for Photocatalytic Treatment of Wastewater. J. Chem. (2017), 9, doi:10.1155/2017/7602985.

[4] Robert L. Mott. Mecanica de Fluidos, 6th ed.; Pablo Miguel Guerrera Rosas, Bernardino Gutiérrez Hernández, E. T. H., Ed.; México, (2006), ISBN: 970-26-0805-8.

[5] Tinkercad https://www.tinkercad.com/#/ (accessed Apr 19, 2020).

[6] J. Canales-Vázquez, G. B. Sánchez, J.R.Marín, V. Yagüe & J.J. López. Method for Obtaining Ceramic Barbotine for the Production of Filaments for 3D-FDM Printing, Barbotine Obtained Using Said Method, and Ceramic Filaments. WO2017191340A1, 2017.

[7] Brooks, H. L.; Rennie, A. E. W.; Abram, T. N.; McGovern, J.; Caron, F. Variable Fused Deposition Modelling - Analysis of Benefits, Concept Design and Tool Path Generation. Innov. Dev. Virtual Phys. Prototyp. - Proc. 5th Int. Conf. Adv. Res. Rapid Prototyp. (2012), 511–517, doi:10.1201/b11341-83.

[8] Dachille, F.; Simons, P. Y.; Roy, R. Pressure-Temperature Studies of Anatase, Brookite, Rutile and TiO_2 (II): A Reply. Am. Mineral. (1969), 54 (9–10), 1481–1482,.

[9] Nie, X.; Zhuo, S.; Maeng, G.; Sohlberg, K. Doping of TiO_2 Polymorphs for Altered Optical and Photocatalytic Properties. Int. J. Photoenergy (2009), 22, doi:10.1155/2009/294042.

[10] Nichols, John W. Anthony, Richard A. Bideaux, Kenneth W. Bladh, and M. C. Anatase Physical and Chemical Properties. In Handbook of Mineralogy; America, M. S. of, Ed.; USA, (1997); p 628, ISBN: 0962209724.

[11] Nichols, John W. Anthony, Richard A. Bideaux, Kenneth W. Bladh, and M. C. Rutile Physical and Chemical Properties. In Dictionary Geotechnical Engineering/Wörterbuch GeoTechnik; America, M. S. of, Ed.; Springer Berlin Heidelberg: Berlin, Heidelberg, (2014); pp 1154–1154 doi:10.1007/978-3-642-41714-6_183890.

[12] Nichols, John W. Anthony, Richard A. Bideaux, Kenneth W. Bladh, and M. C. Brookite Physical and Chemical Properties. In Handbook of Mineralogy; America, M. S. of, Ed.; USA, (1997); p 628, ISBN: 0962209724.

[13] Hanaor, D. A. H. Fabrication of Single- and Mixed-Phase Titanium Dioxide Photocatalysts. The University of New South Wales, (2011).

[14] Hanaor, D. A. H.; Sorrell, C. C. Review of the Anatase to Rutile Phase Transformation. J. Mater. Sci. (2011), 48, 855–874, doi:10.1007/s10853-010-5113-0.

[15] Li, J.; Ishigaki, T. Brookite - Rutile Phase Transformation of TiO 2 Studied with Monodispersed Particles. Acta Mater. (2004), 52, 5143–5150, doi:10.1016/j.actamat.2004.07.020.

[16] Hanaor, D. A. H.; Sorrell, C. C. Review of the Anatase to Rutile Phase Transformation. J. Mater. Sci. (2011), 46 (4), 855–874, doi:10.1007/s10853-010-5113-0.

[17] Ohno, T.; Tokieda, K.; Higashida, S.; Matsumura, M. Synergism between Rutile and Anatase TiO_2 Particles in Photocatalytic Oxidation of Naphthalene. Appl. Catal. A Gen. (2003), 244 (2), 383–391, doi:10.1016/S0926-860X(02)00610-5.

[18] Sun, J.; Gao, L.; Zhang, Q. Synthesizing and Comparing the Photocatalytic Properties of High Surface Area Rutile and Anatase Titania Nanoparticles. J. Am. Ceram. Soc. (2003), 86 (10), 1677–1682, doi:10.1111/j.1151-2916.2003.tb03539.x.

[19] Ohno, T.; Sarukawa, K.; Matsumura, M. Photocatalytic Activities of Pure Rutile Particles Isolated from TiO_2 Owder by Dissolving the Anatase Component in HF Solution. J. Phys. Chem. B (2001), 105 (12), 2417–2420, doi:10.1021/jp003211z.

[20] Kavan, L.; Grätzel, M.; Gilbert, S. E.; Klemenz, C.; Scheel, H. J. Electrochemical and Photoelectrochemical Investigation of Single-Crystal Anatase. J. Am. Chem. Soc. (1996), 118 (28), 6716–6723, doi:10.1021/ja954172l.

[21] Tran, H. T. T.; Kosslick, H.; Ibad, M. F.; Fischer, C.; Bentrup, U.; Vuong, T. H.; Nguyen, L. Q.; Schulz, A. Photocatalytic Performance of Highly Active Brookite in the Degradation of Hazardous Organic Compounds Compared to Anatase and Rutile. Appl. Catal. B Environ. (2017), 200, 647–658, doi:10.1016/j.apcatb.2016.07.017.

[22] Jiang, J.; Zhu, S.; Xu, W.; Cui, Z.; Yang, X. Synthesis and Photocatlytic Performance of Nano-Sized TiO_2 Materials Prepared by Dealloying Ti-Cu-Pd Amorphous Alloys. Mater. Res. Bull. (2015), 65, 302–306, doi:10.1016/j.materresbull.2015.01.050.

[23] Li, K.; Peng, J.; Zhang, M.; Heng, J.; Li, D.; Mu, C. Comparative Study of the Effects of Anatase and Rutile Titanium Dioxide Nanoparticles on the Structure and Properties of Waterborne Polyurethane. Colloids Surfaces A Physicochem. Eng. Asp. (2015), 470, 92–99, doi:10.1016/j.colsurfa.2015.01.072.

[24] PanReac AppliChem. Methylene Blue https://www.itwreagents.com/iberia/en/product/methylene-blue-ci-52015reag-ph-eur-for-analysis/121170 (accessed Apr 22, 2020).

[25] Soltani, T.; Entezari, M. H. Photolysis and Photocatalysis of Methylene Blue by Ferrite Bismuth Nanoparticles under Sunlight Irradiation. J. Mol. Catal. A Chem. (2013), 377, 197–203, doi:10.1016/j.molcata.2013.05.004.

[26] Li, M.; Qiang, Z.; Pulgarin, C.; Kiwi, J. Accelerated Methylene Blue (MB) Degradation by Fenton Reagent Exposed to UV or VUV/UV Light in an Innovative Micro Photo-Reactor. Appl. Catal. B Environ. (2016), 187, 83–89, doi:10.1016/j.apcatb.2016.01.014.

[27] Lachheb, H.; Puzenat, E.; Houas, A.; Ksibi, M.; Elaloui, E.; Guillard, C.; Herrmann, J. M. Photocatalytic Degradation of Various Types of Dyes (Alizarin S, Crocein Orange G, Methyl Red, Congo Red, Methylene Blue) in Water by UV-Irradiated Titania. Appl. Catal. B Environ. (2002), 39 (1), 75–90, doi:10.1016/S0926-3373(02)00078-4.

[28] Yu, W.; Liu, X.; Pan, L.; Li, J.; Liu, J.; Zhang, J.; Li, P.; Chen, C.; Sun, Z. Enhanced Visible Light Photocatalytic Degradation of Methylene Blueby F-Doped TiO 2. Appl. Surf. Sci. (2014), 319 (1), 107–112, doi:10.1016/j.apsusc.2014.07.038.

[29] Du, P.; Bueno-López, A.; Verbaas, M.; Almeida, A. R.; Makkee, M.; Moulijn, J. A.; Mul, G. The Effect of Surface OH-Population on the Photocatalytic Activity of Rare Earth-Doped P25-TiO_2 in Methylene Blue Degradation. J. Catal. (2008), 260 (1), 75–80, doi:10.1016/j.jcat.2008.09.005.

[30] Mohamed, M. M.; Al-Esaimi, M. M. Characterization, Adsorption and Photocatalytic Activity of Vanadium-Doped TiO_2 and Sulfated TiO_2 (Rutile) Catalysts: Degradation of Methylene Blue Dye. J. Mol. Catal. A Chem. (2006), 255 (1–2), 53–61, doi:10.1016/j.molcata.2006.03.071.

[31] Naraginti, S.; Stephen, F. B.; Radhakrishnan, A.; Sivakumar, A. Zirconium and Silver Co-Doped TiO_2 Nanoparticles as Visible Light Catalyst for Reduction of 4-Nitrophenol, Degradation of Methyl Orange and Methylene Blue. Spectrochim. Acta - Part A Mol. Biomol. Spectrosc. (2015), 135, 814–819, doi:10.1016/j.saa.2014.07.070.

[32] Umebayashi, T.; Yamaki, T.; Tanaka, S.; Asai, K. Visible Light-Induced Degradation of Methylene Blue on S-Doped TiO_2. Chem. Lett. (2003), 32 (4), 330–331, doi:10.1246/cl.2003.330.

[33] Xiao, Q.; Zhang, J.; Xiao, C.; Si, Z.; Tan, X. Solar Photocatalytic Degradation of Methylene Blue in Carbon-Doped TiO_2 Nanoparticles Suspension. Sol. Energy (2008), 82 (8), 706–713, doi:10.1016/j.solener.2008.02.006.

[34] Xu, N.; Shi, Z.; Fan, Y.; Dong, J.; Shi, J.; Hu, M. Z. C. Effects of Particle Size of TiO_2 on Photocatalytic Degradation of Methylene Blue in Aqueous Suspensions. Ind. Eng. Chem. Res. (1999), 38 (2), 373–379, doi:10.1021/ie980378u.

[35] Dariani, R. S.; Esmaeili, A.; Mortezaali, A.; Dehghanpour, S. Photocatalytic Reaction and Degradation of Methylene Blue on TiO_2 Nano-Sized Particles. Optik (Stuttg). (2016), 127 (18), 7143–7154, doi:10.1016/j.ijleo.2016.04.026.

[36] Shimizu, N.; Ogino, C.; Dadjour, M. F.; Murata, T. Sonocatalytic Degradation of Methylene Blue with TiO_2 Pellets in Water. Ultrason. Sonochem. (2007), 14 (2), 184–190, doi:10.1016/j.ultsonch.2006.04.002.

[37] Fabiyi, M. E.; Skelton, R. L. Photocatalytic Mineralisation of Methylene Blue Using Buoyant TiO_2-Coated Polystyrene Beads. J. Photochem. Photobiol. A Chem. (2000), 132 (1–2), 121–128, doi:10.1016/S1010-6030(99)00250-6.

[38] Ling, C. M.; Mohamed, A. R.; Bhatia, S. Performance of Photocatalytic Reactors Using Immobilized TiO_2 Film for the Degradation of Phenol and Methylene Blue Dye Present in Water Stream. Chemosphere (2004), 57 (7), 547–554, doi:10.1016/j.chemosphere.2004.07.011.

[39] Lee, B. N.; Liaw, W. D.; Lou, J. C. Photocatalytic Decolorization of Methylene Blue in Aqueous TiO_2 Suspension. Environ. Eng. Sci. (1999), 16 (3), 165–175, doi:10.1089/ees.1999.16.165.

[40] Nogueira, R. F. P.; Jardim, W. F. Photodegradation of Methylene Blue: Using Solar Light and Semiconductor (TiO_2). J. Chem. Educ. (1993), 70 (10), 863–864, doi:10.1021/ed070p861.

[41] A new Circular Economy Action Plan for a Cleaner and More Competitive Europe (EU Circular Economy Action Plan). Europrean Commission. https://ec.europa.eu/environment/circular-economy/ (accessed May 1, 2020).

[42] General measures about circular economy. Internal Market, Industry, Entrepreneurship and SMEs. https://ec.europa.eu/growth/industry/sustainability/circular-economy_en (accessed May 1, 2020).

[43] Wang, F.; Min, S.; Han, Y.; Feng, L. Superlattices and Microstructures Visible-Light-Induced Photocatalytic Degradation of Methylene Blue with Polyaniline-Sensitized TiO_2 Composite Photocatalysts. Superlattices Microstruct. (2010), 48 (2), 170–180, doi:10.1016/j.spmi.2010.06.009.

[44] Dou, L.; Gao, L.; Yang, X.; Song, X. Hierarchical Architectures TiO_2: Pollen-Inducted Synthesis , Remarkable Crystalline-Phase Stability , Tunable Size , and Reused Photo-Catalysis. J. Hazard. Mater. (2012), 203–204, 363–369, doi:10.1016/j.jhazmat.2011.12.043.

[45] Subba, K. V.; Subrahmanyam, M.; Boule, P. Immobilized TiO_2 Photocatalyst during Long-Term Use: Decrease of Its Activity. (2004), 49, 239–249, doi:10.1016/j.apcatb.2003.12.017.

[46] Nawi, M. A.; Zain, S. Enhancing the Surface Properties of the Immobilized Degussa P-25 TiO 2 for the Efficient Photocatalytic Removal of Methylene Blue from Aqueous Solution. Appl. Surf. Sci. (2012), 258 (16), 6148–6157, doi:10.1016/j.apsusc.2012.03.024.

[47] Sharma, P. C.; Jain, A.; Jain, S.; Pahwa, R.; Yar, M. S. Ciprofloxacin: Review on Developments in Synthetic, Analytical, and Medicinal Aspects. J. Enzyme Inhib. Med. Chem. (2010), 25 (4), 577–589, doi:10.3109/14756360903373350.

[48] Ciprofloxacin https://www.drugs.com/monograph/ciprofloxacin.html (accessed Apr 23, 2020).

[49] Chaudhry, N. A.; Flynn, H. W.; Murray, T. G.; Tabandeh, H.; Mello, M. O.; Miller, D. Emerging Ciprofloxacin-Resistant Pseudomonas Aeruginosa. Am. J. Ophthalmol. (1999), 128 (4), 509–510, doi:10.1016/S0002-9394(99)00196-8.

[50] Hassani, A.; Khataee, A.; Karaca, S.; Karaca, C.; Gholami, P. Sonocatalytic Degradation of Ciprofloxacin Using Synthesized TiO_2 Nanoparticles on Montmorillonite. Ultrason. Sonochem. (2017), 35, 251–262, doi:10.1016/j.ultsonch.2016.09.027.

[51] Feng, X.; Wang, P.; Hou, J.; Qian, J.; Ao, Y.; Wang, C. Significantly Enhanced Visible Light Photocatalytic Efficiency of Phosphorus Doped TiO_2 with Surface Oxygen Vacancies for Ciprofloxacin Degradation: Synergistic Effect and Intermediates Analysis. J. Hazard. Mater. (2018), 351, 196–205, doi:10.1016/j.jhazmat.2018.03.013.

[52] Deng, J.; Wu, G.; Yuan, S.; Zhan, X.; Wang, W.; Hu, Z. H. Ciprofloxacin Degradation in UV/Chlorine Advanced Oxidation Process: Influencing Factors, Mechanisms and

Degradation Pathways. J. Photochem. Photobiol. A Chem. (2019), 371, 151–158, doi:10.1016/j.jphotochem.2018.10.043.

[53] Paul, T.; Dodd, M. C.; Strathmann, T. J. Photolytic and Photocatalytic Decomposition of Aqueous Ciprofloxacin: Transformation Products and Residual Antibacterial Activity. Water Res. (2010), 44 (10), 3121–3132, doi:10.1016/j.watres.2010.03.002.

[54] Paul, T.; Miller, P. L.; Strathmann, T. J. Visible-Light-Mediated TiO_2 Photocatalysis of Fluoroquinolone Antibacterial Agents. Environ. Sci. Technol. (2007), 41 (13), 4720–4727, doi:10.1021/es070097q.

[55] Albini, A.; Monti, S. Photophysics and Photochemistry of Fluoroquinolones. Chem. Soc. Rev. (2003), 32 (4), 238–250, doi:10.1039/b209220b.

[56] Marinas, M.; Sa, E.; Rojas, M. M.; Moalem, M.; Urbano, F. J.; Guillou, C.; Rallo, L. A Nuclear Magnetic Resonance (1 H and 13 C) and Isotope Ratio Mass Spectrometry (d 13 C , d 2 H and d 18 O) Study of Andalusian Olive Oils. Rapid Commun. Mass Spectrom. (2010), 24, 1457–1466, doi:10.1002/rcm.

[57] Palominos, R.; Freer, J.; Mondaca, M. A.; Mansilla, H. D. Evidence for Hole Participation during the Photocatalytic Oxidation of the Antibiotic Flumequine. J. Photochem. Photobiol. A Chem. (2008), 193 (2–3), 139–145, doi:10.1016/j.jphotochem.2007.06.017.

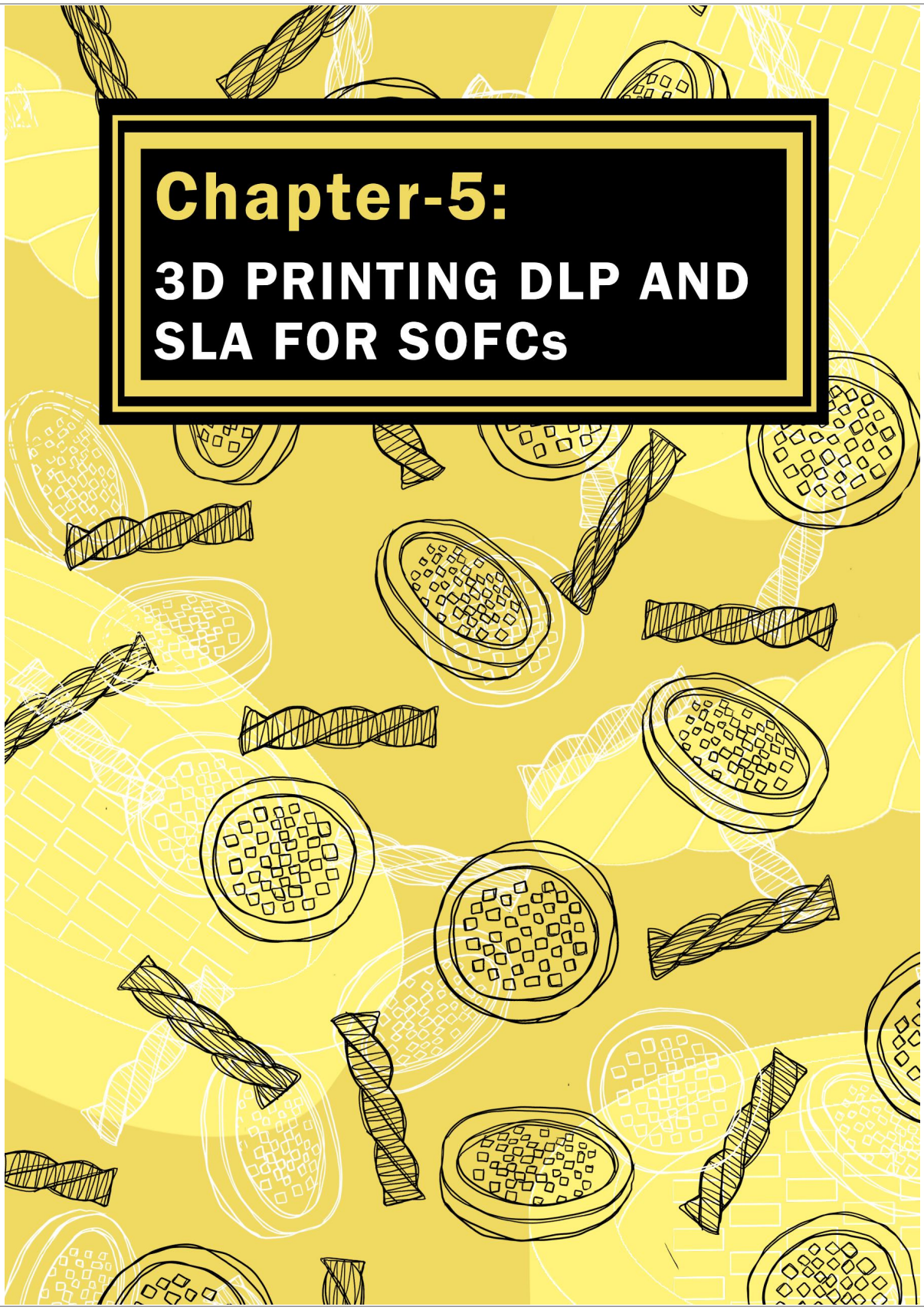

5. 1 Device architecture and preliminary considerations

As presented in *Chapter 1*, SOFC components can be obtained by ceramic 3D printing, simplifying the number of steps during the cell fabrication and reducing the waste material. In this chapter, we will focus on achieving 3D printed electrolytes for SOFCs. The first goal is to optimize the fabrication of YSZ electrolytes by using a DLP printer prototype called Spid3r (developed by Print3D Solutions). This will be done by comparison of the DLP-printed flat electrolytes with analogue reference electrolytes manufactured using a SLA commercial printer from 3DCeram (at the Catalonia Institute for Energy Research, IREC). This chapter is complemented with *Appendix 7*, dedicated to the development of robocasting electrode deposition, for the ultimate goal of fabricating complete SOFC cells by 3D printing.

One important parameter of the SOFCs is the resistance of the electrolyte. This resistance is directly related to the conductivity and geometry of the part. As presented in *Chapter 2, Section 2.3.1*, the resistance of the electrolyte is inversely proportional to the conductivity, while it is directly proportional to the thickness sample and inversely proportional to its surface area ($R=L/(\sigma*S)$). Considering the abovementioned, the purpose of this work is developing a 3D printed electrolyte where the thickness is as small as possible, and the area is as big as possible. To reach this goal, flat electrolytes will be printed first trying to minimize the thickness while afterwards, 3D structures will be produced to increase the electrolyte performance by increasing the area.

Figure 5. 1 show the digital design of the electrolyte with expected dimensions for each printer. As depicted in the figure, H-like pieces with flat electrolytes of 500 µm in thickness will be printed first with the SLA commercial printer to optimise the cathode attachment and serve as a reference. Afterwards, these electrolytes will be compared with equivalent electrolytes obtained via our DLP prototype.

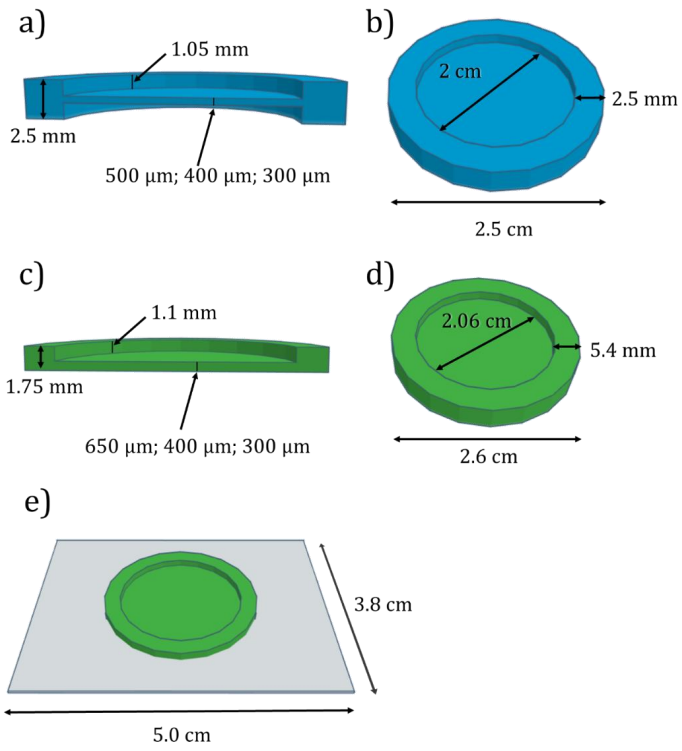

Figure 5. 1 H-like flat electrolyte design for SLA printing (a) cross section, (b) top view. Electrolyte design for DLP printing (c) cross section, (d) top view, (e) electrolyte with platform to ensure a good attachment to the build platform of the printer

It is important to notice here that, in the case of the SLA 3D printer, the dimensions of the printed structure will be the same as in the digital design, *Figure 5. 1 (a & b),* since the machine has a software able to introduce geometrical corrections occurring during debinding and sintering processes (for an optimized slurry). However, for the DLP printer prototype, the digital design must be optimised to achieve a printed structure with the desired aspect depending on the slurry. In this case, the sintering shrinkage must be studied for each slurry in order to achieve a final structure with the proposed height, width and depth. Once the shrinkage factor and the difference between the dimensions of the design and the printed object are studied, the digital design must be modified. In this way, the printed architecture will be exactly as the digital design. Consequently, the dimensions of the electrolyte for DLP, *Figure 5. 1 (c & d)* are not the same that electrolyte for SLA, *Figure 5.1 (a & b)*. In addition, it is necessary to add a platform on the DLP digital design, *Figure 5. 1 (e)*, to raise the attached surface of the cured slurry to the build platform,

preventing the tank drags the cured paste in its path. *Figure 5. 2* show 3D structured electrolytes designs.

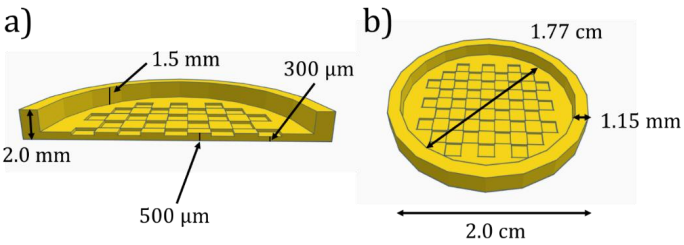

Figure 5. 2 Structured electrolyte design for SLA printing(a) cross section, (b) top view.

5.2 Slurry development

Slurries for the DLP printer were developed during this thesis. DLP slurries are typically based on monomer resin, photo-initiator, solvent, dispersant and ceramic powders. Although there are some commercial resins that directly contains the monomer and the photo-initiator, in all cases, the ratio of the slurry components, the procedure and the printing parameters must be optimized. This is the main purpose of this work. In the next sections, the components used for the development of the mixture and their effect on the rheology and printability of the pastes will be described.

5.2.1 Organic vehicle: monomer and photoinitiator

A resin was developed using polyethylene glycol diacrylate (PEGDA) as monomer and Irgacure 819 [Bis(2,4,6-trimethylbenzoyl)-phenylphosphineoxide] as photoinitiator. The optimum amount of photoinitiator was optimized by trying to achieve the best resolution of cured layers at the lowest curing time possible since depending on the photoinitiator ratio employed, the absorption region of the light spectrum varies.

In this regards, Irgacure 819 changes its maximum absorption wavelength depending on its concentration.[1,2] This fact is due photoinitiator interacts with the solvent. As PI molecules are sensitive to charge acceptor and donor species, could interact with the solvent modifying the energy levels, which leads the photoinitiator to change its absorption maximum to other new wavelengths. However, there are not a lot studies in the bibliography due to once 1-5% of the monomer is cure after photoinitiator absorbs light, the formulation of the mixture becomes very complex. So, some parameters as rate constants, quantum yields applied on photo-reactions or understanding how chain reactions works, is inapplicable to mixture with photoinitiatior without

solvent. Therefore, the knowledge of behaviour and reactivity of the photoinitiators in solvents has restricted application to real systems.[3] *Figure 5. 3* shows the effect of the concentration of the photoinitiator on the change in the maximum of absorption, which is between 360 - 440 nm (corresponding to UVA/visible range) for high concentrations while between 280 - 340 nm (corresponding to UVB/UVA range) for low ones. It is good to keep this fact in mind when using mixtures where the solvent plays a fundamental role in the rheology of the pulp. However, in cases where the photoinitiator is used by itself, this fact will not be relevant and we will work in the wavelength zone where it presents its characteristic absorption maximum.

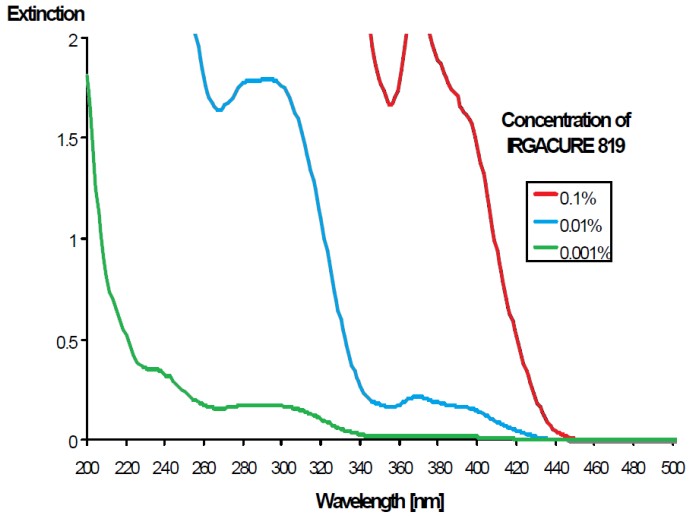

Figure 5. 3 Irgacure 819 absorption spectrum according to the concentration (diluted in acetonitrile)[1]

Accordingly, in this work, different amounts of Irgacure 819 were added to PEGDA resin formulations, namely, 0.5, 0.7 and 1 wt. %., to optimize the curing process. Lower concentration values were discarded because the curing time was above one minute to reach defined patterns. The best result was obtained when 1wt. %. Irgacure 819 was employed, obtaining a good resolution after only 3 seconds, *Figure 5. 4*.

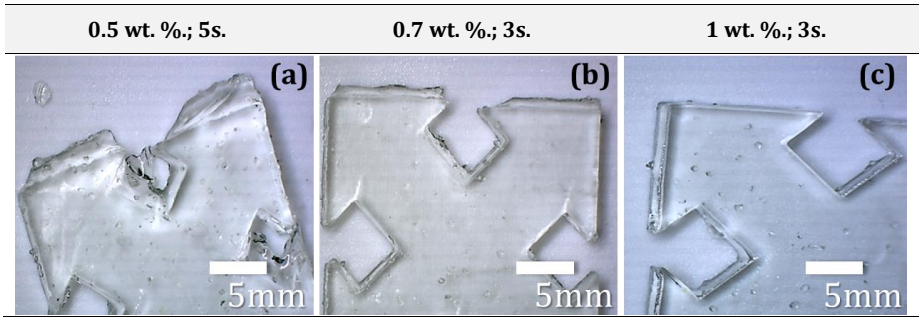

Figure 5. 4 Cured layers using the resin made by PEGDA and Irgacure 819 (a) 0.5wt. %. Irgacure 819 cured after 5 seconds (b) 0.7wt. %. Irgacure 819 cured after 3 seconds (c) 1wt. %. Irgacure 819 cured after 3 seconds

However, when the mixture is mixed with YSZ powder, the curing time needs to be increased at least up to 10 seconds. During this extra time, over-curing of the areas out of the pattern mask is taking place, i.e. the parts exposed to the "black light" of the projector (typically a dim white light). In order to improve this over-curing phenomena due to long exposition, a photoninitiator combination was employed in order to improve the adsorption spectrum in the UV-visible zone. With this purpose the photoinitiator called Sudan I (1-Phenylazo-2-naphthol)[4] was added to the mixture. However, using Sudan I the resin did not cure in spite of increasing the concentration (0.06 - 0.1 wt. % range). Because of this poor behaviour, this approach was finally discarded.

Due to the issues with the photoinitiators, commercial resins with maximum absorption in the UV-visible were also evaluated in our DLP system. Specifically, three different resins were tested from Standard Blend, corresponding to red, black and unpigmented resin. The formulation of this family of resins is based on acrylate monomers, glycol diacrylate monomers and phosphine oxide based photo initiator according to the MSDS sheets[5] supplied by the manufacturer. Regarding the curing time, the company reported that all proposed resins cure between 2 and 4 seconds when a DLP projector of 2500-3000 lm is employed.[6]

The maximum absorption of the unpigmented resin lays between 225 nm and 415 nm, presenting a maximum at 405 nm, according to the manufacturer. In order to verify this important specification for our application, its absorbance was measured in our lab by using a UV-Vis spectrophotometer. *Figure 5. 5* shows the absorption spectrum of the resin by irradiation with wavelengths between 200 - 2000 nm. Confirming the manufacturer's specifications, the resin absorbs in UV and in an interval of the visible range (380 – 450 nm), showing its suitability for our projector. Different dilutions of the resin were measured, *Figure 5. 5 (and inset)*, corroborating that more diluted resin absorbs at shorter wavelengths. The absorption intensity of the sample

does not decrease, but it was displaced to lower wavelengths because of the new chemical species present created by the interactions between resin molecules with the solvent.

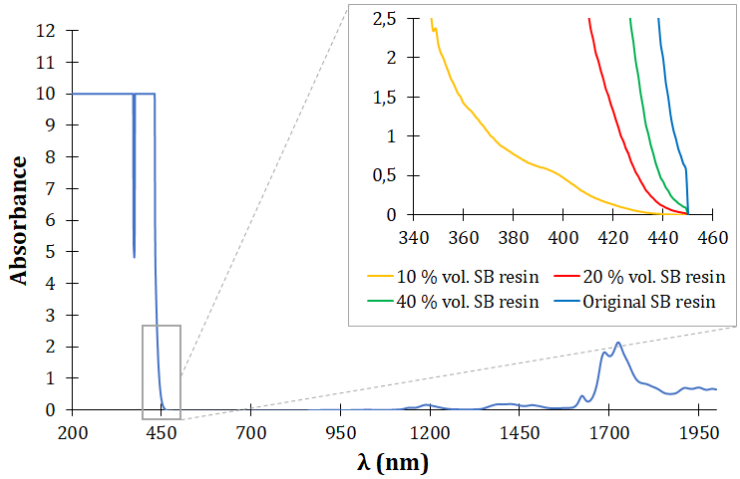

Figure 5. 5 Standard Blend (SB) Unpigmented resin absorption spectrum (200 – 2000 nm) (original and diluted in ethanol)

Regarding the curing tests, all resins were evaluated for curing times of 3 and 5 seconds to compare with our home-made mixture of PEGDA and Irgacure 819 (1 wt. %.). In *Figure 5.* 6 the resolution achieved using the different Standard Blend resins is presented (see a detailed study in the next *Section 5.3.2*). Unpigmented resins offered the best results for curing times of 3 seconds, *Figure 5. 6* (a). The other resins have not a good definition at the same curing time, *Figure 5. 6* (c, e). For all the resins, curing times of 5 seconds induced over-curing effects, *Figure 5. 6* (b, d, f).

Overall, these results indicate that Standard Blend Unpigmented resin can be an appropriate organic vehicle to be employed on our DLP Spid3r printer, in particular, for the fabrication of the YSZ electrolyte for SOFCs.

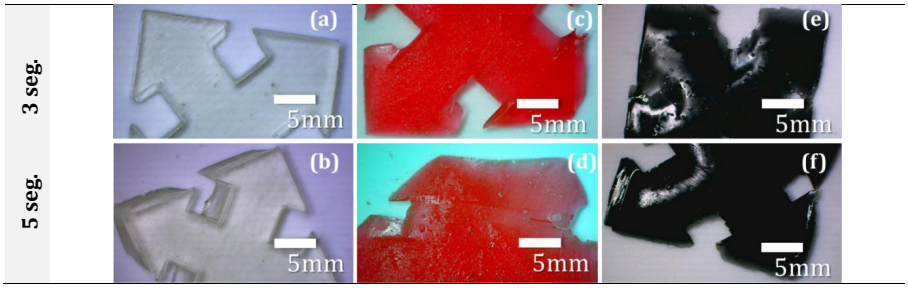

Figure 5. 6 Standard Blend resins (for DLP prototype printer) cured at 3 and 5 seconds. (a) Unpigmented resin 3 s. cured (b) Unpigmented resin 5 s. cured (c) Red resin 3 s. cured (d) Red resin 5 s. cured (e) Black resin 3 s. cured (f) Black resin 5 s. cured

5.2.2 Dispersant

Once the organic vehicle is chosen, the next step is to achieve a good mixture with the highest content of 8YSZ solid load as possible. Previous studies on YSZ slurries for DLP have explored solid loads between 30 and 50 vol %.[7–9] **In this thesis, the maximum solid load reached values of 70 wt. %.** Nevertheless, due to the high viscosity of the obtained slurries, solvent and dispersant were necessarily added to adequate the rheology to the printing process. The addition of a dispersant was carried out to avoid the flocculation and stabilise the suspension. Ethanol was employed as a solvent for preparing solutions, but due to its low boiling point (78°C), it was evaporated before using the mixture for printing process.

More specifically, Triton™ X-100 (t-Octylphenoxypolyethoxyethanol) was employed as a dispersant. It adsorbs onto the ceramic particles surface by Van Der Waals attraction,[10] achieving a steric stabilization as was showed in *Figure 2. 16 (a), Chapter 2*. The optimum amount of dispersant added was set studying its effect on the particle distribution and on the viscosity of the sample, which will be detailed in the *Section 5.2.4*. Before detailing the rheology study, the distribution of ceramic particle aggregates is presented in *Section 5.2.3*.

5.2.3 Distribution of particles

Previous research findings into particle size distribution have been focused on the Triton X-100 role as dispersant,[11–13] being established its use to modify the diameter of particles agglomerates in nanoscience. The particle size distribution of the 8YSZ slurry was measured for the ceramic powder in the absence and presence of Triton X-100. With this purpose, the commercial powder was mixed with different weight percentages of Triton X-100 using ethanol as a solvent, until solvent is evaporated. The measurements were carried out using a laser scattering equipment (Mastersizer 2000 in SEGAI), as mentioned in *Chapter 2, Section 2.2.4*. *Figure 5. 8* shows the particle distribution without and with the dispersant. When the YSZ powder was tested without dispersant, two different particle size distributions centred in d_1= 3 µm and d_2= 65 µm (with a total volume of particles v_1= 2.9 % and v_2= 3.7 %, respectively, at the maximum) were observed. When the dispersant was employed, the particle size of the first distribution decreased until d_1= 1.5 µm (but the volume of particles increased up to 4.6 %) while the number of particles with a diameter centred around d_2= 65 µm was decreasing as the amount of dispersant increased, *Figure 5. 8 (orange and red lines).* Therefore, one can easily conclude that the YSZ particle size

distribution depends on the presence of the dispersant agent in the mixture (and the mixing process), achieving a higher amount or particles with smaller diameters of 1.5 µm than without the use of dispersant.

It is important to mention here that when 3 wt. % of dispersant was employed the distribution of bigger particles substantially changed its centre, from d_2= 65 µm to d_2= 28 µm, *Figure 5. 7 (yellow line).* This effect was visually observed because liquid slurry was obtained, which is not desirable. However, decreasing a bit the amount of dispersant (2.85 wt. %) it is possible to recover the previous rheology, *Figure 5. 8 (green line)*. To avoid this instability approaching 3 wt. %, **the formulation with 2 wt. % Triton X-100 as dispersant was the choice for the rest of experiments**.

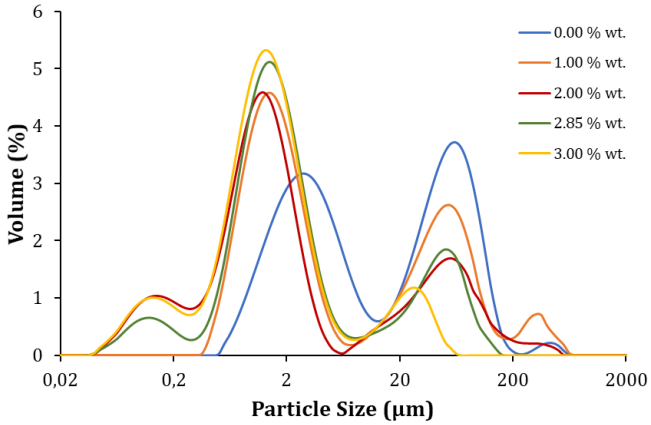

Figure 5. 7 Particle size distribution of YSZ powder using different concentration of dispersant Triton X-100 for DLP prototype printer.

5.2.4 Rheology of the ceramic slurry

Once the ideal amount of dispersant was optimised, the paste was formulated by combining the dispersed ceramic with the organic vehicle described before. The main goal was trying to achieve a printable paste with the maximum possible solid load while keeping its printability. In order to reach this objective, pastes with different solid loading were prepared, their viscosities were measured (at 20°C) and their printability was tested. Since Spid3r is a prototype printer, there is not a commercial material to be employed as a reference.

Figure 5. 8 shows the impact of the solid loading on the viscosity of the sample pastes. First, it can be observed that slurries with 80 wt. % show considerably higher viscosity than the rest. Up to 70 wt. %. the viscosity trend was maintained with increasing solid loading. This fact was associated

with the printability of the sample, because all slurries (40 wt. % - 70 wt. %) could be printed but the slurry with 80 wt. % of solid loading. **The printable paste with the highest solid loading was set at 70 wt. %. of YSZ**, *Figure 5. 8 (red triangular line)* **and presents a viscosity of 106 Pas at the typical shear rate of the Spid3r (0.071 s^{-1})**. These values are higher compared well with commercial slurries employed in SLA/DLP printers, where most of them the viscosity does not exceed 3 Pa*s to achieve an acceptable recoating.[14–16]However, this fact is because of the printer design. DLP printers usually print via bottom up, for this reason is necessary a low viscosity for the self-recovery. But the DLP printer developed in this thesis work top down, allowing to increase the viscosity of the slurries since these pastes are going to be deposited thanks to the path of a tank with the mixture above the building platform.

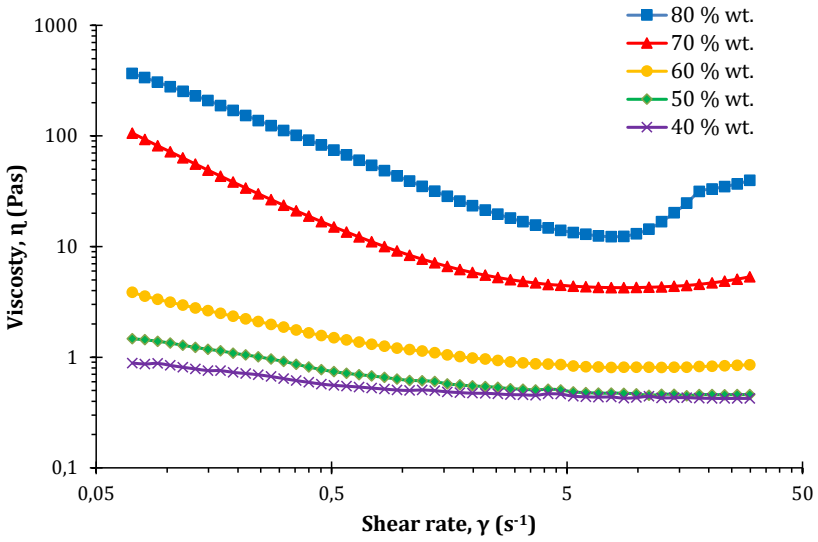

Figure 5. 8 Viscosity measurements for YSZ slurries with different solid loads: 40 wt. %. (brown), 50 wt. %. (green line), 60 wt. %. (yellow line), 70 wt. %. (violet line) and 80 wt. %. (red line).

5. 3 Printing process optimization

5.3.1 Depth curing

Depth curing relies on several parameters, which were named in *Section 2.1.4.2.1 on Chapter 2*, i.e. particle size, refractive index of the resin, minimum intensity required to cure, etc. However, when the ceramic slurry is stablished, the depth curing is directly associated to the curing time. So, the longer the curing time is, the higher will be the layer thickness. In this work, the layer thickness after curing was directly measured for the best performing slurry (68.6 wt. %. YSZ + 29.4 wt. %.

SB resin + 2.0 wt. %. Triton X-100 dispersant). Curing times between 1 and 15 seconds were used for the calibration of the curing depth while the homogeneity of the curing process was determined by measuring the thickness of the layer at different points employing a digital microscope Leica DFC420. *Figure 5. 9* shows pictures of the layers printed and cured for different times. Although good results are obtained for all the curing times, it is important to notice that **after 8 seconds, the resolution is affected by the previously mentioned over-curing phenomenon**.

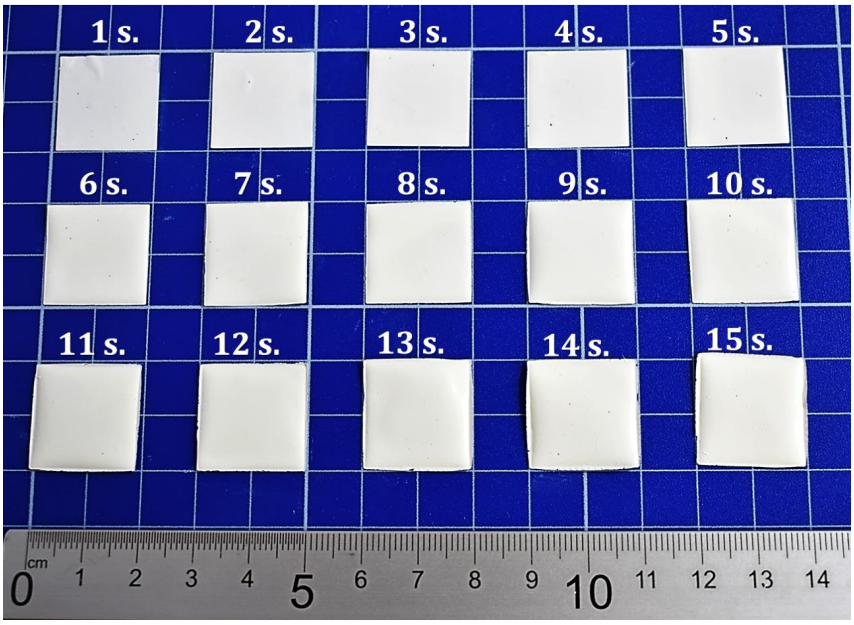

Figure 5. 9 YSZ printed single layers for different curing times

Figure 5. 10 (and *Table 5.1*) shows the curing depth as a function of the time. The average thicknesses are presented as symbols while the different measurements of each sample are represented as bars. Although it is not a linear behaviour, **it is clear that increasing the exposure time the depth curing increases** (and the thickness of the layer). **After the first four seconds, a linear relationship can be established as defined by *depth(μm) = 5.5 * time(s) + 134***.

As observed in the graph and listed in *Table 5. 1*, the thickness of the cured layers was not totally homogeneous, undergoing standard deviation between 2 and 6 μm depending on the exposure time. These inhomogeneity represents less than 5% of the total thickness in all the cases and can be considered reasonable for a prototype. It is important to remind here that depth curing is not

only relevant to control the layer thickness but also because it defines how much the z-axis of the printer must move after each layer deposition (in order to cure the total amount of mixture deposited and attach the new layer to the previous cured one). An accurate layer curing avoids remaining uncured slurry between layers and prevents from producing defects during the printing process, i. e. displacement of layers, dragging of cured parts with the passage of the slurry tank, etc.

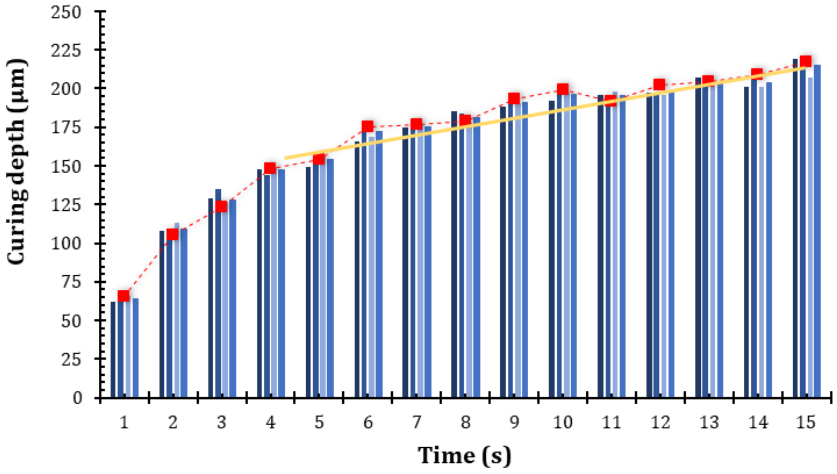

Figure 5. 10 Depth curing of YSZ slurry (68.6 wt. %.) developed for DLP Spid3r printer

Table 5. 1. Curing depth (at different points of a single layer) for different curing times

Curing time (s)	Curing depth (µm)				Average (µm)	Standard deviation (µm)
1	62	64	66	66	64	2
2	108	109	113	106	109	3
3	129	128	125	124	128	5
4	148	147	149	148	147	2
5	149	154	156	155	154	3
6	166	172	169	175	172	5
7	175	176	176	177	176	1
8	185	182	178	179	182	3
9	188	191	191	193	191	2
10	192	196	197	200	196	3
11	196	195	198	192	195	2
12	197	198	196	202	198	2
13	207	204	202	205	204	2
14	201	204	201	209	204	3
15	219	215	207	218	215	5

5.3.2 Resolution

SLA and DLP technologies present the highest resolution compared with FDM (and other 3D printing techniques). However, there are differences between SLA and DLP mainly due to the nature of the light sources. Stereolithography employs a laser and, therefore, the maximum resolution will depend on the laser spot size. On the other hand, digital light processing (DLP) uses a projector, so the maximum resolution achieved will depend on the pixel size, see *Figure 5. 11*. Typically, a higher quality and resolution can be achieved with SLA printers even for bigger laser spot sizes than pixel sizes in DLP (due to fact that DLP printers use a matrix of squared pixels which achieve a lower quality printing, see *Figure 5. 11)*.[17] Moreover, due to over-curing effects, the resolution of a DLP printer depends on curing time and distance of the projector to the building platform.

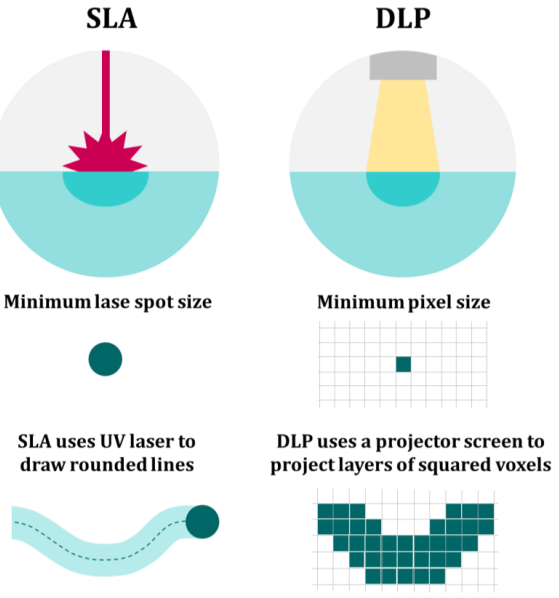

Figure 5. 11 Resolution of SLA vs DLP. (Figure adapted from literature) [17,18]

The resolution of the Spid3r prototype printer is studied, in this work, using several organic vehicles and YSZ formulated slurries.

Regarding the XY resolution, it was studied by printing digital designs specifically conceived for resolution analysis and calibration purposes (see *Figure 5. 12*). This design was printed using all proposed resins and the YSZ slurry to corroborate the preliminary tests reported in *Section 5.2.1* for the resin choice. The curing time employed for all organic vehicles was 3 seconds while, for

the YSZ slurry, three different times with expected good performance (after experiments in *Figure 5. 9*) were employed, namely, 3, 5 and 10 seconds.

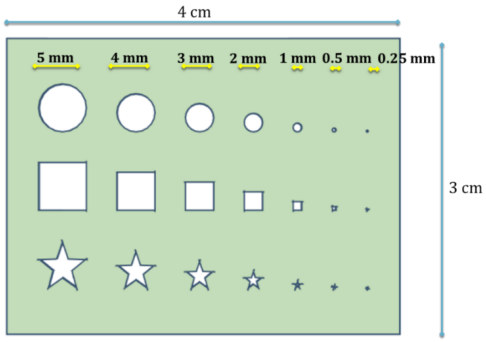

Figure 5. 12 Digital design employed to test the XY resolution of the printer

A number of printed patterns were obtained after curing for the home-made PEGDA and Irgacure formulation (*Figure 5. 13)* and the commercial Standard Blend Black (*Figure 5. 14),* Red *(Figure 5. 15)* and Unpigmented (*Figure 5. 16).* The quality of the patterns was qualitatively analysed by visual inspection and quantitatively by measuring the diameter of the holes and sides of the geometrical figures of the mask.

Regarding the home-made resin, it is clearly shown that over-curing effects are dominating the printing, which makes difficult to obtain a defined structure even after very few layers (*Figure 5. 13)*. **This study confirms the initial decision of discarding the PEGDA and Irgacure based resin**.

For the commercial resins from Standard Blend, different resolutions were observed. The resin that presented less over-curing effect was the black, *Figure 5. 14*, as clearly observed by the final dimensions of the holes, which were closer to the projected designs. However, using this resin the shapes were not well-defined. A better balance was achieved by the un-pigmented resin (*Figure 5. 16*) that reasonably maintained the original dimensions while offering much excellent shapes. From these results, **it was concluded that the best resin in terms of resolution was the SB Un-pigmented,** which matches well with the result obtained by the fast curing tests in *Section 5.2.1*.

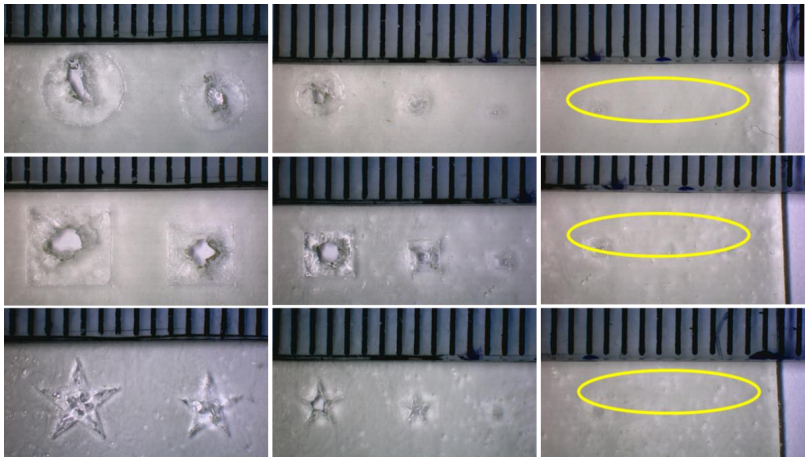

Figure 5. 13 XY resolution for developed resin based on PEGDA and Irgacure (curing time: 3s.)

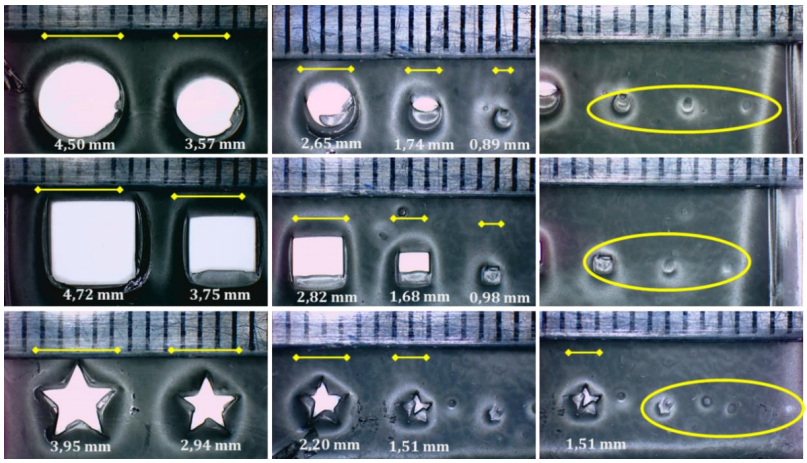

Figure 5. 14 XY resolution for Standard Blend Black resin (curing time: 3s.)

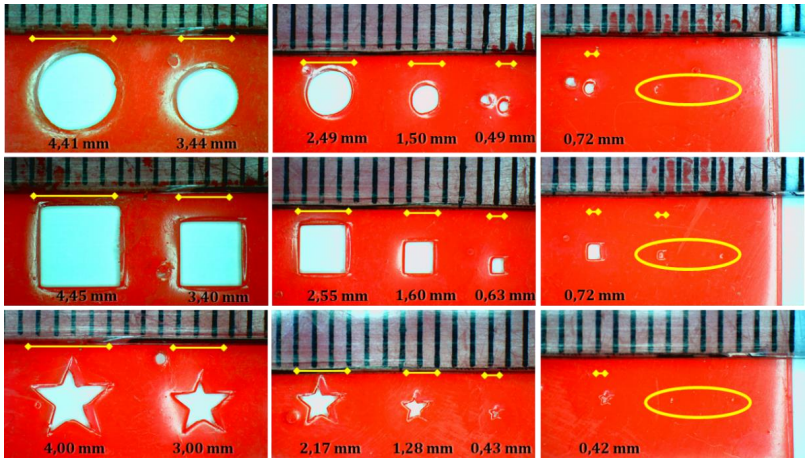

Figure 5. 15 XY resolution for Standard Blend Red resin (curing time: 3s.)

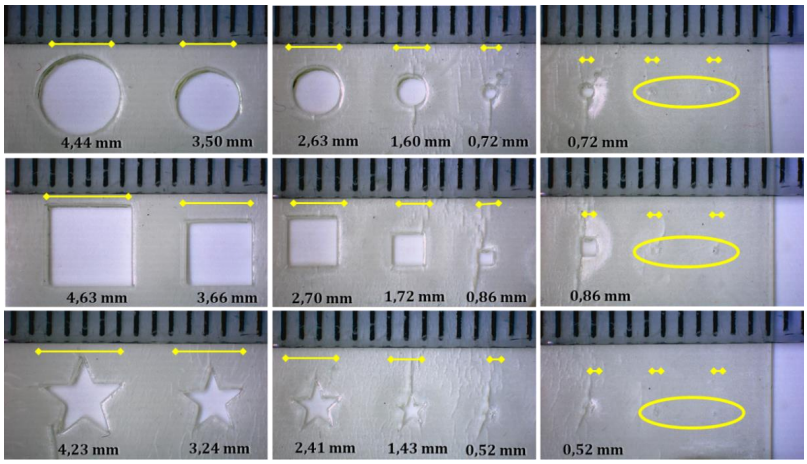

Figure 5. 16 XY resolution for Standard Blend Un-pigmented resin (curing time: 3s.)

Regarding the *xy* resolution for the YSZ slurry, similar calibration patterns were printed as shown in *Figure 5. 17.* These tests were done using curing times of 3s, 5s, and 10 s. **It is possible to observe that the over-curing effect is higher when higher is the curing time, decreasing the printing resolution.** The optimum result is obtained using low curing times, nevertheless, it may affect to the layer attachment (not enough cross linking of the two consecutive layers).

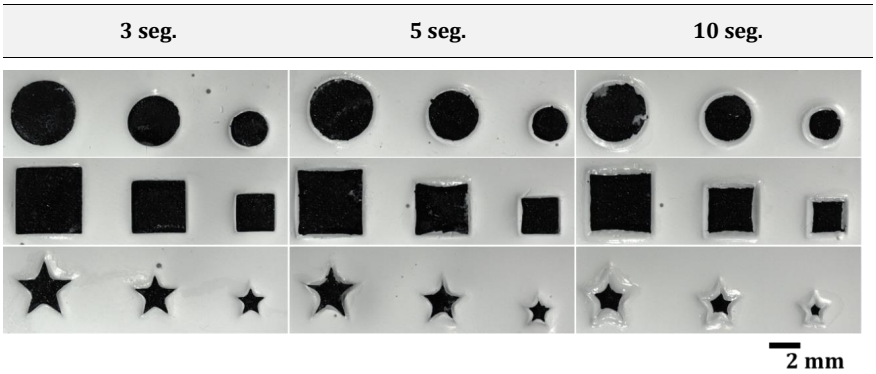

Figure 5. 17 Resolution of the Spid3r using YSZ developed slurry at different curing times: 3 s., 5s. and 10s.

In order to achieve a good trade-off between the curing time, the achieved resolution and a good attachment between successive cured layers, a 3D structure (with several layers) was printed using different curing times. In this was, it was also possible to study the resolution in the Z axis. The digital design proposed for this purpose includes different shapes with different dimensions and heights as sketched in *Figure 5. 18*.

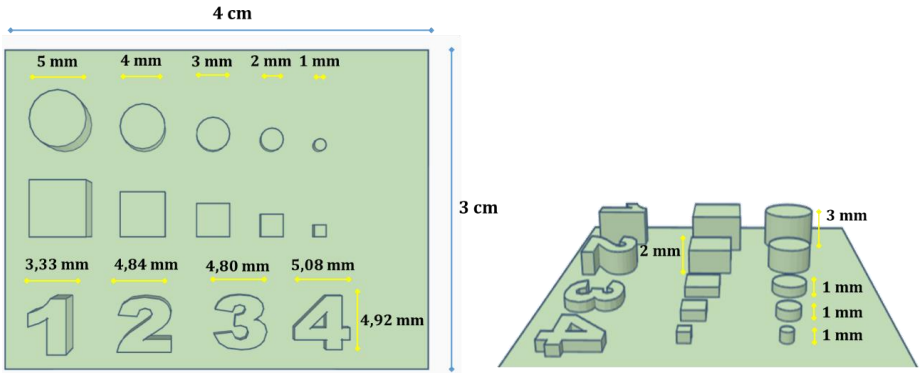

Figure 5. 18 Digital design used to study the resolution on the three axes

First, **for a curing time of 3 seconds, the thickness layer was set at 100 µm in the printer**. The printing of the digital design was finished successfully, **however, during the cleaning process using ethanol, the different layers of the final 3D printed structure presented clear signs of detachment** (*Figure 5. 19*). Although the observed resolution was reasonably good, a displacement of several layers of the printed part could be observed due to the poor attachment (*Figure 5. 19(a)).*

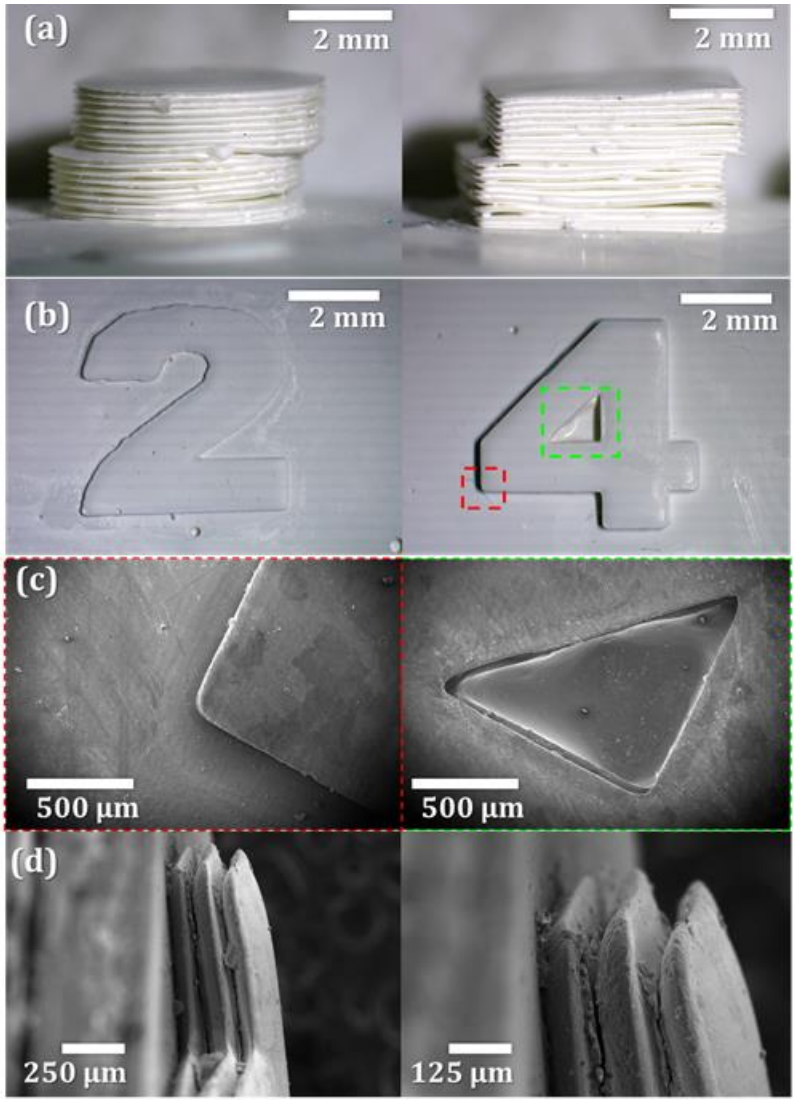

Figure 5. 19 3D printed design for resolution test using 3 second for the curing time

The same test was repeated using curing times of 5s and a thickness layer of 150 µm. A similar effect was observed, which indicated that using 5 s was not still enough to solve the attachment issues.

Finally, longer curing times of 10s were tested. Keeping the layer thickness at 150 µm, the printing of the 3D design was successfully finished, and the cleaning process could be easily carried out (*Figure 5. 20*). Although a worse resolution is observed for 10 seconds, this is the only

time that allowed completely printing 3D objects that not suffer from dramatic failure during the printing or the cleaning process due to the delamination.

Overall, it is possible to conclude that a printer resolution of 150 µm on the *z*-axis and 1 mm on the *xy*-plane is achievable for curing times of 10 seconds when using the formulated YSZ slurry.

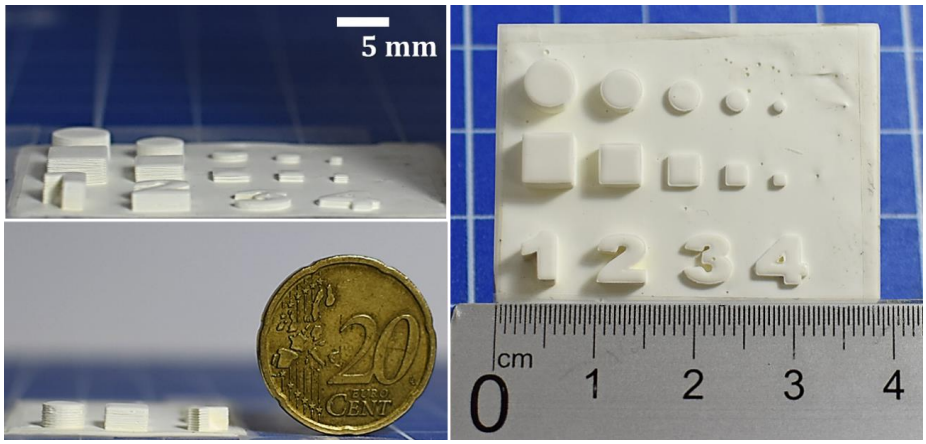

Figure 5. 20 3D printed design for resolution test using 10 seconds for the curing time

5. 4 Electrolyte printing

This section is focused on the printed electrolytes fabricated via our Spid3r prototype printer, which will be compared with 3D-SLA printed electrolytes manufactured using SLA commercial printer of 3DCeram (at IREC).

The first manufactured designs were H-like circular pellets that would facilitate further electrochemical characterisation by ensuring an easy sealing to the test station. The design shown in *Figure 5. 1(a & b)* was employed for electrolytes made with the SLA printer while the design of *Figure 5. 1 (c & d)* was employed for electrolytes obtained using the DLP Spid3r printer. The SLA printer used 8YSZ pastes previously developed in the EU project Cell3Ditor (coordinated by IREC and participated by the ULL), while the DLP printer employed 8YSZ developed slurry as described before. Printing parameters for both machines are shown in *Table 5. 2*. The debinding and sintering process of the green bodies printed using Spid3er DLP followed the thermal program described in *Chapter 2, Section 2.1.4.2.3.3*, for a final sintering temperature of 1350°C. The thermal program used for SLA printed electrolytes was developed in the previously mentioned Cell3Ditor project reaching up to 1450°C.

Table 5. 2 Printing parameters for manufacturing 8 YSZ electrolytes via SLA and DLP techniques

Printing parameters	DLP	SLA
Thickness layer (µm)	150	100
Raster speed (mm/s)	25	5000
Curing light wavelength (nm)	360-405 (max 380)	355
Curing Time (s) / Intensity laser (%)	10	93

5.4.1 Electrolytes printed using a DLP Spid3R printer

Figure 5. 21 (a & b) shows green bodies of DLP-electrolytes with different geometries (flat and squared), while *Figure 5. 21 (c & d)* shows the green body and the sintered parts for the same design, which allows the determination of the shrinkage factor. First, it can be observed that a clear over-curing effect took place by comparing the printed mask with the digital design, *Figure 5. 21 (b.1 and b.2)*. The same issue can also be observed in the perimeter of the DLP-electrolytes, which are not completely circular. In addition, over-cured areas can be appreciated on squared pattern where corners were rounded. As previously discussed, this phenomenon originates from an excessive curing time of 10 seconds needed for avoiding dramatic delamination of the printed pieces.

Regarding the change in size shown in *Figure 5. 21 (c & d)*, the dimensions of the samples were measured in order to calculate the shrinkage factor of the printed samples after the thermal treatment. *Table 5. 3* lists the changes in dimensions for the different geometries before and after sintering. **The shrinkage factor is around 31 – 35% on *xy* axis for flat samples while around 36- 37 % for squared patterns**. Complementary manufactured samples verify that the shrinkage of the material was different between samples with a different structure. **Regarding the shrinkage factor on the *z* axis**, it was more homogeneous and independent of the different geometries of the sample showing **values between 20-24% in all the cases**.

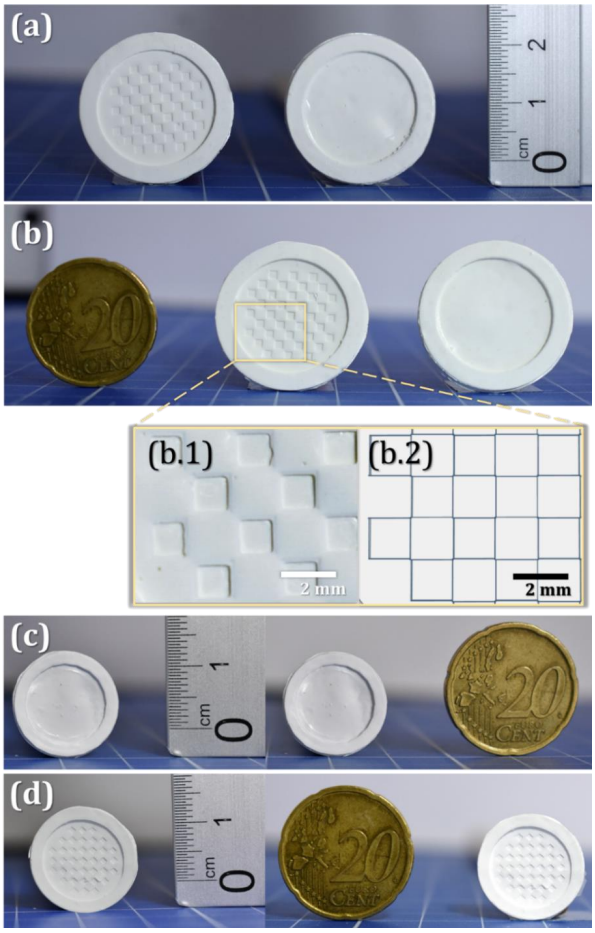

Figure 5. 21 3D structured YSZ electrolytes manufactured via DLP Spid3r printer

Table 5. 3 Dimension values of the printed samples and sintered samples and their shrink factor on each axis

Sample	Axis	Green body	Sintered	Shrinkage Factor
Flat	***x***	2.51 ± 0.01 cm	1.71 ± 0.01 cm	- 32 ± 1%
	y	2.55 ± 0.01 cm	1.68 ± 0.01 cm	- 34 ± 1%
3D Structured	***x***	2.64 ± 0.01 cm	1.66 ± 0.01 cm	-37 ± 1%
	y	2.60 ± 0.01 cm	1.67 ± 0.01 cm	-36 ± 1%

Overall, it is possible to conclude that flat and structured electrolytes were easy to manufacture using the Spid3r prototype printer and the YSZ slurries developed in this work, therefore, reaching the major goal of manufacturing structured electrolytes for SOFCs.

5.4.2 Electrolytes printed using a SLA printer

Figure 5. 22 directly shows the sintered flat and structured designs obtained by SLA printing, being possible to observe clear evidences of a better resolution. This better finishing essentially comes from specific features of the printer such as: i) a more precise deposition of the layers (double doctor blade); ii) a better controlled curing process (tuneable power laser); iii) an improved lateral and vertical resolution by laser focusing capabilities and iv) a deeper understanding of the debinding process. In this case, **the shrinkage factor is integrated in the software of the printer having a value of 29% on *xy* axis and 27% on *z* axis**. Despite the big difference between both samples, pieces printed with the DLP machine still offer interesting features for the application in SOFCs.

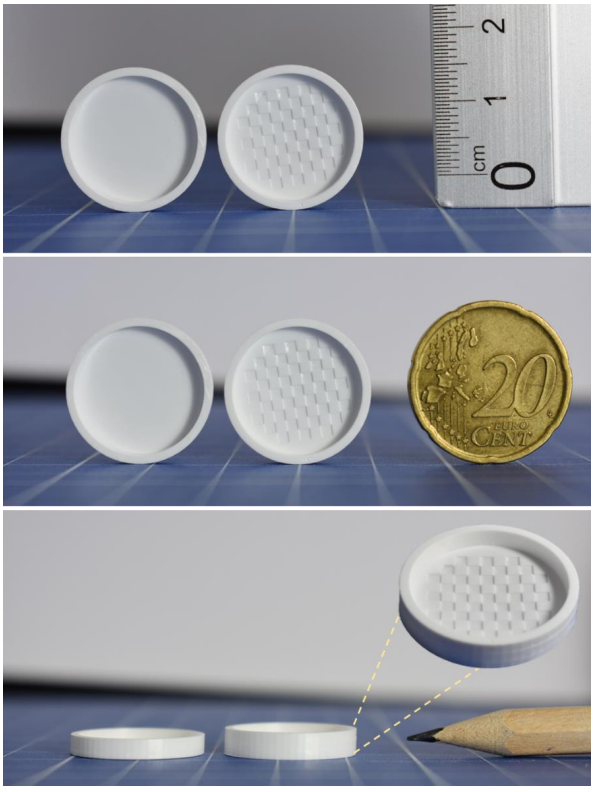

Figure 5. 22 3D structured YSZ electrolytes manufactured via SLA- 3D Ceram printer

5.5 Symmetrical cells based on 3D printed electrolytes and microstructural characterization

After sintering the printed electrolytes as described in the previous sections, they were functionalized with electrode (cathode) to configure symmetrical Solid Oxide Fuel Cells. The deposition and thermal treatment steps required for this complete cell fabrication. Firstly, a YSZ rugosity layer was sprayed and sintered at 1150°C/1h. Then electrodes were manually deposited trying to achieve a thickness of 35 µm at least. LSM-YSZ cathode were employed to optimise the cathode temperature attachment. The range of studied temperatures was 1100°C-1200°C. Gold was deposited as interconnector material using even a gold mesh to improve the attachment with the connections of the probostat cell. All the details of this process were described in *Chapter 2, Section 2.1.3.4.* The next sections are devoted to a detailed characterization of the so-fabricated cells.

5.5.1 Electrolyte characterization

Electrolytes employed for **optimising electrode deposition had a flat geometry, having been designed for a thickness of 500 µm**. *Figure 5. 23* show SEM pictures of sintered electrolytes fabricated with the DLP Spid3er printer, *Figure 5. 23 (a, b & c)*, and, for comparison, using the SLA printer, *Figure 5. 23 (d, e & f)*. In these images, first, it is possible to observe that the printing processes were highly reproducible since the thickness of the three replicas was similar. The measured thickness for 3D-DPL electrolytes was of 488 ± 8 µm while for 3D-SLA electrolytes was 498 ± 7 µm. Second, the mages clearly show the absence of notable delamination between layers or bubble formation.

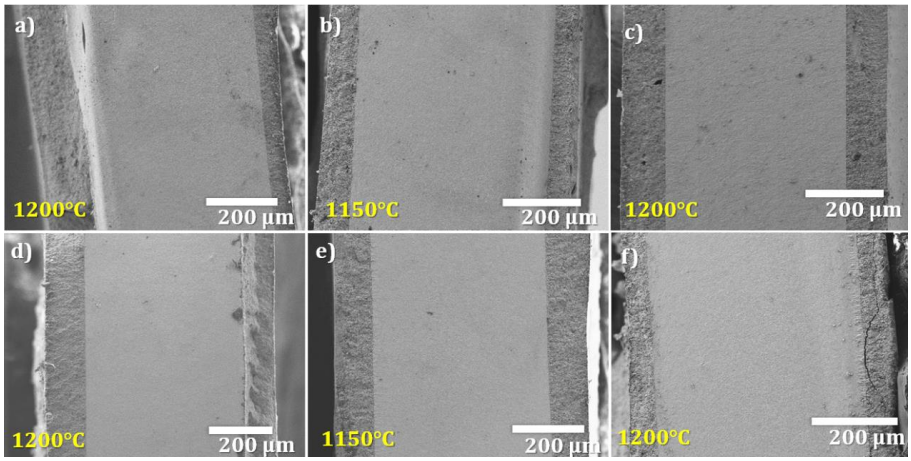

Figure 5. 23 Sintered 3D electrolytes manufactured via SLA 3DCeram printer (a, b & c) and via DLP Spid3r prototype (d, e & f) with LSM cathode deposited on both faces.

In order to study the densification during the sintering process, higher magnification SEM images were acquired for DLP- and SLA-printed electrolytes. *Figure 5. 24* shows SLA electrolyte (a) and DLP electrolyte (b) sintered at 1450°C and 1350°C respectively. In both cases, almost fully dense electrolytes are observed with an apparent small amount of open porosity.

It is important to mention here, that thermal debinding and sintering procedure for SLA takes ~100 hours in total, while the thermal program proposed in this thesis only takes 34 hours in total. As it is shown**, DLP electrolyte shows a higher porosity than SLA electrolyte**. So, thermal process must be longer for DLP electrolytes in order to achieve a better density.

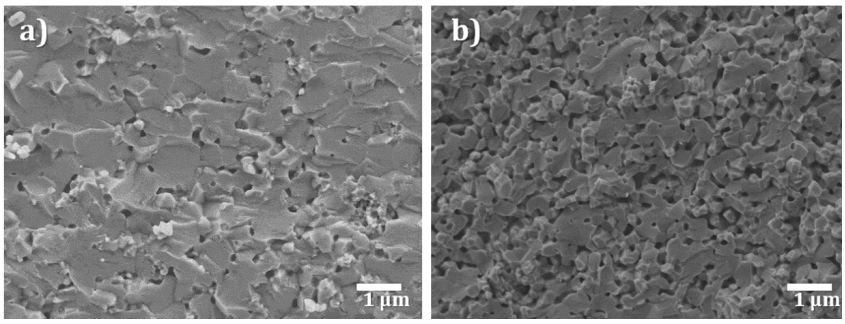

Figure 5. 24 (a)SLA sintered electrolyte at 1450°C (b) and DLP sintered electrolyte at 1350°C

5.5.2 Electrodes characterisation

This section is focused on the characterisation of the electrodes painted on the sides of the printed and sintered electrolytes. The focus of the analysis will be in the thickness and the porosity of the layer and the quality of the attachment to the electrolyte. The importance of these parameters was previously discussed in *Chapter 2*. *Figure 5. 25* shows SEM cross section images of each DLP-electrolyte after being functionalised with LSM-YSZ electrodes on both sides, configuring a symmetrical cell. The electrode deposition was carried out manually, therefore, a certain variability in the cathode thickness is expected and observed (with values between 100 and 115 µm). These values represent reasonable thicknesses for a highly porous electrode according to our previous experience.

To study the porosity of the layers and the quality of the electrolyte-electrode attachment, higher magnification images were acquired. *Figure 5. 25* shows the interface at different temperatures of attachment for electrolytes manufactured via DLP while *Figure 5. 26* shows the interface SLA-electrolyte - LSM electrode for the different attachment temperatures. **Regarding DLP electrolytes, it can be determined that a better mix of YSZ and LSM material was achieved**

at 1100°C presenting a good porosity better homogeneity of the grain size throughout all deposited cathode layer than electrode attached at 1150°C and 1200°C.

Besides, it is possible to observe in *Figure 5. 26 (c)* that the attachment between both phases is better than at higher temperatures, defining a better TPB zone as it is shown in *Figure 5. 27* (electrolyte: right zone; electrode: left zone). However, the porosity of the cathode is lower than for lower temperatures. Regarding the SLA electrolyte, the difference between the highest temperatures with the lowest one is significant. In spite of the particle size at 1200°C, *Figure 26 (a),* and 1150°C, *Figure 26 (b),* were smaller, **at 1100°C was achieved a porous structure where the pores seem connected each other facilitating the gas flow through the electrode until TPB zone**, *Figure 26 (c)*.

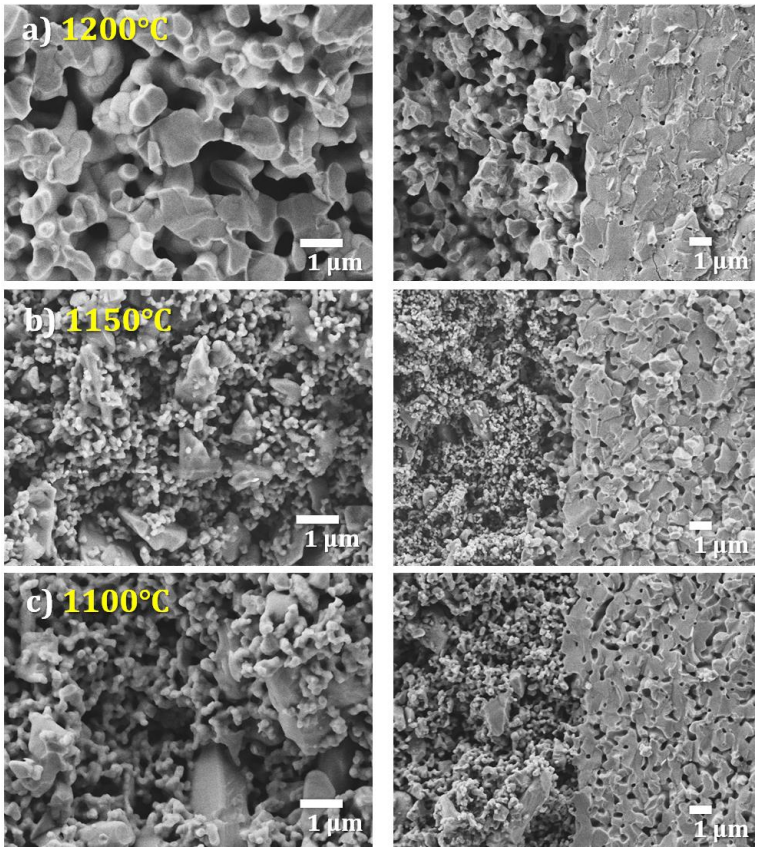

Figure 5. 25 LSM electrode – YSZ electrolyte (DLP) interface symmetrical cells, where the electrode was sintered at different temperatures (a) 1200°C; (b) 1150°C and (c) 1100°C

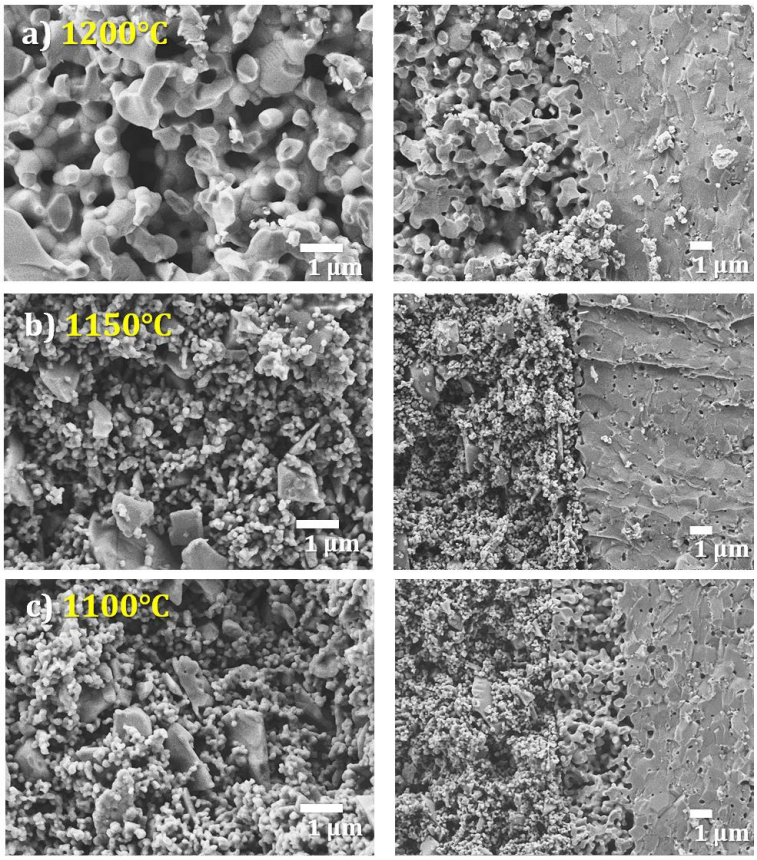

Figure 5. 26 LSM electrode – YSZ electrolyte (SLA) interface symmetrical cells, where the electrode was sintered at different temperatures (a) 1200°C; (b) 1150°C and (c) 1100°C.

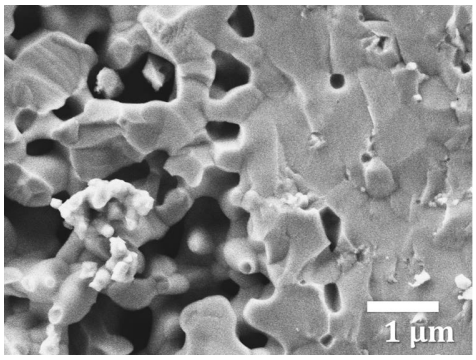

Figure 5. 27 Detail of the attachment at 1100°C of the LSM-YSZ cathode to the 3D printed electrolyte

5.5.3 Roughness layer

According to the procedure described in *Chapter 2, Section 2.1.3.4*, YSZ roughness layers were sprayed on both electrolyte sides to improve the electrode attachment between the YSZ electrolyte and the YSZ-LSM cathode. SEM images clearly show (artificial colouring) this roughness layer for DLP, *Figure 5. 28 (a & b),* and SLA electrolytes, *Figure 5. 28 (c & d),* and the interface between cathode-roughness layer-electrolyte. Different thicknesses are observed due to the manual application of the layer, however, due to the considerable thickness of the electrolyte (electrolyte-supported cells) **this variability is not considered relevant for the final performance of the cell**.

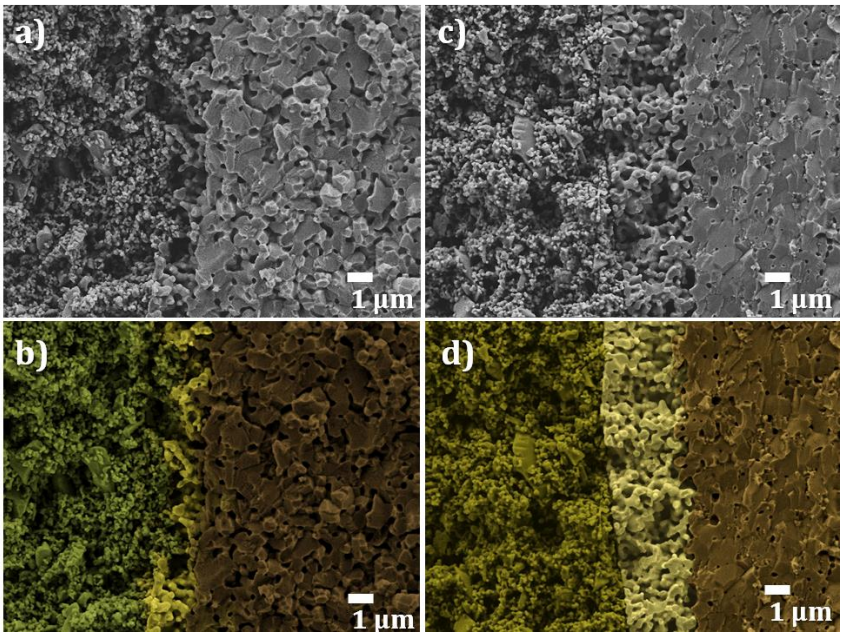

Figure 5. 28 Cross-section SEM images of the microstructure of the interface cathode-roughness layer-electrolyte for (a) 3D-SLA electrolyte and (b) its coloured image; (c) and for 3D-DLP electrolyte and (d) its coloured image. [Cathode (green), roughness layer (yellow) and electrolyte (brown)]

5. 6 Electrochemical performance

Symmetrical cells (Au/LSM-YSZ/YSZ/LSM-YSZ/Au) were studied via impedance spectroscopy (EIS) for measuring the ionic conductivity of the electrolytes manufactured using the DLP Spid3r printer and the SLA industrial printer, employing the material listed in *Table 5. 4.* In order to

measure the performance of these SOFCs, the fabricated cells were sealed on a Probostat system, as shown in *Chapter 2, Figure 2. 23*, using Ceramabond™.

Nyquist plots of the different symmetrical cells obtained via DLP and SLA, whose cathodes were sintered at 1100°C, 1150°C y 1200°C, are shown of *Figure 5. 29*. They were measured by EIS different temperatures (700–900 °C) in synthetic air (symmetrical atmosphere).

Table 5. 4 SOFC materials employed and geometrical dimensions of the symmetrical LSM-YSZ/YSZ/LSM-YSZ cells measured. (T_{att}: Attachment temperature)

	Material	Technique	T_{att}	Thickness	Area
Electrolyte	8 YSZ	DLP	1350°C	490 µm	2.41 cm^2
Electrolyte	8 YSZ	SLA	1400°C	500 µm	1.77 cm^2
Cathode	LSM-YSZ	Painted	1200°C 1150°C 1100°C	100 µm $_{DLP}$ 120µm $_{SLA}$	-
Current collector	Au	Painted and mesh	800°C	-	-

Nyquist plots were fitted using an equivalent circuit with physical meaning (*Figure 5. 30*). The model includes an inductance (L_1), typically associated to the setup, in series with an ohmic resistance (R_1), related to the contribution of the YSZ electrolyte and contact resistances, which is in series with two arcs (RC) corresponding to the polarization resistances from the LSM-YSZ electrodes (R_2CPE_2 and R_3CPE_3). The results regarding R_1 are very important because they $_{contain}$ information on the quality of the attachment since the connected area between electrolyte and electrode (effective contact surface) and the resistance associated to the current collection through the electrode directly contribute to this element. That means, R_1 gives an idea about the electrode percolation, that is if the gasses can flow through it without problem. Regarding the information straightforwardly related to the electrolyte conductivity, it can only be extracted for the optimum attachment temperature (involves assuming a contact resistance smaller than the electrolyte). The data resulting from the fitting of the EIS curves is shown in *Table 5. 5*.

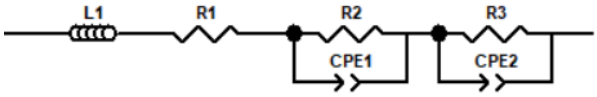

Figure 5. 30 Equivalent circuit for fitting EIS curves

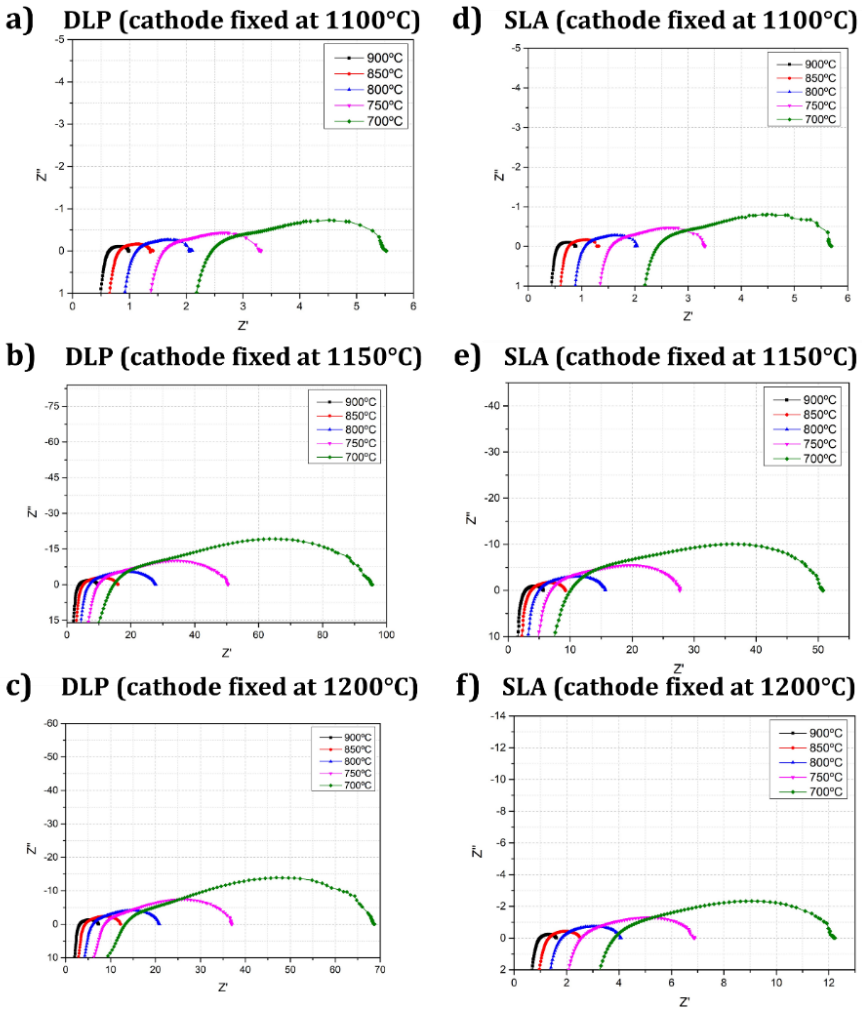

Figure 5. 29 Nyquist plots of the EIS spectra of the symmetrical LSM-YSZ/YSZ/YSZ-LSM cells using the electrolyte manufactured via DLP and SLA printing

Figure 5. 31 and *Figure 5. 32* illustrate the Arrhenius plots of the respective contributions of the serial (R_s) and polarization (R_p=R_2+R_3) resistances as a function of the inverse of temperature. It is clearly observed in both plots that cathodes fixed at 1100°C result in the lowest values of serial and polarization resistances for both DLP and SLA electrolytes. This **can be confirmed with the result shown in *Table 5. 5* where lower values were achieved for the attachment done at 1100°C, resulting in conductivity values pretty similar for both electrolyte types**. This is in

good agreement with the cross-section images that were previously discussed, where the higher the temperature the coarser and sintered the microstructure was.

So, it can be concluded that the optimum temperature for electrodes attachment is 1100°C.

Table 5. 5 Circuit elements values obtained at different temperatures (T = 700–900 °C) for the cells whose Nyquist plot are represented in Figure 5. 29

		DLP			SLA		
T_{att}	T (°C)	R_s (Ω)	R_2 (Ω)	R_3 (Ω)	R_s (Ω)	R_2 (Ω)	R_3 (Ω)
1100	900	0.5	0.4	0.06	0.6	0.4	0.02
	850	0.6	0.6	0.1	0.6	0.5	0.2
	800	0.8	0.5	0.9	0.8	0.7	0.5
	750	1.2	1.3	0.9	1.2	2.3	0.5
	700	1.8	1.7	2.1	1.8	1.9	2.2
1150	900	2.1	2.2	5.5	2.5	2.5	0.6
	850	4.1	1.7	10.2	3.0	1.1	5.1
	800	5.2	6.1	16.6	4.8	2.1	8.8
	750	8.1	7.4	36.0	6.7	4.1	17.2
	700	10.1	23.8	62.8	9.0	8.8	34.8
1200	900	2.1	2.2	3.1	0.9	0.6	0.1
	850	3.4	7.3	1.8	1.1	1.2	0.2
	800	5.0	2.2	14.8	1.6	2.1	0.4
	750	8.0	4.0	26.6	2.3	4.0	0.9
	700	11.3	9.1	54.0	3.3	7.0	2.4

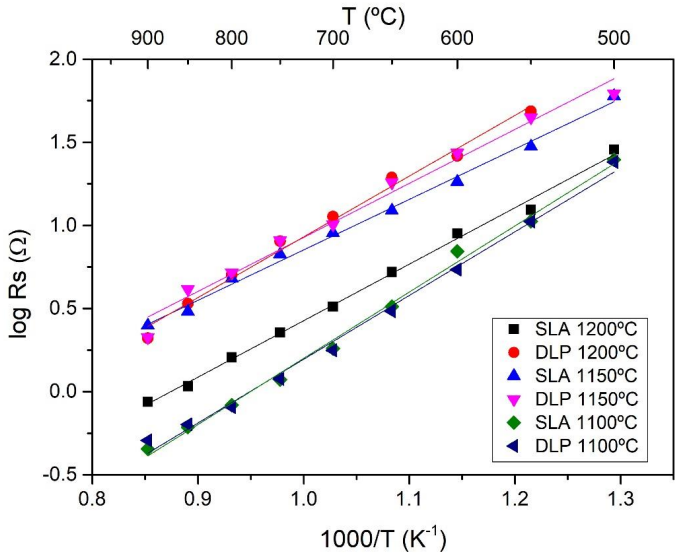

Figure 5. 31 Arrhenius plot of the serial resistance associated to cells with cathodes attached at different temperatures (T_{att}=1100, 1150 and 1200°C)

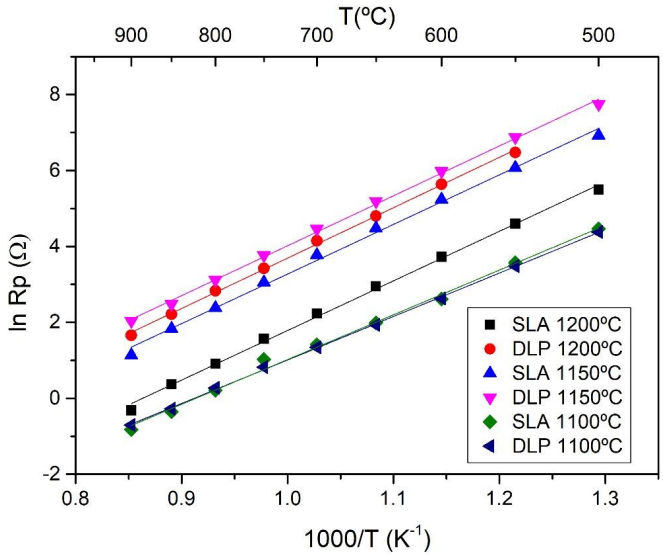

Figure 5. 32 Arrhenius plot of the polarization resistance associated to cells with cathodes attached at different temperatures (T_{att}=1100, 1150 and 1200°C)

As previously mentioned, from the optimized cells, it is possible to extract the ionic conductivity of the electrolyte (assuming that the ohmic resistance associated to the contact and current collection at the electrodes is negligible compared with the resistance of the electrolyte). Therefore, it is possible to plot the ionic conductivity of the DLP and SLA electrolytes for the cells with cathodes attached at 1100°C, *Figure 5. 33*. The Arrhenius behaviour is confirmed by linear fitting. From the slope of the fitted lines, it is possible to extract the activation energies (*Table 5. 6*), which are close for the typical values for YSZ (~Ea= 0.8 – 1.2 eV).[19–22] **The ionic conductivities values at 900°C achieve a maximum of 0.054 ± 0.013 S/cm for the electrolyte printed via DLP while 0.046 ± 0.011 S/cm for SLA** (*Table 5. 6*). Both values are in excellent agreement with other reported conductivities for 8YSZ at the same temperature (0.08 - 0.09 S/cm at 900°C).[22–26]

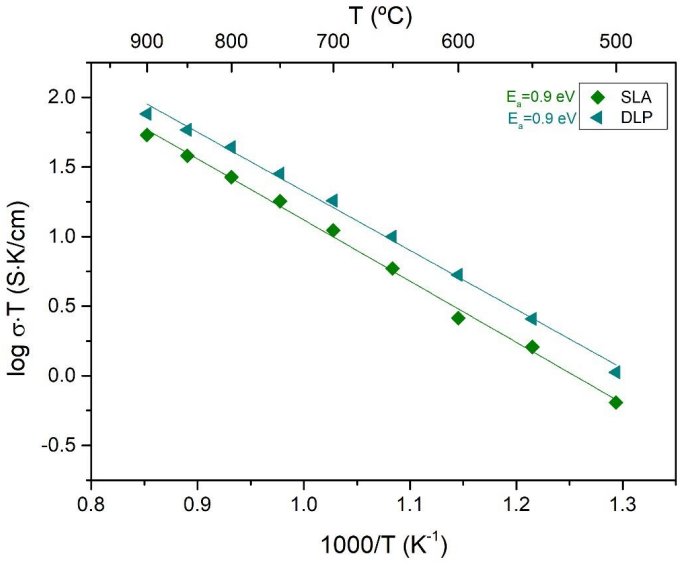

Figure 5. 33 Arrhenius plot of the ionic conductivity of the 3D printed 8YSZ electrolytes achieved for each symmetrical cell with a cathode attached at 1100°C

Table 5. 6 Ionic conductivity at T=900 °C and activation energies for SLA and DLP YSZ electrolytes, obtained from the optimum electrode attachment temperature (T_{att}=1100°C)

Samples	E_a (eV)	σ (S/cm)
SLA T_{att}= 1100°C	0.9 ± 0.1	0.046 ± 0.011
DLP T_{att}= 1100°C	0.9 ± 0.1	0.054 ± 0.013

Figure 5. 34 represents the ASR (Area Specific Resistance, ASR=R/A) of the electrode ($ASR_{pol}/2$) and half cell ($ASR_{tot}/2$) for the optimized cell (T_{att}=1100°C). Additionally, a horizontal dashed line is plotted at ASR=0.5 Ω·cm². This value of ASR is considered a threshold below which the cells perform sufficiently well (P~0.5W/cm²). This representation allows us to **conclude that the fabricated electrolyte-electrode layers are suitable for operation at T=750°C ($ASR_{pol}/2$=0.5 Ω·cm²) or 850°C ($ASR_{tot}/2$=0.5 Ω·cm²)**.

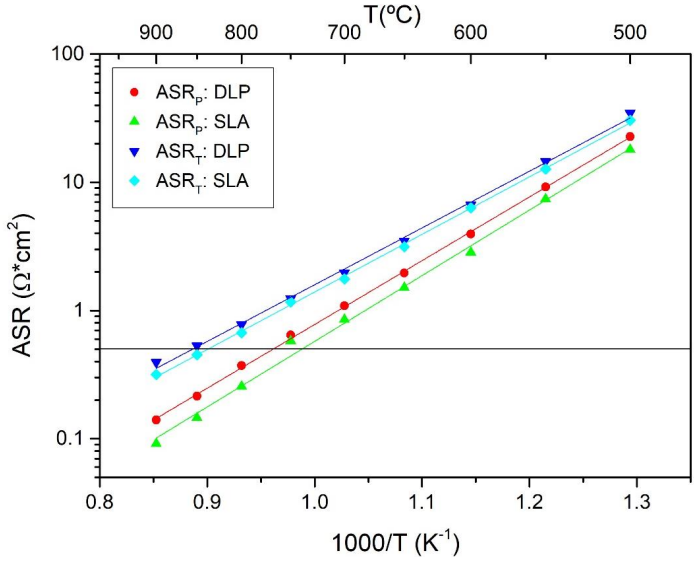

Figure 5. 34 ASR plot of half of the symmetrical cell with electrolyte manufactured via SLA and DLP technique, and cathode deposited at 1100°C

To summarize, it can be concluded that it is possible to fabricate 8YSZ electrolytes employing DLP and SLA techniques, giving acceptable results for SOFC cells.

5. 7 References

[1] Ciba Specialty Chemicals Inc. Photoinitiator IRGACURE 819 http://www.xtgchem.cn/upload/20110629045602.PDF.

[2] Dietliker, K. A Compilation of Photoinitiators: Commercially Available for UV TodayTitle; SITA Technology, Ed.; Edinbergh, London, (2002)ISBN: 0947798676 9780947798673.

[3] Igor V. Khudyakov. Photoinitiators https://dymax-oc.com/images/pdf/literature/papers/photoinitiators.pdf.

[4] Di Anibal, C. V.; Odena, M.; Ruisánchez, I.; Callao, M. P. Determining the Adulteration of Spices with Sudan I-II-II-IV Dyes by UV-Visible Spectroscopy and Multivariate Classification Techniques. Talanta (2009), 79 (3), 887–892, doi:10.1016/j.talanta.2009.05.023.

[5] Fun To Do. Standard Blend Resin MSDS sheet http://www.funtodo.net/docs-info.html (accessed Jul 3, 2020)

[6] Domotek. Standard Blend resin https://domotek.es/producto/resina-funtodo-standard-blend (accessed Jul 2, 2020).

[7] Xing, B.; Cao, C.; Zhao, W.; Shen, M.; Wang, C.; Zhao, Z. Dense 8 mol% Yttria-Stabilized Zirconia Electrolyte by DLP Stereolithography. J. Eur. Ceram. Soc. (2020), 40 (4), 1418–1423, doi:10.1016/j.jeurceramsoc.2019.09.045.

[8] Wei, L.; Zhang, J.; Yu, F.; Zhang, W.; Meng, X.; Yang, N.; Liu, S. A Novel Fabrication of Yttria-Stabilized-Zirconia Dense Electrolyte for Solid Oxide Fuel Cells by 3D Printing Technique. Int. J. Hydrogen Energy (2019), 44 (12), 6182–6191, doi:10.1016/j.ijhydene.2019.01.071.

[9] Varghese, G.; Moral, M.; Castro-García, M.; López-López, J. J.; Marín-Rueda, J. R.; Yagüe-Alcaraz, V.; Hernández-Afonso, L.; Ruiz-Morales, J. C.; Canales-Vázquez, J. Fabrication and Characterisation of Ceramics via Low-Cost DLP 3D Printing. Boletín la Soc. Española Cerámica y Vidr. (2018), 57 (1), 9–18, doi:10.1016/j.bsecv.2017.09.004.

[10] M. N. Rahaman. Ceramic Processing, Second Edi.; CRC Press, Ed.; (2017) ISBN: 978-1-4987-1641-3.

[11] Yao, L.; Xu, G.; Dou, W.; Bai, Y. The Control of Size and Morphology of Nanosized Silica in Triton X-100 Based Reverse Micelle. Colloids Surfaces A: Physicochem. Eng. Asp. (2008), 316, 8–14, doi:10.1016/j.colsurfa.2007.08.016.

[12] Gritti, F.; Bell, D. S.; Guiochon, G. Particle Size Distribution and Column Efficiency. An Ongoing Debate Revived with 1.9µm Titan-C18 Particles. J. Chromatogr. A (2014), 1355, 179–192, doi:10.1016/j.chroma.2014.06.029.

[13] Horiba Scientific. Dispersing Powders in Liquid for Particle Size Analysis. HORIBA Instruments, Inc (2013), 7.

[14] Hinczewski, C.; Corbel, S.; Chartier, T. Stereolithography for the Fabrication of Ceramic Three-Dimensional Parts. Rapid Prototyp. J. (1998), 4 (3), 104–111, doi:10.1108/13552549810222867.

[15] Li, K.; Zhao, Z. The Effect of the Surfactants on the Formulation of UV-Curable SLA Alumina Suspension. Ceram. Int. (2017), 43 (6), 4761–4767, doi:10.1016/j.ceramint.2016.11.143.

[16] Komissarenko, D. A.; Sokolov, P. S.; Evstigneeva, A. D.; Shmeleva, I. A.; Dosovitsky, A. E. Rheological and Curing Behavior of Acrylate-Based Suspensions for the DLP 3D Printing of Complex Zirconia Parts. Materials (Basel). (2018), 11 (12) doi:10.3390/ma11122350.

[17] Formlabs. What does resolution mean in 3D printing? https://formlabs.com/blog/3d-printer-resolution-meaning/.

[18] Engineering Product Design & 3DHubs. Vath Photo-polymerization https://engineeringproductdesign.com/knowledge-base/vat-photo-polymerization/ (accessed Jul 4, 2020).

[19] Devanathan, R.; Weber, W. J.; Singhal, S. C.; Gale, J. D. Computer Simulation of Defects and Oxygen Transport in Yttria-Stabilized Zirconia. Solid State Ionics (2006), 177 (15–16), 1251–1258, doi:10.1016/j.ssi.2006.06.030.

[20] Krishnamurthy, R.; Yoon, Y. G.; Srolovitz, D. J.; Car, R. Oxygen Diffusion in Yttria-Stabilized Zirconia: A New Simulation Model. J. Am. Ceram. Soc. (2004), 87 (10), 1821–1830, doi:10.1111/j.1151-2916.2004.tb06325.x.

[21] Pornprasertsuk, R.; Ramanarayanan, P.; Musgrave, C. B.; Prinz, F. B. Predicting Ionic Conductivity of Solid Oxide Fuel Cell Electrolyte from First Principles. J. Appl. Phys. (2005), 98 (10), 103513, doi:10.1063/1.2135889.

[22] Ruiz-Morales, J. C.; J, P.-M.; P, M. L.; Romero, D. P. C. Dn. C. Pb. P. Bc. V. Jg. Pilas de Combustible de Óxidos Sólidos (SOFC), 2nd ed.; Centro de la Cultura Popular Canaria, Ed.; Santa Cruz de Tenerife, (2008) ISBN: 978-84-7926-567-0.

[23] Kendall, S. C. S. K. High-Temperature Solid Oxide Fuel Cells: Fundamentals, Design and Applications; Elsevier, Ed.; Oxford, (2004) ISBN: 9780080508085.

[24] Zhang, C.; Li, C. J.; Zhang, G.; Ning, X. J.; Li, C. X.; Liao, H.; Coddet, C. Ionic Conductivity and Its Temperature Dependence of Atmospheric Plasma-Sprayed Yttria Stabilized Zirconia Electrolyte. Mater. Sci. Eng. B Solid-State Mater. Adv. Technol. (2007), 137 (1–3), 24–30, doi:10.1016/j.mseb.2006.10.005.

[25] Ghatee, M.; Shariat, M. H.; Irvine, J. Production of High Conductivity Composite Zirconia Solid Oxide Electrolytes with Good Mechanical Strength through Net-Shape. J. Mater. Chem. (2008), 18 (43), 5237–5242, doi:10.1039/b811486b.

[26] Pesce, A.; Hornés, A.; Núñez, M.; Morata, A.; Torrell, M.; Tarancón, A. 3D Printing the next Generation of Enhanced Solid Oxide Fuel and Electrolysis Cells. J. Mater. Chem. A (2020), 8 (33), 16926–16932, doi:10.1039/d0ta02803g.

Chapter-6:

CONCLUSIONS

The present thesis explores the introduction of the additive manufacturing techniques for ceramic device manufacturing in the energy and environmental field. Complementing the state-of-the-art of these technologies with the microstructural control of the studied materials and its connection with the performance on contaminant degradation devices and clean energy production via solid oxide fuel cell.

On the one hand, regarding the environmental applications, two different 3D printing method were addressed, binder jetting and fused deposition modelling, in order to study if print the catalyst support via BJ is better or not than directly catalyst printing via FDM.

In both 3D printing processes a helicoidal ceramic structure was fabricated with dimensions of 40×6 mm with an active area of 691.22 mm^2 each one. Thanks to the use of BJ and FDM technologies, several monoliths of $CaSO_4$ were obtained using BJ and other of TiO_2 were achieved via FDM with a high reproducibility during the fabrication on both processes. To measure the photodegradation of the methylene blue as emergent contaminant, four monoliths were used.

$CaSO_4$ monoliths were functionalised with the in-situ generation of TiO_2 via the route of $TiCl_4$ hydrolysis showing good adherence to the BJ 3D printed ceramic porous support after being fixed at 150°C. According photodegradation tests, it shows a 22% of MB absorbance and a 50% of degraded contaminant after 6 hours and almost a total conversion after 24 hours with a 92% of MB photoconverted. Fitting the photoconversion with a pseudo-second-order kinetic model, obtaining $k_{conversion}=1.71\times10^{-4}$ $mol^{-1}\cdot L\cdot min^{-1}$.

Porous and dense TiO_2 direct printed monolith were fabricated. Porous monolith had a 70% of inorganic powder of which 30% were pore former. Printing parameters were optimised at 215°C of extrusion temperature, 3.5 shell thickness, using a nozzle of 0.4 mm, a speed of printing of 25 mm/s and 0.1 mm of layer thickness. After printing structures were treated thermally under argon atmosphere at 900°C and sintered under air at 1200°C, achieving a shrinkage of 21% (*z axis)*, 25% (*y axis)* and 17% (*x axis)*. Adsorption test of dense and porous structures were pretty similar. Regarding photodegradation of MB porous the photocatalytic activity of dense devices is slightly lower than for porous catalyst with an 87% of MB conversion compared with 89% for the porous after 24 hours. Meaning that by increasing the porosity or achieving a nano-porosity, the fraction of photo-converted MB could be even higher. Also, the reutilisation of the catalyst was studied, resulting a better reutilisation for porous catalyst due to it experimented an 8% loss compared with a 62.7% loss for the dense monolith. Fitting the photoconversion with a pseudo-second-order kinetic model, $k_{porous}=5.44\times10^{-4}$ $mol^{-1}\cdot L\cdot min^{-1}$ and $k_{dense}=4.24\times10^{-4}$ $mol^{-1}\cdot L\cdot min^{-1}$.

Therefore, if the absorption of MB via two described processes are compared, the result is higher for the 3D direct catalyst than for the functionalised support. Which implies that the first nine

hours the percentage of photodegradation for the direct printed catalyst is higher, however, after 24 hours the total percentage of MB photoconverted is higher for the functionalised support. Hence, kinetics is higher for direct catalyst obtained via FDM, but the final result is better for the functionalised support obtained via BJ.

On the other hand, concerning to energy applications, other two different 3D printing methods were employed, stereolithography and digital light processing, to manufacture electrolytes for solid oxide fuel cells. Using in this work an SLA-commercial and a DLP-prototype printer with this purpose. Electrolytes were successfully produced using Spid3r printer (DLP prototype) employing a 70 wt.% of 8 %mol YSZ as ceramic powder, 2 wt.% of Triton™ X-100 as dispersant and Standard Blend resin as monomer and photoinitiator. This slurry presents a viscosity of 106 Pas at the typical shear rate of the Spid3r (0.071 s-1). The electrolytes were printed using 10 seconds as curing time achieving around 196 µm thickness layer. Three-dimensional plane electrolytes were sintered at 1350°C. The shrinkage factor is around 31–35% on *xy* axis and 20-24% on *z* axis. Finally, electrolyte 500 µm thickness were electrochemically characterised making a symmetrical cell LSM-YSZ/YSZ/LSM-YSZ. The optimum temperature for cathode attaching was 1100°C, achieving ionic conductivities values at 900°C of 0.054 ± 0.013 S/cm. Regarding the ASR data, finally it was concluded that the fabricated electrolyte-electrode layers are suitable for operation at T=750°C ($ASR_{pol}/2$=0.5 Ω·cm^2) or 850°C ($ASR_{tot}/2$=0.5 Ω·cm^2).

APPENDIX I: PRELIMINARY TESTS FOR ELECTRODES MANUFACTURING VIA ROBOCASTING

7.1 Introduction

Robocasting is a direct ink writing technique that is well known by its simplicity. As described in previous chapters, the slurry is contained into a syringe for extrusion by a nozzle when applying pressure. Objects are fabricated, layer-by-layer, by moving the nozzle to materialize the specific design. Robocasting relies on the rheology of the deposited paste and on the process from which each layer achieves consistency after deposition.

The great advantage of this process is the possibility of using different nozzles to print multiple materials with a single machine. However, each slurry should be developed individually since different chemical compositions require different optimization routes. On the other hand, the same feedstock can be used in formulations based on aqueous, solvent or photocurable vehicles giving the technique a great versatility. Despite this, in the ceramic field, robocasting has not been widely employed (compared to other 3D printing techniques such as inkjet). Nevertheless, an increasing interest is showed in the last years on the manufacturing of advanced ceramic materials[1] for specific fields such as catalysis with environmental applications, biocompatible materials with medical applications or electroceramic compounds for energy.[1–3]

In the literature, a common example of material employed for environmental applications is titanium dioxide that presents excellent catalytic, photocatalytic and sensing capabilities combined with a good bioactivity, biocompatibility, photocatalytic properties, catalytic performance, sensing capabilities, etc. Aleni *et al.*[4] developed robocasting slurries of this material and achieved barely dense (8.6% of porosity) and foamy structures with 180μm pore size (65% of porosity). Recently, Hajimirzaee[5] *et al.* reported catalytic material based on Pd:Pt, doped on Al_2O_3/HY zeolite and promoted by CeO_2, ZrO_2 and TiO_2 which was robocasted with a mesh cylinder shape with different angle rotation of the filament to achieve different porosity grades, in order to be employed in catalytic oxidation of methane.

In the field of biomedical materials production,[6] alumina,[7–10] hydroxyapatite,[11,12] zirconia[13] and tricalcium phosphate[14] are some examples of ceramic materials with well-controlled architecture. Lewis[12,15] was pioneer in this field making 3D ceramic structures of hydroxyapatite with submicron features more than a decade ago, which were though for bone scaffold. A decade after, Fu *et al.*[7] achieved lattices and auxetic alumina structures with a heterogeneous texture controlling this last parameter complementing robocasting technique with templated grain growth, being possible to achieve denser or more porous structures as needed. However, typically porous structures have been achieved due to solid loading and the debinding process, as Moon[8] or Rueschhoff [9] reported few years ago.

Finally, extensive research of functional ceramic for energy devices is reported in the literature, as supercapacitors and batteries[16–19] or solid oxide fuel cells [20–23]. *Lewis* and co-workers[19] reported $Li_4Ti_5O_{12}$ and $LiFePO_4$ microbattery on a gold current collector using multi-material printing via a robocaster with two nozzles, being favourably compared against literatures results in terms of both areal energy and power density. Carbon materials also were printed via robocasting for energy applications, an example of it was reported by Chen *et al.*[24] who printed full-packaged single wall carbon nanotube as supercapacitor, having a high energy density of 1.18 mWh cm^{-3}at a power density of 11.8 W cm^{-3}. Following with the same type of material, Zhu et al.[25] robocasted some graphene composite aerogel electrodes using a mesh pattern with thicknesses in the order of the millimetre. Two of these pieces were stacked together exhibiting a maximum gravimetric capacitance of 4.76 F g^{-1} at a current density of 400 mA g^{-1}.

In the last few years, 3D printing techniques have been employed for build SOFCs too, despite most of the AM process were not robocasting,[26] there are some research works focused on micro SOFCs. Kuhn *et al.*[21,23] have reported in some occasions μ-SOFC, firstly they developed anode and cathode printable slurries and optimizing the sintering process.[23] Then, they reported printed NiO anode and LSM cathode on a YSZ plate with two different curvilinear electrode geometries, achieving in both cases a power density of 0.9 V and 2.3 mWcm^{-2} at 700ºC.[21] In the same direction, Kim *et al.*[22] produced a similar cell but using a planar geometries for the electrodes, showing an open circuit voltage of 1.82 V and a maximum power of 35 mW at 800ºC.

As solid oxide fuel cell performance depends on many aspects, including the active surface of its components, this can be improved by modifying the geometry of the electrolyte and electrodes, hence the importance of applying 3D printing techniques for SOFC devices fabrication. As referenced, electrode fabrication by robocasting is still a matter of study, for this reason this work shows preliminary tests for electrode printing to develop LSM-YSZ formulations and further characterization slurries and optimisation of the printing. The goal is achieving a symmetrical cell completely via 3D printing process.

Specifically, depending on the chemical and physical properties of the materials to print, the robocasting technique could be applied using a slurry composition based on (i) aqueous, (ii) organic or (iii) photocurable formulation. The routes based on aqueous and organic formations require a controlled drying process that can generate fragile structures. The photocuring approach presents a better controlled and uniform consolidation process. However, it is not appropriate for ceramic compounds with high refractive index or absorption.[3] Alternative strategies based on thermo-curable processing, where polymerization is induced by the temperature, represents a more universal approach. This work will employ a combination of these processes.

7.2 Device Architecture

Several designs were used for this proof of concept. Cube and cylinder, *Figure 7. 1*) electrolyte shapes were designed in order to achieve a self-supported printed structure, which allows a standalone YSZ membrane. Filled circles were used for printing electrodes in both electrolyte faces, *Figure 7. 2*. The YSZ electrolyte was printed via SLA at IREC (Catalonia Institute for Energy Research) using the Ceramaker industrial printer already described in *Chapter 2, Section 2.1.3.1*. while the electrodes were deposited by robocasting BioX Cellink at DTU.

The electrolyte membrane has a diameter of 2.0 cm supported by an external ring of 2.5 cm of diameter. Regarding the YSZ thickness, two designs were proposed with 300 µm and 400 µm in thickness.

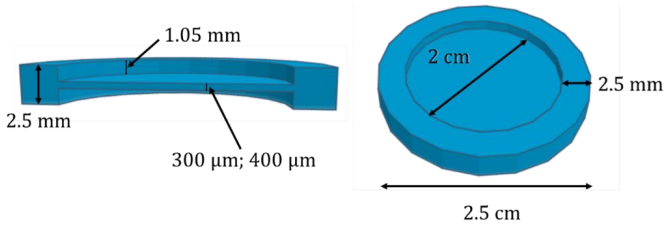

Figure 7. 1 Electrolyte design, cross section and top view

Regarding the electrode layer (yellow area), it presented a diameter of 1.5cm and 1.0mm in thickness.

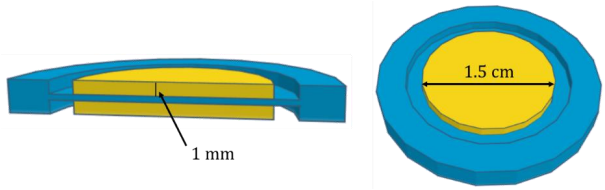

Figure 7. 2 Electrode design (yellow area)

7.3 Slurry composition

Most robocasting studies use evaporation of the solvent for solidification of the printed pastes, but this step consumes a lot of time and generally the resulting structures exhibit low mechanical resistance. For this reason, this work aims to explore different paste formulations where solidification takes place via a polymerization process, avoiding solvent evaporation.

The polymerization reaction needs to be initialized. In this work, thermal energy will be employed as initiator because the alternative UV-activation is hindered by the LSM strong absorption of the

UV-light. Thus, using thermal initiators, radicals are provided for the cross-linked polymeric matrix creation.

Thermal energy can be generated using a laser to enable local heating. However, this would need a complete and deep characterization of the thermal profile to ensure a good resolution. In this work, this is not required, and such a resolution study is out of the scope of the application in SOFCs.

The following sections describes the formulation of the employed robocasting slurries. Several factors influence the rheology of the slurry, so understanding them is useful to formulate an optimal suspension. As previously mentioned in Chapter 2, some of these parameters are size and morphology of the powder, particle interactions and viscosity of the paste.[27] *Table 7. 1* compiles the formulation of all the trial slurries employed in this annex. Please, refer to this table all along this annex in order to better understand how the performance of the different formulations correlate with their printability.

7.3.1 Ceramic powders

Electrode slurries were based on Lanthanum Strontium Manganite (LSM) material from Kceracell. Yttria-Stabilized Zirconia (YSZ) 8% mol (TOSOH) was employed for the electrolyte fabrication and also, in combination with LSM, for composite electrodes.

Two different LSM powders were employed during the development, namely, as-received and after calcination for 2h at 800ºC. According to results observed along this work, more problems arise using calcined LSM due to a poor rheological behaviour (see next section). Observing their microstructure, calcined LSM powder shows agglomerates (*Figure 7. 3 (c, d)*), not observed in as-received powder (*Figure 7. 3 (a, b)*). The particle agglomeration and the irregular shapes of the grains are likely in the origin of more viscous and unprintable pastes (see next section).

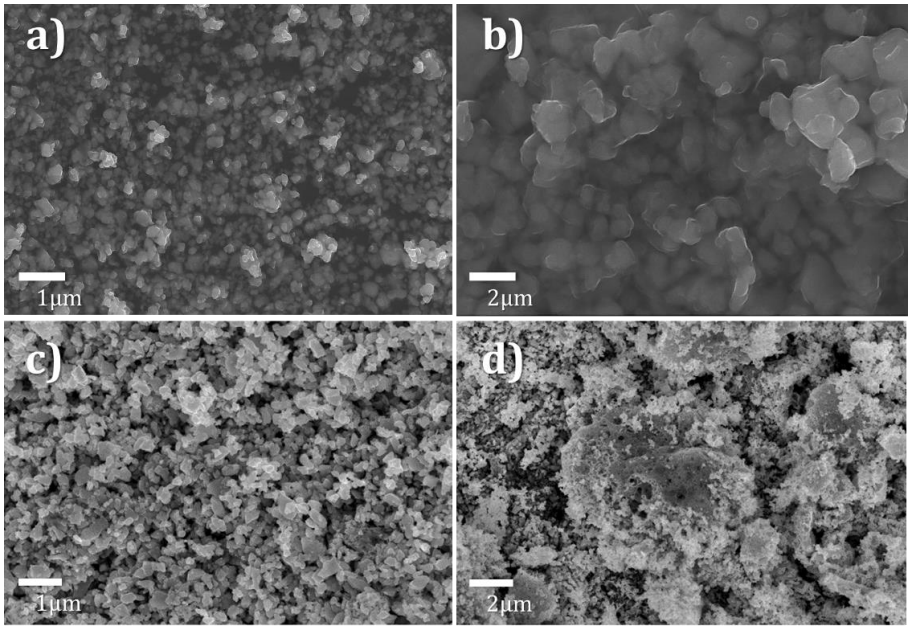

Figure 7. 3 (a & b) As-received LSM microstructure (c & d) Calcined LSM microstructure

7.3.2 Solvent

First formulation tests were based on water. It is generally known that YSZ is well dispersed in polar solvents as the water. However, LSM dispersion is a critical point because of its fast sedimentation. Previous research achieved a very low LSM dispersion at pH=10.[28] Beyond pure water-based solutions, propylene glycol (PG) was added in different proportions without a satisfactory result. Therefore, dispersant addition was studied in order to achieve a good stabilization for LSM powder.

7.3.3 Dispersant

As it was described in *Chapter 2, Section 2.1.5.3.3*, there are two different approaches for achieving a good dispersion: (i) use a dispersant as gelling agent (ii) use a dispersant that amplifies the inter-particles interactions. In this work, both strategies were employed to try to stabilize the powder solutions. The printability of the different slurry compositions, when different dispersants were added combined with other components, are shown in *Table 7. 1*.

7.3.3.1 Pluronic

According to the first approach, Pluronic F-127 was used as a gelling agent. Preliminary tests with different proportion of Pluronic were done, *Table 7. 1*. Different proportions of Pluronic were tested, adapting the ceramic powder, solvent and pH conditions. All the experiments used cold Pluronic (T <5˚C), which was in liquid state. However, when reaching room temperature, its viscosity substantially increased needing ball milling for a proper mixing. Therefore, mixtures were always done using ball milling at 200rpm for 10 min.

According with *Table 7. 1*, different percentages (1-4 wt. %) of Pluronic F-127 were added to the slurries (Slurry 1 - Slurry 6) using water and PG as solvent, but none of the formulas was printable. Using water, the issue was the bubbles presence in the paste because at room temperature the Pluronic was more viscous, being impossible to inject it. When PG was employed as solvent was not even possible to dissolve the dispersant.

Despite the fact that Pluronic is widely used as a gelling agent, usually added in 20 – 30wt. % to aqueous solutions to form a hydrogel, it was not a good strategy here, even decreasing the amount added. That could be due to the features of the LSM and YSZ, the size of the particles or even the temperature of the laboratory. If the printing process could be done at lower temperature (<22˚C), maybe Pluronic would be more liquid and printable slurry would be possible to prepare.

In summary, Pluronic is not a good dispersant for LSM and YSZ slurries because the mixture was extremely viscous mixing by stirring. On the other hand, mixing on a planetary milling resulted in the formation of bubbles caused by temperature rise.

7.3.3.2 Dispex® and Dolapix

Regarding the second strategy, Dispex® A40 (ammonium salt solution of an acrylic polymer in water) (Ciba-BASF, UK) and Dolapix CE64 ($C_4H_6O_2NH_4^+$) (Zschimmer & Schwarz) where used as a dispersant since they provide electrosteric stabilization of colloidal dispersions.

First of all, LSM sedimentation tests were carried out. In a test tube, calcined LSM was mixed with Dispex® (2.3 & 6.9 wt. %) using water as a solvent and modifying the pH by KOH addition. Then, sonication was employed studying the sedimentation of the solid particles in the tube. Despite different conditions were examined, all experiments end up with total sedimentation after 15 min. The same test was repeated using as-received LSM, which sedimented too, while YSZ formed a perfect suspension. Therefore, the difficulties to achieve a good suspension for LSM powder were confirmed being even more difficult if LSM was previously calcined. Changing sonication by planetary ball milling and using 1.5 wt. % Dispex®, the quality of the dispersions slightly improved

without presenting satisfactory results yet. When calcined LSM was used, agglomerations were formed in the slurry. For calcined YSZ the mixture presented a gritty aspect.

The results were improved, and printable paste was fabricated using LSM and YSZ (both as-received) mixed (1:1) using a range between 1.5 - 2.0 wt. % of Dispex®. However, after the fast drying and hardening, the cross section of the material shows a strong segregation of YSZ and LSM, *Figure 7. 4*. These globule aggregations suggest that segregation was driven by the minimization of the interaction area between the two materials.

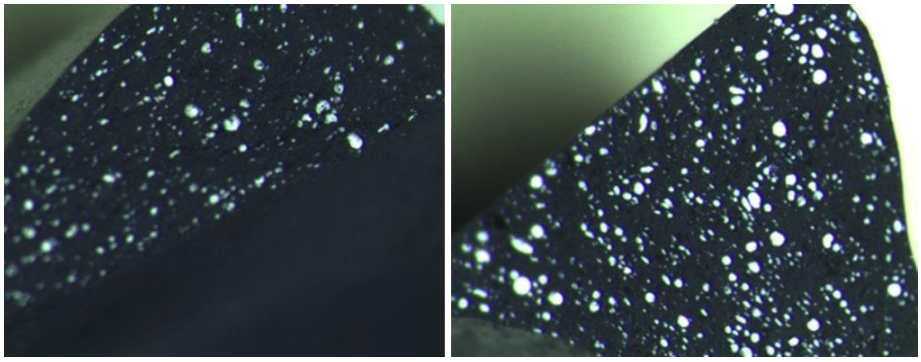

Figure 7. 4 YSZ and LSM segregation with Dispex® as dispersant

To avoid the fast drying and clogging into the nozzle, some additional tests were carried out adding some propylene glycol with water (1:1) trying to decrease the evaporation rate on the slurry. But the results were pretty similar than when only water is added.

As fast drying can be avoided changing the solvent, a new dispersant (Darvan) was employed in order to verify if YSZ segregation could be dismissed, but the results were not significantly improved.

At this point, the formula with Dispex®, whose results were most promising, was chosen. So the monomer (Am) and the crosslinker (BisA), *Chapter 2, Section 2.1.5.3.4*, were added to see if its effect improved the rheology of the paste to be printable, *Slurry 7, Table 7. 1*. The appearance of the mixture notably improved. Both powders were well suspended, and the viscosity decreased, which would facilitate the extrusion by a nozzle. Despite the good extrudability, the drying of the paste was still very fast clogging the injection system, not showing good enough printability.

As lower amount of powder cannot be either employed, since results in liquid slurries and LSM sedimentation, the use of Dispex® and Darvan were dismissed and new trials were carried out using Dolapix.

Dolapix-based pastes showed a promising printability, so following the formulation used for Am and BisA addition, *Slurry 8, Table 7. 1*. This time fast drying was reduced avoiding clogging the syringe (< 1min.).

Due to the promising results catalyst (TEMED) and initiator ($Na_2S_2O_8$) were added *Slurry 9 & 10, Table 7. 1*, but they reduced the viscosity, so 3D printed structures were not self-supported, losing the mechanical resistance and collapsing towards the centre of the objects as shown in *Figure 7. 5.* Despite catalyst and initiator amount were raised the result did not change.

Figure 7. 5 a) Digital square design; b) Fresh printed paste; c) Dried printed paste

7.3.3.3 Polyethylene glycol

To solve self-supporting issues, new formulations were proposed adding polyethylene glycol (PEG) as dispersant additive together with Dolapix, which provided mechanical stabilization mechanic steric due to its long chains, raising the viscosity and supplying better mechanical stability.

Different molar weights PEGs were used: 600 and 400,000 g/mol (Aldrich). Firstly, the PEG (MW: 600 g/mol) solubility in water was studied, managing to dissolve more than 60 wt. % resulting successful.

Beyond manual trials employed in previous formulations, from here on printable pastes were tested using the 3D printer, so other issues appeared due to printing parameters need to be optimized for each slurry formulation. For the best slurries, printing parameter are showed in the next section.

Continuing with the formulation of slurries, needle clogging was still a problem. It was also observed that printed structures dried first from the bottom (instead of from the surface). The absence of stabilised LSM particles in the paste could explain this phenomenon, because LSM would sediment in the bottom having less solvent than on the surface, therefore drying first. This hypothesis would explain why needles clogged, because in this case LSM particles would have preference drying in the walls of the needle, generating a solid film that blocks the extrusion.[29]

Analogue formulations employing LSM and YSZ powders were fabricated and compared to confirm if the clogging problems were directly related to a different powder nature. YSZ paste

(*Slurry 12, Table 7. 1)* is printable using plastic G18 and G20 nozzle while using the equivalent LSM slurry the nozzles clogged (*Slurry 13, Table 7. 1)*. This indicates that the different morphology of YSZ and LSM powder strongly affects the printability of the slurry.

As previously mentioned, in order to solve self-supporting issues, LSM pastes using increasing contents of PEG (MW: 400,000 g/mol) were fabricated, namely, *Slurries 14, 15 & 16, Table 7. 1.* Adding 0.4% of PEG *in Slurry 15* resulted in an acceptable printability. Using this optimum dispersant value, LSM and YSZ were added, *Slurry 18, Table 7. 1,* being possible to print a mesh cube. When monomer and crosslinker were added the viscosity decreased *Slurries 19 & 20, Table 7. 1*. Even so, it was possible to print them reaching a mesh structure. The printing parameter of the printed structures using the formulation of Slurry 17, 18, 19 and 20 will be described next *Section 7.3.4*.

7.3.4 Pore former

In the following formulations, graphite was added in order to raise the viscosity, to achieve a greater porosity of the electrode and to avoid clogging during printing. Different proportions of graphite were tested, using the same paste formulation and increasing graphite proportion, *Slurries 21, 22, 23 & 24, Table 7. 1*. The goal was to discover the maximum amount of graphite that could be added resulting in a printable slurry, being this amount 14.4wt. % as introduced in *Slurry 23*.

Introducing graphite had a big impact on the viscosity of the slurries as proved by measuring viscosities of slurries 21-24 with a rheometer (*Figure 7. 6*). Viscosity was compared to a commercial gel specifically optimized for robocasting applications (Cellink) showing higher values in all cases, which suggest the origin of most of the reported printing issues.

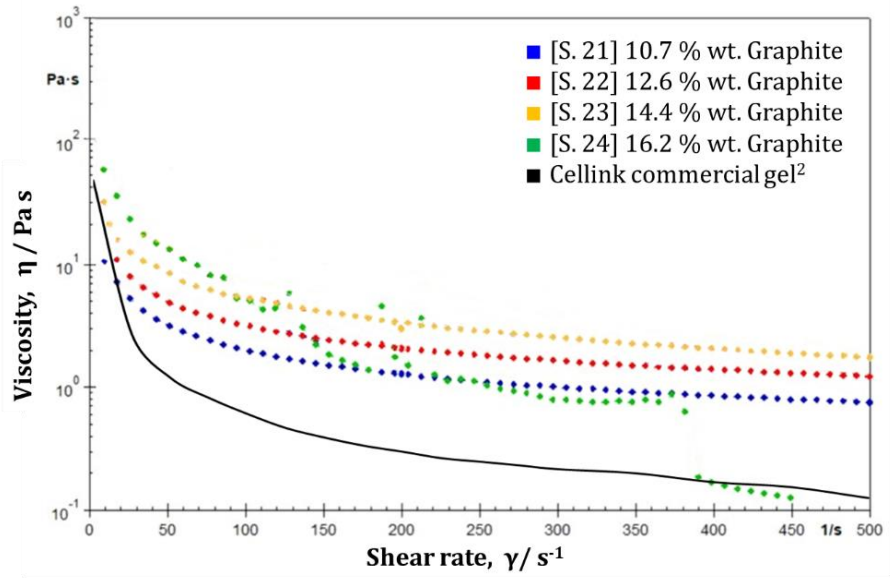

Figure 7. 6 Viscosity as a function of the shear rate for LSM-YSZ slurries with graphite. Slurry 21 with 10.7 wt. % of Graphite (blue); Slurry 22 with 12.6 wt. % of Graphite (red); Slurry 23 with 14.4 wt. % of Graphite (yellow); Slurry 24 with 16.2 wt. % of Graphite (green); Commercial robocasting gel (Cellink) is included for comparison.

Table 7. 1 Composition and printability of ceramic slurries developed for robocasting employing different types of solvents (water and PG), dispersants (Pluronic, Dispex and Dolapix) and other components as monomer, cross linker, catalyst. Initiator and pore former

Slurry	Powder	Solvent	Dispersant	Monomer	Crosslinker	Catalyst	Initiator	Pore former	Slurry characteristics / Printing issues	Printability
1	YSZ 80 %wt.	H_2O 16 %wt.	Pluronic 4%wt.	-	-	-	-	-	Too viscous to be injected	Not printable
2	LSM 74 %wt.	H_2O 22.2 %wt.	Pluronic 3.7%wt.	-	-	-	-	-	Too viscous to be injected	Not printable
3	YSZ-LSM (1:1) 80.7 %wt.	H_2O (pH=10) 18.3 %wt.	Pluronic 1%wt.	-	-	-	-	-	Bubbles presence. Gritty slurry	Not printable
4	YSZ-LSM (1:1) 79.3 %wt.	H_2O (pH=7) 18 %wt.	Pluronic 2.7%wt.	-	-	-	-	-	Bubbles presence. Gritty slurry	Not printable
5	YSZ-LSM (1:1) 73.9 %wt	PG 24.6%wt	Pluronic 1.5%wt.	-	-	-	-	-	Pluronic is insoluble in PG	Not printable
6	YSZ-LSM (1:1) 73.5 %wt	PG 24.5 %wt	Pluronic 2%wt.	-	-	-	-	-	Pluronic is insoluble in PG	Not printable
7	LSM-YSZ (1:1) 80 %wt.	H_2O 75.9 %wt.	Dispex® 1.8 %wt.	Am 3.5 %wt.	BisA 0.23 %wt.	-	-	-	Well dispersed powders, lower viscosity and easily extrusion by a nozzle. But clogs very fast.	Not enough printable
8	LSM-YSZ (1:1) 75.9 %wt.	H_2O 17.3 %wt.	Dolapix 3.1 %wt.	Am 3.5 %wt.	BisA 0.2 %wt.	-	-	-	Promising paste, it dries slower than Slurry 7.	Good promising printability

9	3.5 g of Slurry 8				TEMED 1.08%wt.	$Na_2S_2O_8$ 1.72%wt.	-	This mixture was printable and curable, but it is no self-supported. It needs more viscosity	Pintable but not self-supported
10	3.5 g of Slurry 8				TEMED 2.09%wt.	$Na_2S_2O_8$ 3.34%wt.	-	This mixture was printable and curable, but it is no self-supported. It needs more viscosity	Pintable but not self-supported
11	LSM-YSZ (1:1) 74.9 %wt.	H_2O (pH=10) 17.0%wt.	Dolapix 3.1 %wt. + PEG (600g/mol) 1.4%wt.	Am 3.4 %wt.	BisA 0.2 %wt.	-	-	LSM sedimentation	Printable but it does not dry
12	YSZ 77.8 %wt.	H_2O (pH=10) 17.7%wt.	Dolapix 3.2 %wt. + PEG (600g/mol) 1.3%wt.	-	-	-	-	Homogeneous and less viscous	Easy printable (plastic G18 G20)
13	LSM 77.8%wt.	H_2O (pH=10) 17.7%wt.	Dolapix 3.2 %wt. + PEG (600g/mol) 1.3%wt.	-	-	-	-	LSM clogs the nozzles	Not printable
14	LSM 78.7%wt.	$17.9H_2O$ (pH=10) %wt.	Dolapix 3.2 %wt. + PEG (400,000g/mol) 0.2%wt.	-	-	-	-	Good viscosity	Printable

15	LSM 78.6%wt.	H_2O (pH=10) 17.8%wt.	Dolapix 3.2 %wt. + PEG (400,000g/mol) 0.4%wt.	-	-	-	-	-	Printable
16	LSM 78.4 %wt.	H_2O (pH=10) 17.8%wt.	Dolapix 3.2 %wt. + PEG (400,000g/mol) 0.6%wt.	-	-	-	-	Too viscous	Not printable
17	LSM-YSZ (1:1) or YSZ 75.6 %wt.	H_2O (pH=10) 17.2 %wt.	Dolapix 3.1 %wt. + PEG (400,000g/mol) 0.5%wt.	Am 3.5 %wt.	BisA 0.2 %wt.	-	-	Good viscosity (but a bit liquid to be self-supported) for both mixtures.	Printable (metallic G18)
18	LSM-YSZ (1:1) 78.6 %wt.	H_2O (pH=10) 17.8%wt.	Dolapix 3.2 %wt. + PEG (400,000g/mol) 0.4%wt.	-	-	-	-	More viscous. The extrusion is self-supported. The paste dried after 1'41''	Printable and self-supported (metallic G18 and G20)
19	LSM-YSZ (1:1) 75.5 %wt.	H_2O (pH=10) 17.1%wt.	Dolapix 3.1 %wt. + PEG (400,000g/mol) 0.7%wt.	Am 3.5 %wt.	BisA 0.2 %wt.	-	-	Slurry 16 with monomer and crosslinker. Lower viscosity but a bit granulated	Printable (metallic G18)

20	LSM-YSZ (1:1) 75.7 %wt.	H_2O (pH=10) 17.2%wt.	Dolapix 3.1 %wt. + PEG (400,000g/mol) 0.3%wt.	Am 3.5 %wt.	BisA 0.2 %wt.	-	-	-	Slurry 18 with monomer and crosslinker. Lower viscosity. YSZ agglomeration after printed.	Printable (metallic G20)
21	LSM-YSZ (1:1) 65.4 %wt.	H_2O (pH=10) 18.7 %wt.	Dolapix 1.3 %wt.	Am 3.7 %wt.	BisA 0.2 %wt.	-	-	Graphite 10.7 %wt.	Very liquid	Printable but not self-supported
22	LSM-YSZ (1:1) 64 %wt.	H_2O (pH=10) 18.25%wt.	Dolapix 1.3 %wt.	Am 3.6 %wt.	BisA 0.2 %wt.	-	-	Graphite 12.6 %wt.	Very liquid	Printable but not self-supported
23	LSM-YSZ (1:1) 62.7 %wt.	H_2O (pH=10) 17.9%wt.	Dolapix 1.3 %wt.	Am 3.6 %wt.	BisA 0.2 %wt.	-	-	Graphite 14.4 %wt.	Better viscosity	Printable
24	LSM-YSZ (1:1) 61.5 %wt.	H_2O (pH=10) 17.5%wt.	Dolapix 1.2 %wt.	Am 3.5 %wt.	BisA 0.2 %wt.	-	-	Graphite 16.1 %wt.	Very viscous	Not printable

7.4 Printing process

Robocasting technique resolution depends on different printing parameters, including (i) nozzle size, (ii) pressure, (iii) speed of extrusion, and (iv) density of the design. However, these parameters change according to the rheology of the mixtures. Therefore, the control of the rheology is essential in this technology. Parameter printing optimization will be detailed for each printable slurry within this section.

Compositions of slurry 17 and 18 are similar with the only difference of the addition of Am and BisA in slurry 17, which notably influenced on the viscosity. That is why slurry 18 was more viscous than slurry 17, needing a higher pressure and a speed than slurry 17 (50 kPa; 10mm/s vs 40 kPa; 15 mm/s).

Tables 7. 2 & 7. 3 show 3D structures printed with slurry 17 (only small high was possible) and using slurry 18 (3D grid cube was produced), which was the mixture without the monomer and the crosslinker. Slurry 18 had walls so well defined that only a small portion of the surface was in contact between them. In the image perfect filaments touching them in a small point can be observed. This is a desired achievement from the technical point of view, but for electrodes application is not the best structuration possible. This fact means that for electrode fabrication more liquid pastes are required.

Alternatively, slurry 17 was employed to produce YSZ parts, being more successful than with LSM-YSZ mixtures[30] For this reason, both receipts were modified for LSM-YSZ mix powders. Slurry 17 was modified increasing the amount of and, accordingly to the results obtained with slurry 18, adding Am and BisA obtaining a more liquid paste.

Table 7. 2 Slurry 17: printing parameters and printed structures

Slurry 17			
Nozzle size	G18 (metallic)		
Extrusion Pressure	40kPa		
Printing Speed	15 mm/s		
Fill density	90 %	10mm	10mm

Table 7. 3 Slurry 18: printing parameters and printed structures

Slurry 18		
Nozzle size	G18-G20 (metallic)	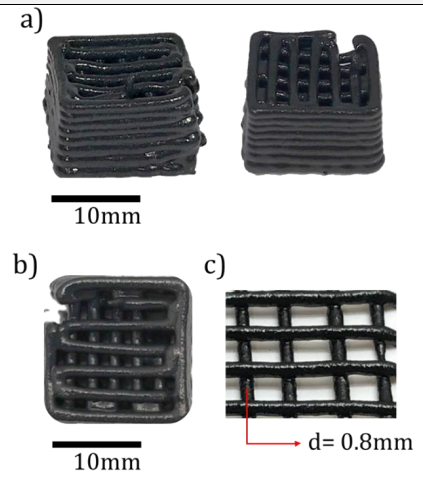
Pressure	50 kPa	
Speed	10 mm/s	
Fill density	80 %	

When printability of slurry 19 was studied, *Table 7. 4*, the nozzle size and printing speed kept as the in previous pastes (G18; 15 mm/s) but an increasing of required pressure was observed due to its higher amount of added PEG. This mixture had a granulated aspect that reduced the printing resolution. So, it is corroborated that an slight excess of PEG 400,000 produces a jump in viscosity.[31] For this reason, this slurry was discarded although the printed parts were optimum.

Table 7. 4 Slurry 19: printing parameters and printed structures

Slurry 19		
Nozzle size	G18 (metallic)	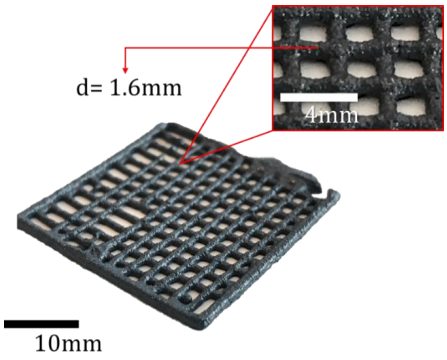
Pressure	80 kPa	
Speed	15 mm/s	
Fill density	70 %	

Printing parameters related to slurry 20, *Table 7. 5* show that a smaller nozzle size could be employed (G20), which ultimately would improve the resolution. That is due to the presence of monomer and crosslinker in the sample. When it was printed, agglomeration of YSZ particles was

observed indicating poor dispersion of LSM and YSZ powders. It can be due to when Am and BisA addition since the proportion of the other compounds decrease regarding the total mixture weight, discarding the Slurry 20 for this agglomeration.

Table 7. 5 Slurry 20: printing parameters and printed structures

Slurry 20		
Nozzle size	G20 (metallic)	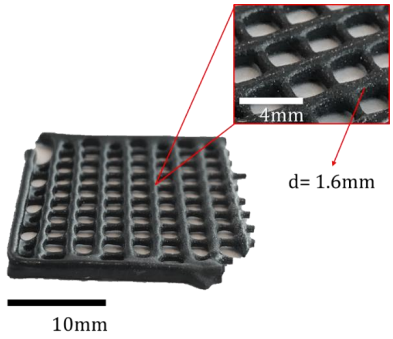
Pressure	45 kPa	
Speed	10 mm/s	
Density	60%	

Finally, mixture with pore former, slurry 23, was printed using the parameters showed in Table 7. 10. Effectively, graphite produced a better lubrication avoiding nozzle clogging. Therefore, G20 nozzles could be used and the 3D structure was completely homogeneous. The walls were not so sharply defined as with previous slurries, but they were stiff enough to allow stacking of layers. Pressure raised due to a smaller nozzle, but good flow of the slurry was finally achieved. Overall, similar appearance than slurry 17 was reached. In summary, graphite addition led to viscosity stabilization raising and good printability.

Table 7. 1 Slurry 23: printing parameters and printed structures

Slurry 23		
Nozzle size	G20 (metallic)	
Pressure	90 kPa	
Speed	15 mm/s	
Density	90%	

7.5 Preliminary test on full cells fabrication

Different layer combination was explored to study a single step sintering program (co-sintering) for a full cell with electrodes and electrolyte. For this, it is essential to match the shrinkages of both materials (including removal of organics). As this is a critical point, different approaches were preliminary tested to produce the cells in the future: (i) the use of robocasting technique for the cathode and the electrolyte fabrication, (ii) the use of robocasting for the cathode and inkjet printing for the electrolyte production (iii) the use of robocasting for the cathode and SLA for the electrolyte.

i. Robocasting for the combined cathode and electrolyte production

For this approach, slurry 17 was chosen for the electrolyte production, while slurry 23 was used for cathode production. The proposed symmetrical cell had a pyramidal architecture, *Figure 7. 7*, to avoid that slurry of the cathode was in contact and producing short-circuits.

During printing process, the printer had to be calibrated between different materials, because different pastes require different printing parameters.

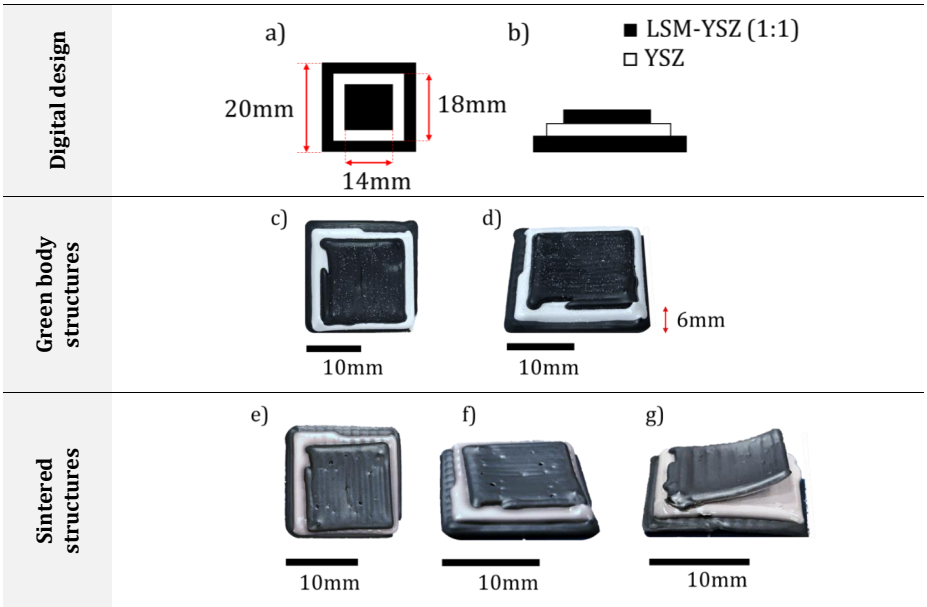

Figure 7. 7 Symmetrical SOFC composition designs produced by robocasting [LSM(graphite)-8YSZ/8YSZ/LSM(graphite)-8YSZ]. a) Digital design top view; b) Digital design front view; c) Green body of SOFC top view; d) Green body of SOFC front view, e) Sintered SOFC top view; f & g) Sintered SOFCs front view

In total, three layers of 2 mm in thickness were printed. Two different tests were carried out, using YSZ slurry with and without one drop of catalyst and initiator, to achieve polymerization process via thermal activation (30 min, 45-50°C). As-printed structures were both similar, but after the curing process of the acrylamide, cracking occurred because they were dried and a bit bended before polymerising. This effect could be originated by the stress generated while water was evaporating giving place to cracks. After the sintering program, the results were different because the polymerised cell conserved its shape, *Figure 7. 7 (f)*, while the one not polymerised presented delamination *Figure 7. 7 (g)*. Therefore, the polymerization process seems a critical step during the manufacturing process and should be carried out avoiding a fast drying.

The sintering coefficient was measured by comparing initial and final dimensions, and it results of ca. 20%. The microstructure was measured by SEM. *Figure 7. 8.* shows its cross section that reveals an almost full densification without interconnected porosity. *Figure 7. 8 (a)* presents the microstructure of the cross section of the cell. Air bubbles are observed, probably introduced during the printing process. Since the printing pressure is constant, the origin of the bubbles it is likely coming from a bad filling of the syringe. Due to the high viscosity of the pastes, it was not possible to follow the usual air removal of the pastes by sonication before the filling of the cartridges. *Figure 7. 8 (a, b, c & d)* show images of the interface between the YSZ electrolyte and the LSM-YSZ electrode. The attachment seems to be adequate and homogenous all along the interface. *Figure 7. 8 (e & f)* shows the densification level of the electrolyte and the electrode. It can be observed an electrolyte that is not fully dense, although open porosity is not present. This indicates that the sintering temperature is still low to achieve a fully dense electrolyte but, probably, it could be used since gas tightness is possible with closed porosity. On the other hand, the electrode looks porous but not as much as expected for electrodes. In *Figure 7. 8 (f)* elongated pores can be observed likely due to the graphite pore former, nevertheless they were not connected forming a percolating network.

Overall, the current level of density of the electrolyte could be enough for practical applications indicating the suitability of the robocasting technique for printing this element. However, the limitation in thickness of the robocasting layers should be considered since thinner electrolytes are always preferred. In this regard, inkjet printing is considered a better option. Regarding the electrode, formulations presented here should be improved to increase the porosity of final layer (at least at the high sintering temperature presented here). Different pore formers and in higher proportion could allow to reach this goal, especially those intended for generating interconnected porosity.

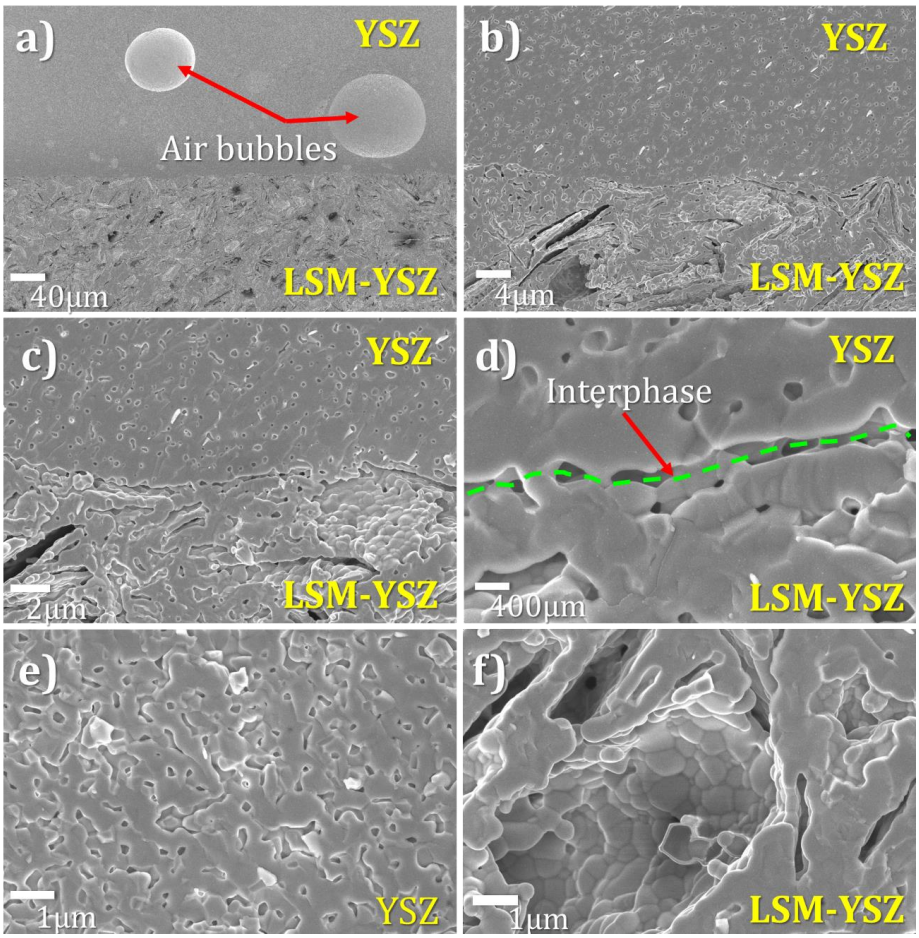

Figure 7. 8 Cross section of cell robocasted with slurry 23 for the LSM-YSZ cathode (yellow), and slurry 17 for the YSZ electrolyte (green). (a, b, c & d) Interphase between electrolyte and electrode magnification; (e) YSZ electrolyte; (f) LSM-YSZ cathode electrode.

ii. Robocasting for the cathode and inkjet printing for the electrolyte production

In order to reduce the thickness of the electrolyte, inkjet printing was proposed for its fabrication. Two trials were attempted, printing YSZ electrolytes made of 3 layers, *Figure 7. 9 (c)* and of 18 layers, *Figure 7. 9 (d).*

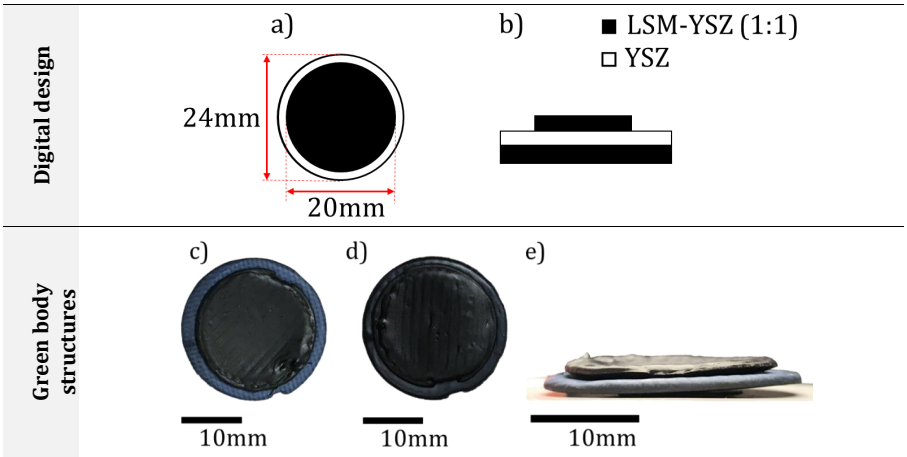

Figure 7. 9 Symmetrical SOFC composition designs. Cathode produced by robocasting and electrolyte made by inkjet printing. [LSM(graphite)-8YSZ/8YSZ/LSM(graphite)-8YSZ. a) Digital design top view; b) Digital design front view; c) Green body of SOFC with 3 layers of electrolyte, top view; d) Green body of SOFC with 18 layers of electrolyte, top view, e) Dried SOFC with 18 layers of electrolyte, front view.

Firstly, the cathode was done via robocasting. Once it was dried, the electrolyte was inkjet printed and, finally, the second cathode was fabricated on top of the bilayer via robocasting. Top cathode layer was delaminated after drying due to a poor attachment between the new cathode layer and the smooth inkjet printed electrolyte. In this preliminary test, the need for adhesion layers between inkjet and robocasting layers is evidenced. On the other hand, the quality of the electrolyte is promising. *Figure 7. 10* shows the microstructure a high-density level was achieve when YSZ electrolyte ink-jetted was sintered.

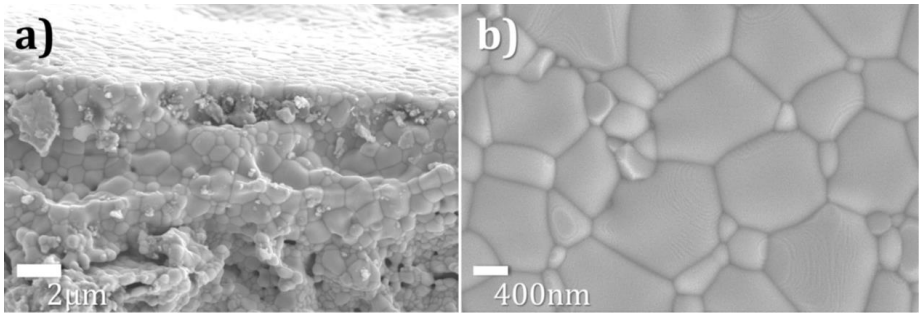

Figure 7. 10 Microstructure corresponding to YSZ ink jetted. (a) Electrolyte cross section (b) Electrolyte top view

In summary, inkjet printing for electrolyte fabrication combined with robocasting for electrode production seems to be a good option, because the attachment is improved. In the future, this work can be recovered after the cathode slurry is optimised with a good level of interconnected porosity.

iii. Robocasting for the cathode and SLA for the electrolyte production

In this last approach, the SLA commercial printer described and employed during the *Chapter 5* is used to print the electrolyte. Printed electrolytes were provided by IREC under the Cell3Ditor EU project. Slurry 23 was employed for robocasting of the electrodes. The digital design was the one explained in *Section 7. 2* of this appendix.

The first cathode face was printed on one side of the cured SLA electrolyte *Figure 7. 11 (a)*. After cathode drying, complete delamination occurred *Figure 7. 11 (b)*. Therefore, it was not possible to even deposit the second cathode neither co-sintering the full piece.

As in the previous trial based on inkjet printed electrolytes, the smoothness of the layer evidenced the need of a well-optimized adhesion layer. A certain improvement could be achieved with another electrolyte designs that secure cathode slurry to electrolyte, (not a plane electrolyte) or even trying to print a roughness layer first and then depositing the electrode. So, can be concluded that there is a lot of work ahead. Part of this work it has been developed in Cell3Ditor project[32] which involved other thesis[33] which continued in this path.

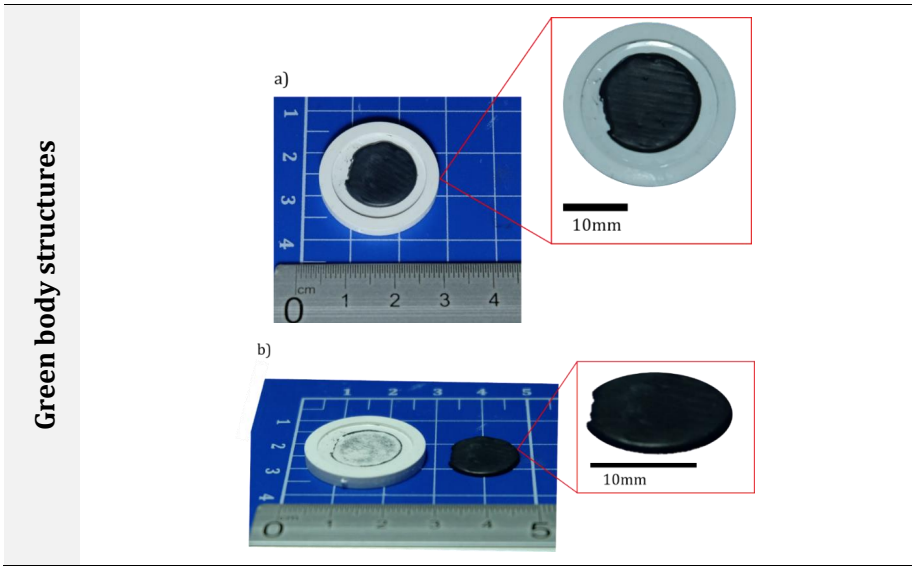

Figure 7. 11 Symmetrical SOFC composition designs. Fresh (a) and dried (b) cathode produced by robocasting and electrolyte made by SLA. [LSM(graphite)-8YSZ/8YSZ/LSM(graphite)-8YSZ

7.6 References

[1] Chen, Z.; Li, Z.; Li, J.; Liu, C.; Lao, C.; Fu, Y.; Liu, C.; Li, Y.; Wang, P.; He, Y. 3D Printing of Ceramics: A Review. J. Eur. Ceram. Soc. (2019), 39 (4), 661–687, doi:10.1016/j.jeurceramsoc.2018.11.013.

[2] Peng, E.; Zhang, D.; Ding, J. Ceramic Robocasting: Recent Achievements, Potential, and Future Developments. Adv. Mater. (2018), 30 (47), 1–14, doi:10.1002/adma.201802404.

[3] Zhang, D.; Jonhson, W.; Herng, T. S.; Ang, Y. Q.; Yang, L.; Tan, S. C.; Peng, E.; He, H.; Ding, J. A 3D-Printing Method of Fabrication for Metals, Ceramics, and Multi-Materials Using a Universal Self-Curable Technique for Robocasting. Mater. Horizons (2020), 7 (4), 1083–1090, doi:10.1039/c9mh01690b.

[4] Aleni, A. H.; Kretzschmar, N.; Jansson, A.; Ituarte, I. F.; St-Pierre, L. 3D Printing of Dense and Porous TiO2 Structures. Ceram. Int. (2020), 46 (10), 16725–16732, doi:10.1016/j.ceramint.2020.03.248.

[5] Hajimirzaee, S.; Doyle, A. M. 3D Printed Catalytic Converters with Enhanced Activity for Low-Temperature Methane Oxidation in Dual-Fuel Engines. Fuel (2020), 274 (April), 117848, doi:10.1016/j.fuel.2020.117848.

[6] Entezari, A.; Liu, N. C.; Roohani, I.; Zhang, Z.; Chen, J.; Sarrafpour, B.; Zoellner, H.; Behi, M.; Zreiqat, H.; Li, Q. On Design for Additive Manufacturing (DAM) Parameter and Its Effects on Biomechanical Properties of 3D Printed Ceramic Scaffolds. Mater. Today Commun. (2020), 23 (March) doi:10.1016/j.mtcomm.2020.101065.

[7] Fu, Z.; Freihart, M.; Wahl, L.; Fey, T.; Greil, P.; Travitzky, N. Micro- and Macroscopic Design of Alumina Ceramics by Robocasting. J. Eur. Ceram. Soc. (2017), 37 (9), 3115–3124, doi:10.1016/j.jeurceramsoc.2017.03.052.

[8] Moon, Y. W.; Choi, I. J.; Koh, Y. H.; Kim, H. E. Macroporous Alumina Scaffolds Consisting of Highly Microporous Hollow Filaments Using Three-Dimensional Ceramic/Camphene-Based Co-Extrusion. J. Eur. Ceram. Soc. (2015), 35 (16), 4623–4627, doi:10.1016/j.jeurceramsoc.2015.08.017.

[9] Rueschhoff, L.; Costakis, W.; Michie, M.; Youngblood, J.; Trice, R. Additive Manufacturing of Dense Ceramic Parts via Direct Ink Writing of Aqueous Alumina Suspensions. Int. J. Appl. Ceram. Technol. (2016), 13 (5), 821–830, doi:10.1111/ijac.12557.

[10] Feilden, E.; Blanca, E. G. T.; Giuliani, F.; Saiz, E.; Vandeperre, L. Robocasting of Structural Ceramic Parts with Hydrogel Inks. J. Eur. Ceram. Soc. (2016), 36 (10), 2525–2533, doi:10.1016/j.jeurceramsoc.2016.03.001.

[11] Michna, S.; Wu, W.; Lewis, J. A. Concentrated Hydroxyapatite Inks for Direct-Write Assembly of 3-D Periodic Scaffolds. Biomaterials (2005), 26 (28), 5632–5639, doi:10.1016/j.biomaterials.2005.02.040.

[12] Lewis, J. A.; Smay, J. E.; Stuecker, J.; Cesarano, J. Direct Ink Writing of Three-Dimensional Ceramic Structures. J. Am. Ceram. Soc. (2006), 89 (12), 3599–3609, doi:10.1111/j.1551-2916.2006.01382.x.

[13] Stanciuc, A. M.; Sprecher, C. M.; Adrien, J.; Roiban, L. I.; Alini, M.; Gremillard, L.; Peroglio, M. Robocast Zirconia-Toughened Alumina Scaffolds: Processing, Structural Characterisation and Interaction with Human Primary Osteoblasts. J. Eur. Ceram. Soc. (2018), 38 (3), 845–853, doi:10.1016/j.jeurceramsoc.2017.08.031.

[14] Miranda, P.; Saiz, E.; Gryn, K.; Tomsia, A. P. Sintering and Robocasting of β-Tricalcium Phosphate Scaffolds for Orthopaedic Applications. Acta Biomater. (2006), 2 (4), 457–466, doi:10.1016/j.actbio.2006.02.004.

[15] Sun, L.; Parker, S. T.; Syoji, D.; Wang, X.; Lewis, J. A.; Kaplan, D. L. Direct-Write Assembly of 3D Silk/Hydroxyapatite Scaffolds for Bone Co-Cultures. Adv. Healthc. Mater. (2012), 1 (6), 729–735, doi:10.1002/adhm.201200057.

[16] Zhu, C.; Liu, T.; Qian, F.; Chen, W.; Chandrasekaran, S.; Yao, B.; Song, Y.; Duoss, E. B.; Kuntz, J. D.; Spadaccini, C. M.; et al. 3D Printed Functional Nanomaterials for Electrochemical Energy Storage. Nano Today (2017), 15, 107–120, doi:10.1016/j.nantod.2017.06.007.

[17] Wei, M.; Zhang, F.; Wang, W.; Alexandridis, P.; Zhou, C.; Wu, G. 3D Direct Writing Fabrication of Electrodes for Electrochemical Storage Devices. J. Power Sources (2017), 354, 134–147, doi:10.1016/j.jpowsour.2017.04.042.

[18] Jiang, P.; Ji, Z.; Zhang, X.; Liu, Z.; Wang, X. Recent Advances in Direct Ink Writing of Electronic Components and Functional Devices. Prog. Addit. Manuf. (2018), 3 (1–2), 65–86, doi:10.1007/s40964-017-0035-x0123456789.

[19] Sun, K.; Wei, T. S.; Ahn, B. Y.; Seo, J. Y.; Dillon, S. J.; Lewis, J. A. 3D Printing of Interdigitated Li-Ion Microbattery Architectures. Adv. Mater. (2013), 25 (33), 4539–4543, doi:10.1002/adma.201301036.

[20] Ruiz-Morales, J. C.; Tarancón, A.; Canales-Vázquez, J.; Méndez-Ramos, J.; Hernández-Afonso, L.; Acosta-Mora, P.; Marín Rueda, J. R.; Fernández-González, R. Three Dimensional Printing of Components and Functional Devices for Energy and Environmental Applications. Energy Environ. Sci. (2017), 10 (4), 846–859, doi:10.1039/c6ee03526d.

[21] Kuhn, M.; Napporn, T.; Meunier, M.; Therriault, D.; Vengallatore, S. Fabrication and Testing of Coplanar Single-Chamber Micro Solid Oxide Fuel Cells with Geometrically Complex Electrodes. J. Power Sources (2008), 177 (1), 148–153, doi:10.1016/j.jpowsour.2007.11.013.

[22] Kim, Y. B.; Ahn, S. J.; Moon, J.; Kim, J.; Lee, H. W. Direct-Write Fabrication of Integrated Planar Solid Oxide Fuel Cells. J. Electroceramics (2006), 17 (2–4), 683–687, doi:10.1007/s10832-006-6005-11083200660051.

[23] Kuhn, M.; Napporn, T.; Meunier, M.; Vengallatore, S.; Therriault, D. Direct-Write Microfabrication of Single-Chamber Micro Solid Oxide Fuel Cells. J. Micromechanics Microengineering (2008), 18 (1) doi:10.1088/0960-1317/18/1/015005.

[24] Chen, B.; Jiang, Y.; Tang, X.; Pan, Y.; Hu, S. Fully Packaged Carbon Nanotube Supercapacitors by Direct Ink Writing on Flexible Substrates. ACS Appl. Mater. Interfaces (2017), 9 (34), 28433–28440, doi:10.1021/acsami.7b06804.

[25] Zhu, C.; Liu, T.; Qian, F.; Han, T. Y. J.; Duoss, E. B.; Kuntz, J. D.; Spadaccini, C. M.; Worsley, M. A.; Li, Y. Supercapacitors Based on Three-Dimensional Hierarchical Graphene Aerogels with Periodic Macropores. Nano Lett. (2016), 16 (6), 3448–3456, doi:10.1021/acs.nanolett.5b04965.

[26] Zhakeyev, A.; Wang, P.; Zhang, L.; Shu, W.; Wang, H.; Xuan, J. Additive Manufacturing: Unlocking the Evolution of Energy Materials. Adv. Sci. (2017), 4 (10) doi:10.1002/advs.201700187.

[27] M. N. Rahaman. Ceramic Processing, Second Edi.; CRC Press, Ed.; (2017) ISBN: 978-1-4987-1641-3.

[28] Gómez, L.; Colomer, M. T.; Escobar, J.; Moreno, R. Manufacture of a Non-Stoichiometric LSM Cathode SOFC Material by Aqueous Tape Casting. J. Eur. Ceram. Soc. (2013), 33 (6), 1137–1143, doi:10.1016/j.jeurceramsoc.2012.12.002.

[29] M'Barki, A.; Bocquet, L.; Stevenson, A. Linking Rheology and Printability for Dense and Strong Ceramics by Direct Ink Writing. Sci. Rep. (2017), 7 (1), 1–10, doi:10.1038/s41598-017-06115-04159801706.

[30] Shao, H.; Zhao, D.; Lin, T.; He, J.; Wu, J. 3D Gel-Printing of Zirconia Ceramic Parts. Ceram. Int. (2017), 43 (16), 13938–13942, doi:10.1016/j.ceramint.2017.07.124.

[31] Nojoomi, A.; Faghihi-Sani, M. A.; Khoshkalam, M. Shear-Rate Dependence Modeling of Gelcast Slurries: Effects of Dispersant Content and Solid Loading. Ceram. Int. (2014), 40 (1 PART A), 123–128, doi:10.1016/j.ceramint.2013.05.112.

[32] IREC, DTU, FAE, 3DCeram, Promethean Particles, ULL, SAAN Energy, H. Cell3Ditor project http://www.cell3ditor.eu/.

[33] Rosa, M. Development of Printing Media for Digital Manufacturing of Fuel Cells., Technical Univeristy of Denmkar (DTU), (2019).

APPENDIX II: PRELIMINARY TESTS TO USE OF 3D PRINTING BIOFUEL PRODUCTION

8.1 Introduction

As mentioned in *Chapter 1, Section 1.2.4*, one of the alternatives to reduce fossil fuel consumption is biofuel production. Biofuels assists to reduce both (i) waste, because it can be used as starting material during biofuel synthesis, and (ii) the emission of hydrocarbons, particles and carbon monoxide into the atmosphere.

One route for biofuel production is via the transesterification of vegetables oils, including the use of cooking oil waste.[1] This reaction happens in the presence of an alcohol (methanol) in order to produce fatty acid alkyl esters and glycerol, *Figure 1. 13*.[2] However, the Achilles' heel of this process was the possible hydrolysis and saponification reactions during the course of the main reaction, due to the presence of water and free fatty acids in the media.
A possibility for improving this reaction is by using a catalyst. As described, the goal is to carry out a heterogeneous catalytic reaction because it offers some advantages, i.e. the possibility of recycling and reusing several times the catalyst. In this context, 3D printing techniques are a good strategy to fabricate this catalyst, allowing: (i) saving time and minimising waste, and (ii) the possibility of generating complex geometries that will offer novel approaches to boost the performance.

Previous studies were based on catalysts placed into the fixed-bed reactor[3,4] or suspended.[5] However, a new goal is proposed in this work, based on preliminary tests that apply AM techniques to produce structured catalysts. More specifically, the goal was to produce a structured 3D catalyst that may simultaneously act as stirring system, thereby improving the contact with the reactants, avoiding the use of slurry reactors and allowing easier reusability of the catalytic material.

8.2 Device architecture

This work employed FDM technique using PLA filament to fabricate negative polymeric moulds that will be filled with a slurry containing the catalyst (pumice) and removed to achieve the shaped monolithic catalyst.

At the beginning, several bladed designs with different shapes were proposed: star, asterisk and gear, *Figure 8. 1 (a, b & c)*. As blades must be as long as possible to ensure a good stirring during the reaction, but they should offer the lowest resistance to the solution. In the case of the second model, *Figure 8. 1 (b)*, the blades exhibit the same width both at the end and the base (7mm). As with the third design, *Figure 8. 1 (c)*, blades are even wider at the ends (11mm) than at the base (8mm). Thus, both designs offered a high mechanical resistance during the stirring, which caused blades breaking down as the tension at their ends was larger than at the centre of the design. On

the other hand, the star design, *Figure 8 .1 (a)* offered the opposite of the other designs. Therefore, star design was chosen for the trials.

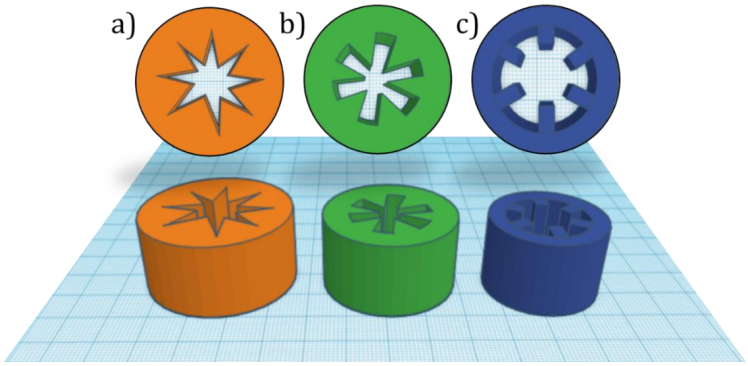

Figure 8. 1 Bladed designs for the catalyst stirrer

The design was further optimised by fabricating an eight-pointed symmetric star with a cylinder in the middle to avoid a design whose parts are subjected to stress gradients that could trigger the monolith collapse during the experiment. *Figure 8. 2* shows the mould dimensions appropriate for the cylindrical reactor whose diameter is 7 cm.

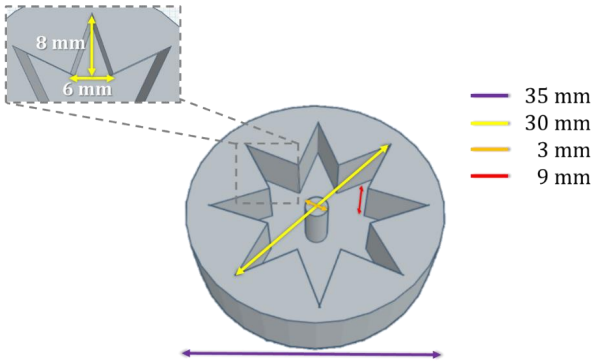

Figure 8. 2 Digital design measurements of the mould for the catalyst

8.3 Optimization of the fabrication

In this section, the procedure for the manufacture of the catalyst paste and the implementation process of the FDM technique for its shaping are described.

8.3.1 Feedstock

Among all possible catalysts for biodiesel production commented in *Chapter 1*, this work used potassium hydroxide loaded on an amorphous aluminium silicate support. This support is naturally occurring as an extremely porous volcanic rock known as pumice, although in the present work, commercial pumice was the choice (pumice stone granules technical grade, PanReac).

As mentioned before, this work used FDM for printing the negative mould for the catalyst, but the catalyst was not directly 3D printed. However, it was a preliminary test as proof of concept of the catalyst slurry which could be employed in Robocasting technique, avoiding the mould manufacturing and producing a complex structure

Robocasting is a direct printing, hence it is necessary to print self-supported parts. To achieve that a viscous slurry must be done. This fact implies a very load solvent or a cured slurry using UV or IR light (depending on the printer).

The paste developed was based on typical tape casting slurries adapted to pumice material. The slurry is composed by: (i) catalyst powder, (ii) solvent, (iii) dispersant, (iv) plasticizer and (v) binder as detailed on *Table 8. 1*.

Table 8. 1 Composition of pumice paste

Components	Amount (g)
Pumice	10
Butanone & ethanol (3:2, w/w)	10
Triton-Q	0,5
Dibutyl phthalate	2
Butvar® B98	1

Firstly, the pumice was conditioned via ball milling. 15 g of pumice powder were placed into zircona milling jars with 6 zirconia balls (d=10mm) and covered with acetone. The mixture was ball-milled at 200 rpm for 20h. Then, it was dried at 70°C for 30 min to acetone evaporation rendering the powders ready for paste preparation. The slurry was prepared by first mixing all the liquid components by mild magnetic stirring and then the pumice powders were added. The resulting slurry was further ball milled at 200 rpm for 2h.

8.3.2 Fabrication process

The negative moulds were 3D-printed using the next printing parameters:,(i) at a 50 mm/s speed printing, (ii) thickness layers of 100µm, (iii) extruder temperature at 215°C, (iv) bed temperature at 30°C, (v) and a 30% of infill. Once the moulds and pumice paste were ready, the moulds were filled. Initially, few drops of the solvent were added to the mould to ensure that all the corners were filled, thus avoiding free spaces formed by surface tension of the mixture with the mould.

Paste filling was carried out using a Pasteur pipette. To avoid holes inside the monolithic catalyst, mould filling was performed in a layer by layer fashion and waiting between them to allow solvent evaporation at room temperature. Depending on the thickness layer, evaporation could take be between 15-60 min. This process was repeated until covering all the negative mould.

In this work, removing the catalyst from the rigid PLA mould was difficult and consequently a thermal treatment was done at 1000°C for 4h (5°C/min) to generate the shaped catalyst. Then, a second thermal treatment was performed at 1400°C for 4h (5°C/min) to sinter the catalyst structure. The final structure is shown in *Figure 8. 3 (b)*. Nevertheless, flexible PLA could be employed in order to remove easily the catalyst at room temperature, avoiding the first thermal treatment, which would have saved time and energy.

On the other hand, in the future this slurry could be applied for robocasting technique, though the amount of solvent must be decreased to achieve a higher viscosity of the paste and avoiding longer times for solvent evaporation. In addition, solvent evaporation could be assisted by UV or IR light or increasing the bed temperature of the printer.

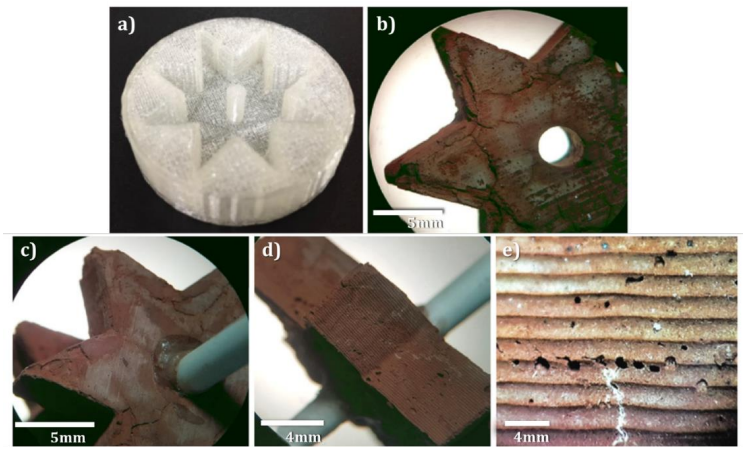

Figure 8. 3 (a) PLA Negative mould printed by FDM. (b,c,d) Structured pumice catalyst sintered at 1400°C. (e) Sintered pumice catalyst with holes due to solvent evaporation

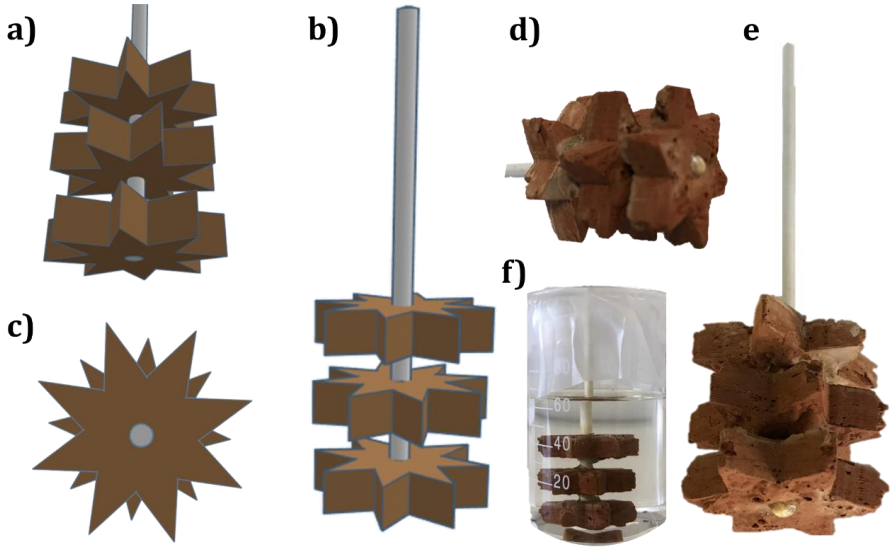

Figure 8. 4 Digital scheme of the catalyst stirring structures joined to stirrer axis (a &b) front view and (c) bottom view. Real catalyst structures joined to stirrer axis (d & e) front view, (f) structures submerged on KOH solution for activation.

Biodiesel production was studied according to the number of catalytic stirrers present on the solution *Figure 8. 4*. The experiment was carried out using one, two and three catalyst pieces to confirm that using more catalytic pieces, the performance raised. These results will be discussed on the next section related to catalytic performance.

8.3.3 Functionalization

Catalytic structures were attached to the rotating axis of the stirring system. Before functionalisation with K, pumice monoliths were dried at 120°C for 2h to avoid the presence of water during the transesterification reaction. Potassium hydroxide (KOH) loading was carried out via immersion in KOH 1M solution for 24h and further dried at 120°C.

The catalytic activity depends mainly on the KOH loading[3,6,7] and, on the amount of catalyst used. Thus, before using the 3D printed catalytic stirrers for biodiesel production reaction, KOH loading was optimized in a previous work using catalytic particles in the2.4-4.0 mm range in a packed-bed reactor.[8] The best results were achieved for 6.2wt. % KOH loading.

8.4 Characterization

Functionalization studies were carried out via infrared spectroscopy (IR) using a Thermo Nicolet Avatar 360 FTIR, using KBr disks in the 400–4000 cm^{-1} range.

The FT-IR spectra, *Figure 8. 5*, reveals the characteristic peaks of pumice at 400, 800 and 1100cm^{-1}. The first two (400 and 800 cm^{-1}) may result from Si–O bending strength vibrations of the amorphous quartz, which constitutes the structure of the pumice. The strong peak (1100 cm^{-1}) may come from Si–O stretching vibrations.[9,10] The peaks detected at 1640 and 3400 cm^{-1} are associated to OH stretching vibrations of the water[11] that was adsorbed by the catalyst sample, which is further evidence of the need of drying stages. However, the OH stretching vibration of the hydroxyl groups due to KOH are around 1400cm^{-1} and are not present in the IR spectrum of the support.[12]

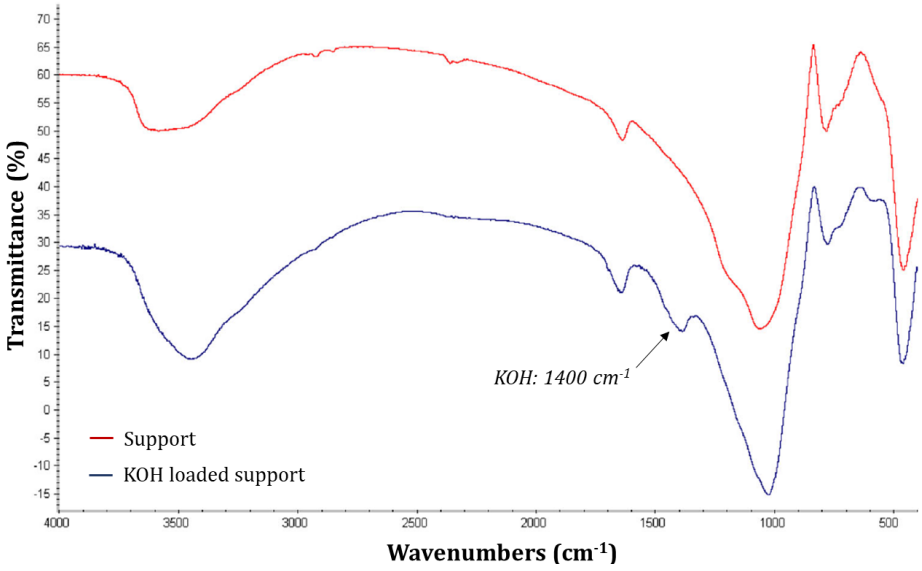

Figure 8. 5 IR spectra of pumice support and functionalised support

Finally, the microstructure characterisation was carried out via SEM. *Figure 8. 6* show SEM images of the catalytic support material *(a & b)* and the same material after activation with 6.2 wt. % of KOH load *(c, d, e & f)*.

According to XRD, *Figure 8. 7*, pumice is amorphous and the corresponding SEM images reveals irregular morphologies and 0.5 – 2.0 µm pores the micrographs, pumice (aluminium silicate) is amorphous and present irregular shapes and 0.5 - 2.0 µm pores. In addition, it is important to emphasize that these pores did not intersect each other, *Figure 8. 6 (a & b).*

In summary, these images illustrate the little of porosity of the material that could provide a large surface area for KOH attachment, which in turn increases the active sites to boost the system performance.

Subtle changes were observed after the KOH treatment, *Figure 8. 6 (c, d, e & f),* including a lower proportion of pores and the presence of needle-shaped crystals produced during the impregnation. Even *Figure 8. 6 (c, d, e & f)* shows the fiber of KOH produced as result of the impregnation.

Regarding KOH distribution EDS was done for pumice and KOH loaded pumice sample, *Figure 8. 8*. On the one hand it shows different elements in a colour range where the base of the sample is yellow corresponding to Si and green for the O which are the principal elements of the pumice as it is shown on *Figure 8. 8 (a).* On the other hand, *Figure 8. 8 (b)* clearly shows an orange distribution corresponding to K element, being uniform in all the surface. In summary, the material surface after KOH loading revealed a good dispersion. Therefore, it can be concluded that the morphology of the raw material was modified when the sample was impregnated on KOH solution.

Hg porosimetry and N_2 adsorption-desorption measurements revealed further information regarding the porosity of the specimens. The specific surface area was measured via N_2 adsorption-desorption, the catalytic support presented 0.587 m^2/g, while the catalytic support impregnated with KOH presented 0.389 m^2/g, as previously reported by Soetaredjo *et al.*[13] Finally, regarding the meso or macroporous surface, bulk porosity and the pore diameter were obtained via Hg porosimetry. The results are shown in *Table 8. 2* and they prove that the porous structure changed as consequence of KOH loading producing a macroporous sample (pore diameter > 50 nm).

Table 8. 2 Structural characteristics of the tested material

Sample	S_{BET} (m^2/g)	S (m^2/g)	ε (%)	D (nm)
Catalytic support	0.587	27.63	56.3	76.3
Catalytic support impregned with KOH (6.2 wt. %)	0.389	10.93	43.9	145.3

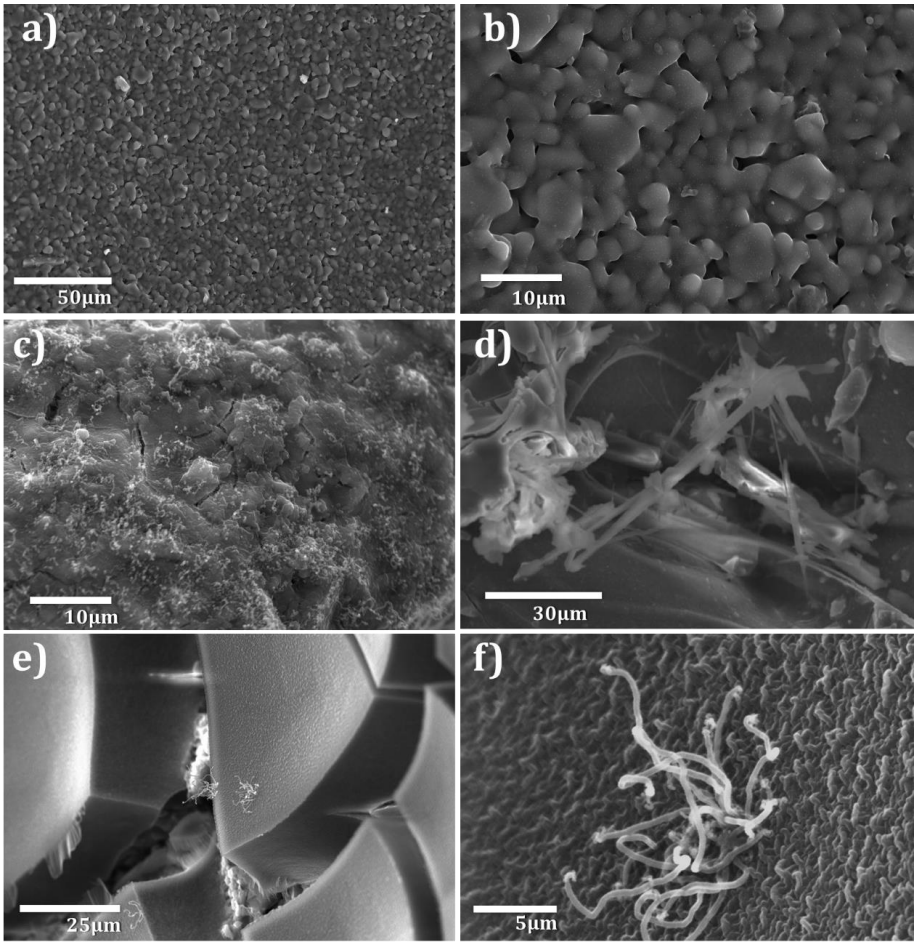

Figure 8. 6 SEM images of the (a & b) catalytic support material, (c & d) the catalytic support material after the KOH-loading impregnation (6.2 wt. %) and (e & f) a magnification of KOH loaded pumice sample with fibrous structure of KOH

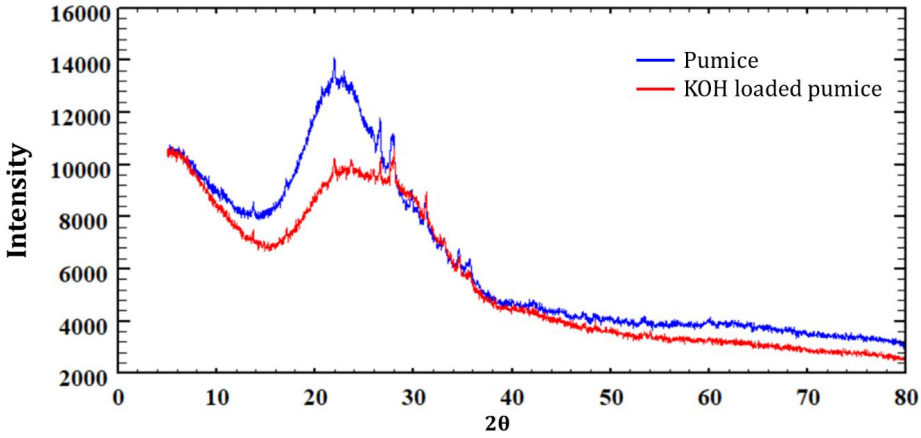

Figure 8. 7 XRD of the pumice sample and the KOH loaded pumice sample

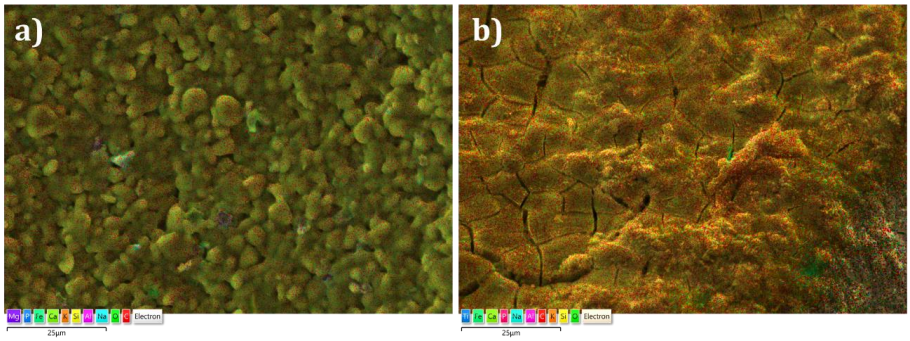

Figure 8. 8 EDS of the (a) pumice sample and (b) the KOH loaded pumice sample

8.5 Catalytic Performance

Regarding the catalytic test for biodiesel production, they were carried out at 55°C in an Autoclave Engineers PA USA reactor (200 ml) equipped with a methanol condenser and mechanical stirring system.

Commercial sunflower oil and methanol were employed for biodiesel production, with 24:1 molar ratio (methanol/oil). Also, free fatty acid model compound was added (0.2-6% %wt.) based on oil weight, for testing the activity of pumice.

When the reaction was finished, biodiesel was collected after the products were separated from the catalyst, methanol was evaporated, and glycerol was separated using a funnel.

The impact of the number of catalytic stirrers on the reaction was evaluated and there were no reaction rate differences under these experimental conditions. However, the biodiesel production increased with the number of catalytic stirrers used (% of catalyst amount related to methanol/oil), *Figure 8. 9*. In order to measure the performance of the experiment, the pieces of the catalyst were extracted from the reactor after the reaction finished. Then methanol was evaporated and glycerol (a derivate of the reaction) was separated. Finally, the biodiesel was analysed by ^{1}H nuclear magnetic resonance spectrometry using the method reported in literature.[14,15] The maximum yield was 96% which was attained after 2h using 3 catalytic stirrer pieces. This 96% of yield corresponds with 73% and 26% for biodiesel and glycerine products, respectively. This yield is the same to that obtained using particles of the catalytic material in a slurry reaction.

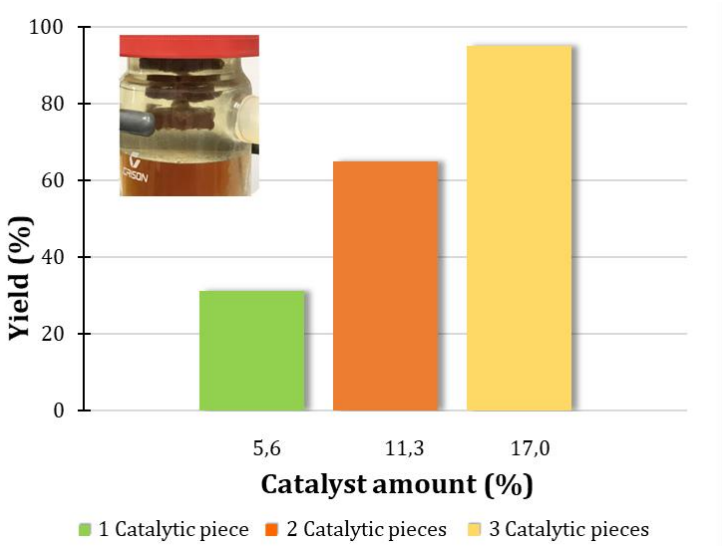

Figure 8. 9 Biodiesel production yields using different numbers of catalyst stirrer pieces

8.6 Conclusions

Following a conventional tape casting recipe, a pumice-based slurry was produced to fill polymeric moulds and generate structured monolithic catalysts. A negative mould made by FDM with PLA was 3D printed and filled with the developed mixture in a layer by layer fashion. The main step of this process was waiting for each filled layer to dry as evaporation of the solvent must be gradual to avoid crack formation, which could compromise the structure of the monolith.

Once dried, the mould was burnt at 1000°C for 4h and structured monolithic catalyst was obtained. Finally sintering thermal process was realised at 1400°C for 4h.

The catalytic material, 3D micro-structured for the stirring system, showed enough mechanical strength and, indeed, the monoliths did not break during the reaction despite being subjected to great stress during the experiment as they also act as stirrers. Therefore, it can be concluded that they are an efficient and reusable catalytic system, showing the same high activity for the biodiesel production reaction than the catalytic particles used in a slurry reaction system.

Some advantages of using this 3D catalyst stirrer are an easy product separation and continuous operation point of view were observed. So, it can be concluded that using 3D printing for biofuel production is a novelty that brings good solutions for catalyst production.

Concluding that this preliminary test is successful, being the next step the application of the pumice slurry for robocasting.

8.7 References

[1] Ooi, X. Y.; Gao, W.; Ong, H. C.; Lee, H. V.; Juan, J. C.; Chen, W. H.; Lee, K. T. Overview on Catalytic Deoxygenation for Biofuel Synthesis Using Metal Oxide Supported Catalysts. Renew. Sustain. Energy Rev. (2019), 112, 834–852, doi:10.1016/j.rser.2019.06.031.

[2] Yazdani, S. S.; Gonzalez, R. Anaerobic Fermentation of Glycerol: A Path to Economic Viability for the Biofuels Industry. Curr. Opin. Biotechnol. (2007), 18, 213–219, doi:10.1016/j.copbio.2007.05.002.

[3] Borges, M. E.; Díaz, L. Catalytic Packed-Bed Reactor Configuration for Biodiesel Production Using Waste Oil as Feedstock. Bioenergy Res. (2013), 6, 222–228, doi:10.1007/s12155-012-9246-7.

[4] Rodríguez, L. D. Procesos de Catálisis Heterogénea Para La Obtención de Biodiésel. Utilización de Aceite de Jatropha Curcas y Aceites de Fritura Como Materias Primas., (2017).

[5] Borges, M. E.; Díaz, L.; Alvarez-Galván, M. C.; Brito, A. High Performance Heterogeneous Catalyst for Biodiesel Production from Vegetal and Waste Oil at Low Temperature. Appl. Catal. B Environ. (2011), 102, 310–315, doi:10.1016/j.apcatb.2010.12.018.

[6] Díaz, L.; Borges, M. E. Low-Quality Vegetable Oils as Feedstock for Biodiesel Production Using k-Pumice as Solid Catalyst. Tolerance of Water and Free Fatty Acids Contents. J. Agric. Food Chem. (2012), 60 (32), 7928–7933, doi:10.1021/jf301886d.

[7] Borges, M. E.; Ruiz-Morales, J. C.; Díaz, L. Improvement of Biodiesel Production through Microstructural Engineering of a Heterogeneous Catalyst. J. Ind. Eng. Chem. (2013), 19 (3), 791–796, doi:10.1016/j.jiec.2012.10.019.

[8] Borges, M. E.; Hernández, L.; Ruiz-Morales, J. C.; Martín-Zarza, P. F.; Fierro, J. L. G.; Esparza, P. Use of 3D Printing for Biofuel Production: Efficient Catalyst for Sustainable Biodiesel Production from Wastes. Clean Technol. Environ. Policy (2017), 19 (8), 2113–2127, doi:10.1007/s10098-017-1399-9.

[9] Ersoy, B.; Sariisik, A.; Dikmen, S.; Sariisik, G. Characterisationof Acidic Pumice and Determination of Its Electrokinetic Properties in Water Characterization of Acidic Pumice

and Determination of Its Electrokinetic Properties in Water. Powder Technol. (2010), 197 (1–2), 129–135, doi:10.1016/j.powtec.2009.09.005.

[10] Guler, U. A.; Sarioglu, M. Removal of Tetracycline from Wastewater Using Pumice Stone: Equilibrium , Kinetic and Thermodynamic Studies. J. Environ. Heal. Sci. Eng. (2014), 12 doi:10.1186/2052-336X-12-79.

[11] Grim, R. E. Clay Mineralogy; McGraw-Hill, Ed.; New York, (1968)0070248362 9780070248366.

[12] Li, Y.; Qiu, F.; Yang, D.; Li, X.; Sun, P. Preparation, Characterization and Application of Heterogeneous Solid Base Catalyst for Biodiesel Production from Soybean Oil. Biomass and Bioenergy (2011), 35 (7), 2787–2795, doi:10.1016/j.biombioe.2011.03.009.

[13] Soetaredjo, F. E.; Ayucitra, A.; Ismadji, S.; Maukar, A. L. KOH/Bentonite Catalysts for Transesterification of Palm Oil to Biodiesel. Appl. Clay Sci. (2011), 53 (2), 341–346, doi:10.1016/j.clay.2010.12.018.

[14] Gelbard, G.; Brès, O.; Vargas, R. M.; Vielfaure, F.; Schuchardt, U. F. 1H Nuclear Magnetic Resonance Determination of the Yield of the Transesterification of Rapeseed Oil with Methanol. J. Am. Oil Chem. Soc. (1995), 72 (10), 1239–1241, doi:10.1007/BF02540998.

[15] Borges, M. E.; Díaz, L.; Gavín, J.; Brito, A. Estimation of the Content of Fatty Acid Methyl Esters (FAME) in Biodiesel Samples from Dynamic Viscosity Measurements. Fuel Process. Technol. (2011), 92 (3), 597–599, doi:10.1016/j.fuproc.2010.11.016.

FINANCIAL SUPPORT

This doctoral thesis has been realized by the next financial support:

- Convocatoria proyecto de investigación dentro del Programa Estatal de Investigación, Desarrollo e Innovación Orientada a los "Retos de la Sociedad" del Ministerio de economía y competitividad, Gobierno de España. Ref. ENE2013-47826-C4-1-R.

- Convocatoria proyecto de investigación dentro del Programa Estatal de Investigación, Desarrollo e Innovación Orientada a los "Retos de la Sociedad" del Ministerio de economía y competitividad, Gobierno de España. Ref. ENE2016-74889-C4-2-R.

- Convocatoria proyecto de investigación bajo el marco del Programa Horizon 2020, bajo RIA-FCH2-JU, de la Unión Europea. Ref. 700266-Cell3Ditor.

- Convocatoria de becas destinadas a cursar estudios universitarios de grado y posgrado (Concurso General de Becas), curso 2015/2016; 2016/2017; 2017/2018; 2018/2019; 2019/2020.

- Convocatoria de becas de movilidad europea de estudiantes, bajo el Programa Erasmus+, bajo la modalidad "Student Mobility for Traineeship (STM)", curso 2018/2019.

NATIONAL AND INTERNATIONAL STAYS

During the preparation of this thesis, the PhD student has realized stays in relevant research centres for his own formation as scientific researcher:

- Advanced Material for Energy department, in Catalonia Institute for Energy Research (IREC), Barcelona, Spain. This stay was supervised by Dr. Albert Tarancón Rubio, from 14th November 2016 to 25th de November 2016

- St Andrews Centre for Advanced Materials, School of Chemistry of the University of St. Andrews, Scotland, United Kingdom. This stay was supervised by John T.S. Irvine from 20th April 2017 to 20th June 2017

- Fuel Cells and 3D printing laboratory research team, in Institute of renewable energies in University of Castilla La Mancha, Albacete, Spain. This stay was supervised by Jesús Canales Vázquez from 9th July 2018 to 31st July 2018

- Department of Energy Conversion and Storage in the Technical University of Denmark. This stay was supervised by Vincenzo Esposito, from15th November 2018 and 3rd January 2019

- Advanced Material for Energy department, in Catalonia Institute for Energy Research (IREC), Barcelona, Spain. This stay was supervised by Dr. Albert Tarancón Rubio, from 3rd June 2019 to 2nd August 2019

CONFERENCE ATTENDANCE

- XI Congreso de estudiantes de la Sección de Química, San Cristóbal de La Laguna, **Spain**, 2015
  Impresión 3D de materiales cerámicos para aplicaciones medioambientales

- 17ª Reunión Bienal del Grupo Especializado de Química Inorgánica de la RSEQ y la 11ª Reunión Bienal del Grupo Especializado de Química del Estado Sólido de la RSEQ (QIES), Torremolinos, **Spain**, 2016
  Impresión 3D de materiales cerámicos para aplicaciones medioambientales

- XX Semana Científica Antonio González, San Cristóbal de La Laguna, **Spain**, 2016.
  Impresión 3D de biomateriales utilizando luz visible

- XIII Congreso de Estudiantes de la Sección de Química, San Cristóbal de La Laguna, **Spain**, 2017.
  Impresión 4D de polímeros con memoria de forma

- XXXVI Reunión BIENAL de la Real Sociedad Española de Química 2017, Sitges, **Spain**, 2017.
  Caracterización electroquímica de componentes de Pilas de Combustible de Óxidos Sólidos impresas en 3D

- XXI Semana Científica Antonio González, San Cristóbal de La Laguna, **Spain**, 2017.
  Impresión 3D para producción de biodiesel

- 2º International Conference on 3D Printing Technology and Innovations, London, **UK**, 2018
  SLA-3D Printed Electrolytes for Solid Oxide Fuel Cells

- 2º International Conference on 3D Printing Technology and Innovations, London **UK**, 2018
  3D Printing to biodiesel production by photocatalysis - [Award-winning]

- XIV Congreso de Estudiantes de la Sección de Química, San Cristóbal de La Laguna, **Spain**, 2018
  Aplicaciones de la impresión 3D usando materiales conductores

- 18ª Reunión Del Grupo Especializado De Química Inorgánica y 12ª Reunión Del Grupo Especializado De Química De Estado Sólido (QIES), San Cristóbal de La Laguna, **Spain**, 2018

Impresión 3D mediante SLA de electrolito de YSZ para pilas de combustibles SOFC

- 13th EUROPEAN SOFC & SOE FORUM, Luzern, **Switzerland**, 2018
  SLA 3D Printed electrolytes for solid oxide fuel cells

- Young Ceramist Additive Manufacturing Forum (yCAM), Mons, **Belgium**, 2019
  SLA 3D Printing for solid oxide fuel cells

- *7th Shaping Conference, Aveiro, **Portugal**, 2019*
  TiO_2-Based energy devices produced by FDM 3D printing - [Award-winning]

PUBLICATIONS

- **Fabrication and characterisation of ceramics via low-cost DLP 3D printing**
  Giftymol Varghese; Mónica Moral; Miguel Castro García; Juan José López López; JuanRamón Marín Rueda; Vicente Yagüe Alcaraz; Lorena Hernández Afonso; Juan Carlos Ruiz Morales; Jesus Canales Vázquez
  Boletín de la Sociedad Española de Cerámica y Vidrio, 57, 9 – 18, ELSEVIER, (2017)

- **Use of 3D printing for biofuel production: efficient catalyst for sustainable biodiesel production from wastes.**
  M. E. Borges, L. Hernández, J. C. Ruiz-Morales, P. F. Martín-Zarza, J. L. G. Fierro, P. Esparza
  Clean Technologies and Environmental Policy,19, 2113–2127, (2017)

- **Ceramic-Based 3D Printed Supports for Photocatalytic Treatment of Wastewater**
  Lorena Hernández-Afonso; Ricardo Fernández González; Pedro Esparza; María Emma Borges; Selene Díaz González; Jesús Canales Vázquez; Juan Carlos Ruiz Morales.
  Journal of Chemistry, 0 – 9, (2017)

- **Three dimensional printing of components and functional devices for energy and environmental applications**
  Juan Carlos Ruiz Morales; Albert Tarancón; Jesús Canales Vázquez; Jorge Méndez Ramos; Lorena Hernández-Afonso; Pablo Acosta Mora; Juan Ramón Marín Rueda; Ricardo Fernández González.
  Energy & Environmental Science, 10, 846-859, (2017)